The Dissertation Committee for Xu Liu Certifies that this is the approved version of the following Dissertation:

Application of Reactive Melt Extrusion for Bioavailability Enhancement and Modified Drug Release

Committee:

Feng Zhang, Supervisor

Robert O. Williams, III

Hugh D.C. Smyth

James C. DiNunzio

Application of Reactive Melt Extrusion for Bioavailability Enhancement and Modified Drug Release

by

Xu Liu

Dissertation

Presented to the Faculty of the Graduate School of

The University of Texas at Austin

in Partial Fulfillment

of the Requirements

for the Degree of

Doctor of Philosophy

The University of Texas at Austin

May 2020

Dedication

To my parents and grandparents for their unconditional love and encouragement during this

journey !

Acknowledgements

The completion of my doctoral degree and dissertation would have been impossible without the support and encouragement of many people over the last five years. Firstly, I would like to express my deepest appreciation and gratitude to my supervisor, Dr. Feng Zhang for his excellent mentorship, generous help, and continuous support throughout the journey of my graduate studies. Dr. Feng Zhang's passion for research and his dedication fundamentally influence my career and life. In addition, I would like to thank Dr. Chuanbin Wu's recommendation and supporting my decision to pursue a Ph.D. degree at the University of Texas at Austin. I also want to express my great appreciation to my committee members, Dr. Robert O. Williams for his generous guidance on my courses and research projects, Dr. Hugh D. C. Smyth for his precious suggestion on my paper writing and graduate study. Dr. James C. DiNunzio's valuable advice during my internship at Merck.

Many thanks to my mentors during my COOP at Merck. Dr. Hanmi Xi, Dr. Majid Mahjour, Dr. Yongchao Su's creative and constructive guidance significantly increase my horizon and impact my career path. I would like to express my appreciation to Dr. Wei Xu, Dr. Michael McNevin, Dr. Daniel Skomski, Dr. Zhen Liu, Dr. Jingtao Zhang, Dr. Kenneth Rosenberg and all preformulation group members for their active input and valuable advice.

I am grateful to work with all faculty members, graduated and current students at Molecular Pharmaceutics and Drug Delivery department. I wish to express my thankfulness to Dr. Maria A. Croyle and Dr. Debadyuti Ghosh's support on my TA work. Dr. Zhengrong Cui's valuable advice and guidance on my research and career life. I also would like to thank Dr. Meng Fan, Mr. Tongzhou Liu, Ms. Nada Kittikunakorn, Dr. Shahab Kashani Rahimi, Mr. Yi Zhang, Ms. Jamie Spahn, Dr. Abbe Haser, Dr. Zachary Warnken, Dr. Julien Maincent, Dr. Ju Du and Dr. Ping Du, Mr. Xiangyu Ma, Ms. Willy Sawittree Sahakijpijarn, Dr. Chaeho Moon, Dr. Hairui Zhang, Ms. Yajie Zhang, Mr. Xinquan Liu, Dr. Scott Jermain, Dr. Soraya Hengsawas, Dr. Siyuan Huang,

Abstract

Application of Reactive Melt Extrusion for Bioavailability Enhancement and Modified Drug Release

Xu Liu, Ph.D.

The University of Texas at Austin, 2020

Supervisor: Feng Zhang

Hot melt extrusion (HME) has been widely applied to prepare amorphous solid dispersions (ASD) to improve the oral bioavailability of BCS Class II and Class IV compounds by increasing their kinetic solubility and dissolution rate. During the HME process, drug, polymer and other excipients are introduced into the barrel at different temperature setting and feed rates. The intermeshing screws mix and melt all materials using heat and an intense mechanical shearing force to achieve distributive and dispersive mixing and excellent homogeneity. The molecular level mixing allows close contact between API and excipients at high frequencies, which provide favorable environment to build drug-excipient intermolecular interactions to improve the physicochemical properties of ASD.

Even though there are extensive reports about the pharmaceutical application of HME, most of the studies have been restricted to the manufacture of drug delivery systems where no clearly defined molecular level interaction are produced. Since the extrusion process is a high temperature and aggressive molecular level mixing process, lot of interactions would occur during the extrusion process, such as the ionic interaction, hydrogen bonding, pi-pi interaction, Van der Walls forces and lipophilic-lipophilic interactions. The rational design interactions between drug and excipients during the HME process would provide an inspiring strategy to overcome the drawback of HME, such as the thermal degradation of drug, poor physical stability of drug during the storage time or dissolution process. For ASD development, the polymer carriers play a critical

role in stabilizing the drug amorphous state. Polymer selection to prepare the ASDs is largely empirical. There is a need for rational polymer selection, enabling design of stable amorphous solid dispersion. Drug-polymer interactions have been observed to improve the physical stability of ASDs. Supramolecular synthon approach has been applied to design cocrystal with adjusting physicochemical properties. What's more, supramolecular synthon approach has been exploited to design ASD with exceptional physical stability. Based on all those non-covalent interactions, it is possible to achieve the in-situ modification of solid forms of active pharmaceutical ingredients by mechanochemistry using extrusion process, without changing the pharmacology of the API.

The major goal of this research is to explore rational design interaction between drug and excipients during the HME process to prepare salt, polyelectronic complexes, nanocomposites, cocrystal and coamorphous to improve the oral bioavailability of poorly water-soluble drugs and adjusting drug release rate. In Chapter 1, we reviewed the most commonly used methods for characterization of ASDs both in solid state or in aqueous media. The advantage and disadvantage of each method is briefly summarized. All methods are divided into three different categories: microscopic and surface analysis methods, thermal analysis methods and spectroscopic methods. The latest characterization techniques are also introduced. Last, we discuss how these methods are applied at different stages in the ASDs product development life cycle. In Chapter 2, we investigate the reaction between naproxen and meglumine at elevated temperature with different molar ratio and study the impact of this reaction on the physical stabilities and in vitro drug-release properties of melt-extrudated naproxen amorphous solid dispersion. In Chapter 3, we use reactive melt extrusion to prepare sustained release lidocaine polyelectrolyte complex. In this study, the influence of the drug form (freebase vs. hydrochloride salt) on lidocaine-Eudragit L100-55 interactions, physical stability, and dissolution properties of extrudates was investigated. In Chapter 4, we prepare exfoliated montmorillonite-Eudragit RS nanocomposites using reactive melt extrusion and investigate the influence of clay loading, clay types on clay-polymer interactions and drug release properties. The clays are used as the filler material with Eudragit RS at different concentration and theophylline was

the model compound. The resulting structure of the nanocomposites were characterized using TEM and XRPD. The hygroscopicity of the nanocomposites was investigated using DVS. The effect of the interfacial interaction between the polymer and the clay sheet, the clay loading as well as the clay type on the drug release behavior were further studied by the dissolution testing.

Table of Contents

List of Tables

List of Figures

Chapter 1: Characterization of Amorphous Solid Dispersions[1]

1.1 ABSTRACT

The study of amorphous solid dispersions (ASDs) is currently one of the most exciting areas in pharmaceutics. Research has shown that ASDs offer unique advantages in improving the bioavailability of poorly water-soluble drugs over conventional delivery systems. The various formulations and manufacturing processes of ASDs affect their physicochemical stability, processability, and drug release characteristics. Therefore, the characterization of ASDs is critical in all stages of product development, including preformulation screening, formulation development, process scale-up, and commercial manufacturing. Proper characterization allows for the rational selection of formulation composition and manufacturing processing methods and allows for high-quality drug products. In this review, we present the most commonly used methods for characterizing the solid-state properties of ASDs, and we discuss their mechanisms, applications, advantages, and disadvantages. We also provide a brief overview of the methods used to characterize ASDs behavior in aqueous media. These methods are divided into three different categories: microscopic and surface analysis methods, thermal analysis methods, and spectroscopic methods. In addition, this article discusses a number of emerging techniques. Last, we discuss how these methods are applied at different stages in the ASDs product development life cycle.

1.2 INTRODUCTION

Combinatory chemistry and high-throughput screening in drug discovery have resulted in a higher percentage of drug candidates that have poor aqueous solubility and poor dissolution characteristics. Up to 90% of the drugs under investigation and up to 40% of marketed drugs are poorly water soluble [1]. Oral delivery of these drug candidates is challenging.

A number of strategies have been developed to enable oral delivery of these poorly water-soluble drugs. These strategies include the use of salts, prodrugs, cocrystals, self-emulsifying formulations, and amorphous solid dispersions (ASDs) [2]. Among these methods, the use of ASDs is demonstrably the most promising approach to improve the dissolution characteristics and absorption of poorly water-soluble drugs [3].

The most common definition of ASD is "a molecular dispersion of one or more active ingredients in an inert carrier in the solid state prepared by the melting, solvent, or melt-solvent method" [4]. The improvement in bioavailability using ASD is attributed to a combination of thermodynamic and kinetic factors.

In terms of thermodynamics, a significant increase in the dissolution rate and transient solubility of the API in an amorphous state occurs because the energy that would be required to disrupt the crystal lattice of crystalline drugs is not required to dissolve drugs in an amorphous state [5]. In terms of kinetics, the interactions between polymer and API molecules could delay or inhibit nucleation and crystal growth in the dissolution medium. As a result, the supersaturation of the drug could be maintained over an extended period of time to maximize drug absorption [6].

As more and more commercial ASD products enter the marketplace, ASD is becoming the preferred approach to improve the dissolution rate and apparent solubility of poorly water-soluble drugs. Due to the complex physicochemical properties of ASDs,

multifaceted analytical methods are needed to enable comprehensive characterization of the materials to help understand the relationship between the formulation and process variables and the in vivo performance of ASDs.

In an ASD, all components are mixed on a molecular level. The challenges of ASD characterization arise from the desire to characterize the interaction between the drug and the polymer, phase separation during storage, the dissolution process, and physical stability prediction [7]. Many analytical techniques are now available to address these ASD characterization challenges. Fortunately, emerging sensitive technologies are providing more quantitative and qualitative information about the physicochemical properties of ASDs.

A combination of characterization techniques are commonly used to characterize ASDs at different stages of product development. Several review articles simply focus on one particular technique in ASD characterization, so they do not offer a complete picture of ASD research [8-12]. In this paper, we offer a detailed discussion of the measuring principle, and we summarize the advantages and disadvantages of most classical methods. Last, we discuss the applications of different techniques to characterize ASDs at different product development stages.

The characterization of ASDs in solid state can be performed using a wide variety of analytical techniques. There is no single superior method that can provide the full structural information of an ASD. The best approach is to apply a combination of techniques to achieve a comprehensive understanding of the solid-state properties of ASDs. Generally, ASD characterization methods can be divided into two major categories: methods that characterize ASDs in solid state, and methods that characterize the behavior of ASDs in aqueous media.

Table 1.1 shows the solid-state characterization methods. These methods can be classified based on their characterization level: the molecular level, the particulate level, and the bulk level. Molecular level methods characterize properties that can be detected between individual molecules. Particulate level methods characterize properties that can be detected through the analysis of particles. And, bulk level methods characterize properties that can be measured by using a relatively large amount of material [13].

Table 1.1: Classification of ASD characterization methods

Molecular level	Particulate level	Bulk level
FTIR	Fluorescence spectroscopy	Density
Raman	PXRD	Contact angle
NIR	DSC	Flowability
SSNMR	MDSC	Karl Fischer titration
	TGA	
	PLM	
	SEM	
	TEM	
	XPS	
	AFM	
	Terahertz spectroscopy	
	Dielectric spectroscopy	

Solution state characterization always includes not only the standard dissolution testing, which is covered by various regulatory guidance (e.g., USP, PhEur, JP), but also the solution-mediated phase transformation, recrystallization, and supersaturation that occur during the dissolution process. Characterizing the behavior of ASDs in aqueous media is the most challenging task in the study of ASDs. This paper focuses on solid-state characterization methods. However, a brief discussion of solution-state methods is also presented. Last, the conjunction method and new characterization techniques are also discussed.

4

1.3   METHODS USED TO CHARACTERIZE THE SOLID-STATE PROPERTIES OF ASDS

In this review chapter, solid-state characterization methods are divided into three categories based on the mechanisms of analysis: (1) microscopic and surface analysis methods, (2) thermal analysis methods, and (3) spectroscopic methods. This section presents a detailed discussion of the methods in each category.

1.3.1   Microscopic and surface analysis methods

Microscopy is a powerful solid-state characterization technique. It is a versatile, rapid, and nondestructive process for analyzing small samples for a wide range of physicochemical properties, such as particle size, particle morphology, crystallinity, surface properties, and even dissolution behavior and thermal behavior [14]. In general, the microscopic and surface analysis methods employed in ASD characterization include polarized light microscopy (PLM), scanning electron microscopy (SEM), transmission electron microscopy (TEM), atomic force microscopy (AFM), and X-ray photoelectron spectroscopy (XPS). Table 1.2 summarizes the measurement time, sample status, application, advantages, and disadvantages of each technique.

Table 1.2: An overview of microscopic and surface analysis methods in ASD characterization. (+) or (-) indicate whether the analytical technique is sample destructive or non-destructive, respectively.

Analytical method	Information	Advantages	Disadvantages	Sample destructiveness
				Measurement time
PLM (HSPLM)	• Crystallinity (Birefringence), Amorphous, • Crystalline morphology & size • Polymorphic transitions • Crystallization route	• High sensitive • Small sample size • Very little sample preparation • Easy to use	• Semi-quantitative	(-)
				Min-sec
SEM (EDS)	• Particle morphology and size • Rapid measure surface crystal • Chemical distribution map (EDS)	• High resolution • Small sample size	• Require sample preparation (coating and vacuum setting)	(-)
				Min-hour
TEM	• Identify crystalline • Detect crystallinity degree • Drug-polymer miscibility	• High resolution • Small sample size • Quantitative	• Tedious sample preparation • Risk of electron beam damage for some samples	(-)
				Hours
AFM	• Surface topography • Phase separation • Drug-polymer miscibility	• High resolution (nanoscopic) • Small sample size	• Require sample preparation • (smooth sample surface)	(-)
				Hours
XPS	• Surface chemical composition • Drug-polymer interaction	• High sensitive • Quantitative	• Limited testing area (1μm) • Require sample preparation (high vacuum setting)	(-)
				Hours

1.3.1.1 Polarized light microscopy (PLM) and hot-stage polarized light microscopy (HSPLM)

Among all the types of microscopy methods, PLM is one of the most useful for detecting small amounts of crystalline materials in ASDs. Solid forms can be distinguished by their optical properties when observed using plane polarized light and crossed polarizers, and this is especially true for crystalline and amorphous materials.

Amorphous solids are isotropic, which means their molecules are oriented randomly with no long-range order. As a result, they have no double refraction, are nonbirefringent, and do not exhibit any interference colors when observed between crossed polarizers. However, most crystalline solids are anisotropic, which means their molecules are packed in a regular, long-range, three-dimensional order. Therefore, crystalline solids show interference colors or polarization colors, which allows for rapid detection based on birefringence.

Telang et. al [15] used PLM to observe the onset of crystallization in ASDs with different formulations, and they found that PLM is a more sensitive tool than XRPD for investigating drug recrystallization in physical stability studies. Combined with other analytical approaches, PLM can be used to assess the kinetics of drug crystallization, polymorphic transitions, and crystallization in solid state or in aqueous media [16, 17].

Hot-stage polarized light microscopy (HSPLM) is another rapid and versatile method for observing the thermal behavior of samples using a polarized light microscope. In this method, the sample is heated in a furnace in which the heating or cooling rate can be accurately controlled. HSPLM is extensively applied in the initial formulation screening studies of ASDs.

During the process development of ASD, HSPLM is frequently applied to observe how the drugs interact with polymers in mixtures at elevated temperatures. Strong interactions (e.g., hydrogen bonding, ionic interaction) between the drug and excipients contributes to a lower drug melting point, improved stability of ASDs during storage, and enhanced dissolution performance [18]. During the heating process, the molten drug should be miscible with the polymer at a specific drug loading. During cooling, the drug should not recrystallize from the polymer–drug matrix.

HSPLM is particularly useful to interpret or confirm the results acquired by differential scanning calorimetry (DSC), especially when overlapping events are observed on DSC thermal profiles. Liu et. al applied HSPLM to observe the *in-situ* formation of cocrystal and salt between drug and other excipients at elevated temperature [19, 20]. New crystalline phase was observed during the heating process, which was attributed to the reaction between the drug and excipients. The HSPLM results corresponded well with the DSC data. Although PLM is a powerful tool for characterizing ASD, it is not an infallible method for detecting birefringence to distinguish amorphous from crystalline materials. Some crystalline materials are isotropic, so they do not show birefringence or interference colors (and the reverse is true for anisotropic materials). In addition, it is difficult to use PLM to quantify the degree of crystallinity in a crystal or a mixture. In general, to fully characterize the crystalline state of a sample, PLM should be used in combination with other techniques such as X-ray diffraction or DSC.

1.3.1.2 Scanning electron microscopy (SEM) and energy dispersive X-ray microanalysis (EDX)

SEM is widely applied in the characterization of ASDs. SEM analysis uses a monochromatic electron beam to probe the surface and near-surface area of materials at a

higher magnification and resolution than a traditional light microscope. Compared to light microscopy, SEM has the following three major advantages: (1) an upper magnification of about 250,000X, (2) a large depth of field, and (3) a lateral spatial resolution of 3 nm or higher.

SEM can be used to examine the effects of processing methods (e.g., spray drying, hot melt extrusion, electrospinning) on particle morphology [21-23]. It can also be used to observe changes in the morphology of the ASD sample after dissolution or a physical stability study [24, 25].

Energy dispersive X-ray microanalysis (EDX) is often combined with SEM to provide elemental information about the area probed by the electron beam. EDX analyzes the X-ray emission from the inner shells of atoms that have been ionized by the SEM beam. EDX analysis is ideal for the rapid and nondestructive elemental screening of samples.

Figure 1.1 shows SEM–EDX mapping images of a pure drug sample and an ASD sample prepared by hot-melt extrusion (HME). A generally even distribution of chlorine (only present in the drug) is observed, and this is consistent with a homogeneous dispersion at the spatial resolution limit of this technique (i.e., several micrometers).
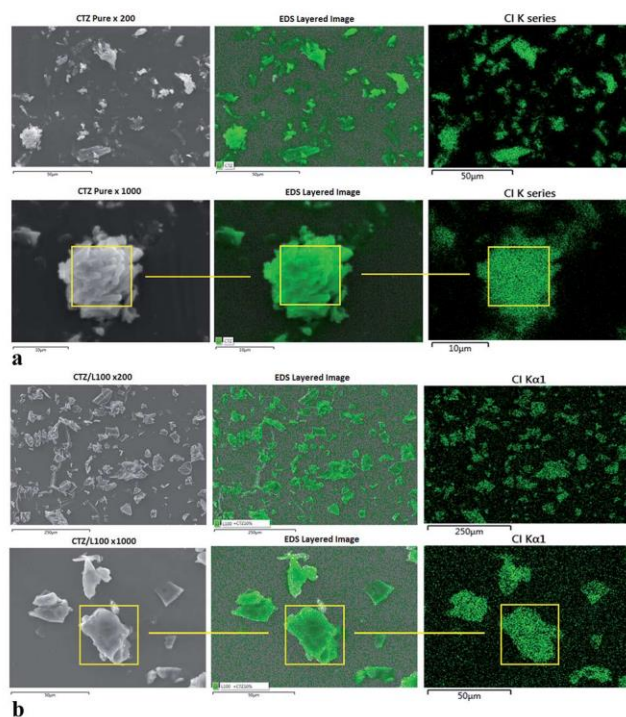
Figure 1.1: (a) SEM-EDX mapping images of a chlorine atom detected on pure drug particle. (b) SEM-EDX mapping images of a chlorine atom detected on an ASD prepared by HME. Adapted from reference [22].

1.3.1.3 Transmission electron microscopy (TEM)

In addition to SEM, transmission electron microscopy (TEM) is a highly useful technique in the study of ASDs. It can produce both real-space images and electron diffraction patterns to identify crystalline drugs in ASDs [26]. Using TEM, Ricarte et al. [27] detected an overall 3% crystallinity in a spray-dried ASD based on hydroxypropyl methylcellulose acetate succinate (HPMCAS), which is below the practical lower detection limit of wide-angle X-ray scattering. When combined with EDX, TEM can be used to evaluate drug–polymer mixing status in ASD in the early stages of formulation and process development [28]. Figure 1.2 presents the results. In this study, the TEM micrograph reveals a continuous matrix without the definite boundary or localization of element within

10

the ASD. EDX line scan data show that the drug is homogeneously mixed with the polymer across the particle.
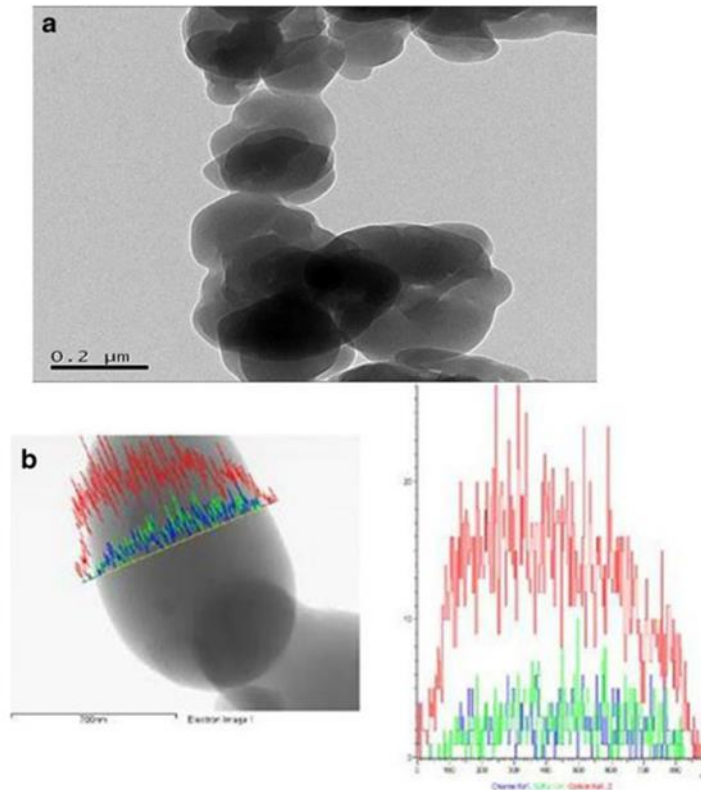
Figure 1.2: (a) TEM image of the ASD. (b) EDX line scan of a particle. Red represents carbon, green is sulfur, and blue is chlorine. Only the drug contains sulfur and chlorine. Adapted from reference [28].

1.3.1.4 Atomic force microscopy (AFM)

The main application of atomic force microscopy (AFM) in the study of ASDs is measuring the surface topography at sub-nanometer resolution. During AFM testing, a sharp probe tip (usually made of silicon (Si) or silicon nitride (Si3N4) located on the underside of a flexible cantilever raster scans over the sample surface. The detailed working mechanism of AFM is presented in these review articles [29, 30].

Many characteristics of samples can be visualized directly using AFM, such as underlying molecular de-mixing mechanisms, mixture-specific separation rates, and bulk and surface evolution. These parameters are intrinsic and fundamental in the prediction of the long-term stability of an ASD [31]. Lamm et al. [32] used AFM to evaluate the phase behavior and morphology of solid dispersions consisting of copovidone and TPGS 1000 prepared by hot-melt extrusion with various processing parameters and formulations. They concluded that AFM is a powerful technology for characterizing the effects of processing and composition on the phase behavior of the resulting extrudates. In summary, AFM is a robust method to study the phase behavior and molecular structure of ASDs, and it provides a novel analytical tool for the optimization of the ASD preparation process [33, 34].

1.3.1.5 X-ray photoelectron spectroscopy (XPS)

X-ray photoelectron spectroscopy (XPS) is a surface analysis technique that can analyze the chemical composition of the surface of a substance based on atomic concentrations. The XPS spectrum is specific to the binding energies of most elements of interest in organic materials. The shift in the chemical bonding energy can be used to study drug and excipient interactions in ASDs. Specifically, XPS has excellent sensitivity in assessing the extent of protonation by measuring the shifts in the binding energy of selected atoms [35]. A discussion of the mechanism and basic theory of XPS analysis can be found in Lee and Flynn [36].

As XPS instruments become more readily available, more applications of XPS in ASD characterization have been published. Dahlberg et al. [37] used XPS to quantify the amount of drug present on the surface of ASDs prepared by spray drying and rotary evaporation. They found that the chemical surface composition directly influenced the wettability of the ASDs, which had a direct impact on dissolution performance and the

physical stability in the solid state. XPS offers a rapid screening tool for the selection of carrier and drug loading in the early development of ASDs. Song et al. [38, 39] applied XPS to investigate the acid–base interactions between the drug and excipient in ASDs. They used XPS to detect an increase in the binding energy of the basic nitrogen atoms in the drug, which indicated protonation of these nitrogen atoms.

1.3.1.6 X-ray diffraction

X-ray diffraction has been described as the gold standard in characterizing pharmaceutical materials in the solid state. It has shown great promise for the fingerprinting, quantification, and even the modeling of amorphous pharmaceutical systems [9]. X-ray diffraction is generally categorized into single-crystal diffraction and powder X-ray diffraction.

Powder X-ray diffraction (PXRD) is more widely used than single-crystal diffraction for ASD solid characterization. It provides information on at least three important material attributes [40]. Table 1.3 summarizes the measurement time, sample status, application, advantages, and disadvantages of PXRD.

Table 1.3: A brief summary of PXRD in ASD characterization. (+) or (-) indicate whether the analytical technique is sample destructive or non-destructive, respectively.

Analytical method	Information	Advantages	Disadvantages	Sample destructiveness
				Measurement time
PXRD (scattering pair distribution function, PDF)	- Polymorph screening, - Amorphous identification - Detect crystallinity degree - Recrystallization kinetic - Drug-polymer miscibility (PDF) - Microstructure of ASD (PDF)	• Small sample size • Very little sample preparation • Easy to use • Qualitative and quantitative	• Less sensitive (>5% crystallinity) • No chemical structure information	(-)
				Mins

To understand the basic theory and working mechanism of powder X-ray diffraction, the readers are recommended to read these articles written by Dinnebier and Gilmore [41, 42].

The first use of PXRD is to examine changes in the crystallinity and polymorphism of ASDs after manufacture or during stability studies. Because PXRD operates on bulk powders, it is very useful for the overall quantitative analysis of the crystalline content of a batch of ASD. A number of examples for the application of PXRD in the analysis of residual crystalline content in ASDs have been reported [43, 44].

Amorphization generally results in broad, diffuse scattering signals, while the signals for crystal materials are sharp Bragg reflections. For a mixture of amorphous and crystalline materials, the degree of crystallinity is the ratio of integrated crystalline intensity to the total integrated amorphous and crystalline intensity. The typical detection limits for crystalline content are in the 1–5% (w/w) range, depending on the reflection methods [7].

The second use of PXRD in the study of ASDs is the direct characterization of miscibility and amorphous structure with the total scattering pair distribution function (PDF). The PDF is obtained through an inverse Fourier transform of the reduced total scattering structure function F(Q), which is the subtracted, corrected, and normalized background diffracted intensity that includes both Bragg and diffuse scattering. The detailed theory and general application of PDF in PXRD are presented in [45, 46].

Nollenberger et al. [47] applied PDF to show that subtle changes in the polymer structure at the molecular level have a significant impact on the drug release profile of ASDs. Newman et al. [48] developed a method that uses PXRD coupled with PDF to assess the miscibility between amorphous drugs and polymers. They found that the PDF method is more sensitive than DSC for detecting phase separation. However, due to the inherent

limitations of conventional copper-anode X-ray laboratory sources, the PDF analysis data may not be reliable and may generate ambiguous and potentially incorrect results [49, 50].

The development of high-energy X-rays produced by synchrotron radiation allowed the use of short wavelengths to achieve a higher detection range. Araujo et al[40] used synchrotron X-ray diffraction and PDF to investigate the local chemical structure and ionic drug–polymer interactions in a lapatinib ASD prepared with hypromellose phthalate (HPMCP) and hypromellose (HPMC-E3). Based on the total PDF results, they found that the drug did not pack in the same way in these two formulations due to the different interactions between the drug and polymer carriers.

Recent developments in PXRD can also provide useful information under non-ambient conditions, such as PXRD equipped with variable temperature and humidity control, which provides new insights into the crystallization kinetics of amorphous drugs in ASDs [51]. Furthermore, when PXRD is used in conjunction with other techniques, such as second-harmonic generation microscopy, the sensitivity of PXRD for detecting drug crystallinity increases dramatically [52].

1.3.2 Thermal analysis methods

The thermal analysis method is an indispensable and well-established routine tool for the characterization of ASD. The basic process of thermal analysis is measuring a material's response (e.g., changes in energy, temperature, mass) to a change in the temperature of the sample. Thermal analysis methods are normally used to monitor endothermic processes (e.g., glass transition, melting, solid-solid phase transition) and exothermic processes (e.g., crystallization, chemical degradation). Commonly used thermal analysis methods include thermogravimetric analysis (TGA), differential scanning calorimetry (DSC), modulated differential scanning calorimetry (MDSC) and micro-nano

thermal analysis. Table 1.4 summarizes the measurement time, sample status, application, advantages, and disadvantages of each technique.

Table 1.4: A brief summary of TGA and DSC (MDSC) in ASD characterization. (+) or (-) indicates whether the analytical technique is sample destructive or nondestructive, respectively.

Analytical method	Information	Advantages	Disadvantages	Sample destructiveness / Measurement time
TGA	• Thermal stability • Moisture content • Solvent evaporation rate	• Small sample size • Very little sample preparation • Easy to use	• Difficult to identify chemical composition • Sample destroyed during analysis	(+) Min-hour
DSC (MDSC)	• Melting point • Glass transition temperature (T_g) • Identify crystalline and amorphous state • Detect crystallinity degree • Heat capacity • Drug crystallization tendency • Drug–polymer miscibility • Molecular mobility • Drug–drug and drug–polymer interaction	• Small sample size • Very little sample preparation • Easy to use • Qualitative and quantitative	• Sample destroyed during analysis • No information on the nature of the thermal events • Unable to resolve overlapping thermal events at the same time	(+) Min-hour
Micro-nano-	• Phase separation	• Small sample size	• Time consuming	(-)

Table 1.4: continued.

thermal analysis	• Drug distribution uniformity assessment	• Very little sample preparation • Identify phase chemical compositions based on transition temperature	• Potential confusion of glass transition with other softening response	
				Hour-day

1.3.2.1 Thermogravimetric analysis (TGA)

TGA is one of the oldest thermal analytical methods. It has been used extensively in material characterization. This method involves monitoring the weight of a sample in a chosen atmosphere (air or nitrogen) as a function of temperature. In ASD characterization, TGA is routinely used to determine the thermal stability and volatile components analysis of the drug and polymer. This information can be used to define the temperature window in hot-melt extrusion to avoid thermal degradation [19]. TGA has also been used to study the evaporation profile of feed solutions for spray drying. TGA analysis has revealed that the drying kinetics of the binary solvent has a significant impact on the surface chemistry and particle morphology of spray-dried ASDs [53, 54]. TGA is commonly combined with other spectroscopic detection methods, such as IR or gas chromatography, to allow for the chemical identification of volatile materials released from samples.

1.3.2.2 Differential scanning calorimetry (DSC)

Differential scanning calorimetry (DSC) and modulated differential scanning calorimetry (MDSC) may be the most widely used methods in ASD characterization. In these techniques, the energy input associated with heating materials can be measured to detect thermal transitions such as the melting point, glass transition, polymorphic form transformation, and recrystallization. The theoretical background of DSC and MDSC can be found in [55].

Although DSC is an invaluable analytical tool, DSC has certain limitations when thermal transitions are weak or overlap. MDSC was designed to address these limitations. MDSC can separate overlapping thermal events and has higher sensitivity in measuring heat capacity. MDSC has been used to measure the crystallization tendency of drugs,

20

miscibility between the drug and polymer, glass transition, crystallinity/crystallization (e.g., crystal growth rate, degree of crystallinity), and molecular mobility (e.g., structural relaxation, viscosity) [8].

1.3.2.2.1   Crystallization tendency

Discerning the crystallization tendency of a drug is important in the development of an ASD. The crystallization tendency of an ASD is determined by the crystallization tendency of the drug [56-58]. DSC can be used to measure the drug crystallization tendency. Taylor's group developed a simple DSC method to assess the crystallization tendency of organic molecules by using a heating–cooling–heating cycle [59]. Based on the melting and recrystallization behavior during the temperature cycle, the drug crystallization tendency is classified as Class I (strong), Class II (middle) and Class III (weak). Other DSC methods used to measure crystallization tendency include the reduced glass transition temperature rule (Trg, 2/3 rule) [60] and the fragility parameter [61]. In another case, Feng et al. [62] utilized an improved kinetic equation to evaluate the recrystallization process of melt-extruded ASD by fitting the DSC data into a mathematical model using a multivariate regression method. The recrystallization rate constant was assessed under accelerated conditions to predict the long-term crystallization tendency of the ASD.

1.3.2.2.2   Miscibility between drug and polymer

DSC is commonly used as a "rule of thumb" technique to evaluate the miscibility between the drug and polymer. Good miscibility is a prerequisite to form a physically stable ASD. A miscible ASD is defined as an ASD that consists of a single chemically homogeneous phase in which all components are mixed at the molecular level [8]. Since

21

ASD is a high-energy drug dispersion system, phase separation could occur due to thermodynamic factors (i.e., enthalpy, entropy of mixing) or environment factors (e.g., temperature, moisture). Figure 1.3 illustrates two potential routes of ASD recrystallization. Phase separation and crystallization have a negative impact on the performance of an ASD both in vitro and vivo.
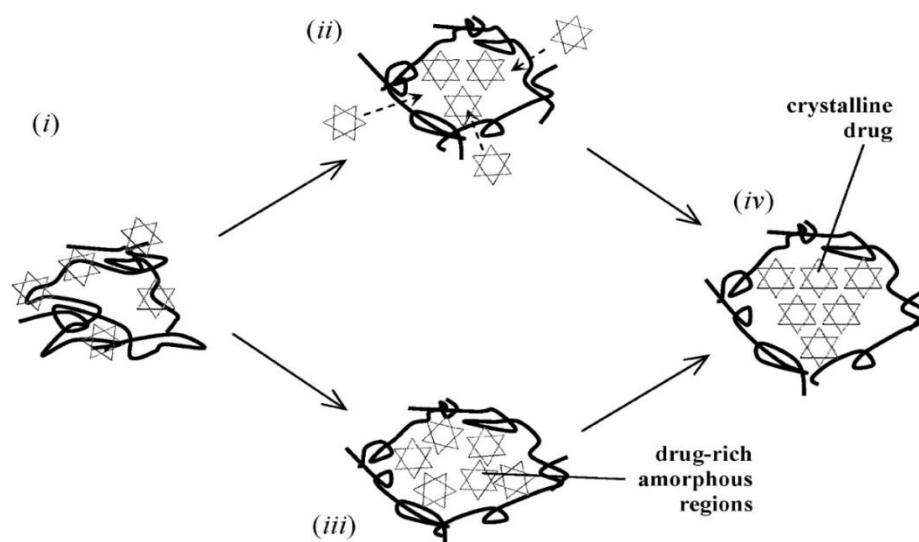
Figure 1.3: Two potential drug recrystallization routes from ASD. Adapted from reference [64].

Numerous articles have reported that the single T_g method indicates miscibility of the binary or ternary ASD [63-65]. However, the presence of a single T_g is not an infallible indicator of miscibility for a number of reasons [66]. First, some drugs and polymers have similar T_g s, and their glass transitions may overlap on DSC thermograms, which makes them difficult to discern. Second, the domain size in phase-separated ASD may fall below the DSC detection limit [48]. Last, but not the least, some drugs and polymers have broad

glass transitions or a small heat capacity change at T_g, which makes it difficult to measure the T_g.

Besides the single T_g method, many other methods are used to evaluate mixing homogeneity, such as melting point depression [67], evaluation of drug solubility in polymers (i.e., the solubility parameters method) [68, 69], solution calorimetry [70].

1.3.2.2.3 Glass transition temperature

For amorphous materials, the glass transition temperature (T_g) is a unique temperature range in which the properties of the material shift from the properties of a liquid to those of a solid. Figure 1.4 shows the relationships between temperature and volume, and enthalpy and entropy. Certain critical properties of ASDs are dependent on their glass transition temperature. These properties include the physical state of the drug and polymer [71], the miscibility between the drug and polymer [72, 73], and specific interactions [74, 75]. In addition, T_g can be used to guide the selection of the storage conditions for ASDs [76]. Gordon-Taylor, Fox, and Kwei equations can be used to calculate the theoretical T_g of multicomponent ASDs. The deviation of the experimental T_g from the theoretical T_g can be used to determine the mixing behavior and physical interaction between the drug and polymer [77].
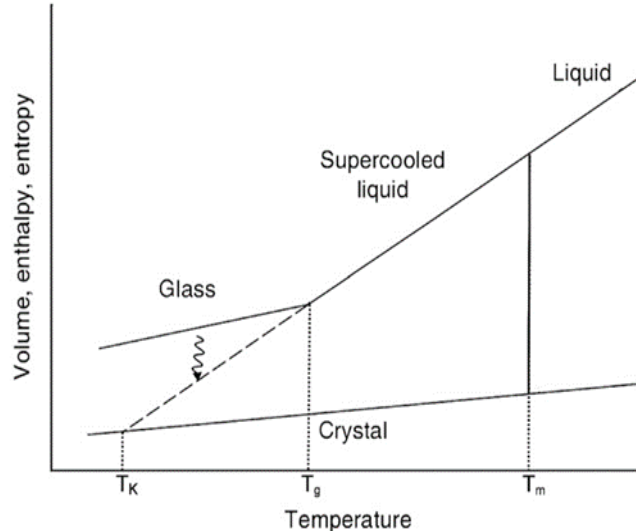
Figure 1.4: Volume, enthalpy, and entropy of the amorphous state in comparison to a crystal, including the supercooled liquid and glass regions. Tm represents the melting temperature, and Tk represents the Kauzmann temperature. Adapted from reference [8].

1.3.2.2.4   Residual crystallinity

It is important to monitor the residual crystallinity of ASDs during their processing and storage, because recrystallization of the drug reduces the dissolution rate, which could reduce bioavailability. Comparing the melting enthalpy of the residual crystalline drug in ASDs against the melting enthalpy of the crystalline form of the pure drug can be used to determine the residual crystallinity [78]. Shah et al. [79] summarize the various thermal methods used to study the crystallization of ASDs.

In summary, DSC is useful for both qualitative and quantitative analysis drug crystallization in ASDs. Although DSC may not detect low levels of crystalline material in ASDs, DSC is commonly combined with other techniques (e.g., XRPD, solid-state NMR) to monitor the crystallization in ASDs.

1.3.2.2.5   Molecular mobility

24

The molecular mobility of a drug and polymer is generally considered a key attribute that determines the physical stability of ASDs. High molecular mobility can lead to faster phase separation, drug nucleation, and crystal growth. A large body of research focuses on the correlation between molecular mobility and physical stability [80, 81]. The most common indicators of molecular mobility are viscosity, structural relaxation time, and dielectric relaxation time [8]. Since all these properties are temperature dependent, DSC is the most commonly used method to measure molecular mobility as a function of temperature. Aso et al. [82] used DSC to study the crystallization rate of amorphous drugs and the relationship between changes in the structural relaxation time of amorphous drugs both in the absence povidone and in the presence of povidone. They found that the presence of povidone decreased the molecular mobility of amorphous drugs as the structural relaxation time of the drug increased, and they found that the recrystallization rate of the drug decreased in the presence of povidone.

In summary, DSC and MDSC have a wider range of application in studying ASDs, ranging from testing the properties of the drug and polymer to preformulation screening of ASDs. Furthermore, with the development of new DSC thermal analytical methods and the combination of DSC with other spectroscopic and imaging methods, the application of DSC in ASD characterization continues to expand.

1.3.2.3 Micro-nano thermal analysis

Traditional thermal analysis can provide useful information on the bulk properties of ASDs. However, in some cases, it may be more desirable to analyze the surface properties rather than the bulk properties. The properties of free surfaces are directly responsible for crystal growth on the surfaces of ASDs [83]. Micro-nano thermal analysis

is a particularly important method of thermal analysis to identify the nature of the different phases present at the surface of ASDs [84, 85].

So far, the reported micro-nano thermal analysis methods include localized nanothermal analysis, thermal transition mapping, and thermal analysis by structural characterization. In localized nanothermal analysis, the traditional silicon-based AFM tip is replaced with a specialized micro-fabricated silicon-based probe with a miniature heater. This new probe not only allows researchers to generate topographic images, but also to conduct local thermal analyses at defined points on a surface [86, 87].

Zhang et al. [88] used nanothermal analysis to characterize the heterogeneity of carbamazepine ASD. By combining the topographic and phase images, they found that a 5% drug-loading formulation formed a solid solution. At 50% drug loading, a portion of drug is dispersed as nanocrystals in the polymeric carrier. Figure 1.5 illustrates the work principle of local thermal analysis and thermal transition mapping. Qi et al. [89] applied thermal transition mapping to study the phase separation behavior of felodipine ASD. They found that thermal transition mapping was useful to identify both the size and chemical composition of the phase separation, which is difficult to achieve by conventional analytical methods. Thermal analysis by structural characterization is another micro-nano thermal analysis method recently developed to study the glass transition kinetics and thermal dissolution behavior of materials. Alhijjaj et al. [90, 91] used this method to analyze the influence of drug–excipient miscibility on the heterogeneity and spatial distribution of phase separation in ASDs.
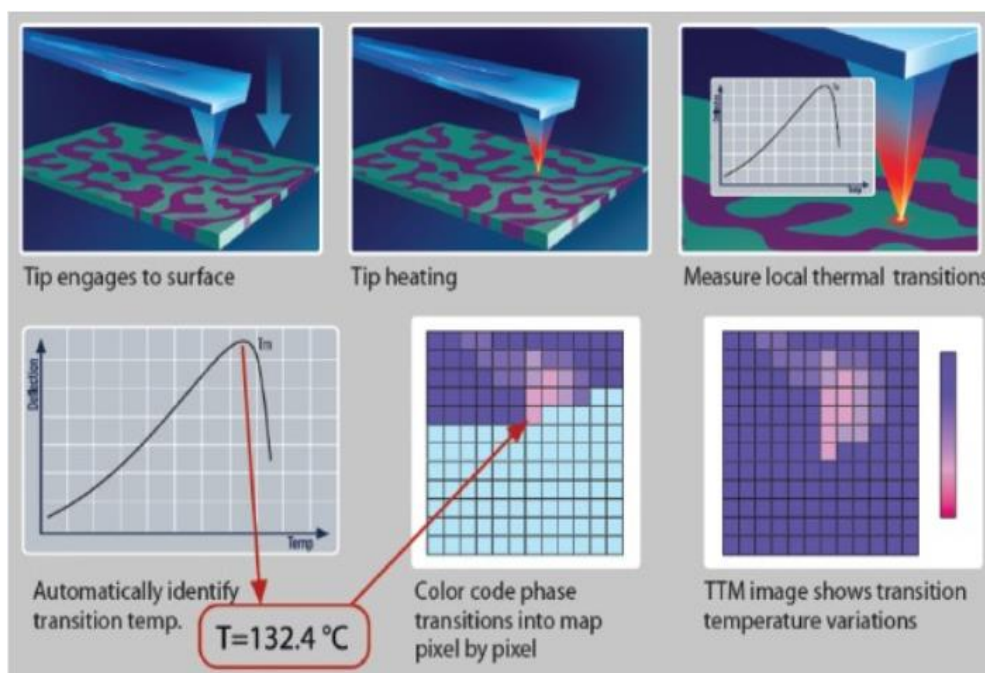
Figure 1.5: The principle of localized nanothermal analysis and thermal transition mapping. Adapted from reference [86].

1.3.3 Spectroscopic methods

Spectroscopic methods are based primarily on molecular and atomic-level changes that occur when the material is exposed to electromagnetic radiation. The changes include electronic transitions, vibrational transitions, and nuclear spin transitions. Based on the energy gap between the ground and excited states, spectroscopy methods can be divided into fluorescence spectroscopy, infrared spectroscopy, near-infrared spectroscopy, Raman spectroscopy, and nuclear magnetic resonance. Terahertz-pulsed spectroscopy is a new technique used to probe low-energy vibrations, such as intramolecular torsional vibrations, and intermolecular vibrations such as translations and liberations [92].

Using different setups, spectroscopy imaging may be performed on the macro-, micro-, and even nano- scales. For ASD characterization, spectroscopy could provide molecular-level information about local structure in amorphous solids, such as drug–

polymer interaction, phase separation, and crystallization. Furthermore, spectroscopic tools can be applied in the on-line monitoring of ASDs during manufacturing process. Table 1.5 summarizes the measurement time, sample status, application, advantages, and disadvantages of each technique.

Table 1.5: A brief summary of spectroscopy method in ASD characterization. (+) or (-) indicates whether the analytical technique is sample destructive or nondestructive, respectively.

Analytical method	Information	Advantages	Disadvantages	Sample destructiveness / Measurement time
Fluorescence spectroscopy	• Drug–polymer miscibility • Phase separation • Drug dissolution behavior in ASD	• High sensitive • Small sample size • Very little sample preparation • Easy to use	• Semi-quantitative	(-) sec
FTIR	• Drug–drug and drug–polymer interaction • Polymorph screening • Crystalline and amorphous identification • Phase separation • Spatial chemical information with mapping setup	• Fast data acquisition • Small sample size • Easy to use • No sample preparation required for ATR	• Environmental humidity influence • Probes are not yet common	(-) sec
NIR	• Identify crystalline polymorphs and solvates • Sensitive to different water states • Spatial chemical information with mapping setup	• Fast data acquisition • Small sample size • Easy to use • No sample preparation required • Use of probes • Ability to penetrate glass containers	• Weak intensity • Significant baseline slope	(-) sec
Raman	• Drug–drug and drug–polymer interaction • Phase separation • Drug–polymer miscibility • Drug dissolution behavior in ASD	• Fast data acquisition • Small sample size • Easy to use • No sample preparation required • Use of probes • Ability to penetrate glass containers • Insensitive to water	• Local heating of sample • Sample fluorescence • Photodegradation	(-/+) sec
Terahertz spectroscopy	• Identify crystalline and amorphous state	• Fast data acquisition • Small sample size	• Spectrum affected by water	(-)

Table 1.5: continued.

Analytical method	Information	Advantages	Disadvantages	Sample destructiveness
				Measurement time
	• Detect crystallinity degree • Polymorph screening • Crystallization kinetic		• Baseline slope • Relatively expensive	sec
Dielectric spectroscopy	• Molecular mobility • Drug crystallization tendency	• Fast data acquisition • Small sample size • No sample preparation required	• Complicated mathematical modeling • Not a "fingerprint" technique	(+)
				Min-hour

1.3.3.1 Fluorescence spectroscopy

Fluorescence spectroscopy has been used to study the physical properties and dissolution behaviors of ASDs. It detects the fluorescence emitted when a substance is excited by UV-visible radiation. Fluorescence spectroscopy can be performed in different modes, including (1) emission scans with a constant excitation wavelength, (2) excitation scans with a constant emission wavelength, (3) synchronous scans of both monochromators, and (4) total luminescence scans.

Fluorescence spectroscopy provides new approaches for probing the local behavior of drugs in ASDs (e.g., miscibility, phase separation) and the correlation of these behaviors to ASD performance. Tian et al. [93] have used fluorescence spectroscopy to evaluate drug–polymer miscibility and to investigate the correlation between miscibility and the physical stability of ASDs. The fluorescence spectroscopy data indicated that drug loading had a significant impact on the drug–polymer miscibility and indicated a strong correlation between poor miscibility and reduced physical stability. They observed a significant difference in intensity and emission maxima between crystalline Form I, a hypromellose-

30

based ASD, and the povidone-based ASD. The difference between the fluorescence spectra of these two solid dispersions was attributed to the differences in the mobility of diflunisal in the glassy solid [94]. Fluorescence spectroscopy has also been used to study the dissolution behaviors of ASDs in aqueous environments [95, 96]. In these studies, the fluorophore was added to the aqueous phase and the emission spectrum was monitored as the drug concentration was increased. Liquid–liquid phase separation was observed in povidone-based ritonavir ASDs.

1.3.3.2 Infrared spectroscopy

Infrared spectroscopy (IR) is a form of vibrational spectroscopy that measures the absolute frequencies at which a sample absorbs various forms of radiation. The vibration occurs when there is a change in dipole moment. Based on the spectral range, infrared spectroscopy could be divided into far-IR (FIR: 400–20 cm^{-1}), mid-IR (MIR: 4,000–400 cm^{-1}), and near-IR (NIR: 12,500–4,000 cm^{-1}). All three IR regions have been employed to study ASDs [7].

IR spectroscopy can be used to measure drug–polymer interactions in ASDs by observing changes in peak shape or position. The changes in wavelength, bandwidth, and band intensity can also provide molecular-level information on the solid-state form of both the drug and polymer [11]. Therefore, FTIR can be used to identify molecular interactions and to evaluate the physical stability of ASDs. In addition, FTIR is a useful tool for measuring the distribution of the drug in the polymer matrix as well as phase separation.

FTIR imaging has been used to study the moisture-induced phase separation in melt-extruded ASDs [97, 98]. FTIR spectroscopy has also been used successfully in combination with other analytical techniques (e.g., XRPD, DSC, AFM) [63, 99]. In-line NIR has been applied to monitor phase transformations during ASD production, such as

31

hot-melt extrusion and spray drying [100, 101]. Furthermore, the development of FTIR imaging technology has made possible the real-time monitoring of drug release from ASDs [102, 103].

Compared to other techniques, the advantage of FTIR is that samples in different physical states can be analyzed in a fast and noninvasive manner and with high chemical specificity. Given recent advancements in hardware and software, FTIR will continue to play a key role in ASD characterization, coupled with other advanced characterization methods.

1.3.3.3 Raman spectroscopy

Raman spectroscopy is a complement to IR spectroscopy. Raman spectroscopy depends on changes in the polarizability of a molecule while IR spectroscopy depends on changes in the dipole moment. Raman spectroscopy measures the relative frequencies at which a sample scatters radiation. This is unlike IR spectroscopy, which measures the absolute frequencies at which a sample absorbs radiation.

Because light of shorter wavelengths is used, it is more common to combine Raman with microscopic analysis, as in confocal Raman microscopy [104, 105]. In addition, Raman spectroscopy has been extensively used to characterize ASDs in the investigation of drug–polymer interactions, miscibility, and phase distribution [106, 107]. Furthermore, chemical mapping with Raman spectroscopy has been employed to investigate in situ, real-time dissolution mechanisms of ASDs [108].

1.3.3.4 Solid-state nuclear magnetic resonance

Solid state nuclear magnetic resonance (SSNMR) has been proven to be a powerful tool for gathering molecular-level information on the dynamics and phase compositions of

ASDs based on dipolar correlation, spin diffusion, and relaxation measurements [109]. Table 1.6 summarizes the measurement time, sample status, application, advantages, and disadvantages of each technique. SSNMR is a stand-alone, nondestructive technique for the analysis of crystallization tendency [110], molecular mobility [111], miscibility, drug–polymer interactions [112], degree of crystallinity, and crystallization kinetics of ASDs [113].

Table 1.6: A brief summary of SSNMR in ASD characterization. (+) or (-) indicates whether the analytical technique is sample destructive or nondestructive, respectively.

Analytical method	Information	Advantages	Disadvantages	Sample destructiveness
				Measurement time
SSNMR	- Amorphous identification - Detect crystallinity degree - Recrystallization kinetic - Drug–polymer miscibility - Drug–drug and drug–polymer interaction - Molecular mobility - Microstructure of ASD	- Small sample size - Very little sample preparation - Qualitative and quantitative	- Risk of recrystallization during the analysis process - Relative expensive	(-)
				Hour-day

SSNMR has even been used to monitor the dissolution behavior of ASDs. A strong correlation has been found between the crystallization rate of amorphous drugs and their molecular mobility as measured by their enthalpy relaxation and H^1 NMR relaxation times. The observation of spin diffusion effects with the 2D cross-polarization heteronuclear correlation experiment was used to probe the association between the amorphous drug and polymer.

Proton-relaxation measurement using variable temperature SSNMR (VT-SSNMR) is a valuable new thermal analysis method for predicting the physical stability of amorphous pharmaceuticals. ^{13}C and ^{15}N SSNMR are often used to examine hydrogen bonding between donors and acceptors. In addition, the application of standalone T_1 relaxation, or T_1 relaxation in combination with $T_{1\rho}$ measurements, has been used to determine whether an ASD has multiple domains or is homogeneous [112].

Song et al. [114] used SSNMR to investigate drug–excipient interaction in lapatinib ASDs. ^{15}N SSNMR, $^1HT1$, and $1HT_{1\rho}$ provided direct spectroscopic evidence for the ionic interaction between lapatinib and HPMCP. This interaction was the key driver in stabilizing lapatinib ASDs. Dahlberg et al. [115] employed NMR imaging technology to study the flutamide release profile of compacts of flutamide/HPMC ASDs in D_2O at the beginning and after 6 h. The NMR data vividly demonstrated that the drug dissolution process from HPMC–based ASDs resulted from the following chain of events: water ingression of the tablet, hydration, mobilization, and the upward growth of the polymer gel layer.

1.4   METHODS FOR CHARACTERIZING ASD BEHAVIOR IN AQUEOUS MEDIA

The ultimate success of an ASD in improving the bioavailability of a poorly water-soluble drug is determined by its performance in the gastrointestinal tract after oral administration. The ability to monitor the extent and rate of drug solubilization is particularly important, since the drug release is the rate-limiting step in the absorption of these drugs. Inconsistent drug release from an ASD might lead to changes in bioavailability and concerns about safety or efficacy. Therefore, dissolution analysis is a critical characterization step in formulation screening, manufacturing process selection, and the monitoring of the physicochemical stabilities of ASDs during storage. The standardized dissolution test description and apparatus can be found in USP general chapter <711> [116].

The typical dissolution profiles of ASDs that show rapid initial buildup of drug supersaturation and then retardation of precipitation have been qualitatively characterized as a "spring and parachute." It is challenging to explore the ASD dissolution mechanisms because several dissolution processes occur simultaneously. Figure 1.6 shows that the main contributors to the final dissolution performance of ASDs are (a) the recrystallization of the drug in the ASD or after precipitation from a supersaturated solution, (b) the formation of nanoparticles and microparticles during the dissolution, and (c) the dissolution of polymeric carriers [60].
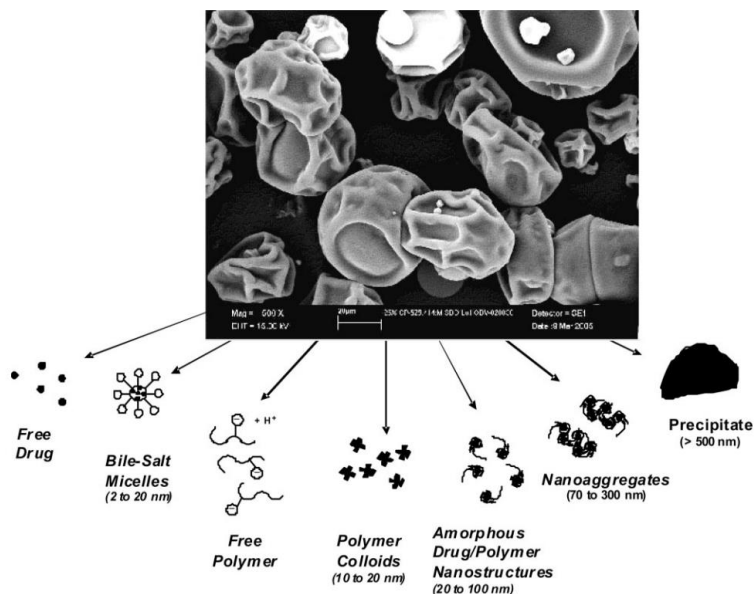
Figure 1.6: Species generated when ASDs are added to aqueous solution simulating duodenal and intestinal contents. Adapted from reference [60].

Conventional dissolution methods only measure the drug concentration in dissolution media; they fail to offer any chemically or spatially resolved information about potential changes in the solid forms during the dissolution process. Given the limitations of conventional methods, innovative approaches have been developed in an attempt to provide a more holistic picture of drug release from ASDs. These approaches include UV imaging [117, 118], mid-IR [99, 102], NIR [119], Raman spectroscopy [104, 108, 120], magnetic resonance imaging [121, 122], 1H-NMR [123], particle analysis (e.g., asymmetrical flow field–flow fractionation, cryogenic TEM) [124, 125].

UV imaging provides not only the drug dissolution rate in real-time, but also information on how the polymer influences drug recrystallization in the dissolution medium [126]. Tres et al. (2015) combined integrated magnetic resonance imaging, a UV-Vis flow cell system, and 1H-NMR to obtain a clear picture of drug release while

simultaneously measuring the dissolution profiles and the rates of both drug and polymer release from ASDs. MRI and 1H-NMR data showed that a compact containing 5% of the drug eroded linearly. A model drug and KollidonVA64 were released at approximately the same rate from the molecular dispersion. At high drug loading (e.g., 30%), the data indicated a slower water ingress into the compact, which corresponded to a slower dissolution rate of both drug and polymer [122].

IR and Raman spectroscopy can provide chemically specific information. Raman spectroscopy is not as sensitive to water as IR spectroscopy. Therefore, Raman spectroscopy is more suited to characterizing dissolution behavior in aqueous environments. Tres et al. (2015) utilized Raman spectroscopic imaging along with multivariate curve resolution (MCR) analysis to study real-time, in situ dissolution mechanisms that underpin ASDs, and these were collected directly from the dosage form itself. Their study found that amorphous felodipine crystallized at different rates in different regions of the compact surface, indicating that crystallization followed an initial stage of heterogeneous nucleation [108].

Langham and Booth et al. [121] used MRI to study the dissolution mechanism of spray-dried felodipine ASDs, and they found that drug loading has a profound impact on the physical behavior of the compact surface, which directly influenced drug dissolution performance.

Each of these techniques has been applied to study the dissolution behavior of ASDs. A better understanding of drug release can be achieved when these techniques are used in rational combination.

1.5   CHARACTERIZATION TOOLS USED IN CONJUNCTION

Most research studies combine different characterization techniques to build the most comprehensive profile of an ASD. Since each technique has specific limitations, the best practice is to combine two or more methods to provide sample information that cannot be achieved using a single method. In addition, simultaneous multi-method measurements on the same sample complement each other and either reveal important properties of ASD or increase confidence in the data interpretation of these complex systems [127]. Reported conjunction tools include DSC–FTIR [128, 129], DSC–Raman [130], DSC–PXRD [131], IR–AFM [99, 132], and MRI–FTIR–Raman imaging.

Another example is the combined DSC–FTIR technique, a quick and easy analytical method used for collecting real-time thermodynamic and spectroscopic data from ASDs as they undergo thermal modifications [128]. FTIR provides real-time qualitative information that complements the heat flow changes measured by DSC. Lin et al. [133] used DSC–FTIR to investigate heat-induced drug–polymer interactions.

The combined AFM–IR method is another promising technique for the evaluation of polymer–polymer and polymer–drug miscibility. AFM can achieve nanoscale resolution, but it fails to identify the chemical composition of different phases. IR can provide specific information about chemical composition, but it is typically limited in spatial resolution. Li et al. [134] successfully used AFM–IR to characterize drug–polymer miscibility, and they found that AFM–IR is a unique analytical tool for the study of the microstructure of ASDs. The information collected from their AFM–IR analysis contributed to a mechanistic understanding of ASD phase behaviors.

Punčochová, Ewing et al. [104] employed three chemical imaging methods (MRI, ATR–FTIR spectroscopic imaging, and confocal Raman mapping) to understand the behavior of drug release from ASDs in a mixed polymer matrix. Each imaging method

contributed a different aspect of the dissolution process, as shown in Figure 1.7. A combination of these methods provides a powerful approach that can reveal the mechanisms and phenomena that control drug release from ASDs. They can also paint a global picture of different water penetration and polymer dissolution rates, which none of these techniques could conclusively determine alone.
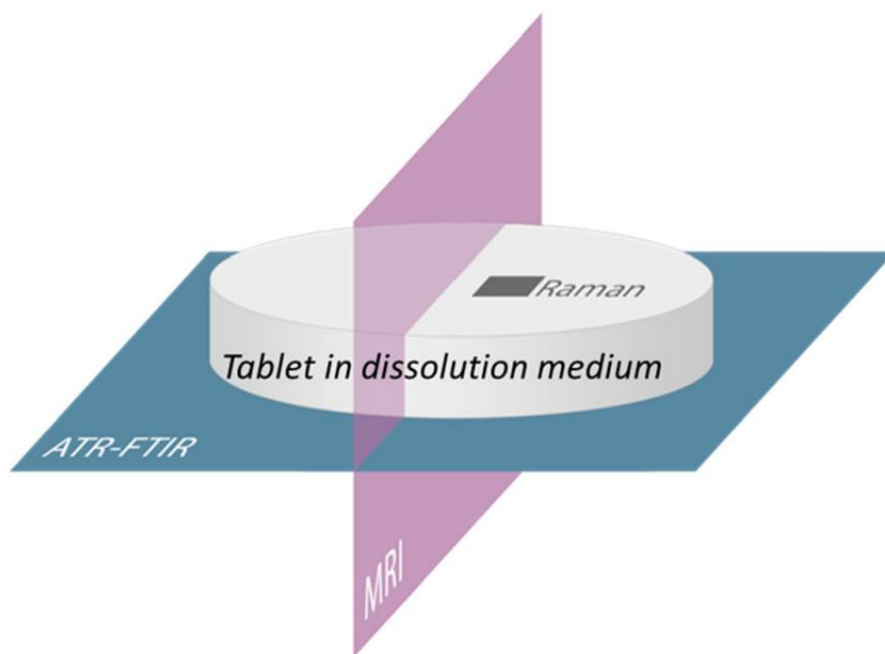
Figure 1.7: Scheme of image position relative to the tablet, provided by each imaging method. Adapted from reference [104].

1.6 EMERGING NEW TECHNIQUES

1.6.1 Terahertz spectroscopy

Terahertz spectroscopy (TPS) is a nondestructive technique that uses spectral information in the far-IR region of the electromagnetic spectrum to probe the long-range crystalline lattice vibrations, low-energy torsion, and hydrogen-bonding vibrations of pharmaceutical materials [12]. Over the past several years, TPS has received considerable

attention in the field of pharmaceutics research. TPS and imaging technology provide novel approaches to characterize ASDs.

Since TPS relates to the intermolecular vibrations inside the lattice structure rather than intramolecular vibrations, TPS of amorphous materials shows no distinct spectral bands. Any recrystallization in an ASD may be monitored and qualified using TPS [135]. Using in situ temperature-dependent TPS, the distinctive spectral changes that occur with increasing temperature provide essential information about relaxation and crystallization processes [136]. In addition, TPS can be used to determine the onset and strength of molecular mobility, which underpins the crystallization of amorphous drugs [137].

1.6.2 Dielectric spectroscopy

In dielectric spectroscopy, dipoles that have sufficient mobility respond to an external electric field. This response allows for the detection of molecular motions that have a relaxation time of $10-3–109$ s over a wide temperature range ($-170–300$ °C) [138]. Dielectric spectroscopy is widely used to study complex systems in materials science, and it is attracting increasing attention as a powerful tool for the characterization of pharmaceutics materials [139].

Dielectric spectroscopy has been used to directly measure the time scale of intramolecular and molecular motion, since both the cooperative and noncooperative motion of drug molecules can be obtained from this analysis. Various models can be used to analyze the dielectric data that capture the functional dependence of the dielectric response on the frequency, time, or temperature of ASDs. Fitting the data to these models, or applying the appropriate curve resolution to deconvolute various overlapping motions, provides an insight into the temperature and frequency dependence of each mode of

motion. The time scale of physical instability can then be measured after identifying a link between specific modes of molecular motion and the crystallization tendency [80, 140].

1.6.3   X-ray micro-computed tomography

X-ray micro-computed tomography is a 3D image reconstruction technique that uses X-rays for medical imaging and materials science analyses. Compared to X-ray diffraction methods in which X-rays are reflected by an ordered array of atoms, X-ray micro-computed tomography generates 3D X-ray images based on the electron density differences observed between different phases contained within a sample. X-ray micro-computed tomography has been used in ASD characterization to visualize and quantify the structure of spray drying particles, such as wall thickness and internal structures [141, 142].

It is difficult to use X-ray micro-computed tomography to distinguish samples that have similar attenuation coefficients, such as amorphous and crystalline materials. This limitation can be overcome by applying synchrotron radiation to improve the phase contrast [143]. Qi et al. [91]   have used X-ray micro-computed tomography as a quantitative method to characterize the drug phase separation in patches prepared by hot-melt extrusion and injection molding.

1.7   CHARACTERIZATION METHODS IN DIFFERENT STAGES OF PRODUCT DEVELOPMENT

The final quality of ASD-based products (including in vitro stability, in vitro dissolution, and in vivo performance) can be governed by the various physiochemical properties of ASD intermediates and ASD final products. These properties include molecular mobility, miscibility, glass transition temperature, hygroscopicity, and crystallinity. It is critical to characterize the primary quality attributes of ASDs at different stages in the product life cycle to ensure final product quality and meet project timelines.

Figure 1.8 provides a brief overview of the various characterization techniques used at different stages of ASD-based product development.

ASD characterization techniques

Preclinical	Clinical			Commercial product manufacturing
- API physicochemical properties - Polymer screening (miscibility study) - Primary dissolution, supersaturation study - Accelerated stability study	**Phase I** - Manufacture process selection - Drug-polymer interaction study - Process induced miscibility - Biorelevant dissolution study	**Phase II** - ASD product development (excipient compatibility study) - Influence of downstream processing - Stability prediction	**Phase III** - Commercial product manufacturing - Process analysis techniques - Drug real time release test - ICH accelerated stability study	- Long term stability study - Manufacturing scale up - Technology transfer - Consistence of physical and chemical stability study
TGA DSC (MDSC) PLM (HPLM) PXRD FTIR Raman	DSC (MDSC) PLM PXRD Raman NIR ssNMR	AFM XPS TPS ssNMR Chemical imaging	Raman NIR PXRD ssNMR	DSC PXRD Spectroscopy method ssNMR

Figure 1.8: An overview of the application of various characterization methods at different stages of ASD-based product development. Modified from reference [127].

1.7.1   Preclinical studies

The major limitation of ASD products are their thermodynamic instability and their tendency to recrystallize during storage [144, 145]. A desirable ASD product should maintain its amorphous state from the time of manufacture until drug administration. A proper formulation composition and optimal manufacturing process are important to develop a stable amorphous product with enhanced bioavailability. Before using ASD

43

techniques to formulate a poorly water-soluble drug, it is important to understand whether the compound has the desired physiochemical properties (e.g., crystallization tendency, melting point, hygroscopicity, thermal stability) at preclinical stage. It has been proven that a compound must have a low crystallization tendency in order to be formulated as an ASD.

The physiochemical properties of the drug are the primary criteria for selecting the manufacturing process both at the laboratorial scale and the industry scale [146]. Techniques such as PLM (HSPLM), TGA, DSC (MDSC), or PXRD are the most commonly used methods to probe the physicochemical properties of a drug. Polymer screening is another important aspect for ASD development, since good miscibility between the drug and the polymer is generally believed to be the prerequisite for physically stable ASDs. Techniques that have been explored for miscibility evaluation include DSC (MDSC), FTIR, PXRD, SSNMR, AFM, SEM, TEM, and Raman mapping. Last, other equally important aspects of a preformulation study for the development of an ASD include the drug loading, the selection of other formulation ingredients, primary drug dissolution, supersaturation studies, and stability studies.

1.7.2 Clinical phase study

A clinical study generally consists of phase I, phase II, and phase III studies. Each phase has a different purpose and emphasis, so each phase requires different characterization methods to ensure the product meets the clinical study requirements.

In a phase I study, the formulation and process should be selected based on the preformulation study. Comprehensive studies on the kinetic miscibility between the candidate drugs and the selected polymers require various thermal and spectroscopic analyses. DSC (or MDSC), FTIR, NIR, and Raman spectroscopy are the core methods used to characterize the drug–excipient interaction and miscibility. SSNMR and PXRD (PDF)

measurement can be used to determine the intensity of properties such as molecular interaction and crystallinity. Furthermore, the in vitro drug release from ASDs in biorelevant dissolution media is commonly used in the rational screening of formulations for human clinical trials. Finally, process analytical technology (PAT), which includes FTIR, NIR, and Raman spectroscopy, could also be used to monitor the manufacturing process to ensure product quality.

In a phase II study, the intermediate ASDs are always formulated into solid oral dosage forms such as tablets or capsules. The compatibility between the intermediate ASDs and other excipients, such as filler, binders, and lubricants, should be thoroughly investigated using DSC and Raman spectroscopy. In addition, the effects of downstream processing, such as roller compaction, on the physical stability of ASDs should not be ignored.

In a phase III study, reliable PAT methods should be used continuously to monitor the manufacturing process in real time. Since poor physical stability is the inherent shortcoming of ASDs, solid-state analytical methods of higher sensitivity (e.g., solid-state NMR or Raman spectroscopy) should be used to analyze the critical quality attributes of the intermediate and final ASD products.

1.7.3 Commercial product manufacturing

Managing the commercial production of ASD-based products is more challenging than traditional products that contain crystalline drugs. Reports have shown that nearly 100 solid oral dosages of small molecular drug products were recalled by the FDA, and these reports indicate that failure in the dissolution rate specification was the prominent cause for recall. Since the dissolution performance of an ASD product is closely related to the physical state of the drug [147], the commercial manufacturing process should focus on

45

the long-term stability of the product. In addition, qualitative and quantitative analyses of product quality attributes are required to support the technology transfer and manufacturing scale-up.

1.8 SUMMARY

Effective characterization methods play a critical role in the development of ASDs, although the complexities of ASDs present unique characterization challenges. Various techniques have been applied to analyze the critical quality attributes of ASDs. These techniques help us to better understand their thermodynamics and molecular-level processes, such as glass transition, molecular mobility, and the molecular interactions between the drug and polymer. This type of information is essential to the rational selection of formulation compositions and manufacturing processes of ASDs.

Over the past decade, significant progress has been made in the characterization of ASDs. This paper has summarized the basic methods that are widely applied in the characterization of ASDs in both the solid state and solution state. With more sensitive and accessible analytical tools, pharmaceutical scientists are gaining a better understanding of ASDs, which will lead to greater success in the delivery of poorly water-soluble drugs.

1.9 REFERENCE

[1] R.O. Williams III, A.B. Watts, D.A. Miller, Formulating poorly water-soluble drugs, Springer Science & Business Media2011.

[2] S. Jain, N. Patel, S. Lin, Solubility and dissolution enhancement strategies: current understanding and recent trends, Drug Development and Industrial Pharmacy 41(6) (2015) 875-887.

[3] Y. He, C. Ho, Amorphous Solid Dispersions: Utilization and Challenges in Drug Discovery and Development, Journal of Pharmaceutical Sciences (2015) n/a-n/a.

[4] W.L. Chiou, S. Riegelman, Pharmaceutical applications of solid dispersion systems, Journal of pharmaceutical sciences 60(9) (1971) 1281-1302.

[5] H. Grohganz, P.A. Priemel, K. Lobmann, L.H. Nielsen, R. Laitinen, A. Mullertz, G. Van den Mooter, T. Rades, Refining stability and dissolution rate of amorphous drug formulations, Expert Opinion on Drug Delivery 11(6) (2014) 977-989.

[6] L.S. Taylor, G.G.Z. Zhang, Physical chemistry of supersaturated solutions and implications for oral absorption, Advanced Drug Delivery Reviews (2016).

[7] F.G. Vogt, solid state characterization of amorphous solid dispersions, Pharmaceutical Amorphous Solid Dispersions (2015).

[8] J.A. Baird, L.S. Taylor, Evaluation of amorphous solid dispersion properties using thermal analysis techniques, Adv Drug Deliv Rev 64(5) (2012) 396-421.

[9] S. Thakral, M.W. Terban, N.K. Thakral, R. Suryanarayanan, Recent advances in the characterization of amorphous pharmaceuticals by X-ray diffractometry, Advanced Drug Delivery Reviews 100 (2016) 183-193.

[10] M.M. Knopp, K. Löbmann, D.P. Elder, T. Rades, R. Holm, Recent advances and potential applications of modulated differential scanning calorimetry (mDSC) in drug development, European Journal of Pharmaceutical Sciences 87 (2016) 164-173.

[11] A. Hedoux, Recent developments in the Raman and infrared investigations of amorphous pharmaceuticals and protein formulations: A review, Advanced Drug Delivery Reviews 100 (2016) 133-146.

[12] Y.-C. Shen, Terahertz pulsed spectroscopy and imaging for pharmaceutical applications: A review, International Journal of Pharmaceutics 417(1–2) (2011) 48-60.

[13] N. Chieng, T. Rades, J. Aaltonen, An overview of recent studies on the analysis of pharmaceutical polymorphs, Journal of Pharmaceutical and Biomedical Analysis 55(4) (2011) 618-644.

[14] G. Nichols, Light Microscopy, Polymorphism, Wiley-VCH Verlag GmbH & Co. KGaA2006, pp. 167-209.

[15] C. Telang, S. Mujumdar, M. Mathew, Improved physical stability of amorphous state through acid base interactions, Journal of Pharmaceutical Sciences 98(6) (2009) 2149-2159.

[16] S.A. Raina, D.E. Alonzo, G.G. Zhang, Y. Gao, L.S. Taylor, Impact of Polymers on the Crystallization and Phase Transition Kinetics of Amorphous Nifedipine during Dissolution in Aqueous Media, Mol Pharm 11(10) (2014) 3565-76.

[17] T. Cai, L. Zhu, L. Yu, Crystallization of Organic Glasses: Effects of Polymer Additives on Bulk and Surface Crystal Growth in Amorphous Nifedipine, Pharmaceutical Research 28(10) (2011) 2458-2466.

[18] Y. Li, H. Pang, Z. Guo, L. Lin, Y. Dong, G. Li, M. Lu, C. Wu, Interactions between drugs and polymers influencing hot melt extrusion, Journal of Pharmacy and Pharmacology 66(2) (2014) 148-166.

[19] X. Liu, M. Lu, Z. Guo, L. Huang, X. Feng, C. Wu, Improving the chemical stability of amorphous solid dispersion with cocrystal technique by hot melt extrusion, Pharm Res 29(3) (2012) 806-17.

[20] X. Liu, L. Zhou, F. Zhang, Reactive Melt Extrusion to Improve the Dissolution Performance and Physical Stability of Naproxen Amorphous Solid Dispersions, Molecular Pharmaceutics (2017).

[21] J. Moffat, S. Qi, D.M. Craig, Spatial Characterization of Hot Melt Extruded Dispersion Systems Using Thermal Atomic Force Microscopy Methods: The Effects of Processing Parameters on Phase Separation, Pharmaceutical Research 31(7) (2014) 1744-1752.

[22] A. Bohr, M.S. Yang, S. Baldursdottir, J. Kristensen, M. Dyas, E. Stride, M. Edirisinghe, Particle formation and characteristics of Celecoxib-loaded poly(lactic-co-glycolic acid) microparticles prepared in different solvents using electrospraying, Polymer 53(15) (2012) 3220-3229.

[23] X. Ye, H. Patil, X. Feng, R.V. Tiwari, J. Lu, A. Gryczke, K. Kolter, N. Langley, S. Majumdar, D. Neupane, S.R. Mishra, M.A. Repka, Conjugation of Hot-Melt Extrusion with High-Pressure Homogenization: a Novel Method of Continuously Preparing Nanocrystal Solid Dispersions, AAPS PharmSciTech 17(1) (2016) 78-88.

[24] C. Bruce, K.A. Fegely, A.R. Rajabi-Siahboomi, J.W. McGinity, Crystal growth formation in melt extrudates, Int J Pharm 341(1-2) (2007) 162-72.

[25] P.A. Priemel, R. Laitinen, H. Grohganz, T. Rades, C.J. Strachan, In situ amorphisation of indomethacin with Eudragit (R) E during dissolution, European Journal of Pharmaceutics and Biopharmaceutics 85(3) (2013) 1259-1265.

[26] P.J. Marsac, A.C. Rumondor, D.E. Nivens, U.S. Kestur, L. Stanciu, L.S. Taylor, Effect of temperature and moisture on the miscibility of amorphous dispersions of felodipine and poly(vinyl pyrrolidone), J Pharm Sci 99(1) (2010) 169-85.

[27] R.G. Ricarte, T.P. Lodge, M.A. Hillmyer, Detection of pharmaceutical drug crystallites in solid dispersions by transmission electron microscopy, Mol Pharm 12(3) (2015) 983-90.

[28] H. Ma, D.S. Choi, Y.-E. Zhang, H. Tian, N. Shah, H.P. Chokshi, Evaluation on the Drug–Polymer Mixing Status in Amorphous Solid Dispersions at the Early Stage Formulation and Process Development, Journal of Pharmaceutical Innovation 8(3) (2013) 163-174.

[29] Y.T.A. Turner, C.J. Roberts, M.C. Davies, Scanning probe microscopy in the field of drug delivery, Advanced Drug Delivery Reviews 59(14) (2007) 1453-1473.

[30] J. Sitterberg, A. Özcetin, C. Ehrhardt, U. Bakowsky, Utilising atomic force microscopy for the characterisation of nanoscale drug delivery systems, European Journal of Pharmaceutics and Biopharmaceutics 74(1) (2010) 2-13.

[31] M.E. Lauer, O. Grassmann, M. Siam, J. Tardio, L. Jacob, S. Page, J.H. Kindt, A. Engel, J. Alsenz, Atomic Force Microscopy-Based Screening of Drug-Excipient Miscibility and Stability of Solid Dispersions, Pharmaceutical Research 28(3) (2011) 572-584.

[32] M.S. Lamm, J. DiNunzio, N.N. Khawaja, L.S. Crocker, A. Pecora, Assessing Mixing Quality of a Copovidone-TPGS Hot Melt Extrusion Process with Atomic Force

Microscopy and Differential Scanning Calorimetry, AAPS PharmSciTech 17(1) (2016) 89-98.

[33] J. Meeus, D.J. Scurr, X. Chen, K. Amssoms, M.C. Davies, C.J. Roberts, G. Van den Mooter, Combination of (M) DSC and Surface Analysis to Study the Phase Behaviour and Drug Distribution of Ternary Solid Dispersions, Pharmaceutical research (2014) 1-10.

[34] M. Lauer, M. Siam, J. Tardio, S. Page, J. Kindt, O. Grassmann, Rapid Assessment of Homogeneity and Stability of Amorphous Solid Dispersions by Atomic Force Microscopy—From Bench to Batch, Pharmaceutical Research 30(8) (2013) 2010-2022.

[35] J.S. Stevens, S.J. Byard, C.C. Seaton, G. Sadiq, R.J. Davey, S.L.M. Schroeder, Proton transfer and hydrogen bonding in the organic solid state: a combined XRD/XPS/ssNMR study of 17 organic acid-base complexes, Physical Chemistry Chemical Physics 16(3) (2014) 1150-1160.

[36] H.-L. Lee, N.T. Flynn, X-RAY PHOTOELECTRON SPECTROSCOPY, in: D.R. Vij (Ed.), Handbook of Applied Solid State Spectroscopy, Springer US, Boston, MA, 2006, pp. 485-507.

[37] C. Dahlberg, A. Millqvist-Fureby, M. Schuleit, Surface composition and contact angle relationships for differently prepared solid dispersions, European Journal of Pharmaceutics and Biopharmaceutics 70(2) (2008) 478-485.

[38] Y. Song, D. Zemlyanov, X. Chen, H. Nie, Z. Su, K. Fang, X. Yang, D. Smith, S. Byrn, J.W. Lubach, Acid-Base Interactions of Polystyrene Sulfonic Acid in Amorphous Solid Dispersions Using a Combined UV/FTIR/XPS/ssNMR Study, Mol Pharm 13(2) (2016) 483-92.

51

[39] Y. Song, D. Zemlyanov, X. Chen, Z.Y. Su, H.C. Nie, J.W. Lubach, D. Smith, S. Byrn, R. Pinal, Acid-base interactions in amorphous solid dispersions of lumefantrine prepared by spray-drying and hot-melt extrusion using X-ray photoelectron spectroscopy, International Journal of Pharmaceutics 514(2) (2016) 456-464.

[40] G.L.B. de Araujo, C.J. Benmore, S.R. Byrn, Local Structure of Ion Pair Interaction in Lapatinib Amorphous Dispersions characterized by Synchrotron X-Ray diffraction and Pair Distribution Function Analysis, Scientific Reports 7 (2017) 46367.

[41] C.J. Gilmore, X-Ray Diffraction, Solid State Characterization of Pharmaceuticals, John Wiley & Sons, Ltd2011, pp. 35-70.

[42] R.E. Dinnebier, Powder diffraction: theory and practice, Royal Society of Chemistry2008.

[43] A.C. Rumondor, L.A. Stanford, L.S. Taylor, Effects of polymer type and storage relative humidity on the kinetics of felodipine crystallization from amorphous solid dispersions, Pharm Res 26(12) (2009) 2599-606.

[44] I. Takeuchi, K. Shimakura, H. Kuroda, T. Nakajima, S. Goto, K. Makino, Estimation of Crystallinity of Nifedipine–Polyvinylpyrrolidone Solid Dispersion by Usage of Terahertz Time-Domain Spectroscopy and of X-Ray Powder Diffractometer, Journal of Pharmaceutical Sciences 104(12) (2015) 4307-4313.

[45] T. Egami, S.J. Billinge, Underneath the Bragg peaks: structural analysis of complex materials, Newnes2012.

[46] C.A. Young, A.L. Goodwin, Applications of pair distribution function methods to contemporary problems in materials chemistry, Journal of Materials Chemistry 21(18) (2011) 6464-6476.

[47] K. Nollenberger, A. Gryczke, C. Meier, J. Dressman, M.U. Schmidt, S. Brühne, Pair distribution function X-ray analysis explains dissolution characteristics of felodipine melt extrusion products, Journal of Pharmaceutical Sciences 98(4) (2008) 1476-1486.

[48] A. Newman, D. Engers, S. Bates, I. Ivanisevic, R.C. Kelly, G. Zografi, Characterization of Amorphous API:Polymer Mixtures Using X-Ray Powder Diffraction, Journal of Pharmaceutical Sciences 97(11) (2008) 4840-4856.

[49] T. Dykhne, R. Taylor, A. Florence, S.J. Billinge, Data requirements for the reliable use of atomic pair distribution functions in amorphous pharmaceutical fingerprinting, Pharm Res 28(5) (2011) 1041-8.

[50] C. Nunes, A. Mahendrasingam, R. Suryanarayanan, Quantification of crystallinity in substantially amorphous materials by synchrotron X-ray powder diffractometry, Pharm Res 22(11) (2005) 1942-53.

[51] Q. Zhu, S.J. Toth, G.J. Simpson, H.Y. Hsu, L.S. Taylor, M.T. Harris, Crystallization and dissolution behavior of naproxen/polyethylene glycol solid dispersions, The journal of physical chemistry. B 117(5) (2013) 1494-500.

[52] J.A. Newman, P.D. Schmitt, S.J. Toth, F. Deng, S. Zhang, G.J. Simpson, Parts per Million Powder X-ray Diffraction, Analytical Chemistry 87(21) (2015) 10950-10955.

[53] A. Bohr, F. Wan, J. Kristensen, M. Dyas, E. Stride, S. Baldursdottír, M. Edirisinghe, M. Yang, Pharmaceutical microparticle engineering with electrospraying: the role of mixed

solvent systems in particle formation and characteristics, Journal of Materials Science: Materials in Medicine 26(2) (2015) 1-13.

[54] F. Wan, A. Bohr, M. Maltesen, S. Bjerregaard, C. Foged, J. Rantanen, M. Yang, Critical Solvent Properties Affecting the Particle Formation Process and Characteristics of Celecoxib-Loaded PLGA Microparticles via Spray-Drying, Pharmaceutical Research 30(4) (2013) 1065-1076.

[55] G.W.H. Höhne, W. Hemminger, H.-J. Flammersheim, Theoretical Fundamentals of Differential Scanning Calorimeters, Differential Scanning Calorimetry, Springer1996, pp. 21-40.

[56] K. Kawakami, T. Usui, M. Hattori, Understanding the glass-forming ability of active pharmaceutical ingredients for designing supersaturating dosage forms, Journal of Pharmaceutical Sciences 101(9) (2012) 3239-3248.

[57] I. Weuts, D. Kempen, A. Decorte, G. Verreck, J. Peeters, M. Brewster, G. Van den Mooter, Phase behaviour analysis of solid dispersions of loperamide and two structurally related compounds with the polymers PVP-K30 and PVP-VA64, Eur J Pharm Sci 22(5) (2004) 375-85.

[58] B. Van Eerdenbrugh, L.S. Taylor, Small scale screening to determine the ability of different polymers to inhibit drug crystallization upon rapid solvent evaporation, Mol Pharm 7(4) (2010) 1328-37.

[59] J.A. Baird, B. Van Eerdenbrugh, L.S. Taylor, A classification system to assess the crystallization tendency of organic molecules from undercooled melts, J Pharm Sci 99(9) (2010) 3787-806.

[60] D.T. Friesen, R. Shanker, M. Crew, D.T. Smithey, W.J. Curatolo, J.A.S. Nightingale, Hydroxypropyl Methylcellulose Acetate Succinate-Based Spray-Dried Dispersions: An Overview, Molecular Pharmaceutics 5(6) (2008) 1003-1019.

[61] A.M. Kaushal, A.K. Bansal, Thermodynamic behavior of glassy state of structurally related compounds, European Journal of Pharmaceutics and Biopharmaceutics 69(3) (2008) 1067-1076.

[62] X. Feng, X. Ye, J.-B. Park, W. Lu, J. Morott, B. Beissner, Z.J. Lian, E. Pinto, V. Bi, S. Porter, T. Durig, S. Majumdar, M.A. Repka, Evaluation of the recrystallization kinetics of hot-melt extruded polymeric solid dispersions using an improved Avrami equation, Drug Development and Industrial Pharmacy 0(0) (2014) 1-9.

[63] M. Tobyn, J. Brown, A.B. Dennis, M. Fakes, Q. Gao, J. Gamble, Y.Z. Khimyak, G. McGeorge, C. Patel, W. Sinclair, P. Timmins, S. Yin, Amorphous drug–PVP dispersions: Application of theoretical, thermal and spectroscopic analytical techniques to the study of a molecule with intermolecular bonds in both the crystalline and pure amorphous state, Journal of Pharmaceutical Sciences 98(9) (2009) 3456-3468.

[64] A.C.F. Rumondor, P.J. Marsac, L.A. Stanford, L.S. Taylor, Phase Behavior of Poly(vinylpyrrolidone) Containing Amorphous Solid Dispersions in the Presence of Moisture, Molecular Pharmaceutics 6(5) (2009) 1492-1505.

[65] G.P. Andrews, O.A. AbuDiak, D.S. Jones, Physicochemical characterization of hot melt extruded bicalutamide–polyvinylpyrrolidone solid dispersions, Journal of Pharmaceutical Sciences 99(3) (2010) 1322-1335.

[66] F. Qian, J. Huang, Q. Zhu, R. Haddadin, J. Gawel, R. Garmise, M. Hussain, Is a distinctive single Tg a reliable indicator for the homogeneity of amorphous solid dispersion?, International Journal of Pharmaceutics 395(1-2) (2010) 232-235.

[67] P.J. Marsac, T. Li, L.S. Taylor, Estimation of drug-polymer miscibility and solubility in amorphous solid dispersions using experimentally determined interaction parameters, Pharm Res 26(1) (2009) 139-51.

[68] J. Tao, Y. Sun, G.G.Z. Zhang, L. Yu, Solubility of Small-Molecule Crystals in Polymers: d-Mannitol in PVP, Indomethacin in PVP/VA, and Nifedipine in PVP/VA, Pharmaceutical Research 26(4) (2009) 855-864.

[69] A.N. Ghebremeskel, C. Vernavarapu, M. Lodaya, Use of surfactants as plasticizers in preparing solid dispersions of poorly soluble API: Selection of polymer-surfactant combinations using solubility parameters and testing the processability, International Journal of Pharmaceutics 328(2) (2007) 119-129.

[70] M.C. Righetti, C. Cardelli, M. Scalari, E. Tombari, G. Conti, Thermodynamics of mixing of poly(vinyl chloride) and poly(ethylene-co-vinyl acetate), Polymer 43(18) (2002) 5035-5042.

[71] P. Gupta, V.K. Kakumanu, A.K. Bansal, Stability and solubility of celecoxib-PVP amorphous dispersions: a molecular perspective, Pharm Res 21(10) (2004) 1762-9.

[72] M. Vasanthavada, W.Q. Tong, Y. Joshi, M.S. Kislalioglu, Phase Behavior of amorphous molecular dispersions I: Determination of the degree and mechanism of solid solubility, Pharmaceutical Research 21(9) (2004) 1598-1606.

[73] M. Vasanthavada, W.Q. Tong, Y. Joshi, M.S. Kislalioglu, Phase behavior of amorphous molecular dispersions - II: Role of hydrogen bonding in solid solubility and phase separation kinetics, Pharmaceutical Research 22(3) (2005) 440-448.

[74] P. Tong, L.S. Taylor, G. Zografi, Influence of Alkali Metal Counterions on the Glass Transition Temperature of Amorphous Indomethacin Salts, Pharmaceutical Research 19(5) (2002) 649-654.

[75] I. Weuts, D. Kempen, G. Verreck, J. Peeters, M. Brewster, N. Blaton, G. Van den Mooter, Salt formation in solid dispersions consisting of polyacrylic acid as a carrier and three basic model compounds resulting in very high glass transition temperatures and constant dissolution properties upon storage, European Journal of Pharmaceutical Sciences 25(4–5) (2005) 387-393.

[76] L. Yu, Amorphous pharmaceutical solids: preparation, characterization and stabilization, Advanced Drug Delivery Reviews 48(1) (2001) 27-42.

[77] A.C.F. Rumondor, I. Ivanisevic, S. Bates, D.E. Alonzo, L.S. Taylor, Evaluation of Drug-Polymer Miscibility in Amorphous Solid Dispersion Systems, Pharmaceutical Research 26(11) (2009) 2523-2534.

[78] L.C. Grisedale, M.J. Jamieson, P. Belton, S.A. Barker, D.Q.M. Craig, Characterization and Quantification of Amorphous Material in Milled and Spray-Dried Salbutamol Sulfate: A Comparison of Thermal, Spectroscopic, and Water Vapor Sorption Approaches, Journal of Pharmaceutical Sciences 100(8) (2011) 3114-3129.

[79] B. Shah, V.K. Kakumanu, A.K. Bansal, Analytical techniques for quantification of amorphous/crystalline phases in pharmaceutical solids, Journal of Pharmaceutical Sciences 95(8) (2006) 1641-1665.

[80] P. Mistry, S. Mohapatra, T. Gopinath, F.G. Vogt, R. Suryanarayanan, Role of the Strength of Drug–Polymer Interactions on the Molecular Mobility and Crystallization Inhibition in Ketoconazole Solid Dispersions, Molecular Pharmaceutics (2015).

[81] O. Korhonen, C. Bhura, M.J. Pikal, Correlation between molecular mobility and crystal growth of amorphous phenobarbital and phenobarbital with polyvinylpyrrolidone and L-proline, Journal of Pharmaceutical Sciences 97(9) (2008) 3830-3841.

[82] Y. Aso, S. Yoshioka, S. Kojima, Molecular mobility-based estimation of the crystallization rates of amorphous nifedipine and phenobarbital in poly(vinylpyrrolidone) solid dispersions, J Pharm Sci 93(2) (2004) 384-91.

[83] L. Yu, Surface mobility of molecular glasses and its importance in physical stability, Advanced Drug Delivery Reviews 100 (2016) 3-9.

[84] D.Q.M. Craig, V.L. Kett, C.S. Andrews, P.G. Royall, Pharmaceutical Applications of Micro-Thermal Analysis, Journal of Pharmaceutical Sciences 91(5) (2002) 1201-1213.

[85] X. Dai, J.G. Moffat, J. Wood, M. Reading, Thermal scanning probe microscopy in the development of pharmaceuticals, Advanced Drug Delivery Reviews 64(5) (2012) 449-460.

[86] K. Six, J. Murphy, I. Weuts, D.M. Craig, G. Verreck, J. Peeters, M. Brewster, G. Van den Mooter, Identification of Phase Separation in Solid Dispersions of Itraconazole and Eudragit® E100 Using Microthermal Analysis, Pharmaceutical Research 20(1) (2003) 135-138.

58

[87] L. Harding, W.P. King, X. Dai, D.Q. Craig, M. Reading, Nanoscale characterisation and imaging of partially amorphous materials using local thermomechanical analysis and heated tip AFM, Pharm Res 24(11) (2007) 2048-54.

[88] J. Zhang, M. Bunker, X. Chen, A.P. Parker, N. Patel, C.J. Roberts, Nanoscale thermal analysis of pharmaceutical solid dispersions, International Journal of Pharmaceutics 380(1–2) (2009) 170-173.

[89] S. Qi, J.G. Moffat, Z. Yang, Early Stage Phase Separation in Pharmaceutical Solid Dispersion Thin Films under High Humidity: Improved Spatial Understanding Using Probe-Based Thermal and Spectroscopic Nanocharacterization Methods, Molecular Pharmaceutics 10(3) (2013) 918-930.

[90] M. Alhijjaj, M. Reading, P. Belton, S. Qi, Thermal Analysis by Structural Characterization as a Method for Assessing Heterogeneity in Complex Solid Pharmaceutical Dosage Forms, Anal Chem 87(21) (2015) 10848-55.

[91] M. Alhijjaj, S. Yassin, M. Reading, J.A. Zeitler, P. Belton, S. Qi, Characterization of Heterogeneity and Spatial Distribution of Phases in Complex Solid Dispersions by Thermal Analysis by Structural Characterization and X-ray Micro Computed Tomography, Pharmaceutical Research 34(5) (2017) 971-989.

[92] A. Heinz, C.J. Strachan, K.C. Gordon, T. Rades, Analysis of solid-state transformations of pharmaceutical compounds using vibrational spectroscopy, Journal of Pharmacy and Pharmacology 61(8) (2009) 971-988.

[93] B. Tian, X. Tang, L.S. Taylor, Investigating the Correlation between Miscibility and Physical Stability of Amorphous Solid Dispersions Using Fluorescence-Based Techniques, Mol. Pharmaceutics (2016) Ahead of Print.

[94] H.G. Brittain, Spectroscopy of pharmaceutical solids, Taylor & Francis New York2006.

[95] G.A. Ilevbare, L.S. Taylor, Liquid–Liquid Phase Separation in Highly Supersaturated Aqueous Solutions of Poorly Water-Soluble Drugs: Implications for Solubility Enhancing Formulations, Crystal Growth & Design 13(4) (2013) 1497-1509.

[96] S. Raina, D. Alonzo, G.Z. Zhang, Y. Gao, L. Taylor, Using Environment-Sensitive Fluorescent Probes to Characterize Liquid-Liquid Phase Separation in Supersaturated Solutions of Poorly Water Soluble Compounds, Pharmaceutical Research (2015) 1-14.

[97] A.C. Rumondor, L.S. Taylor, Effect of polymer hygroscopicity on the phase behavior of amorphous solid dispersions in the presence of moisture, Mol Pharm 7(2) (2010) 477-90.

[98] X. Feng, A. Vo, H. Patil, R.V. Tiwari, A.S. Alshetaili, M.B. Pimparade, M.A. Repka, The effects of polymer carrier, hot melt extrusion process and downstream processing parameters on the moisture sorption properties of amorphous solid dispersions, J Pharm Pharmacol 68(5) (2016) 692-704.

[99] B. Van Eerdenbrugh, M. Lo, K. Kjoller, C. Marcott, L.S. Taylor, Nanoscale mid-infrared imaging of phase separation in a drug-polymer blend, J Pharm Sci 101(6) (2012) 2066-73.

[100] L. Saerens, C. Vervaet, J.P. Remon, T. De Beer, Process monitoring and visualization solutions for hot-melt extrusion: a review, Journal of Pharmacy and Pharmacology 66(2) (2014) 180-203.

[101] A. Almeida, L. Saerens, T. De Beer, J.P. Remon, C. Vervaet, Upscaling and in-line process monitoring via spectroscopic techniques of ethylene vinyl acetate hot-melt extruded formulations, International journal of pharmaceutics 439(1) (2012) 223-229.

[102] S.G. Kazarian, A.V. Ewing, Applications of Fourier transform infrared spectroscopic imaging to tablet dissolution and drug release, Expert Opinion on Drug Delivery 10(9) (2013) 1207-1221.

[103] M. Pudlas, S.O. Kyeremateng, L.A.M. Williams, J.A. Kimber, H. van Lishaut, S.G. Kazarian, G.H. Woehrle, Analyzing the impact of different excipients on drug release behavior in hot-melt extrusion formulations using FTIR spectroscopic imaging, European Journal of Pharmaceutical Sciences 67(0) (2015) 21-31.

[104] K. Punčochová, A.V. Ewing, M. Gajdošová, T. Pekárek, J. Beránek, S.G. Kazarian, F. Štěpánek, The Combined Use of Imaging Approaches to Assess Drug Release from Multicomponent Solid Dispersions, Pharmaceutical Research (2016) 1-12.

[105] A. Paudel, D. Raijada, J. Rantanen, Raman spectroscopy in pharmaceutical product design, Advanced Drug Delivery Reviews 89 (2015) 3-20.

[106] A. Lust, C.J. Strachan, P. Veski, J. Aaltonen, J. Heinämäki, J. Yliruusi, K. Kogermann, Amorphous solid dispersions of piroxicam and Soluplus®: Qualitative and quantitative analysis of piroxicam recrystallization during storage, International Journal of Pharmaceutics 486(1–2) (2015) 306-314.

[107] G.P. Andrews, H. Zhai, S. Tipping, D.S. Jones, Characterisation of the Thermal, Spectroscopic and Drug Dissolution Properties of Mefenamic Acid and Polyoxyethylene-Polyoxypropylene Solid Dispersions, Journal of Pharmaceutical Sciences 98(12) (2009) 4545-4556.

[108] F. Tres, K. Treacher, J. Booth, L.P. Hughes, S.A.C. Wren, J.W. Aylott, J.C. Burley, Real time Raman imaging to understand dissolution performance of amorphous solid dispersions, Journal of Controlled Release 188(0) (2014) 53-60.

[109] A. Paudel, M. Geppi, G. Van den Mooter, Structural and Dynamic Properties of Amorphous Solid Dispersions: The Role of Solid-State Nuclear Magnetic Resonance Spectroscopy and Relaxometry, Journal of Pharmaceutical Sciences 103(9) (2014) 2635-2662.

[110] Y. Aso, S. Yoshioka, S. Kojima, Relationship Between the Crystallization Rates of Amorphous Nifedipine, Phenobarbital, and Flopropione, and Their Molecular Mobility as Measured by Their Enthalpy Relaxation and 1H NMR Relaxation Times, Journal of Pharmaceutical Sciences 89(3) (2000) 408-416.

[111] Y. Aso, S. Yoshioka, T. Miyazaki, T. Kawanishi, Feasibility of ^{19}F-NMR for Assessing the Molecular Mobility of Flufenamic Acid in Solid Dispersions, Chemical and Pharmaceutical Bulletin 57(1) (2009) 61-64.

[112] T.N. Pham, S.A. Watson, A.J. Edwards, M. Chavda, J.S. Clawson, M. Strohmeier, F.G. Vogt, Analysis of Amorphous Solid Dispersions Using 2D Solid-State NMR and 1H T1 Relaxation Measurements, Molecular Pharmaceutics 7(5) (2010) 1667-1691.

[113] A. Ito, T. Watanabe, S. Yada, T. Hamaura, H. Nakagami, K. Higashi, K. Moribe, K. Yamamoto, Prediction of recrystallization behavior of troglitazone/polyvinylpyrrolidone solid dispersion by solid-state NMR, International Journal of Pharmaceutics 383(1–2) (2010) 18-23.

[114] Y. Song, X. Yang, X. Chen, H. Nie, S. Byrn, J.W. Lubach, Investigation of Drug–Excipient Interactions in Lapatinib Amorphous Solid Dispersions Using Solid-State NMR Spectroscopy, Molecular Pharmaceutics 12(3) (2015) 857-866.

[115] C. Dahlberg, S.V. Dvinskikh, M. Schuleit, I. Furó, Polymer Swelling, Drug Mobilization and Drug Recrystallization in Hydrating Solid Dispersion Tablets Studied by Multinuclear NMR Microimaging and Spectroscopy, Molecular Pharmaceutics 8(4) (2011) 1247-1256.

[116] N. Fotaki, C.M. Long, K. Tang, H. Chokshi, Dissolution of Amorphous Solid Dispersions: Theory and Practice, in: N. Shah, H. Sandhu, D.S. Choi, H. Chokshi, A.W. Malick (Eds.), Amorphous Solid Dispersions: Theory and Practice, Springer New York, New York, NY, 2014, pp. 487-514.

[117] J. Østergaard, J. Lenke, S.S. Jensen, Y. Sun, F. Ye, UV imaging for in vitro dissolution and release studies: initial experiences, Dissolut Technol 21(4) (2014) 27-38.

[118] Y. Sun, J. Østergaard, Application of UV Imaging in Formulation Development, Pharmaceutical Research (2016) 1-12.

[119] S. Wartewig, R.H.H. Neubert, Pharmaceutical applications of Mid-IR and Raman spectroscopy, Advanced Drug Delivery Reviews 57(8) (2005) 1144-1170.

[120] D.E. Alonzo, G.G. Zhang, D. Zhou, Y. Gao, L.S. Taylor, Understanding the behavior of amorphous pharmaceutical systems during dissolution, Pharm Res 27(4) (2010) 608-18.

[121] Z.A. Langham, J. Booth, L.P. Hughes, G.K. Reynolds, S.A.C. Wren, Mechanistic insights into the dissolution of spray-dried amorphous solid dispersions, Journal of Pharmaceutical Sciences 101(8) (2012) 2798-2810.

[122] F. Tres, S.R. Coombes, A.R. Phillips, L.P. Hughes, S.A. Wren, J.W. Aylott, J.C. Burley, Investigating the Dissolution Performance of Amorphous Solid Dispersions Using Magnetic Resonance Imaging and Proton NMR, Molecules 20(9) (2015) 16404-18.

[123] S.R. Coombes, L.P. Hughes, A.R. Phillips, S.A.C. Wren, Proton NMR: A New Tool for Understanding Dissolution, Analytical Chemistry 86(5) (2014) 2474-2480.

[124] J. Kanzer, S. Hupfeld, T. Vasskog, I. Tho, P. Hölig, M. Mägerlein, G. Fricker, M. Brandl, In situ formation of nanoparticles upon dispersion of melt extrudate formulations in aqueous medium assessed by asymmetrical flow field-flow fractionation, Journal of Pharmaceutical and Biomedical Analysis 53(3) (2010) 359-365.

[125] P. Harmon, K. Galipeau, W. Xu, C. Brown, W.P. Wuelfing, Mechanism of Dissolution-Induced Nanoparticle Formation from a Copovidone-Based Amorphous Solid Dispersion, Mol Pharm (2016).

[126] S. Colombo, M. Brisander, J. Haglöf, P. Sjövall, P. Andersson, J. Østergaard, M. Malmsten, Matrix effects in nilotinib formulations with pH-responsive polymer produced by carbon dioxide-mediated precipitation, International Journal of Pharmaceutics 494(1) (2015) 205-217.

[127] A. Paudel, J. Meeus, G.V.d. Mooter, Structural Characterization of Amorphous Solid Dispersions, in: N. Shah, H. Sandhu, D.S. Choi, H. Chokshi, A.W. Malick (Eds.), Amorphous Solid Dispersions: Theory and Practice, Springer New York, New York, NY, 2014, pp. 421-485.

[128] S.-Y. Lin, S.-L. Wang, Advances in simultaneous DSC–FTIR microspectroscopy for rapid solid-state chemical stability studies: Some dipeptide drugs as examples, Advanced Drug Delivery Reviews 64(5) (2012) 461-478.

[129] T. Wu, S.Y. Lin, H.L. Lin, Y.T. Huang, Simultaneous DSC-FTIR Microspectroscopy Used to Screen and Detect the Co-crystal Formation in Real Time, Bioorganic & Medicinal Chemistry Letters (2011).

[130] J. Huang, M. Dali, Evaluation of integrated Raman-DSC technology in early pharmaceutical development: Characterization of polymorphic systems, Journal of Pharmaceutical and Biomedical Analysis 86 (2013) 92-99.

[131] B. Pili, C. Bourgaux, H. Amenitsch, G. Keller, S. Lepêtre-Mouelhi, D. Desmaële, P. Couvreur, M. Ollivon, Interaction of a new anticancer prodrug, gemcitabine–squalene, with a model membrane: Coupled DSC and XRD study, Biochimica et Biophysica Acta (BBA) - Biomembranes 1798(8) (2010) 1522-1532.

[132] A. Dazzi, C.B. Prater, Q. Hu, D.B. Chase, J.F. Rabolt, C. Marcott, AFM–IR: Combining Atomic Force Microscopy and Infrared Spectroscopy for Nanoscale Chemical Characterization, Applied Spectroscopy 66(12) (2012) 1365-1384.

[133] S.-Y. Lin, C.-J. Lee, Y.-Y. Lin, Drug-polymer interaction affecting the mechanical properties, adhesion strength and release kinetics of piroxicam-loaded Eudragit E films plasticized with different plasticizers, Journal of Controlled Release 33(3) (1995) 375-381.

[134] N. Li, L.S. Taylor, Nanoscale Infrared, Thermal, and Mechanical Characterization of Telaprevir–Polymer Miscibility in Amorphous Solid Dispersions Prepared by Solvent Evaporation, Molecular Pharmaceutics 13(3) (2016) 1123-1136.

[135] J. Sibik, K. Löbmann, T. Rades, J.A. Zeitler, Predicting Crystallization of Amorphous Drugs with Terahertz Spectroscopy, Molecular Pharmaceutics 12(8) (2015) 3062-3068.

[136] J.A. Zeitler, P.F. Taday, M. Pepper, T. Rades, Relaxation and crystallization of amorphous carbamazepine studied by terahertz pulsed spectroscopy, Journal of Pharmaceutical Sciences 96(10) (2007) 2703-2709.

[137] J. Sibik, J.A. Zeitler, Direct measurement of molecular mobility and crystallisation of amorphous pharmaceuticals using terahertz spectroscopy, Advanced Drug Delivery Reviews 100 (2016) 147-157.

[138] S.P. Bhardwaj, R. Suryanarayanan, Molecular Mobility as an Effective Predictor of the Physical Stability of Amorphous Trehalose, Molecular Pharmaceutics 9(11) (2012) 3209-3217.

[139] K. Grzybowska, S. Capaccioli, M. Paluch, Recent developments in the experimental investigations of relaxations in pharmaceuticals by dielectric techniques at ambient and elevated pressure, Advanced Drug Delivery Reviews 100 (2016) 158-182.

[140] K. Kothari, V. Ragoonanan, R. Suryanarayanan, The Role of Polymer Concentration on the Molecular Mobility and Physical Stability of Nifedipine Solid Dispersions, Molecular Pharmaceutics 12(5) (2015) 1477-1484.

[141] J.F. Gamble, M. Terada, C. Holzner, L. Lavery, S.J. Nicholson, P. Timmins, M. Tobyn, Application of X-ray microtomography for the characterisation of hollow polymer-stabilised spray dried amorphous dispersion particles, International Journal of Pharmaceutics 510(1) (2016) 1-8.

[142] J. Wong, D. D'Sa, M. Foley, J.G.Y. Chan, H.-K. Chan, NanoXCT: A Novel Technique to Probe the Internal Architecture of Pharmaceutical Particles, Pharmaceutical Research 31(11) (2014) 3085-3094.

[143] M. Álvarez-Murga, P. Bleuet, J.L. Hodeau, Diffraction/scattering computed tomography for three-dimensional characterization of multi-phase crystalline and amorphous materials, Journal of Applied Crystallography 45(6) (2012) 1109-1124.

[144] K. Kawakami, Supersaturation and crystallization: non-equilibrium dynamics of amorphous solid dispersions for oral drug delivery, Expert Opinion on Drug Delivery (2016) 1-9.

[145] S. Janssens, G. Van den Mooter, Review: physical chemistry of solid dispersions, Journal of Pharmacy and Pharmacology 61(12) (2009) 1571-1586.

[146] T. Vasconcelos, S. Marques, J. das Neves, B. Sarmento, Amorphous solid dispersions: Rational selection of a manufacturing process, Advanced drug delivery reviews 100 (2016) 85-101.

[147] Recall, <http://www.fda.gov/Safety/Recalls/ArchiveRecalls/default.htm>. (2011-2013).

Chapter 2: Reactive Melt Extrusion to Improve the Dissolution Performance and Physical Stability of Naproxen Amorphous Solid Dispersions [2]

2.1 ABSTRACT

The purpose of this chapter was to investigate the reaction between naproxen (NPX) and meglumine (MEG) at elevated temperature and to study the effect of this reaction on the physical stabilities and in vitro drug-release properties of melt-extruded naproxen amorphous solid dispersions (ASDs). Differential scanning calorimetry, hot-stage polarized light microscopy, Fourier transform infrared spectroscopy, and X-ray photoelectron spectroscopy analyses demonstrated that in situ salt formation with proton transfer between NPX and MEG occurred at elevated temperature during the melt extrusion process. The amorphous NPX–MEG salt was physically most stable when two components were present at a 1:1 molar ratio. Polymeric carriers, including povidone, copovidone, and SOLUPLUS, did not interfere with the reaction between NPX and MEG during melt extrusion. Compared to the traditional NPX ASDs consisting of NPX and polymer only, NPX–MEG ASDs were physically more stable and remained amorphous following four months storage at 40 °C and 75% RH (relative humidity). Based on non-sink dissolution testing and polarized light microscopy analyses, we concluded that the conventional NPX ASDs composed of NPX and polymers failed to improve the NPX dissolution rate due to the rapid recrystallization of NPX in contact with aqueous medium. The dissolution rate of NPX–MEG ASDs was two times greater than the corresponding physical mixtures and conventional NPX ASDs. This study demonstrated

---

that the acid–base reaction between NPX and MEG during melt extrusion significantly improved the physical stability and the dissolution rate of NPX ASDs.

2.2 INTRODUCTION

Oral drug delivery is preferred due to the convenience of self-administration, the ease of handling of the dosage form by the patient, and the lower manufacturing cost of the final drug product[1]. Oral bioavailability is the most common pharmacokinetic parameter used to assess a drug candidate's suitability for oral administration, which is mainly limited by drug solubility and the dissolution rate in aqueous media. Combinatory chemistry and high-throughput screening techniques have resulted in many drug candidates that have poor aqueous solubility and poor dissolution characteristics, and this presents challenges for developing oral dosage forms. It has been reported that up to 90% of drugs under investigation, and up to 40% of marketed drugs, are poorly water soluble[2]. A number of strategies have been developed to enable oral delivery of poorly water-soluble drugs. Prodrug approach is commonly explored during the lead candidate optimization by drug discovery chemists. Cocrystal, salt form, micronization, nano particulate, self-emulsifying formulation, and amorphous solid dispersion are common strategies used by formulation scientists[3]. Among all these methods, salt formation and amorphous solid dispersion have been proven to be the most promising approaches to improve the dissolution characteristics and kinetic solubility of poorly water-soluble drugs.

Salt formation is the preferred approach for enhancing the aqueous solubility and dissolution rate of poorly water-soluble drugs with ionizable groups[4]. A salt is generally defined as a crystalline or amorphous material that has a solid-state assembly in which a proton is transferred from the acidic moiety to the basic moiety. Salt form is such a common strategy that more than 50% of marketed drugs contain salts in order to optimize their

biopharmaceutical properties[5]. Depending on the type of counterion, salts can be categorized as inorganic, organic, polymeric, or macromolecular salts. It has been confirmed that the solubility and stability of a salt depends largely on the type of counterion and the acid/base strength[6]. Salt forms of drug substances act as self-buffering agents that control the pH of the diffusion layer surrounding the dissolving particles, thereby creating a favorable microenvironment for enhanced drug solubility and a more rapid dissolution rate. In some cases, converting drugs into their salt forms may still not be sufficient to meet the bioavailability requirement, because salts do not offer a markedly improved dissolution advantage. In other cases, weak salts are prone to disproportionately convert to intrinsically less soluble free acids or bases during product storage and in aqueous media[7].

Another strategy for formulating drugs that have poor aqueous solubility and dissolution rate is represented by amorphous solid dispersion[8]. The most widely accepted definition of amorphous solid dispersion is "a molecular dispersion of one or more active ingredients in an inert carrier in the solid state prepared by the melting, solvent, or melting-solvent method"[9].The conversion of a crystalline drug to an amorphous state with disruption of the crystal lattice can lead to a nonequilibrium high-energy state, which improves transient solubility and the dissolution rate. However, the inherent crystallizing tendency of drugs in the amorphous state may lead to a decrease in solubility and dissolution rate upon storage, which has greatly restricted the application of amorphous solid dispersion.

Salts and amorphous solid dispersions are effective strategies for enhancing the solubility and dissolution rates of poorly water-soluble drugs, but both methods have their inherent shortcomings. Therefore, in certain circumstances, it may be desirable to combine these two approaches to prepare amorphous solid dispersion of the salt form of a drug. A

multicomponent amorphous solid dispersion system composed of a drug, a functional excipient, and an amorphous polymer matrix is considered to be a promising system for the enhancement of the dissolution of poorly water-soluble drugs with acceptable physical stability throughout their shelf life[10]. The application of acid–base reaction in preparing amorphous solid dispersions has recently attracted significant attention, and the reaction can provide sufficient intermolecular interactions between the components to inhibit phase separation and recrystallization. The acid–base interactions between drugs and inorganic additives[11], between other low molecular weight components[12, 13], or between polymers[14], play significant and critical roles in both amorphous miscibility and physical stability[15]. Subrata et al. have converted ibuprofen from its crystalline acid to an amorphous salt form by co-milling it with kaolin. The dissolution rate of ibuprofen was improved, and the amorphous kaolin-bound ibuprofen was physically stable at 40 °C and 75% RH for up to 10 weeks[16].

A series of studies conducted by Rades et al. indicated that salt formation was one of the major mechanisms for the increased physical stability and dissolution enhancement of co-amorphous drug delivery systems, which are composed of two or more low molecular weight components that form a homogeneous amorphous single phase[17]. Song et al.[18, 19] revealed the strong intermolecular acid–base interactions of polystyrene sulfonic acid with two weakly basic anticancer drugs, lapatinib and gefitinib. This interaction significantly improved the dissolution of both drugs and effectively inhibited their recrystallization under accelerated storage conditions. Most of the investigation in this research area was conducted using laboratory-scale preparative techniques, such as solvent evaporation, melting methods, or with mechanical activation, which may be difficult for industrial manufacture. There are very limited number of studies combining salts and amorphous solid dispersions to improve the bioavailability of poorly water-soluble drugs.

Currently, most pharmaceutical salts are synthesized in solution state. The use of solvents can cause environmental, health, and safety concerns. In addition, the removal of solvents involves complicated crystallization and purification procedures, which may result in undesired polymorphs and solvates. A very interesting alternative to solution synthesis is the mechanochemical synthesis of pharmaceutical salts without the addition of solvents or by using only nominal amounts of solvents[20]. A salt can be obtained by proton transfer through a solid-state reaction conducted with the assistance of mechanical energy, such as ball milling and solvent-assisted co-grounding. However, the yields of these processes are low, and the scale-up is also challenging.

Among the various methods for preparing amorphous solid dispersions, melt extrusion has attracted much attention due to several advantages: it does not require the use of a solvent, it is easy to scale up, it is a continuous process, and melt-extrudates have favorable physical properties such as denser particles and good flowability[21]. During melt extrusion, the rotating screws provide intensive mixing, and they convert mechanical into the thermal energy so that the drug is dissolved in polymer melt during extrusion. Since it is conducted at an elevated temperature, melt extrusion provides a favorable environment for the solid-state chemical reaction. Reactive melt extrusion has historically referred to combining chemical reactions and polymer melt extrusion into a single process carried out continuously in a screw extruder[22]. It has been widely applied in the plastic and food industries to improve the properties of materials and products, such as mechanical strength of plastic materials and digestibility of food[23, 24]. Even though pharmaceutical melt extrusion has been extensively studied, more research in reactive melt extrusion for pharmaceutical applications is needed. Reactive melt extrusion has been applied to prepare complex drug delivery systems including cocrystals, salts and amorphous solid dispersions[25]. The unique applications of reactive melt extrusion include (a) reducing

73

thermal degradation of the drug in melt extrusion by depressing the melting point of the drug[26], (b) improving physical stability of the amorphous solid dispersion during storage and during the dissolution process[27], and (c) designing sustained, controlled, and targeted drug delivery systems[28].

Table 2.1 presents the chemical structures and critical attributes of the drugs and excipients used in this study. We selected naproxen (NPX) as the model compound. It is a weak acid with a pK_a of 4.15 and a melting point of 155 °C[29]. NPX is a Class II drug according to the biopharmaceutics classification system (BCS). The bioavailability of NPX is rate-limited by its solubility and dissolution rate[30]. Consequently, extensive research has been conducted to improve its dissolution behavior. Due to the strong π–π interaction of the naphthalene ring and the hydrogen bonding of carboxylic acid groups, NPX shows a very strong recrystallization tendency, and it is challenging to prepare physically stable NPX amorphous solid dispersions with high drug loading.

We selected meglumine (MEG) as the salt-forming base in this study. MEG is a highly water-soluble amino sugar with a pK_a of 8.03 and a melting point of 129 °C[31]. It is an FDA-approved excipient commonly used as a salt former for oral and intravenous drug administration.

It is generally accepted that salt formation would be expected if the pK_a between an acid and a base is greater than 3[32, 33]. In our study, based on the pK_a difference between NPX and MEG (ΔpK_a = 3.88), we hypothesized that *in situ* proton transfer between NPX and MEG could occur during melt extrusion. We further hypothesized that this strong intermolecular interaction would effectively enhance the dissolution performance and physical stability of NPX ASDs. We used differential scanning calorimetry (DSC) and hot-stage polarized light microscopy (HSPLM) to study the thermally induced *in situ* acid–base reaction between NPX and MEG, both with and

74

without the presence of polymers. We applied Fourier transform infrared spectroscopy (FTIR) and X-ray photoelectron spectroscopy (XPS) to determine whether proton transfer took place between NPX and MEG. We investigated the dissolution properties of ASDs prepared by reactive melt extrusion under non-sink conditions using 0.1 N HCl solution as the dissolution medium. Finally, we used X-ray powder diffraction (XRPD) and polarized light microscopy (PLM) to determine the physical stabilities of ASDs under accelerated storage conditions.

Table 2.1: Chemical structures and selected physicochemical properties of naproxen, meglumine and polymers.
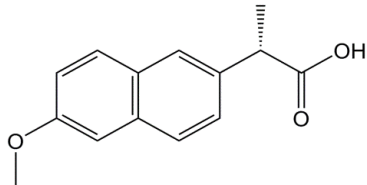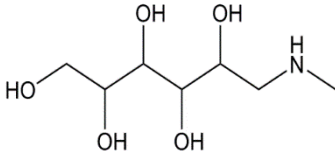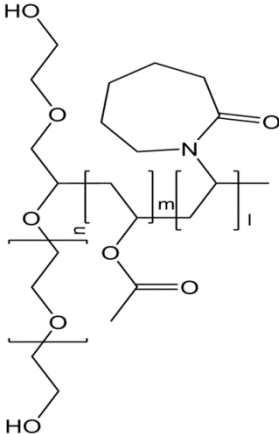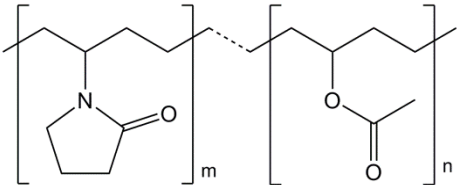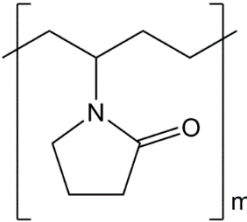
Components	Chemical Structure	Experimental Glass Transition (T_g) and Melting Temperature (T_m) (°C)	Molecular Weight (g/mol)
Naproxen		T_m: 155 T_g: 5	230.26
Meglumine		T_m: 129 T_g: 17	195.22
SOLUPLUS®		T_g: 70	118,000

Table 2.1: continued.

Kollidon®VA64		T_g: 101	45,000
Kollidon®K30		T_g: 149	50,000

2.3 MATERIALS

Naproxen (NPX) was purchased from Nexconn Pharma Techs. Co., Ltd. (Shenzhen, China). Meglumine (MEG) was donated from EMD Millipore (Billerica, MA). Soluplus® (SOLUPLUS), Kollidon®VA64 (PVPVA64), and Kollidon®K30 (PVPK30) were kindly supplied by BASF (Ludwigshafen, Germany). We purchased Acetonitrile (HPLC grade) from Fisher Scientific (Waltham, MA). All other reagents and solvents were analysis grade or better.

2.4 METHODS

2.4.1 Physical Mixture Preparation and NPX–MEG Salt Prepared by Solvent Method

An agate mortar and pestle were used to prepare small-batch physical mixtures of NPX and MEG at various molar ratios (10:1, 10:4, 10:7, 10:10, 7:10, 4:10, and 1:10) for DSC and HSPLM analyses. The large-batch physical mixtures for reactive melt extrusion were initially mixed using a mortar and pestle, then we transferred the physical mixtures

to plastic bottles and further blended them for 30 min in a Turbula shaker mixer to ensure homogenous mixing.

The NPX–MEG salt was prepared for comparison purposes. As modified from a published method[34], the NPX–MEG salt was prepared by dissolving equimolar amounts of NPX (16.11 g, 0.07 mol) and MEG (13.67 g, 0.07 mol) in 100 mL of ethanol. This solution was stirred at room temperature (25 °C) to allow the ethanol to evaporate. Following the complete evaporation of the solvent, we dried the precipitate in a vacuum oven for 24 h and stored it in a desiccator at room temperature.

2.4.2   NPX–MEG Complexes Prepared by Melting Method

The physical mixtures of NPX and MEG at different molar ratios were melted in aluminum dishes in an oven with the temperature setting at 180 °C until a clear melt was observed. The material melted in less than 2 min. The aluminum dishes were removed from oven and cooled down under room temperature. The samples were then stored in a desiccator at room temperature for further analysis.

2.4.3   NPX ASDs Prepared by Reactive Melt Extrusion

We performed reactive melt extrusion using a Leistriz Nano 16 extruder (Leistritz Corporation, Allendale, NJ). The reactive melt extrusion formulations are shown in Table 2.2. The screw configuration and barrel temperatures are shown in Figure 2.1. About 100 g of each formulation was fed into the extruder barrel at a rate of 3.5 g/min using an automatic feeder. The rotation speed of the screw was 150 rpm. Because of the good thermal stability of NPX and MEG, the barrel temperature was set above the melting point of NPX-MEG complex. Barrel temperature for the 1st heating zone, 2nd heating zone, and 3rd heating zone was set at 150, 160 and 175 °C, respectively. The same screw

configuration and barrel temperature setting were used for all the extrusion experiments. The extrudates were collected in a stainless steel pan and cooled to ambient temperature. The extrudates were milled using a coffee grinder and screened through US mesh #30. The milled extrudates were stored in a desiccator at room temperature for further analysis.
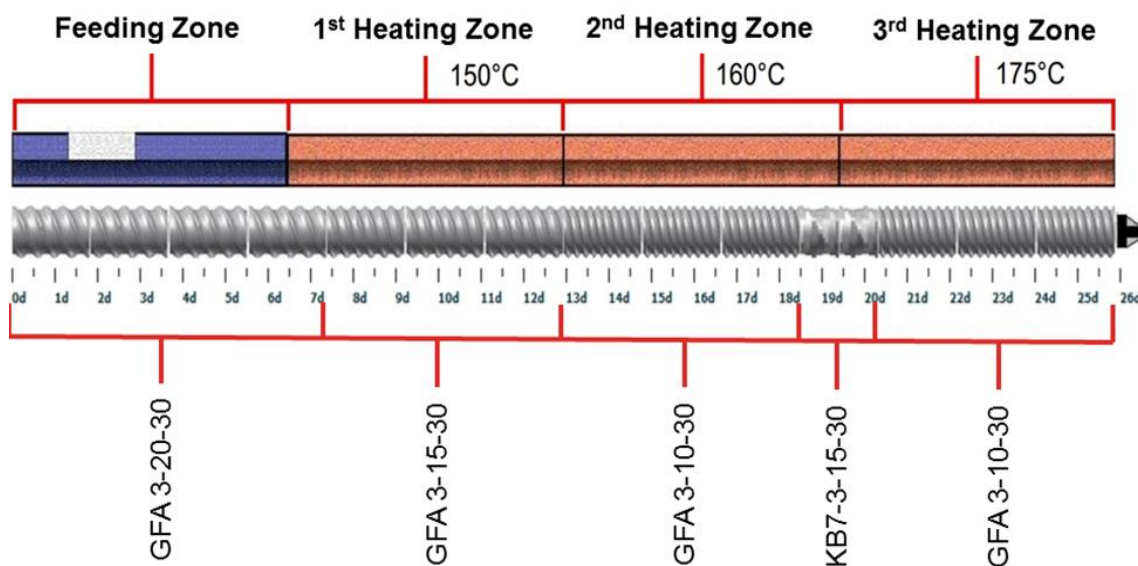
Figure 2.1: Screw configuration and barrel temperature setting for the reactive melt extrusion. Data in the screw code (GFA X-XX-XX) represent the trilobal screw, pitch length (mm) and screw length (mm), respectively. Data in the screw code (KB X-X-XX-XX) indicate the number of kneading segments, trilobal screw, screw length (mm) and the angle (°).

Table 2.2: Composition and glass transition temperature of NPX ASDs prepared by reactive melt extrusion.

Polymer type	NPX (% Wt)	MEG (% Wt)	Polymer (% Wt)	T_g (°C)
SOLUPLUS	48.7	41.3	10.0	27.69
	48.7	-	51.3	31.63
PVPVA64	48.7	41.3	10.0	32.80

78

Table 2.2: continued.

	48.7	-	51.3	43.70
PVPK30	48.7	41.3	10.0	32.25
	48.7	-	51.3	49.00

2.4.4   Differential Scanning Calorimetry (DSC)

DSC analysis was performed using a Model Q20 DSC (TA Instruments, Newcastle, DE) equipped with a refrigerated cooling system 40. We used nitrogen as the purge gas with a flow rate of 50 mL/min. The instrument was calibrated with indium. For sample analysis, 2–5 mg of material was accurately weighed and sealed inside standard TA DSC pans. For the characterization of the NPX and MEG interaction, we heated physical blends from 20 °C to 175 °C, cooled them down to −20 °C, and then heated them again from −20 °C to 175 °C. The temperature ramp rate was kept constant at 10 °C/min. For the characterization of ASD, we used a temperature range of 20°C to 175 °C and a heating rate of 10 °C /min. The DSC data were analyzed using the TA-Universal Analysis 2000 software (TA Instruments, Newcastle, DE). The experimental glass transition temperature (T_g) of various molar ratios of NPX–MEG amorphous mixtures were compared with the theoretical T_g values calculated from Gordon-Taylor equation:

$$T_{g(mix)} = \frac{T_{g1} \cdot W_1 + K \cdot T_{g2} \cdot W_2}{W_1 + K \cdot W_2}$$

where T_g (mix) is the T_g of the NPX–MEG amorphous mixtures. The variables W_1, T_{g1}, and W_2, T_{g2} are weight fractions and glass transition temperatures of the components NPX and MEG, respectively. The letter K is a constant, and it can be further calculated with Simha–Boyer equation:

$$K = \frac{\rho_1 \cdot T_{g1}}{\rho_2 \cdot T_{g2}}$$

where ρ_1 and ρ_2 are the amorphous densities of NPX (1.265 g/cm^3)[30] and MEG (1.100 g/cm^3) [35], respectively.

Quench cooled NPX was analyzed for T_g. NPX was melted in an aluminum pan at 165 °C. The pan was removed from the DSC chamber and quenched in liquid nitrogen to prepare amorphous NPX. For T_g identification, the DSC chamber was equilibrated at -30 °C prior to sample loading. A temperature ramp from -30 °C to 40 °C at 10 °C/min was used to measure the T_g.

2.4.5 Polarized Light Microscopy (PLM) and Hot-Stage Polarized Light Microscopy (HSPLM)

We conducted the PLM measurement using an Olympus BX-53 polarized light microscope (Olympus Corporation of the Americas, Center Valley, PA) equipped with a QImaging QICAM digital camera (QImaging, Surrey, Canada). We mounted samples on the slides, smeared them with silicone oil, covered them with slips, and observed them under the microscope with the same intensity of light. The images were captured using QImaging Ocular software (QImaging, Surrey, Canada).

We used the Linkam T95 hot-stage system (Linkam Scientific Instrument, Tadworth, United Kingdom) for hot-stage analysis. The sample slide was placed in the hot-stage furnace and heated from 25 °C to 180 °C at 10 °C/min. The changes in sample morphology during the heating were recorded with Linksys 32 software for further analysis.

2.4.6   X-Ray Powder Diffraction

The X-ray diffraction pattern of the samples was determined using a Rigaku MiniFlex 600 X-ray diffractometer (Rigaku Corporation, Tokyo, Japan) equipped with a copper X-ray Tube (λ = 1.5406 Å). The measurements were conducted with acceleration voltage of 40 kV and a current of 15 mA. The scanning range was 2–45° (2-theta), with a step width of 0.02°, and the scanning speed was 3°/min. The results were analyzed with software MDI Jade 8.5 (Materials Data, Inc., Livermore, CA).

2.4.7   Fourier Transform Infrared Spectroscopy (FTIR)

We performed FTIR measurements using a Thermo Nicolet iS50 spectrometer (ThermoFisher Scientific, Waltham, MA) equipped with an attenuated total reflection accessory. We placed sufficient samples on the germanium crystal surface, then applied constant torque using the built-in pressure tower to achieve uniform contact between the solid and the crystal. The samples were analyzed at ambient room temperature with the following setting: 4,000–600 cm^{-1}, 64 scans, resolution of 2 cm^{-1}. The peak positions were determined using OMNIC software peak picking function (ThermoFisher Scientific, Waltham, MA).

2.4.8   X-Ray Photoelectron Spectroscopy

We obtained XPS data using a PHI VersaProb II spectrometer (Physical Electronics, Minneapolis, MN) with monochromic Al Kα radiation (1,486.6 eV) at a pass energy of 20 eV and 160 eV for high-resolution and survey spectra, respectively. The pressure during analysis was 8.5×10^{-9} Torr. Before the data analysis, the C–C component of the C 1s peak was set to a binding energy of 284.8 eV to correct for the charge on each sample. We performed quantification and curve fitting in CasaXPS® (Version 2.3.25) using elemental sensitivity factors supplied by the manufacturer.

2.4.9 Non-Sink Dissolution Testing

Non-sink dissolution testing was performed in a simulated gastric fluid (0.1 N hydrochloric acid, pH 1.2, 900 mL) at 37 °C ± 0.5 °C using the USP Type II apparatus (Model Varian VK7025, Agilent Technology Inc., Santa Clara, CA) at a paddle speed of 50 rpm. We introduced powder samples that contained the equivalent of 150 mg of NPX into each dissolution vessel. Three mL dissolution samples were withdrawn at specific time points (2, 5, 10, 15, 30, 45, and 60 min) through Vankel Full Flow® 10-µm filters, without sample replacement. The samples were filtered through a 0.45-µm filter and diluted with an equal volume of acetonitrile to prevent any precipitation. We tested all samples in triplicate.

2.4.10 Intrinsic Solubility of Naproxen in 0.1 N HCl Solution

In order to measure the intrinsic solubility of naproxen, excess amount of naproxen drug substance was added into 0.1 N HCl solution. The vials were stored inside an incubator shaker (Lab-Line Instruments, Melrose Park, IL) set at 37 °C and 100 rpm. After 24 hours of agitation, the suspensions were filtered through 0.2 µm PTFE filters. The filtrates were analyzed using the HPLC method described in 2.4.11.

2.4.11 High-Pressure Liquid Chromatography

The Dissolution samples were analyzed using a Waters 2998 HPLC system (Waters Corporation, Milford, MA) equipped with a Thermo scientific Hypersil GOLD C8, 50 × 3 column, 3 µm (ThermoFisher Scientific, Waltham, MA). We used the mobile phase, consisting of a 75:25 (v/v) mixture of 0.05% (v/v) trifluoroacetic acid in water and acetonitrile at a flow rate of 1.0 mL/min with an injection volume of 10 µL. The retention time for NPX was 3.5 min and was detected at 236 nm. We constructed calibration curves using standard solutions of known concentrations. Empower software was used to

automatically calculate the peak area. The linearity, accuracy and precision of the method were verified.

2.4.12   Physical Stability Evaluation

NPX–MEG complexes prepared using the melting method were sealed in glass bottles and stored in the desiccators under ambient temperature for the physical stability study. Melt-extruded NPX ASDs were sealed in closed HDPE bottles with a silicate desiccator and stored at the ICH (International Council for Harmonization) accelerated stability conditions of 40 °C and 75% RH. We removed the bottles from the stability chamber (Darwin Chambers Company, St. Louis, MO) at specific time points for analysis.

2.5   RESULTS AND DISCUSSION

2.5.1   Reaction between NPX and MEG at Elevated Temperature

2.5.1.1 Characterization of NPX and MEG Interactions at Elevated Temperature Using DSC

The Solid-state reaction between acid and base at elevated temperatures is likely to occur[36]. However, in the literature, there have been few reports on the acid–base reaction during melt extrusion. The pK_a rule is generally accepted to predict salt formation in solution. Since the pK_a difference between NPX and MEG is 3.88, NPX is likely to react with MEG to form an organic salt in solid state at elevated temperature.

The interaction between NPX and MEG in physical mixtures at elevated temperature was initially studied using DSC analysis with a heating-cooling-heating temperature cycle. Figure 2.2A and Figure 2.2B present the thermograms of NPX–MEG mixtures at various molar ratios from the first and second heating scans, respectively. The numbers in the sample labels represent the molar ratio between NPX and MEG. As shown

in Figure 2.2A, pure MEG and NPX melted at 129 °C and 155 °C, respectively. The NPX–MEG binary mixtures demonstrated interesting thermal behaviors. We observed endothermic events (124 °C) below the individual melting points of both NPX and MEG in all binary NPX–MEG mixtures. We attributed these low "eutectic-like" endothermic events to the suppression of MEG melting in the presence of NPX. Except for the 10–4, 10–10 and 1–10 NPX–MEG samples, low "eutectic-like" melting point depression of NPX was also detected in 10–1, 10–7, 7–10, and 4–10 NPX–MEG samples. However, the melting peak of NPX was not observed in the samples of 10–4 and 1–10 NPX–MEG samples. In the 10–4 NPX–MEG sample, a new sharp melting peak at 133 °C appeared after the melting of MEG at 124 °C. The possible reason for this result might be that all of NPX fully formed a eutectic mixture with MEG at this molar ratio. For the 1–10 NPX–MEG sample, we attribute the disappearance of the NPX melting peak to the dissolution of NPX crystals in the molten MEG.
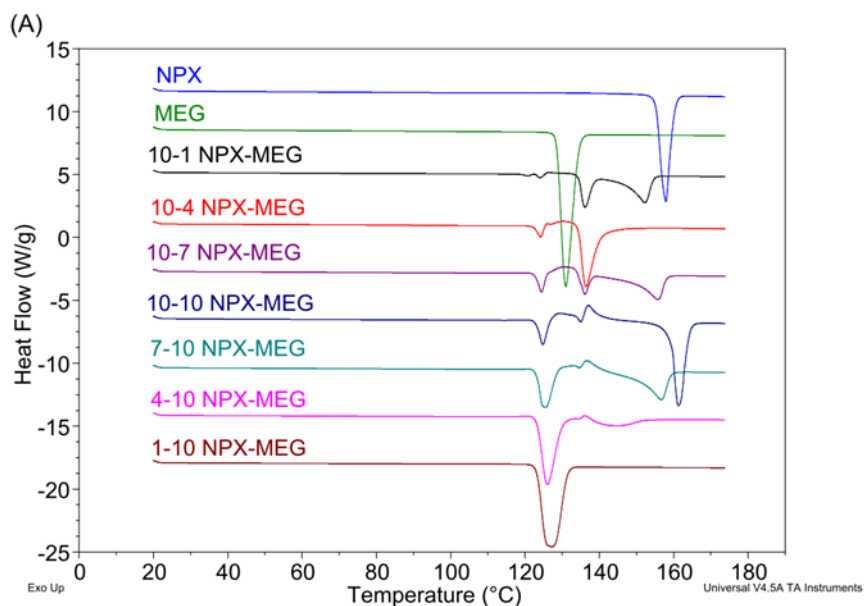
Figure 2.2: continued to next page.
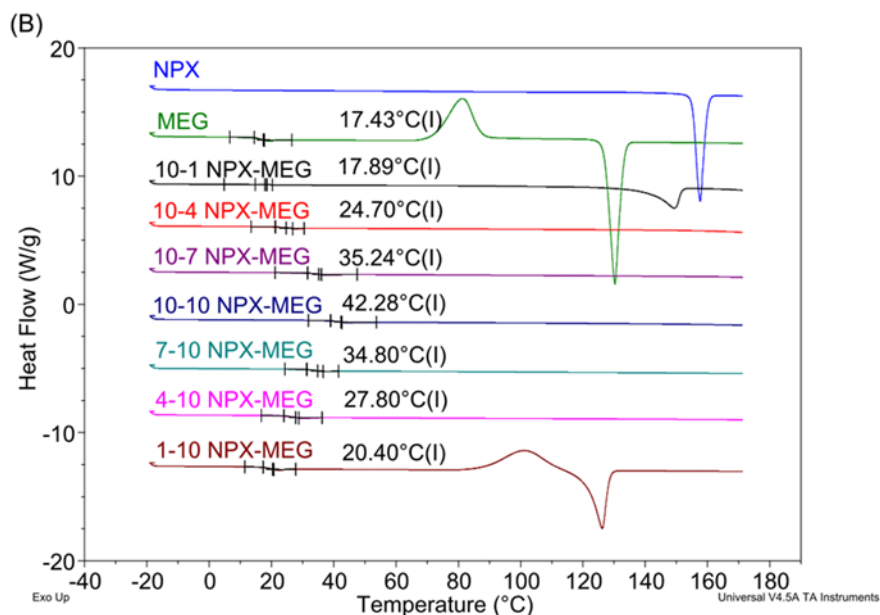
Figure 2.2: DSC thermograms of NPX, MEG and physical mixtures of different molar ratios. (A) The first heating scan; (B) The second heating scan. The numbers in the sample names represent the molar ratio between NPX and MEG. For example, "10–1 NPX–MEG" mixture contains NPX and MEG at 10 to 1 molar ratio.

The most interesting thermogram was observed with NPX and MEG at a 1:1 molar ratio. As shown in Figure 2.2A, it shows an endothermic event at 124 °C, an overlapping endothermic event at 128 °C, an exothermic event at 138 °C, and a sharp endothermic peak at 162 °C. The thermal event at 162 °C is consistent with the melting point of the NPX–MEG salt prepared by solvent method. We hypothesized that these two overlapping thermal events at 128 °C and 138 °C resulted from the reaction between NPX and MEG at the elevated temperature. Figure 2.3 also shows similar thermal behaviors that we observed when polymers including SOLUPLUS, PVPVA64, and PVPK30 were incorporated into the equimolar mixture of NPX and MEG at 10%, w/w.
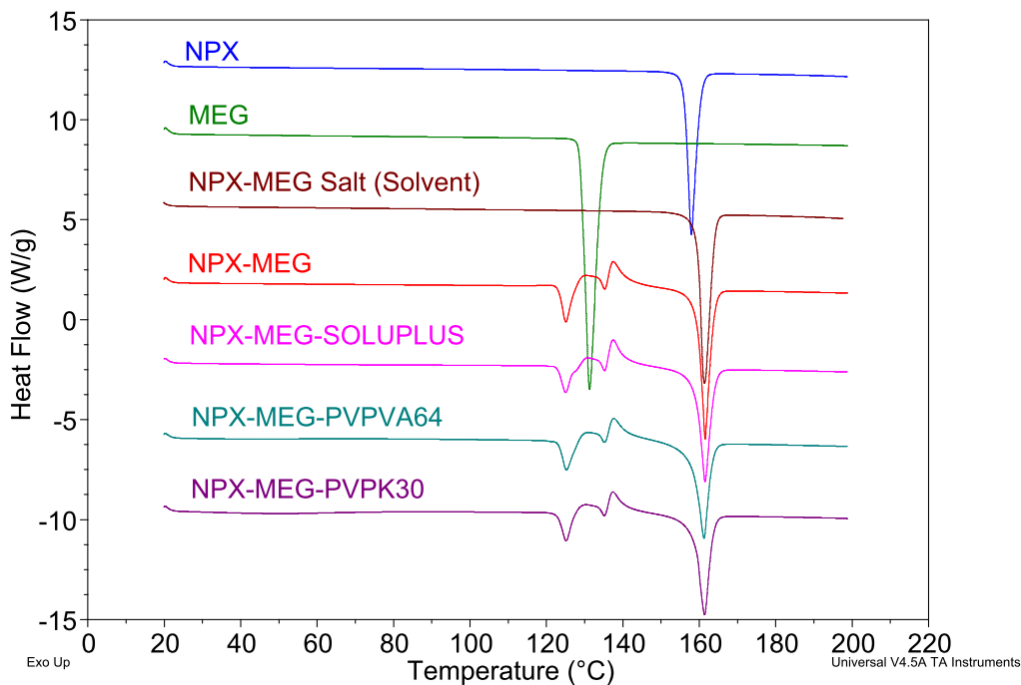
Figure 2.3: DSC thermograms of NPX–MEG physical mixtures with or without the presence of polymers. The molar ratio between NPX and MEG was 1:1 and the percentage of the polymer was 10%, w/w.

The second heating scans of all samples are overlaid in Figure 2.2 B. Pure NPX and MEG showed a very strong recrystallization tendency. NPX melt crystallized during the cooling (data not presented) and melted again at 155 °C in the second heating. We were able to prepare amorphous NPX by quenching NPX melt in liquid nitrogen. T_g of NPX was measured to be 5 °C. MEG remained amorphous during the cooling. In the second heating, the glass transition event was observed at 17 °C. Amorphous MEG recrystallized at 79 °C before melting again at 125 °C. Except for the 10–1 and 1–10 NPX–MEG samples, all samples revealed a single T_g without any additional thermal events in the second heating. We conclude that NPX and MEG each fully dissolved in the other to form a homogenous

86

amorphous dispersion during the first heating. As presented in the later sections, we used PLM and XRPD analysis to confirm the amorphous properties of these samples.

The glass transition temperature (T_g) plays a pivotal role in physical stability, chemical stability, and mechanical properties of amorphous materials. Figure 2.4 presents a comparison between experimental and theoretical T_g as a function of NPX weight percentages. The theoretical T_g was calculated using the Gordon–Taylor equation. This equation was based on the condition that the entropy of mixing in an amorphous mixture is purely combinatorial[37]. Any significant deviation of the experimental T_g from the theoretical T_g indicates strong intermolecular interactions between individual components. In the current study, we observed a large positive deviation of experimental T_g from theoretical T_g, which suggests a strong attractive interaction between NPX and MEG. The largest deviation of 30.96 °C was observed when NPX and MEG were equimolar, which corresponded to 54.12% NPX, w/w. We concluded that the positive deviation in the T_g of amorphous NPX–MEG complexes was due to the strong acid–base interaction between NPX and MEG. Strong interaction between individual components affects not only the miscibility, but also the physical stability of the resulting solid dispersions. This occurs because the stronger the intermolecular interactions are, the higher the T_g and a greater amount of thermal energy is required to attain the molecular mobility necessary to undergo the transition.

This large positive deviation of experimental T_g from theoretical T_g has been reported in a study that investigated various amorphous salt forms of propranolol and nicardipine with different counterions[6]. Similar phenomena have also been reported for polymeric salts and inorganic salts[18, 38]. In addition, the networking of strong ionic interactions and the hydrogen bonding between the multiple components make salts an attractive tool to design supramolecular drug-delivery systems[39, 40].
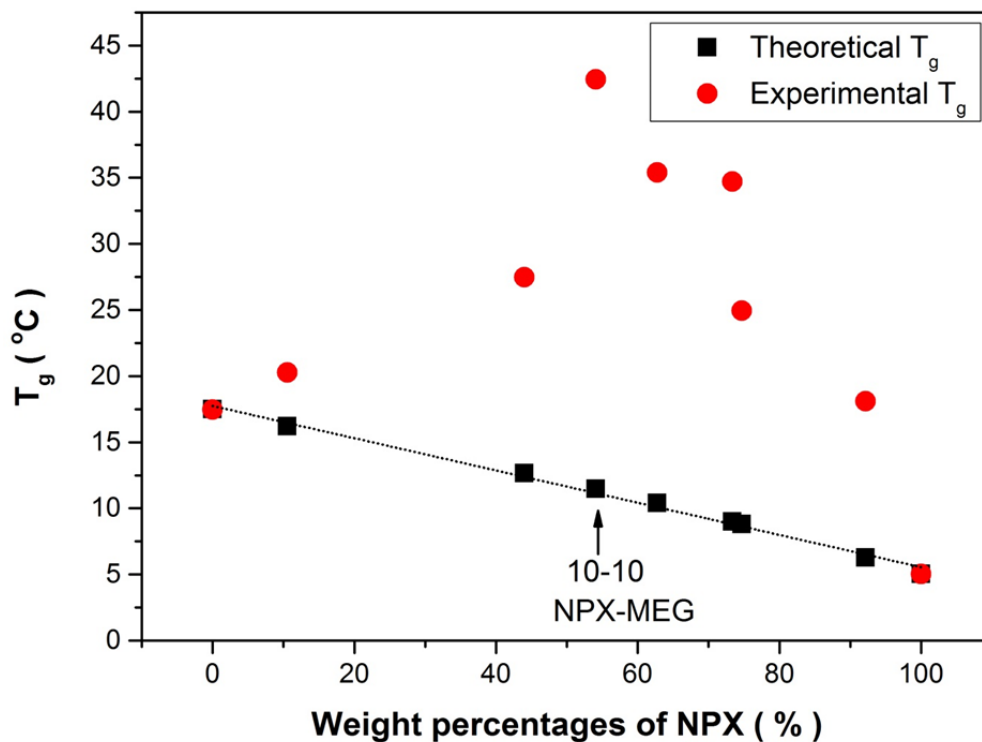
Figure 2.4: Comparison of experimental T_g with theoretical T_g calculated with Gordon-Taylor equation for NPX–MEG complexes containing different percentages of NPX.

2.5.1.2 Characterization of NPX and MEG Interactions at Elevated Temperature Using HSPLM

We applied HSPLM to further understand the thermal events observed in the DSC analysis. Figure 2.5 shows a correlation between the DSC thermogram and the HSPLM photomicrographs observed at the 10 °C/min heating rate for the physical mixture of equimolar NPX and MEG. NPX and MEG were easily distinguishable under a light microscope because NPX crystals are irregularly spherical and MEG crystals are needle shaped. When NPX and MEG were tested individually, no thermal event was observed under HSPLM until the respective melting temperatures (133 °C for MEG and 159 °C for NPX) were reached. For the NPX–MEG physical mixture, MEG began to melt around 125 °C. As NPX crystals gradually dissolved in the molten MEG, a new crystalline phase

began to grow out of the melt. The solubilization of NPX in MEG melt overlapped with the formation of new crystals. The newly formed crystals melted at 165 °C. The melting temperature of this new crystalline material agreed well with that of the NPX–MEG salt prepared with the solvent method. Based on this result, we concluded that the crystalline phase was the crystalline NPX–MEG salt. Similar results were observed in the physical mixture containing 10% (w/w) polymers. These polymers did not interfere with the formation and melting of the NPX–MEG salt. The results of DSC and HSPLM analyses indicate that NPX and MEG reacted with each other and formed an in situ NPX–MEG salt when thermally treated.
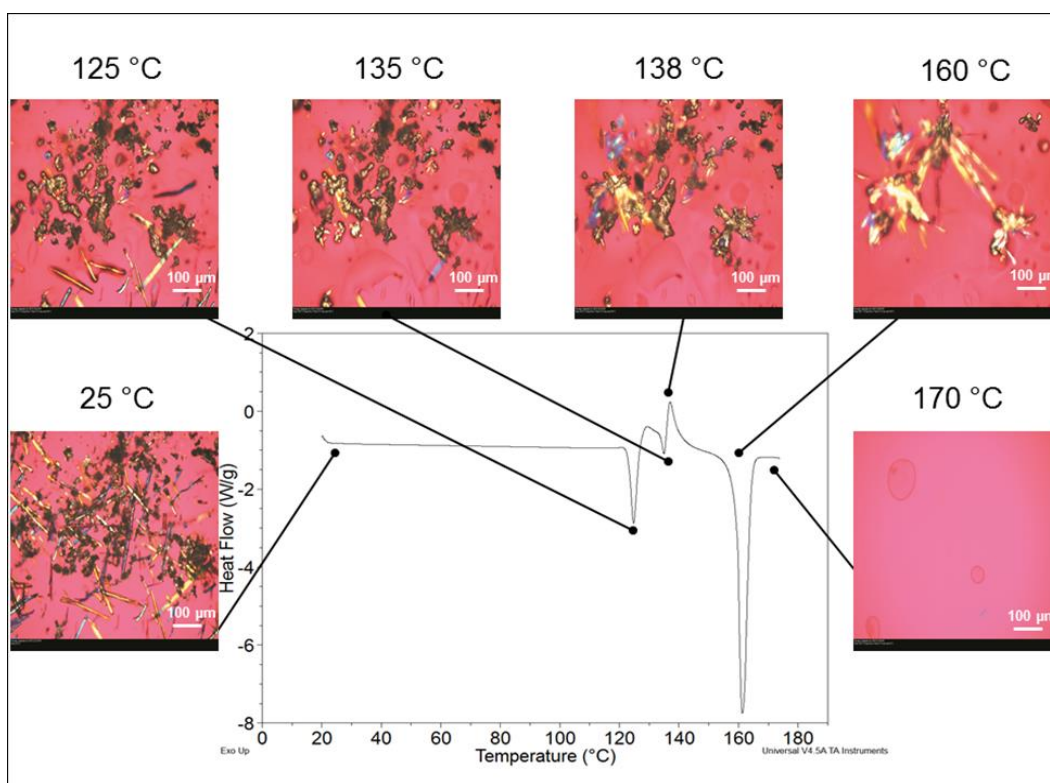
Figure 2.5: DSC thermogram and HSPLM photomicrographic images of an equimolar mixture of MEG and NPX. The heating rate was 10 °C/min. NPX crystals are cubic-like, while MEG crystals are needle-shaped.

89

Crystallization of the molecular complex following the solubilization of one component into the melt of the other component has been reported with other drug delivery systems, including coamorphous materials and cocrystals. Jensen et al.[13] investigated the formation mechanism of coamorphous materials of indomethacin–tryptophan and furosemide–tryptophan during ball milling. It was reported that the formation of the coamorphous material was a continuous solid dissolution process, and the single component that more rapidly amorphized served as a solvent for the other component upon ball milling. The rate of amorphizing was the rate limit step for the formation of the coamorphous material. However, they did not find any intermediate state in the milling process. The reason for this phenomenon was attributed to the rate of amorphizing in ball milling is very slow compared to the melting method. The real-time monitoring of *in situ* formation of intermediates during the mechanochemical milling is challenging[41]. In the current study, the amorphization rate during melting process for the component with the lower melting point was much faster and produced a large amount of "solvent" for the higher melting point component. The higher melting point component first dissolved in the molten component and was then transformed into a more stable crystalline state. Finally, this new crystalline material melted with further increase in temperature. Similar results have been reported in thermally-induced carbamazepine and nicotinamide cocrystal formation[26, 42]. In conclusion, the results from the HSPLM analysis indicate that NPX and MEG formed an NPX–MEG salt *in situ* at elevated temperature.

2.5.1.3 Characterization of NPX–MEG Molecular Interactions Using FTIR and XPS Methods

Acid and base reactions can be categorized as an ionic interaction with proton transfer or a nonionic interaction with varying degrees of proton sharing through H-

bonding[43]. A complete proton transfer between the acidic and the basic components occurs when the ΔpK_a value (pK_a of base $-$ pK_a of acid) is larger than 3.0. The pK_a of NPX and MEG are 4.15 and 8.03, respectively. Therefore, we anticipated the transfer of protons. However, the transfer of protons between the two compounds is also affected by the packing of the molecules and the process conditions[43]. We have utilized spectroscopic tools, including FTIR and XPS, to determine whether the interaction between NPX and MEG was ionic with proton transfer or nonionic with proton sharing.

We applied FTIR to investigate the nature of the intermolecular interaction between NPX and MEG in the complex formed at elevated temperature. The intermolecular ionic and hydrogen bonding in NPX salt, cocrystals, and solid dispersions with PVPK30 have been well explored with FTIR so far[44-46]. Figure 2.6 presents the FTIR spectra of various samples. For NPX–MEG complexes, the most significant spectra change occurred in two regions. The first region is between 3,000 and 3,500 cm^{-1}, a region where the bands for O−H and N−H stretches are positioned. The second region is between 1,500 and 1,800 cm^{-1}, at which the bands for C=O stretch of the carboxylic acid groups are positioned. Within the second region, the symmetric C=O stretch of the unionized carboxylic acid group can be located between 1,700 and 1,725 cm^{-1}, and the antisymmetric C=O stretch of the respective ionized carboxyl group can be located between 1,540 and 1,650 cm^{-1}[47].
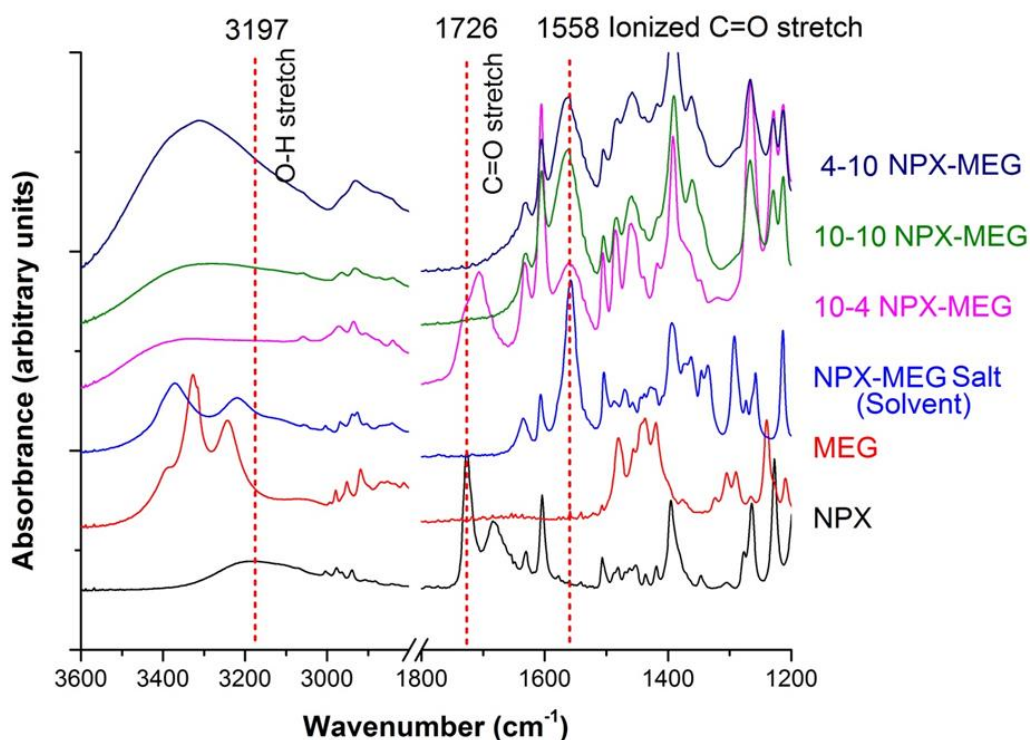
Figure 2.6: FTIR spectra of NPX, MEG, NPX–MEG salt prepared by solvent method, and the selected 10-4 NPX–MEG, 10-10 NPX–MEG and 4-10 NPX–MEG complexes prepared by melting method.

For the NPX drug substance, one broad band at 3,197 cm^{-1} was attributed to hydroxyl group stretching of the carboxyl acid group. Two sharp bands at 1,726 and 1,684 cm^{-1} were assigned to the free carboxylic acid group (monomer) and hydrogen bonded carboxylic acid group (dimer), respectively. Based on the intensity of bands 1,726 and 1,684 cm^{-1}, the majority of the NPX molecules were not engaged in hydrogen bonding. For MEG, two bands at 3,327 and 3,242 cm^{-1} were attributed to the stretch of N−H and O−H groups, respectively. In FTIR spectra of the crystalline NPX–MEG salt prepared by solvent method, a band for the C=O stretch of the ionized carboxyl group was observed at 1,558 cm^{-1}, while the C=O stretch band for the unionized carboxylic acid was absent. Furthermore, the band for N−H stretching shifted from 3,327 cm^{-1} to 3,370 cm^{-1},

92

indicating that the secondary amine group of MEG was involved in the salt formation with NPX.

Compared to the NPX–MEG salt prepared by the solvent method, the 10–10 NPX–MEG sample showed a similar spectrum. The presence of C=O stretching of the ionized carboxyl group at 1,558 cm^{-1} and the absence of C=O stretching of the carboxylic acid group at 1,726 cm^{-1} suggested salt formation between NPX and MEG upon melting. A broader peak at 3,327 cm^{-1} also indicated that the change of the molecular arrangement after amorphization of the salt and the hydroxyl groups of MEG could also be involved in the formation of the stable amorphous system. The similar spectrum was also obtained in the 4–10 NPX–MEG sample, which indicated that most of the NPX complex with MEG forms a salt. For the 10–4 NPX–MEG sample, salt formation also can be inferred from the appearance of the ionized carboxyl group absorption peak at 1,558 cm^{-1}. Due to the excess of NPX, the carboxylic acid peak at 1,726 cm^{-1} still could be observed. This sample showed the presence of both crystalline free acid as well as the ionized form.

XPS generates nitrogen 1s spectra with the binding energy specific to the nitrogen chemical, and the local electronic environment and has recently been shown to be particularly useful at identifying the nature of intermolecular interactions in two-component acid–base systems. This results in a large positive chemical shift due to nitrogen protonation[48, 49]. Figure 2.7 shows the nitrogen 1s peak in the XPS spectra of MEG, the NPX−MEG salt prepared by the solvent method, and the NPX−MEG equimolar complex prepared by the melting method. First, due to the secondary amine group (C−NH−) in the chemical structure of MEG, a single nitrogen 1s photoemission peak around 399.3 eV was observed for pure MEG. For the NPX–MEG salt prepared by solvent method, a new nitrogen 1s photoemission peak was observed at a higher binding energy (401.5 eV) because of the nitrogen protonation of the secondary amine group (C−NH^{2+}−) in MEG.

The binding energy shift as a result of complete protonation is typically in the range of 1.3–2.5 eV for secondary amine group, as reported in the literature[19, 48]. The NPX–MEG complex prepared by the melt method shows the same new nitrogen 1s photoemission peak at 401.5 eV. The nitrogen XPS result reveals that nitrogen atoms of MEG in the NPX–MEG complex ($C-NH^{2+}-$) have acquired a positive charge through proton transfer from the carboxylic acid group of NPX, shifting its photoemission to a higher energy. The XPS result indicates that the interaction in the NPX–MEG complex prepared by the melt method is identical to the ionic bonding in the NPX–MEG salt prepared by solution state.
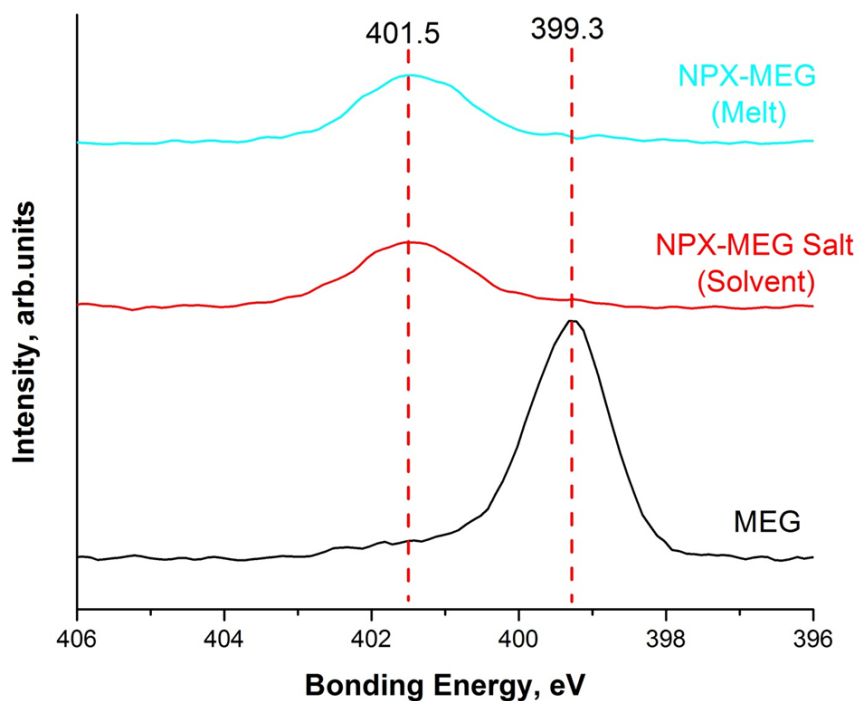
Figure 2.7: N 1s XPS spectra of MEG, NPX–MEG salt prepared by solvent method and NPX–MEG equimolar complex prepared by melting method.

Based on the C=O bond stretch shift in FTIR spectra and based on the binding energy shift in the nitrogen 1s region of the XPS spectra, we conclude that the interaction between NPX and MEG at the elevated temperature was ionic with proton transfer.

94

2.5.1.4 Characterization of the Physical Stability of NPX–MEG Complex Using PLM and XRPD

It was thought that the strength of the ionic interaction will not only affect the T_g but also the physical stability of the amorphous mixtures, which is controlled by thermodynamic and kinetic factors. Both NPX and MEG have a strong crystallization tendency. Pure NPX has a strong recrystallization tendency and amorphous NPX could only be prepared by quenching NPX melt in liquid nitrogen. When exposed to ambient temperature, the resulting amorphous NPX would recrystallize within one minute. The recrystallization tendency of NPX results from the strong stacking tendency of aromatic naphthalene and the hydrogen bonding tendency of carboxylic acid groups[45]. A strong recrystallization tendency is also observed in MEG DSC result, which is a Class II compound according to the classification method proposed by Taylor's group[50].

We used XRPD and PLM to evaluate the physical stability of the NPX–MEG samples prepared by the melting method. We stored samples along with silica gel in glass bottles at 25 °C. As shown in Figure 2.8A, except for the 10–1 and 1–10 NPX–MEG samples, all other samples prepared using the melt method were amorphous at their initial time point. After seven months of storage, all the samples were characterized with XRPD, and the patterns are overlaid in Figure 2.8B. Only the 10–10 and 10–7 NPX–MEG samples remained amorphous. Characteristic peaks (4.358°, 9.177°, 18.161° and 21.881°), which appeared in the 4–10 and 7–10 NPX–MEG samples indicate that both materials recrystallized into a mixture of NPX–MEG salt and MEG crystals. For the 10–1 and 10–4 NPX–MEG samples, the characteristic peaks (6.739°, 12.699°, 18.800° and 22.500°) indicate that crystalline diffraction was primarily attributed to NPX crystals. In conclusion, the component in molar excess was the component that recrystallized during the storage.
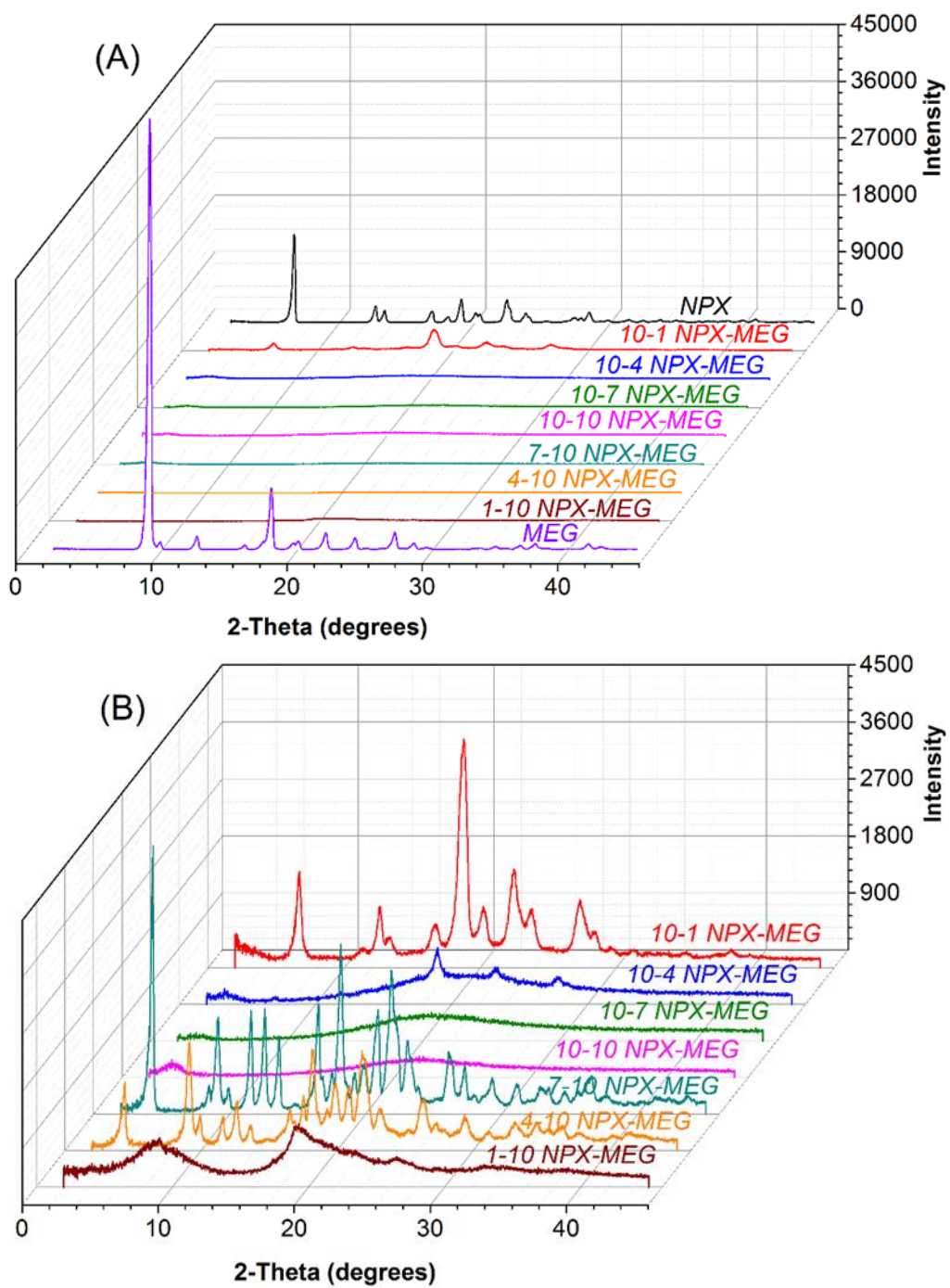
Figure 2.8: XRPD patterns of the NPX–MEG complex at different molar ratios. (A) at initial time point; (B) following 7 months storage at 25 °C/desiccator.

PLM, a more sensitive method than XRPD[12], was also used to further investigate the physical stability of 10–7 and 10–10 NPX–MEG samples, and the results are presented in Figure 2.9. At the initial time point, birefringence was not observed, and both samples were amorphous. The presence of a low level of crystalline material was observed with both samples, and the amount of the crystal clusters for the 10–7 NPX–MEG sample was significantly more than that of the 10–10 NPX–MEG sample following seven months of storage. We conclude that NPX–MEG was the most stable amorphous salt at an equimolar ratio.
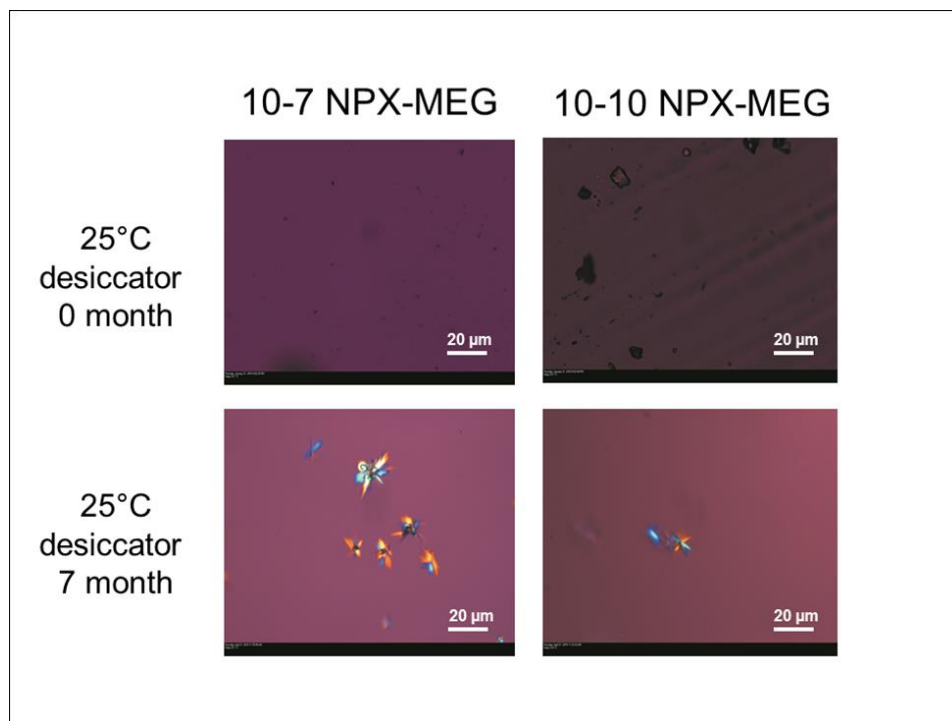
Figure 2.9: PLM images of 10-7 NPX–MEG and 10-10 NPX–MEG samples at t=0 month (Top); and following 7 months storage, at 25 °C sealed in glass bottles with desiccator (Bottom).

The physical stability of amorphous NPX–MEG at an equimolar ratio could be attributed to the highest T_g and the strong ionic interaction between NPX and MEG, as discussed in the thermal analysis section. However, there is no clear correlation between

the T_g values and physical stabilities of 10–7 and 7–10 NPX-MEG samples. Even though both samples have a similar T_g, the 10–7 NPX–MEG sample was more physically stable than the 7–10 NPX–MEG sample. This observation suggests that T_g may not be the only factor in defining the physical stability of NPX–MEG dispersions. Other factors also play a crucial role in governing the physical stability of solid dispersions, such as glass-forming ability, recrystallization tendency of the compounds, and the combining effects of thermodynamic and kinetic factors that govern the formation of nuclei and crystalline growth[51].

A similar phenomenon has been observed for indomethacin–meglumine amorphous salts prepared by the solvent method[12]. In that study, a 1:1 indomethacin–meglumine formulation was more physically stable than a 3:1 indomethacin–meglumine formulation. For a 3:1 indomethacin–meglumine formulation, excess indomethacin crystalized during heating. With the development of co-amorphous drug delivery systems, several reports also focused on the influence of small molecules on the physical stability of the NPX amorphous state[30, 52-54]. The results demonstrated that hydrogen bonding between the carboxylic acid group of NPX and small molecules was the primary reason for the improved physical stability during the storage and for the supersaturation during dissolution testing. The optimal molar ratio between NPX and the small molecules was reported to be 1:1. NPX crystal lattice is based on the π–π interaction between NPX naphthalene rings and the hydrogen bonding between carboxylic groups[45]. Perlovich et al. studied the contribution of different energetic terms of the structural fragments of NPX molecule on stabilizing NPX crystal lattice[55]. It was reported that the most significant impact (43.2%) was attributed to the π–π interaction between NPX naphthalene rings. The crystal structure of MEG is mainly stabilized by the intermolecular hydrogen bonding between the nitrogen atom and one of the hydroxyl groups of an adjacent molecule[35]. In

this study, FT-IR and XPS data indicated the carboxylic acid group of NPX complexed with secondary amine group of MEG by ionic interaction and formed a heterodimer. Based on the energy barrier for the crystallization of NPX, we infer the MEG cations are position between the NPX naphthalene rings. This spacial arrangement attributes to the physical stability of amorphous NPX–MEG complex at equimolar ratio. Similar microstructure has been reported in the flunixin-MEG complex[56]. In its crystal structure, flunixin molecules are inserted between the MEG layers and are linked by hydrogen bonding.

In summary, our data indicate that the ionic interaction between NPX and MEG and the unique microstructure of the NPX–MEG complex improved the physical stability of amorphous NPX by inhibiting the π–π interaction of NPX naphthalene rings and NPX dimer formation induced by the hydrogen bonding between the carboxylic groups of NPX.

2.5.2 Properties of Amorphous NPX Solid Dispersions Prepared by Reactive Melt Extrusion

2.5.2.1 Investigations of NPX and MEG Interaction in ASDs Using FTIR and XPS Methods

The All the samples have been characterized with FTIR after the reactive melt extrusion, and the results are shown in Figure 2.10. The data indicate that the presence of polymers did not impact the NPX–MEG amorphous salt formation during reactive melt extrusion. In Figure 2.10A, for NPX ASDs with MEG prepared by reactive melt extrusion, the significant decreasing peak intensity of the carboxylic acid group at 1,726 and 1,684 cm^{-1} and the appearance of the ionized carboxyl group absorption peak at 1,558 cm^{-1} indicate an acid–base interaction between NPX and MEG during the extrusion process. A broader peak that appeared at 3,327 cm^{-1} also suggests the amorphization of NPX-MEG salt. Although we could still observe small absorption bands at 1,776 cm^{-1} in the NPX–

99

MEG–SOLUPLUS, NPX–MEG–PVPVA64, and NPX–MEG–PVPK30 ASDs, this may be attributed to carbonyl groups from the polymers.
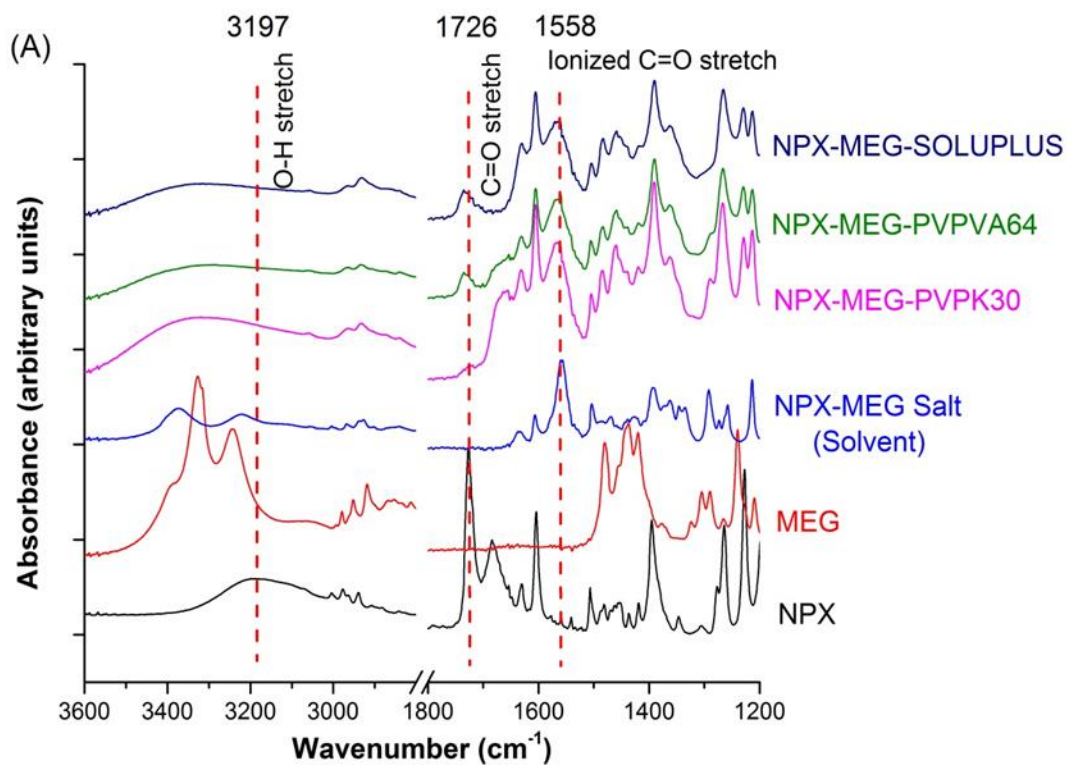
Figure 2.10: continued next page.
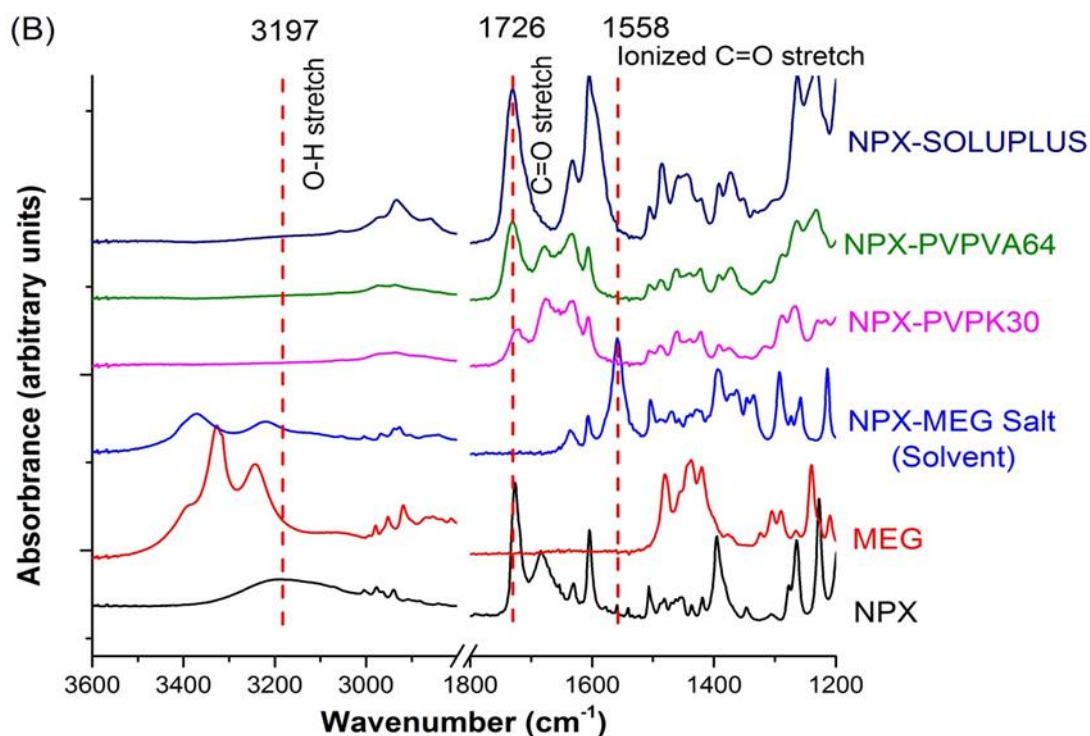
Figure 2.10: FTIR spectra of NPX ASDs with MEG (A) and without MEG (B).

In summary, the FTIR results of the NPX–MEG–SOLUPLUS, NPX–MEG–PVPVA64 and NPX–MEG–PVPK30 ASDs were similar to the samples prepared by the melting method, and the addition of polymers did not influence salt formation. Figure 2.10 B shows the FTIR spectrum of the conventional NPX ASDs without MEG. The ionized carboxyl group absorption peak was not observed with the NPX–SOLUPLUS, NPX–PVPVA64, and NPX–PVPK30 ASDs since the acid–base interactions could not take place between NPX and the polymers. The absorption peak of the free carbonyl group at 1,726 cm^{-1} for NPX still could be observed in the all three ASDs, and the relative peak intensity decreased in the following order: SOLUPLUS > PVPVA64 > PVPK30. The reason for this result could be attributed to the different hydrogen bonding abilities of polymers with NPX. Several reports have shown that the amide group of PVPK30 has a strong hydrogen bonding ability with the NPX carboxylic acid group, leading to the reduction in the peak

101

intensity of the NPX free carbonyl group at 1,726 cm^{-1}[45, 57, 58]. Since PVPVA64 has fewer amide groups than PVPK30, we can infer that the hydrogen bonding ability of PVPVA64 is less than that of PVPK30. The order of reduction in peak intensity at 1,726 cm^{-1} indicates that PVPK30 has the strongest hydrogen bonding interaction with NPX, while SOLUPLUS has the weakest hydrogen bonding interaction with NPX. The interaction between NPX and polymers also affects the physical stability of the solid dispersion as discussed in the following section.

XPS data further confirmed the FTIR results, as shown in Figure 2.11. There are two nitrogen environments in NPX–MEG ASDs. One is the amide group of the polymers (i.e., SOLUPLUS, PVPVA64, and PVPK30 have amide groups in their chemical structures) and the other is the amine group of MEG. The two nitrogen environments result in two X-ray photoemission peaks at 401.5 and 399.7 eV, respectively. The nitrogen 1s photoemission peak that appeared at 399.7 eV is attributed to the amide group of the polymers. Due to the electron-withdrawing nature of the carbonyl group, where the electrons of the nitrogen atom are delocalized by resonance, the amide group of the polymer shows 0.4 eV higher bonding energy than the amine group of the MEG. The nitrogen 1s photoemission peak that appeared at 401.5 eV matched well with the nitrogen 1s photoemission peak of the NPX–MEG salt, which suggests that NPX and MEG formed a salt during reactive melt extrusion.

102
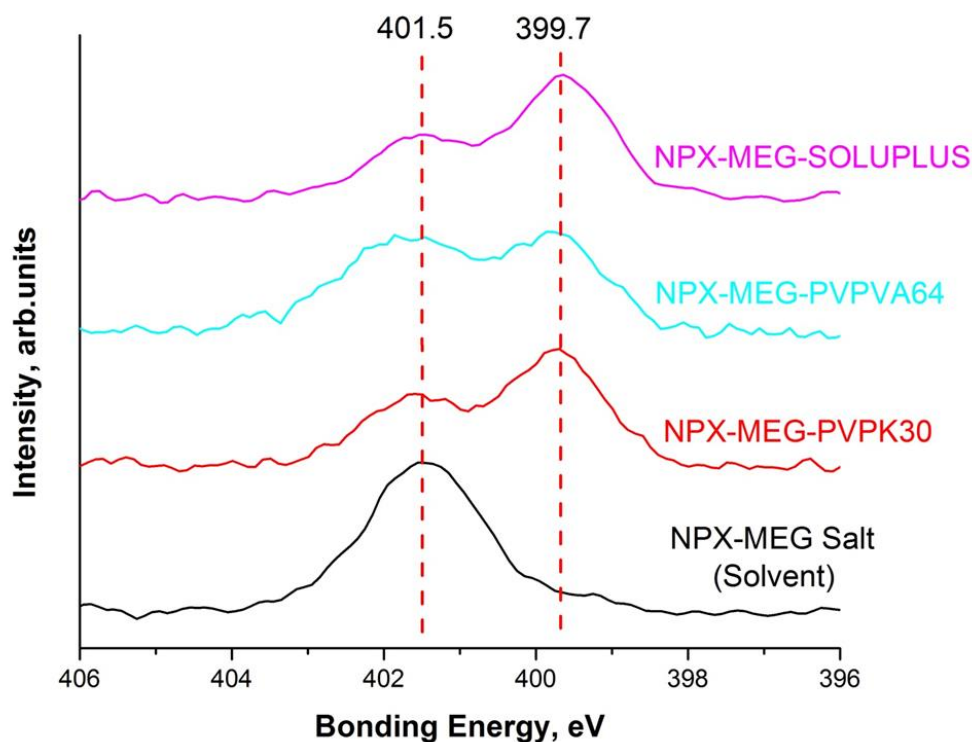
Figure 2.11: N 1s XPS spectra of NPX–MEG salt prepared by solvent method and NPX–MEG ASDs prepared by reactive melt extrusion with different polymers.

2.5.2.2 *Evaluation of Dissolution Performance Using Non-Sink Dissolution Testing*

The solubility enhancement achievable with melt-extruded NPX ASDs was evaluated using a non-sink dissolution testing. The results are presented in Figure 2.12. We used 0.1 N HCl as the dissolution medium to simulate the gastric environment. The equilibrium solubility of NPX in 0.1 N HCl at 37 °C was measured to be 29.21 µg/mL. We used sufficient amounts of ASD samples for the dissolution testing so that the nominal concentration of NPX was 166.7 µg/mL.

When the dissolution profiles (solid circle, Figure 2.12A, C, and E) of the physical mixtures without MEG were compared to the corresponding profiles (open circle, Figure 2.12B, D and F) NPX-polymer ASDs, we found no significant differences. For the physical mixtures, the concentration (ranging between 25 and 29 µg/mL) of NPX at 60 min was

close to its equilibrium solubility in 0.1 N HCl solution. The absence of dissolution improvement in the physical mixtures containing MEG was due to the inability of MEG to elevate both the microenvironment and macroenvironment pH of the dissolution medium. MEG dissolved quickly in 0.1 N HCl solution to impact microenvironment pH. As far as the macroenvironment pH is concerned, dissolved MEG had little impact on the pH of the dissolution media, and it remained the same following the dissolution testing.
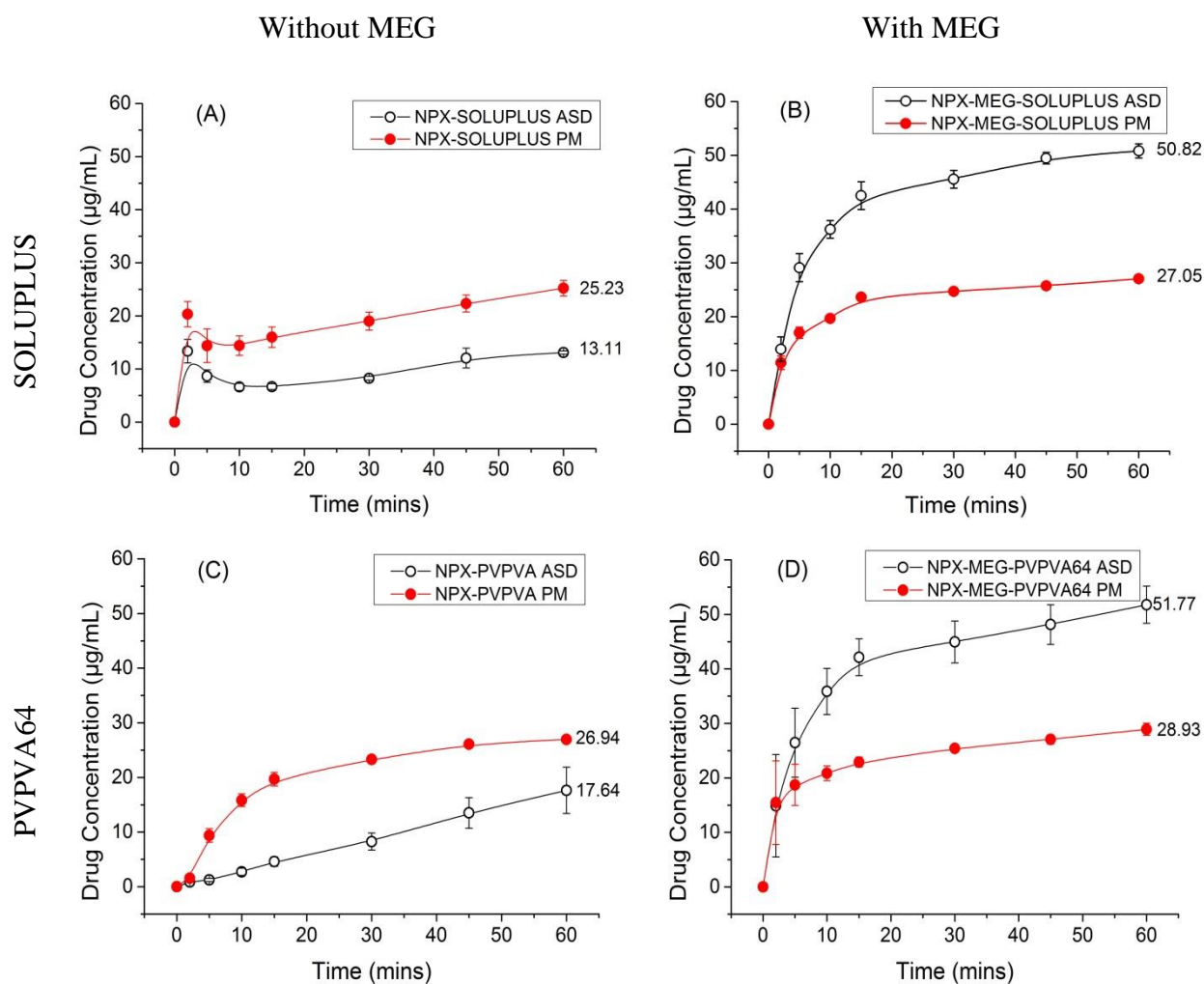
Figure 2.12: continued next page.
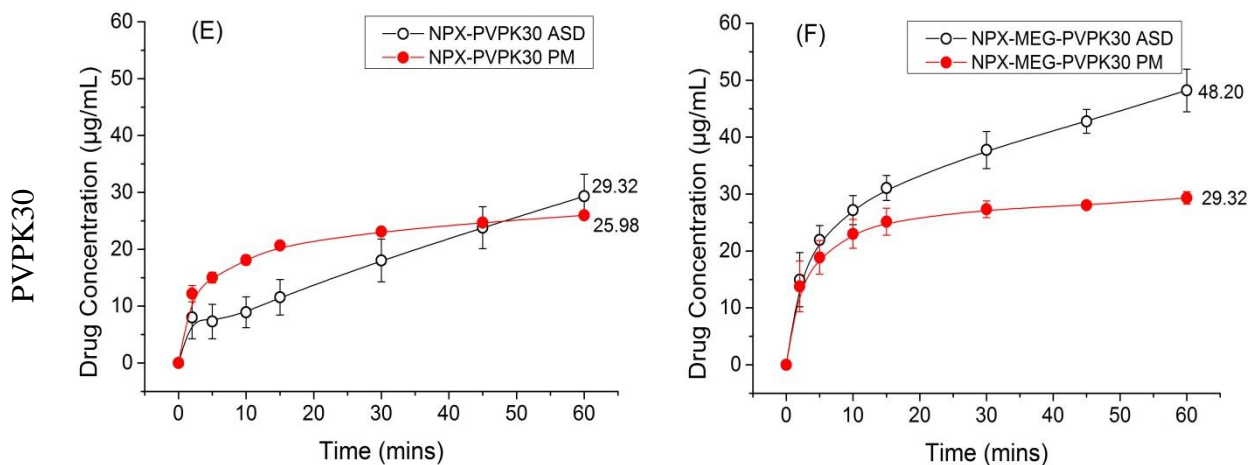
Figure 2.12: Dissolution profiles of NPX melt–extruded ASDs with or without MEG, and their matching physical mixtures in 900 mL 0.1 N HCl solution using USP apparatus II at 50 rpm (n=3).

Surprisingly, the dissolution rate of NPX–polymer ASDs was slower than the corresponding physical mixtures, and supersaturation was not achieved. A comparison of the dissolution profiles of NPX–polymer ASDs and their corresponding physical mixtures are presented in Figure 2.12A (SOLUPLUS), Figure 2.12C (PVPVA64), and Figure 2.12E (PVPK30). The improvement in the dissolution performance of these ASDs was anticipated, since NPX was dispersed at the molecular level and was present at a higher energy stage in these samples. Based on the visual observation, the poor disintegration of these melt-extruded granules and their fast crystallization contributed to the poor dissolution performance of these ASDs. NPX ASD granules aggregated to form large chunks as soon as they were introduced into the dissolution medium. We used the PLM technique to study the behavior of NPX–polymer ASDs in contact with the dissolution medium, and the results are presented in Figure 2.12. When NPX–PVPK30 ASDs came into contact with 0.1 N HCl solution, disintegration of the granules did not occur. Instead, NPX immediately crystallized on the surface of the ASD particles, and we observed rapid growth of the crystals. After 5 min, the surface of the ASDs was fully covered with NPX

105

crystals. The presence of hydrophobic NPX crystals on the surface of the granules could also explain the aggregation of ASD granules in the dissolution medium.

When MEG was present in ASDs, the dissolution rate of NPX ASDs was significantly improved and supersaturation was achieved across all three formulations. A comparison of the dissolution properties of the NPX ASDs containing MEG, and their matching physical mixtures, is presented in Figure 2.12B (SOLUPLUS), Figure 2.12D (PVPVA64), and Figure 2.12F (PVPK30). At 60 min, the concentration of NPX was 174%, 177%, and 165% of equilibrium solubility for NPX–MEG–SOLUPLUS, NPX–MEG–PVPVA64, and MEG–NPX–PVPK30 ASDs, respectively.

We attribute the improved dissolution performance to three factors: (1) MEG and NPX reacted and formed a salt in situ during the melt extrusion; therefore, the microenvironment pH was elevated by MEG to enhance the solubility of NPX. (2) The equilibrium solubility of NPX and the NPX–MEG salt in 0.1 N HCl solution was determined to be 29.21 and 44.87 µg/mL, respectively. (3) The MEG-NPX salt improved the disintegration of the melt-extruded granules and changed the recrystallization behavior of NPX in the dissolution medium.

We also used PLM to examine the behavior of the NPX–MEG–polymer ASDs in contact with 0.1 N HCl solution, and the results are presented in Figure 2.13. As discussed earlier, the granules did not disintegrate, when NPX–PVPK30 ASDs came into contact with the 0.1 N HCl solution. In contrast, NPX–MEG–PVPK30 ASDs granules disintegrated as soon as they came into contact with the 0.1 N HCl solution. After 5 minutes, NPX recrystallization was also observed. However, the NPX crystals were much smaller than the crystals observed with the NPX–PVPK30 ASDs. The same dissolution behaviors were observed in SOLUPLUS and PVPVA64 polymer carrier ASDs as well.
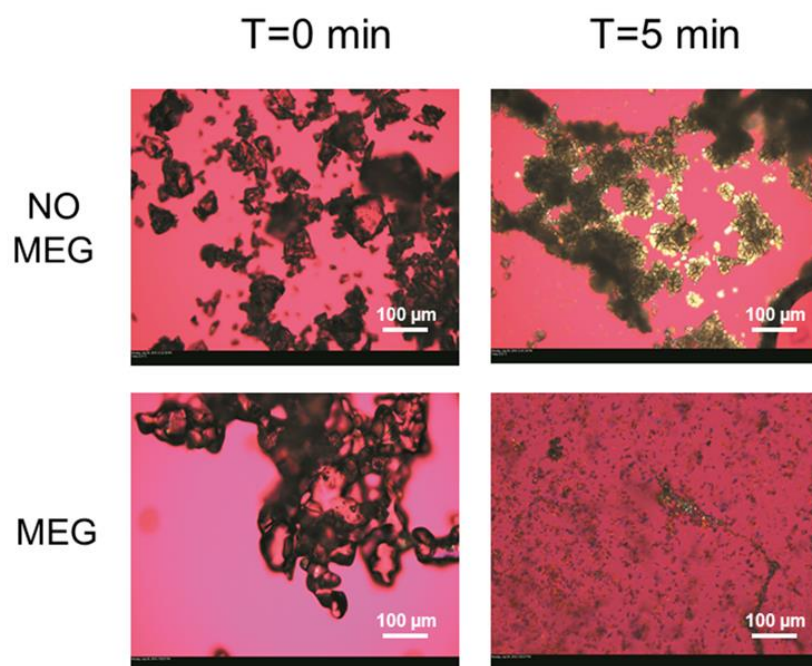
Figure 2.13: PLM images of NPX–MEG ASD and NPX–MEG–PVPK30 ASD in contact with 0.1 N hydrochloric acid solution (X100 magnification).

The incorporation of pH-modifiers in ASDs has been reported to be an effective technology for enhancing the dissolution performance and bioavailability of poorly water-soluble compounds[59, 60]. This enhancement has been attributed to the modulation of microenvironment pH and the maintenance of the structural amorphousness of a drug via the intermolecular hydrogen-bonding between the drug and the polymer carrier. However, in those studies, the investigation of interaction between drugs and pH-modifiers in their solid and aqueous states was not conducted. Our study demonstrates that salt formation between an acidic drug and an alkaline excipient during melt extrusion can substantially change the dissolution property of a drug. Similar observations also have been reported in the freeze drying and spray drying process[61, 62]. Finally, it also has been reported that MEG can form molecular complexes with drugs in solution to achieve the solubilization effect, due to the ionic interaction between drugs and MEG[39, 63]. Our preliminary data

indicate that NPX and MEG have the potential to from a molecular complex in dissolution media. The complexation between NPX and MEG in aqueous media requires further investigation.

2.5.2.3 *Evaluation of Physical Stabilities of NPX ASDs*

We employed PLM and XRPD to determine the physical state of ASDs prepared by reactive melt extrusion and stored along with a desiccant in induction-sealed HDPE bottles stored at 40 °C and 75% RH for four months. Figure 2.14 and Figure 2.15 show the results of PLM and XRPD, respectively. These results indicate that NPX–MEG ASDs were physically more stable than the conventional NPX ASDs without MEG. NPX–MEG–PVPVA64 and NPX–MEG–PVPK30 ASDs remained amorphous following four months of storage under the accelerated storage conditions, and low level of crystallization was observed with NPX–MEG–SOLUPLUS sample. In contrast, the conventional NPX ASDs without MEG showed a different extent of recrystallization. As shown in Figure 2.14A and Figure 2.14A, the PLM and XRPD data indicate that the initial physical state of all samples was amorphous, since no crystal cluster was detected on PLM observation, and the halo patterns were also shown on the XRPD profiles. However, under accelerated storage conditions, the samples presented different physical stabilities. PLM images of samples following 4 months storage are presented in Figure 2.14B. For conventional NPX ASDs without MEG, the type of polymer used has a great influence on physical stability. NPX–SOLUPLUS ASD showed the poorest physical stability. After one week of accelerated stability study, many small crystal clusters were detected by PLM in the NPX–SOLUPLUS ASD (Figure 2.16). As time passed, the small crystal clusters grew quickly and formed long columnar crystals both inside and outside the NPX–SOLUPLUS ASD sample particles after one month of accelerated stability study (Figure 2.16). The characteristic

peak positions shown on the XRPD profile in Figure 2.15B suggests that the recrystallization derives from NPX crystals.

We observed a similar phenomenon in the NPX–PVPVA64 ASD sample after three weeks of accelerated stability study. The XRPD profile suggests that the recrystallization was due to NPX crystals. The major difference is that the crystal morphology changed from acicular crystals to plate-shaped crystals. This can be attributed to the ability of the polymers to hydrogen bond to the surface of the NPX recrystallization particle, leading to a change in NPX crystallization tendency and morphology [64]. Interestingly, no recrystallization was observed in the NPX–PVPK30 ASD sample during the accelerated stability study, which was confirmed by PLM and XRPD.

Similar observations were also found by Paudel and Van den Mooter in their investigation of the miscibility and physical stability of NPX–PVPK25 ASD prepared by the melting method[65]. They found that NPX had a strong hydrogen bonding interaction with the amide group of PVPK25. The solubility of crystalline NPX in PVPK25 was as high as 70% (w/w). The different physical stability of the NPX ASDs with different polymers can be attributed to the anti-plasticizing effect (T_g) and the hydrogen bonding interaction ability of the polymers. Since the T_g of polymers decreased in the following order: PVPK30 ($T_g = 149$ °C) > PVPVA64 ($T_g = 101$ °C) > SOLUPLUS ($T_g = 70$ °C); the T_g of NPX ASDs with different polymers also follow the same order: NPX-PVPK30 ($T_g = 49$ °C) > PVPVA64 ($T_g = 43$ °C) > SOLUPLUS ($T_g = 32$ °C). Furthermore, as discussed in the FTIR characterization section, compared to PVPVA64 and SOLUPLUS, PVPK30 has the strongest hydrogen bonding interaction with NPX. Both of these factors give rise to the excellent physical stability of the NPX–PVPK30 ASD.

Compared to the conventional NPX ASDs without MEG, except for the small amount of recrystallization we observed in NPX–MEG–SOLUPLUS, the NPX–MEG

ASDs were physically more stable and remained amorphous following four months of storage under accelerated storage conditions. As shown in Figure 2.14B, NPX–MEG–SOLUPLUS showed plate-shaped crystals that formed inside the sample particles. The characteristic peak positions shown on the corresponding XRPD profile in Figure 2.15B suggests that this recrystallization results from NPX–MEG salt crystals. In addition, the amount of the recrystallization in NPX–MEG–SOLUPLUS was much less than NPX–SOLUPLUS ASD sample. No recrystallizations were detected by PLM or XRPD during the accelerated stability study in both NPX–MEG–PVPVA64 and NPX–MEG–PVPK30. The results suggest that the addition of MEG in the reactive melt extrusion formulation significantly enhances the physical stability of NPX ASDs.
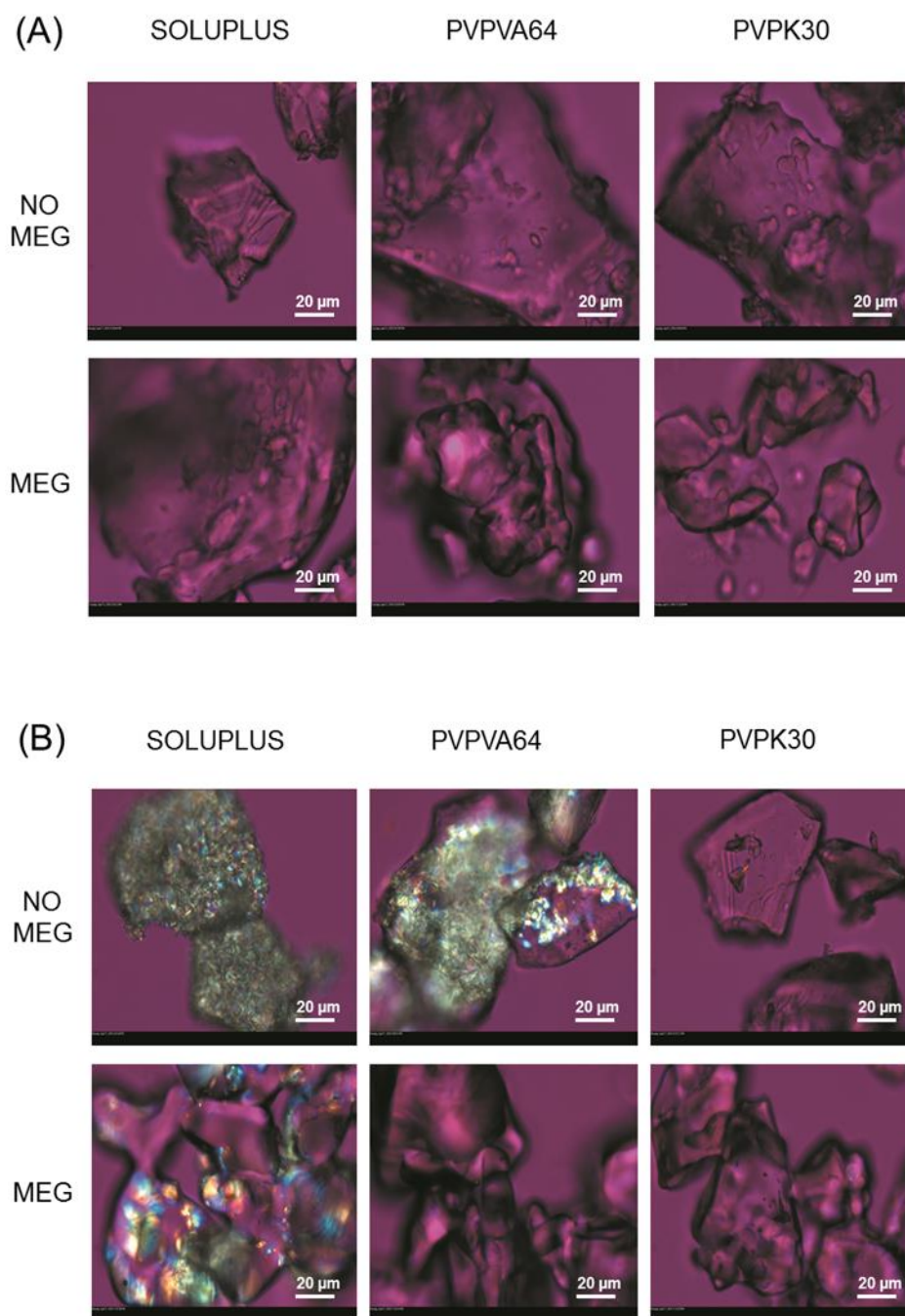
Figure 2.14: PLM images of NPX ASDs prepared by reactive melt extrusion (A) Initial;
(B) Following 4 months storages at 40 °C/desiccator.
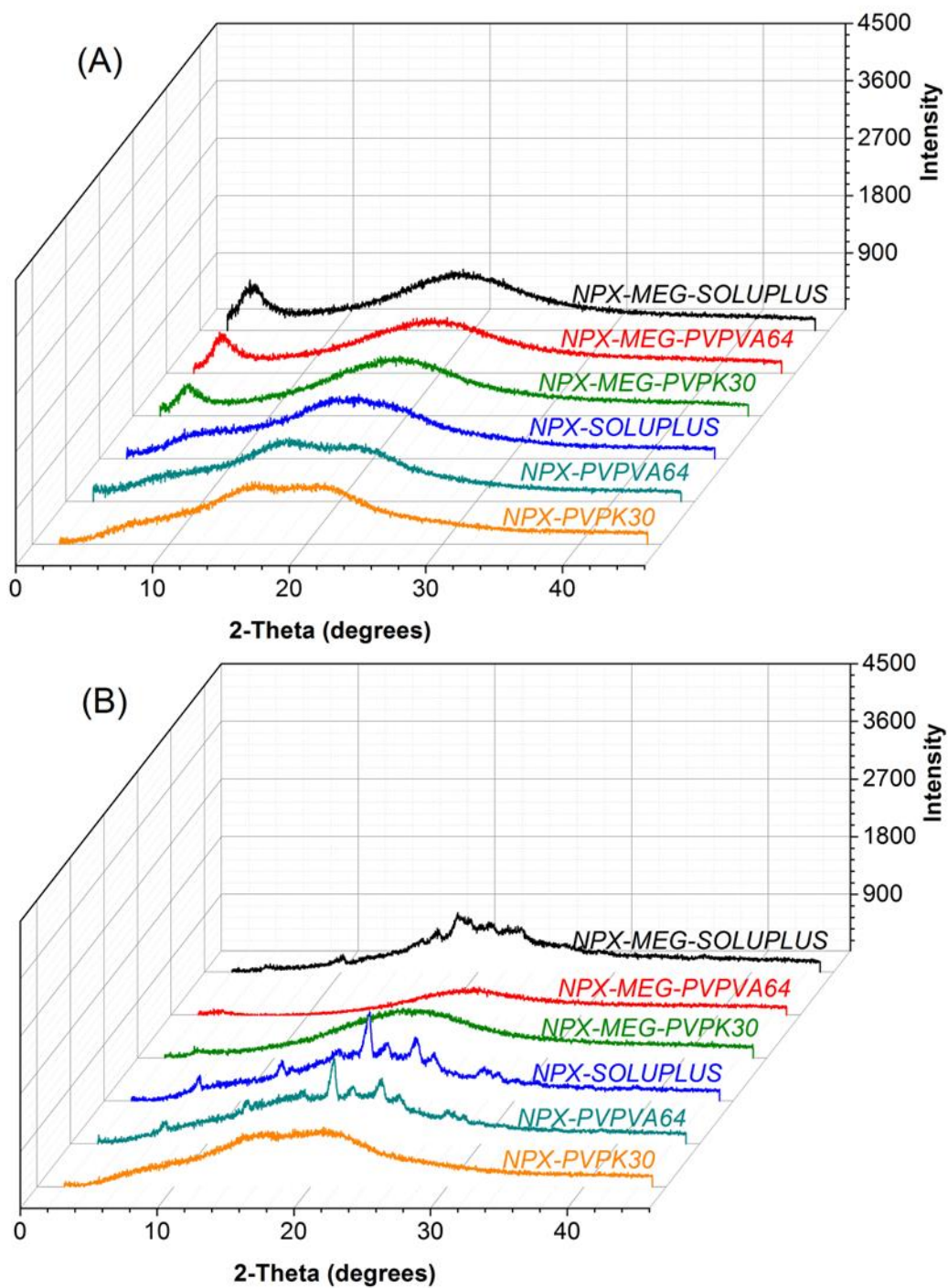
Figure 2.15: XRPD patterns of NPX ASDs prepared by reactive melt extrusion (A) Initial; (B) Following 4 months storages at 40 °C/desiccator.
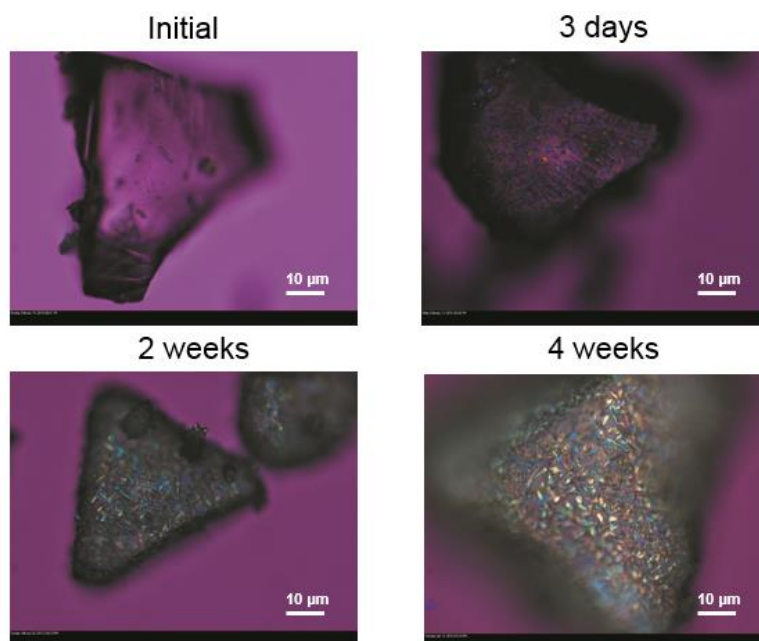
Figure 2.16: PLM images of NPX–SOLUPLUS ASD physical stability at different time points.

2.6 SUMMARY

Our study demonstrated the *in-situ* salt formation between NPX and MEG during the reactive melt extrusion process. We directly observed this reaction using DSC and HSPLM techniques. A large positive deviation from the theoretical values of the experimental T_g of the NPX–MEG complex prepared using the melt method with various molar ratios suggests that a strong ionic interaction occurs between NPX and MEG. The transfer of protons from NPX to MEG during the complex formation was further confirmed by FTIR and XPS analyses. The physically most stable complex was formed when NPX and MEG were present at a 1:1 molar ratio. The presence of a polymer did not interfere with the reaction. We successfully prepared NPX–MEG ASDs with SOLUPLUS, PVPVA64, and PVPK30 by reactive melt extrusion. Non-sink dissolution testing and accelerated stability study indicated that in situ salt formation was an effective approach to improve the dissolution properties and the physical stability of NPX ASDs. The ionic

113

interaction between NPX and MEG contributed to the improved physical stability of NPX ASDs during accelerated stability testing, and it enhanced drug dissolution in aqueous media.

2.7   REFERENCE

1.   Rumondor, A. C. F.; Dhareshwar, S. S.; Kesisoglou, F.   Amorphous solid dispersions or prodrugs: complementary strategies to increase drug absorption. *J. Pharm. Sci.* **2016,** *105*(9), 2498-2508.

2.   Williams III, R. O.; Watts, A. B.; Miller, D. A., Eds. *Formulating poorly water soluble drugs*. Springer: New York, **2012**.

3.   Jain, S.; Patel, N.; Lin, S.   Solubility and dissolution enhancement strategies: current understanding and recent trends. *Drug Dev. Ind. Pharm.* **2015,** *41*(6), 875-887.

4.   Serajuddin, A. T. M. Salt formation to improve drug solubility. *Adv. Drug Delivery Rev.* **2007,** *59*(7), 603-616.

5.   Kumar, L.; Baheti, A.; Bansal, A. K.   Effect of a counterion on the glass transition temperature (T_g) during lyophilization of ganciclovir salt forms. *Mol. Pharmaceutics* **2010,** *8*(1), 309-314.

6.   Towler, C. S.; Li, T.; Wikström, H.; Remick, D. M.; Sanchez-Felix, M. V.; Taylor, L. S.   An investigation into the influence of counterion on the properties of some amorphous organic salts. *Mol. Pharmaceutics* **2008,** *5*(6), 946-955.

7.   Stephenson, G. A.; Aburub, A.; Woods, T. A. Physical stability of salts of weak bases in the solid-state. *J. Pharm. Sci.* **2011,** *100*(5), 1607-1617.

8.   Shah, N.; Sandhu, H.; Choi, D. S.; Chokshi, H.; Malick, A. W., Eds. *Amorphous solid dispersions-theory and practice*, Springer: New York, 2014.

9.   Chiou, W. L.; Riegelman, S. Pharmaceutical applications of solid dispersion systems. *J. Pharm. Sci.* **1971,** *60*(9), 1281-1302.

10.   Lee, T. W.; Boersen, N. A.; Hui, H. W.; Chow, S. F.; Wan, K. Y.; Chow, A. H. Delivery of poorly soluble compounds by amorphous solid dispersions. *Curr. Pharm. Des.* **2014,** *20*(3), 303-324.

11.   Krupa, A.; Majda, D.; Jachowicz, R.; Mozgawa, W. Solid-state interaction of ibuprofen and Neusilin US2. *Thermochim. Acta* **2010,** *509*(1–2), 12-17.

12.   Telang, C.; Mujumdar, S.; Mathew, M. Improved physical stability of amorphous state through acid base interactions. *J. Pharm. Sci.* **2009**, *98*(6), 2149-2159.

13.   Jensen, K. T.; Larsen, F. H.; Cornett, C.; Löbmann, K.; Grohganz, H.; Rades, T. Formation mechanism of coamorphous drug–amino acid mixtures. *Mol. Pharmaceutics* **2015,** *12*(7), 2484-2492.

14.   Weuts, I.; Kempen, D.; Verreck, G.; Peeters, J.; Brewster, M.; Blaton, N.; Van den Mooter, G. Salt formation in solid dispersions consisting of polyacrylic acid as a carrier and three basic model compounds resulting in very high glass transition temperatures and constant dissolution properties upon storage. *Eur. J. Pharm. Sci.* **2005,** *25*(4–5), 387-393.

15.   Laitinen, R.; Löbmann, K.; Strachan, C. J.; Grohganz, H.; Rades, T. Emerging trends in the stabilization of amorphous drugs. *Int. J. Pharm.* **2013,** *453*(1), 65-79.

16.   Mallick, S.; Pattnaik, S.; Swain, K.; De, P. K.; Saha, A.; Ghoshal, G.; Mondal, A. Formation of physically stable amorphous phase of ibuprofen by solid state milling with kaolin. *Eur. J. Pharm. Biopharm.* **2008,** *68*(2), 346-351.

17.   Dengale, S. J.; Grohganz, H.; Rades, T.; Löbmann, K. Recent advances in co-amorphous drug formulations. *Adv. Drug Delivery Rev.* **2016,** *100*, 116-125.

18.   Song, Y.; Yang, X.; Chen, X.; Nie, H.; Byrn, S.; Lubach, J. W. Investigation of drug–excipient interactions in lapatinib amorphous solid dispersions using solid-state NMR spectroscopy. *Mol. Pharmaceutics* **2015,** *12*(3), 857-866.

19.   Song, Y.; Zemlyanov, D.; Chen, X.; Nie, H.; Su, Z.; Fang, K.; Yang, X.; Smith, D.; Byrn, S.; Lubach, J. W. Acid-base interactions of polystyrene sulfonic acid in amorphous solid dispersions using a combined UV/FTIR/XPS/ssNMR study. *Mol. Pharmaceutics* **2016,** *13*(2), 483-492.

20.   Hasa, D.; Perissutti, B.; Cepek, C.; Bhardwaj, S.; Carlino, E.; Grassi, M.; Invernizzi, S.; Voinovich, D. Drug salt formation via mechanochemistry: the case study of vincamine. *Mol. Pharmaceutics* **2013,** *10*(1), 211-224.

21.   Tiwari, R. V.; Patil, H.; Repka, M. A. Contribution of hot-melt extrusion technology to advance drug delivery in the 21st century. *Expert Opin. Drug Delivery* **2016,** *13*(3), 451-464.

22.   Bouvier, J.M.; Campanella, O. H., *Extrusion Processing Technology: Food and Non-Food Biomaterials*. John Wiley & Sons: Hoboken,NJ, **2014**.

23.   Moad, G. Chemical modification of starch by reactive extrusion. *Prog. Polym. Sci.* **2011,** *36*(2), 218-237.

24.   Raquez, J.-M.; Narayan, R.; Dubois, P. Recent advances in reactive extrusion processing of biodegradable polymer-based compositions. *Macromol. Mater. Eng.* **2008,** *293*(6), 447-470.

25.   Daurio, D.; Nagapudi, K.; Alvarez-Núñez, F., Manufacture of pharmaceutically relevant materials by mechanochemistry using twin screw extrusion. In *melt extrusion: materials, technology and drug product design,* Repka, M. A.; Langley, N.; DiNunzio, J., Eds. Springer New York: New York, NY, **2013**; pp 223-242.

26.   Liu, X.; Lu, M.; Guo, Z.; Huang, L.; Feng, X.; Wu, C. Improving the chemical stability of amorphous solid dispersion with cocrystal technique by hot melt extrusion. *Pharm. Res.* **2012,** *29*(3), 806-17.

27.   Kindermann, C.; Matthée, K.; Sievert, F.; Breitkreutz, J. Electrolyte-stimulated biphasic dissolution profile and stability enhancement for tablets containing drug-polyelectrolyte complexes. *Pharm. Res.* **2012,** *29*(10), 2710-2721.

28.   Moustafine, R. I.; Bukhovets, A. V.; Sitenkov, A. Y.; Kemenova, V. A.; Rombaut, P.; Van den Mooter, G. Eudragit EPO as a complementary material for designing oral drug delivery systems with controlled release properties: comparative evaluation of new interpolyelectrolyte complexes with countercharged Eudragit L100 copolymers. *Mol. Pharmaceutics* **2013,** *10*(7), 2630-2641.

29.   Herzfeldt, C. D.; Kümmel, R. Dissociation constants, solubilities and dissolution rates of some selected nonsteroidal antiinflammatories. *Drug Dev. Ind. Pharm.* 1983, *9*(5), 767-793.

30.   Allesø, M.; Chieng, N.; Rehder, S.; Rantanen, J.; Rades, T.; Aaltonen, J. Enhanced dissolution rate and synchronized release of drugs in binary systems through formulation: Amorphous naproxen–cimetidine mixtures prepared by mechanical activation. *J. Controlled Release* **2009,** *136*(1), 45-53.

31.   Svärd, M.; Hjorth, T.; Bohlin, M.; Rasmuson, Å. C. Calorimetric properties and solubility in five pure organic solvents of N-methyl-d-glucamine (meglumine). *J. Chem. Eng. Data* **2016,** *61*(3), 1199-1204.

32.   Childs, S. L.; Stahly, G. P.; Park, A. The salt−cocrystal continuum: The influence of crystal structure on ionization State. *Mol. Pharmaceutics* **2007,** *4*(3), 323-338.

33.   Cruz-Cabeza, A. J.   Acid-base crystalline complexes and the pKa rule. *CrystEngComm* **2012,** *14*(20), 6362-6365.

34.   Veronesi, P. A., Water soluble salts of an NSAID with meglumine/glucamine. U.S. Patent 4,748,174 A, May 31, 1988.

35.   Kraudelt, H.; Schilde, U.; Uhlemann, E., Crystal structures of 1-methylamino-D-1-deoxy-glucitol, C7H17NO5 and 1-methylamino-D-1-deoxy-glucitol hydrochloride, C7H18CINO5. *Z. Kristallogr. − New Cryst. Struct.* **1998**, 213, 177-179.

36.   James, S. L.; Adams, C. J.; Bolm, C.; Braga, D.; Collier, P.; Friscic, T.; Grepioni, F.; Harris, K. D. M.; Hyett, G.; Jones, W.; Krebs, A.; Mack, J.; Maini, L.; Orpen, A. G.; Parkin, I. P.; Shearouse, W. C.; Steed, J. W.; Waddell, D. C. Mechanochemistry: opportunities for new and cleaner synthesis. *Chem. Soc. Rev.* **2012,** *41*(1), 413-447.

37.   Baird, J. A.; Taylor, L. S. Evaluation of amorphous solid dispersion properties using thermal analysis techniques. *Adv. Drug Delivery Rev.* **2012,** *64*(5), 396-421.

38.   Tong, P.; Taylor, L. S.; Zografi, G. Influence of alkali metal counterions on the glass transition temperature of amorphous indomethacin salts. *Pharm. Res.* **2002,** *19*(5), 649-654.

39.   Cassimiro, D. L.; Kobelnik, M.; Ribeiro, C. A.; Crespi, M. S.; Boralle, N. Structural aspects, thermal behavior, and stability of a self-assembled supramolecular polymer derived from flunixin–meglumine supramolecular adducts. *Thermochim. Acta* **2012,** *529*, 59-67.

40.   Stepanovs, D.; Jure, M.; Yanichev, A.; Belyakov, S.; Mishnev, A. Molecular salts of propranolol with dicarboxylic acids: diversity of stoichiometry, supramolecular structures and physicochemical properties. *CrystEngComm* **2015,** *17*(47), 9023-9028.

41.   Friščić, T.; Halasz, I.; Beldon, P. J.; Belenguer, A. M.; Adams, F.; Kimber, S. A. J.; Honkimäki, V.; Dinnebier, R. E. Real-time and in situ monitoring of mechanochemical milling reactions. *Nat. Chem.* **2013,** *5*(1), 66-73.

42.   Seefeldt, K.; Miller, J.; Alvarez-Nunez, F.; Rodriguez-Hornedo, N. Crystallization pathways and kinetics of carbamazepine-nicotinamide cocrystals from the amorphous state by in situ thermomicroscopy, spectroscopy, and calorimetry studies. *J. Pharm. Sci.* **2007,** *96*(5), 1147-1158.

43.   Sun, C. C. Cocrystallization for successful drug delivery. *Expert Opin. Drug Delivery* **2013,** *10*(2), 201-213.

44.   Neurohr, C.; Revelli, A. L.; Billot, P.; Marchivie, M.; Lecomte, S.; Laugier, S.; Massip, S.; Subra-Paternault, P. Naproxen–nicotinamide cocrystals produced by CO_2 antisolvent. *J. Supercrit. Fluids* **2013,** *83*, 78-85.

45.   Bogdanova, S.; Pajeva, I.; Nikolova, P.; Tsakovska, I.; Müller, B. Interactions of poly(vinylpyrrolidone) with ibuprofen and naproxen: Experimental and modeling studies. *Pharm. Res.* **2005,** *22*(5), 806-815.

46.   Mura, P.; Bettinetti, G. P.; Cirri, M.; Maestrelli, F.; Sorrenti, M.; Catenacci, L. Solid-state characterization and dissolution properties of Naproxen–Arginine–Hydroxypropyl-β-cyclodextrin ternary system. *Eur. J. Pharm. Biopharm.* **2005,** *59*(1), 99-106.

47.   Lin-Vien, D.; Colthup, N. B.; Fateley, W. G.; Grasselli, J. G.; Eds. *The handbook of infrared and Raman characteristic frequencies of organic molecules*. Academic Press: New York 1991.

48.   Stevens, J. S.; Byard, S. J.; Seaton, C. C.; Sadiq, G.; Davey, R. J.; Schroeder, S. L. M. Proton transfer and hydrogen bonding in the organic solid state: a combined XRD/XPS/ssNMR study of 17 organic acid-base complexes. *Phys. Chem. Chem. Phys.* **2014,** *16*(3), 1150-1160.

49.   Stevens, J. S.; Newton, L. K.; Jaye, C.; Muryn, C. A.; Fischer, D. A.; Schroeder, S. L. M. Proton transfer, hydrogen bonding, and disorder: Nitrogen near-edge X-ray absorption fine structure and X-ray photoelectron spectroscopy of bipyridine–acid salts and co-crystals. *Cryst. Growth Des.* **2015,** *15*(4), 1776-1783.

50.   Baird, J. A.; Van Eerdenbrugh, B.; Taylor, L. S. A classification system to assess the crystallization tendency of organic molecules from undercooled melts. *J. Pharm. Sci.* **2010,** *99*(9), 3787-806.

51.   He, Y.; Ho, C. Amorphous solid dispersions: Utilization and challenges in drug discovery and development. *J. Pharm. Sci.* **2015,** *104*(10), 3237-3258.

52.   Löbmann, K.; Laitinen, R.; Grohganz, H.; Strachan, C.; Rades, T.; Gordon, K. C. A theoretical and spectroscopic study of co-amorphous naproxen and indomethacin. *Int. J. Pharm.* **2013,** *453*(1), 80-87.

53.   Löbmann, K.; Laitinen, R.; Grohganz, H.; Gordon, K. C.; Strachan, C.; Rades, T. Coamorphous drug systems: Enhanced physical stability and dissolution rate of indomethacin and naproxen. *Mol. Pharmaceutics* **2011,** *8*(5), 1919-1928.

54.   Ueda, H.; Muranushi, N.; Sakuma, S.; Ida, Y.; Endoh, T.; Kadota, K.; Tozuka, Y. A Strategy for co-former selection to design stable co-amorphous formations based on physicochemical properties of non-steroidal inflammatory drugs. *Pharm. Res.* **2016,** *33*(4), 1018-1029.

55.   Perlovich, G. L.; Kurkov, S. V.; Kinchin, A. N.; Bauer-Brandl, A. Thermodynamics of solutions III: Comparison of the solvation of (+)-naproxen with other NSAIDs. *Eur. J. Pharm. Biopharm.* **2004**, *57*(2), 411-420.

56.   Cao, X.J.; Sun, C.R.; Pan, Y.J. The complex of flunixin and meglumine. *Acta Cryst.* **2003**, *59*(10), 1471-1473.

57.   Paudel, A.; Loyson, Y.; Van den Mooter, G. An investigation into the effect of spray drying temperature and atomizing conditions on miscibility, physical stability, and performance of naproxen–PVP K 25 solid dispersions. *J. Pharm. Sci.* **2013,** *102*(4), 1249-1267.

58.   Nair, R.; Nyamweya, N.; Gonen, S.; Martinez-Miranda, L. J.; Hoag, S. W. Influence of various drugs on the glass transition temperature of poly(vinylpyrrolidone): a thermodynamic and spectroscopic investigation. *Int. J. Pharm.* **2001,** *225*(1-2), 83-96.

59.   Tran, T. T.D.; Tran, P. H.L.; Choi, H.G.; Han, H.K.; Lee, B.J. The roles of acidifiers in solid dispersions and physical mixtures. *Int. J. Pharm.* **2010,** *384*(1–2), 60-66.

60.   Tran, P. H. L.; Tran, H. T. T.; Lee, B.-J. Modulation of microenvironmental pH and crystallinity of ionizable telmisartan using alkalizers in solid dispersions for controlled release. *J. Controlled Release* **2008,** *129*(1), 59-65.

61.   Nielsen, L. H.; Gordon, S.; Holm, R.; Selen, A.; Rades, T.; Müllertz, A. Preparation of an amorphous sodium furosemide salt improves solubility and dissolution rate and leads to a faster Tmax after oral dosing to rats. *Eur. J. Pharm. Biopharm.* **2013,** *85*(3, Part B), 942-951.

62.   Kadoya, S.; Izutsu, K.I.; Yonemochi, E.; Terada, K.; Yomota, C.; Kawanishi, T. Glass-state amorphous salt solids formed by freeze-drying of amines and hydroxy carboxylic acids: effect of hydrogen-bonding and electrostatic interactions. *Chem. Pharm. Bull.* **2008,** *56*(6), 821-826.

63.   Zhu, Z.; Yang, T.; Zhao, Y.; Gao, N.; Leng, D.; Ding, P. A simple method to improve the dissolution of repaglinide and exploration of its mechanism. *Asian J. Pharm. Sci.* **2014,** *9*(4), 218-225.

64.   Tomasko, D. L.; Timko, M. T. Tailoring of specific interactions to modify the morphology of naproxen. *J. Cryst. Growth* **1999,** *205*(1–2), 233-243.

65.   Paudel, A.; Nies, E.; Van den Mooter, G. Relating hydrogen-bonding interactions with the phase behavior of naproxen/PVP K 25 solid dispersions: Evaluation of solution-cast and quench-cooled films. *Mol. Pharmaceutics* **2012,** *9*(11), 3301-3317.

Chapter 3: Influence of lidocaine forms (salt vs. freebase) on properties of drug–Eudragit® L100-55 extrudates prepared by reactive melt extrusion [3]

3.1 ABSTRACT

This study examines the preparation of sustained-release lidocaine polyelectrolyte complex using reactive melt extrusion. Eudragit L100-55 was selected as the ionic polymer. The influence of drug forms (freebase vs. hydrochloride salt) on lidocaine–Eudragit L100-55 interactions, physical stability, and dissolution properties of extrudates was investigated. It was confirmed by DSC, FT-IR and Raman spectroscopy that polyelectrolyte could only form via the acid–base reaction between Eudragit L100-55 and lidocaine freebase. Due to this ionic interaction, the lidocaine extrudate was physically more stable than the lidocaine hydrochloride extrudate during the storage under stressed condition. Drug release from lidocaine extrudate was a function of drug solubility, polymer solubility, drug-polymer interaction, and drug-induced microenvironment pH. At 30% drug loading, extrudate exhibited sustained release in aqueous media at pH 1.2 and 4.5. Due to the alkaline microenvironment pH induced by dissolved lidocaine, Eudragit L100-55 was solubilized and sustained-release was not achieved in water and aqueous media at pH 5.5. In comparison, lidocaine hydrochloride induced an acidic microenvironment. Drug release of lidocaine hydrochloride extrudate was similar at pH 1.2, 4.5, 5.5 and water with drug being released over 10 hours. The release of lidocaine hydrochloride from the extrudates in these media was primarily controlled by microenvironment pH. It is

---

concluded that different forms of lidocaine resulted in different drug–polymer interactions and distinctive physicochemical properties of extrudates.

3.2 INTRODUCTION

Over the past decades, great efforts have been made to develop novel drug delivery systems that can sustain drug release to achieve the required duration of therapeutic activity, to control the drug release rate, or to deliver the drug to specific tissues [1]. Pharmaceutics scientists have given considerable attention to polyelectrolyte complexes, which have wide applications in developing sustained drug delivery system, controlled drug delivery, functional nanomaterials, gene therapy, and oral delivery of macromolecules [2-4]. In general, polyelectrolyte complexes result from the association complexes formed between oppositely charged molecules via ionic interaction at stoichiometric or non-stoichiometric ratios [5, 6].

Polyelectrolyte complexes can be categorized based on their components. These categories include polymer–drug, polymer–polymer, polymer–drug–polymer, polymer–surfactant, and polymer–protein [7]. Polyelectrolyte–drug complexes have been widely used in formulations for a variety of purposes, such as improving the dissolution of poorly water-soluble drugs [8], modifying drug release [9, 10], taste masking [11], and improving drug chemical stability [12].

Conventionally, most polyelectrolyte–drug complexes are prepared using the solvent method, in which the polymers and the drug are dissolved separately in an organic solvent, in buffers, or in pure water before they are mixed together [7]. The solvents are removed by freeze drying, spray drying, or other drying technologies when the oppositely charged particles are fully complexed. Right now, most solvent methods used to prepare polyelectrolyte complexes remain in the lab phase due to several disadvantages, such as

low manufacturing efficiency, scale-up difficult, or toxicity of the organic solvent. Very few studies focus on using melt extrusion to prepare polyelectrolyte complexes in solid state.

In recent years, melt extrusion (ME) has proved to be a promising technique to prepare solid dispersions for various applications [13]. In the current study, ME was explored as a method to prepare polyelectrolyte–drug complexes. Compared to traditional processing techniques, the advantages of ME include the fact that it requires no solvent, it is a continuous process with high efficiency, and it is easy to scale up. During the ME process, the drug, polymer, and other excipients are fed into barrels at different temperatures, and the rotating screws mix and melt the materials using heat and intense mechanical shearing forces to achieve molecular-level mixing [14]. Due to the high temperatures and the aggressive mixing environment, ME provides favorable and flexible processing conditions for solid-state chemical reactions.

Reactive melt extrusion (RME) is a special extrusion process in which individual components are bonded by a chemical reaction [15]. It has provided the means to perform continuous, large-scale, and highly efficient mechanochemical synthesis that is adaptable to an industry manufacturing process [16]. It is also widely used in the polymer and food industry to improve the properties of various products [17].
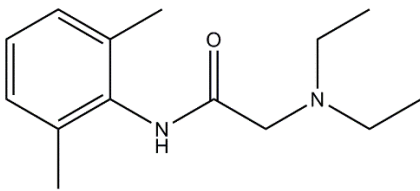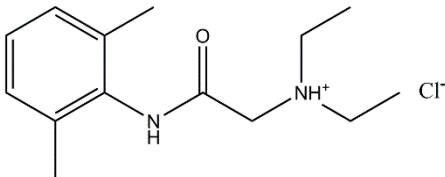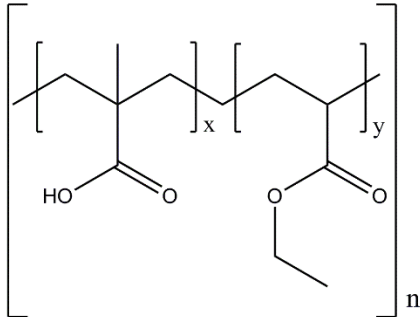
The application of RME to pharmaceuticals is still in the primary stage, although pharmaceutical melt extrusion has been extensively studied and a number of commercial products on the market are produced using extrusion technology. Several reports describe the use of RME to prepare materials such as cocrystals [18, 19] and salts [20, 21]. These reports show the great potential of RME in pharmaceutics. Using RME in pharmaceutical applications provides multiple advantages, among others: (1) RME prevents the thermal degradation of the drug and excipients during the extrusion process, (2) it improves the

126

physical stability of amorphous drugs during dissolution or storage time, and (3) it is useful for the preparation of sustained, controlled, and targeted drug delivery systems [21].

Several studies employ RME to prepare polyelectrolyte–drug complexes to improve the dissolution rate of poorly water-soluble drugs with desirable physical stability [22, 23], taste masking [11], and targeted drug delivery [10]. However, very few studies focus on the influence of the ionization state of the model drug on the formation of polyelectrolyte complexes during the ME process. The literature also reports contradictions regarding the effect of the drug's chemical nature on the drug–polymer ionic interaction. Some reports indicate that the salt form of the drug can still complex with the ionic polymer during ME [24, 25]; however, some of the literature finds that only the free drug can complex with the oppositely charged components in solid state [26, 27]. In this study, we investigate the complexation behavior between an ionic polymer and the same drug in different forms.

For the model drugs in this study, we selected lidocaine and its salt, lidocaine hydrochloride, which are two chemicals commonly used as local anesthetics. As the polymer carrier, we selected Eudragit L100-55, an anionic copolymer based on methacrylic acid and ethyl acrylate (soluble above pH 5.5). Our prototype formulation consists of 30% drug and 70% polymer. At this drug loading level, the molar ratio between the methacrylic acid groups in Eudragit L100-55 and the amine groups in lidocaine is 2.9:1. Table 3.1 presents the chemical structures and critical attributes of the drug and excipients used in this study

Table 3.1: Chemical structures and selected physicochemical properties of lidocaine, lidocaine HCl, and Eudragit L100-55.

Components	Chemical Structure	Experimental Glass Transition (T_g) and Melting Temperature (T_m) (°C)	Molecular Weight (g/mol)
Lidocaine		T_m: 68 T_g: -60	234.34
Lidocaine HCl		T_m: 79 T_g: 34	270.80
Eudragit® L100-55		T_g: 123	320,000

This study compares the interactions between the acidic polymer Eudragit L100-55 and the alkaline drug lidocaine, in either freebase or hydrochloride salt form, in sustained-release hydrophilic matrices prepared by melt extrusion. This study also investigates the

128

influence of the drug–polymer interactions on the physicochemical properties of the extrudates. We investigate the miscibility, and possible interaction, between the drug and polymer using DSC, XRPD, PLM, ATR-IR, and Raman spectroscopy. This study compares the physical stability of lidocaine–Eudragit L100-55 and lidocaine hydrochloride–Eudragit L100-55 extrudates under accelerated storage conditions using PLM and XRPD. The extruded granules' swelling ability and microenvironment pH are also evaluated. Last, dissolution testing is performed in purified water with or without 0.15 M NaCl and in different pH buffer media.

3.3 MATERIALS

Lidocaine and lidocaine hydrochloride were purchased from MP Biomedicals, LLC (Solon, OH, USA). Eudragit® L100-55 was donated from Evonik industries (Darmstadt, Germany). Methanol (HPLC grade) and Bromophenol blue were purchased from Fisher Scientific (Waltham, MA, USA). All other reagents and solvents were of analytical grade or better.

3.4. METHODS

3.4.1 Melt Extrusion

A Haake MiniLab co-rotating twin-screw extruder (Thermo Fisher Scientific, Dreieich, Germany) was used to prepare the extrudates. Process parameters and formulation compositions are summarized in Table 3.2. The drug and polymer are mixed using a Turbula® Shaker-Mixer (Glen Mills, Clifton, NJ) for 10 min. The blends were manually fed into the extruder at approximately 1 g/min. The barrel temperature was set at 155 °C, and the screw speed was at 150 rpm. After cooling to ambient temperature,

extrudates were milled using a coffee grinder and screened into different granule sizes. We used 16 to 18-mesh granules to evaluate physical stability and dissolution.

Table 3.2: Composition and processing conditions for lidocaine and lidocaine HCl extrudates.

Formulation Composition	Eudragit L100-55 (% wt)	Drug	
		Lidocaine (% wt)	Lidocaine HCl (% wt)
Lidocaine Formula	70	30	-
Lidocaine HCl Formula		-	30
Process conditions	Barrel temperature: 155 °C Feeding rate: 1 g/min Screw speed: 150 rpm		

3.4.2   Differential Scanning Calorimetry (DSC)

DSC analysis was performed using a Model Q-20 DSC (TA Instruments, Newcastle, DE) equipped with the RCS 40 (TA Instrument, Newcastle, DE) refrigerated cooling system accessory under a dry nitrogen purge (50 mL/min). Calibration was performed with an indium, and an empty TA aluminum pan was used as a reference. Samples were accurately weighed (3–5 mg) into aluminum pans and crimped with aluminum lids. To characterize drug–polymer miscibility, physical mixtures at various weight ratios were first heated from 20 °C to 180 °C. After being cooled down to -20°C, the mixtures were heated for the second time from -20 °C to 180 °C. Heating from 20 °C to 180 °C at a rate of 10 °C/min was applied to characterize extrudates. The temperature

ramp rate was kept constant at 10 °C/min in this study. DSC data were analyzed using the TA-Universal Analysis 2000 software (TA Instrument, Newcastle, DE).

3.4.3 Polarized Light Microscopy (PLM)

PLM measurement was conducted using an Olympus BX-53 polarized light microscope (Olympus Corporation of Americas, Center Valley, PA) equipped with a QImage digital camera (QImaging, Surrey, Canada). The samples were dispersed in several drops of silicon oil on the slides and covered by slips. The samples were observed with a first-order compensator at 200X magnification. Images were captured using QImaging software (QImaging, BC, Canada).

3.4.4 X-ray Powder Diffraction (XRPD)

XRPD measurement were determined using a Rigaku MiniFlex 600 X-ray diffractometer (Rigaku Corporation, Japan) equipped with a copper X-ray tube. Milled samples were placed on a silicon sample holder and measurement was conducted with an acceleration voltage of 40 kV and a current of 15 mA for angles of 5–45 ° (2-theta) with a speed of 5 °/min and a step size of 0.02 °. The results were analyzed with MDI Jade (version 8.5, Material Data, Inc., Livermore, CA) and plotted with OriginLab (version 9.0, OriginLab Corporation, Northampton, MA).

3.4.5 Fourier Transform Infrared Spectroscopy (FTIR)

Molecular interactions between the drug and polymer were examined with ATR-FTIR. FTIR measurements were performed using a Thermo Nicolet iS50 spectrometer (Waltham, MA). Sufficient samples were placed on the germanium crystal surface, then constant torque was applied using the building-in pressure tower to achieve uniform contact between the solid and the crystal. All samples were analyzed at ambient room

temperature with a total of 32 scans at 4 cm^{-1} resolution of 600–4,000 cm^{-1}. The peak positions were determined using OMNIC software peak picking function (ThermoFisher Scientific, Waltham, MA).

3.4.6 Raman Spectroscopy

All Raman measurements were performed using a Thermo Nicolet iS50 Raman spectrometer (ThermoFisher Scientific, Waltham, MA). The spectrometer was equipped with a 1064 nm diode laser (Innovative Photonic Solution, Monmouth Junction, NJ), a single-element InGaAs detector, and XT-KBr interferometer. The analysis was carried out at room temperature utilizing a laser wavelength of 1,064 nm. Spectra were the average of 128 scans, taken at a 4 cm^{-1} resolution with a laser power of 500 mW. Data were further processed using OMNIC software.

3.4.7 Dissolution Testing

Dissolution testing of extruded granules (16–18 mesh size) was carried out in 900 mL media at 37 °C using USP Type II apparatus (Model Varian VK7025, Agilent Technology Inc., Santa Clara, CA) at a paddle speed of 75 rpm. The dissolution media were purified water, a 0.1 N hydrochloric acid solution (pH 1.2), and citrate–phosphate buffers (pH 4.5, 5.5, 6.8). Samples that contained the equivalent of 120 mg of lidocaine were introduced into each dissolution vessel. Dissolution samples were withdrawn at predetermined time points using an autosampler (Model Varian VK7025, Agilent Technology Inc., Santa Clara, CA). The samples were filtered through Vankel Full Flow 10 µm filters. The drug concentration was measured by the UV method at 240 nm wavelength with an Infinite M200 UV-Vis spectrophotometer (Tecan Group Ltd., Mannedorf, Switzerland). All samples were tested in triplicate.

3.4.8 Comparison of Dissolution Profiles

To compare the drug release profiles in different dissolution media, the similarity factor f_2 was used. As proposed by Moore and Flanner, the f_2 value was calculated using the following equation [28]:

$$f_2 = 50 \times \log\left\{\left[1 + \left(\frac{1}{n}\right)\sum_{t=1}^{n}(R_t - T_t)^2\right]^{-0.5} \times 100\right\}$$

where R_t and T_t are the cumulative percentage of drug released for the reference and test assay, respectively, at time t, and n is the number of time points. The f_2 value is a measure of the similarity between the two release profiles, it and ranges from 0 to 100. Based on the FDA guidelines, the dissolution profiles are similar when the f_2 value falls in the range of 50–100.

3.4.9 Measurement of Surface pH of Extruded Granules by Slurry pH Method

The pH of the concentrated slurry is considered to reflect the pH of the solid surface [29]. The surface pH of the extruded granules was measured using the slurry-pH method. Slurries of granules in distilled water were prepared. The equilibrium pH was measured with a Sartorius pH meter (Denver Instrument, Bohemia, NY). Each sample measurement was repeated three times.

3.4.10 Swelling Ability and Microenvironment pH Measurement

The extruded granules' swelling ability, fronts movements, and microenvironment pH were evaluated using the experimental setting previously reported by Ferrero et al. [30]. Briefly, the devices consisted of two Plexiglass discs (diameter 50 mm, thickness 5 mm) connected by four stainless steel screws. The tablets were clamped between those two discs. The device was introduced into the dissolution apparatus vessel containing 900 mL of dissolution medium at 37 °C with a paddle rotation speed of 100 rpm. At defined time

intervals (5, 30, 180, 300, 480, 660, and 1440 min), the devices were removed from the dissolution apparatus and photographed. The pictures were analyzed using Image J 1.6.0 software (NIH, USA) to measure the matrix swelling and the position of the fronts. The interface between the tablet and the dissolution medium at the beginning of the experiment was set by position 0. The inward movement of the fronts represented by a negative value, while the outward movement was indicated by a positive value.

The tablets were prepared by compressing about 400 mg of lidocaine or lidocaine hydrochloride loaded extruded granules (estimated to contain approximately 120 mg of LC or LH) in a hydraulic press (BVA hydraulics, Kansas City, MO), equipped with flat-faced punches 11 mm in diameter and a compression pressure of 3,000 psi. Each tablet contained 0.05% (w/w) of the pH dye indicator Bromophenol blue, which shows blue color above pH 4.6 and turns yellow below pH 3.0.

3.4.11   Physical Stability of Extrudates

The extrudates were sealed in glass bottles along with a silicate desiccator and stored inside an environmental chamber at 40 °C and 75% RH. Samples were removed from the stability chamber (Darwin Chambers Company, St. Louis, MO) at specific time points to assess the potential crystallization of the drugs upon storage.

3.5   RESULTS AND DISCUSSION

3.5.1   Interactions between Drugs and Eudragit L100-55 at Elevated Temperatures

The DSC was used to assess the effect of different forms of lidocaine (freebase vs. HCl salt) on the interaction with Eudragit L100 55 at elevated temperatures. Figure 3.1 presents thermograms of the drug substances, polymer, and their mixtures with Eudragit L100-55 (30% drug content, as an example). Lidocaine and lidocaine HCl melt at 68 °C

and 75 °C, respectively. The glass transition temperature of EL was measured as 110 °C. Depression of the melting point was observed for both lidocaine (from 68 to 65 °C) and lidocaine HCl (from 75 to 66 °C) in their physical mixtures with Eudragit L100-55 at 30% drug loading level.
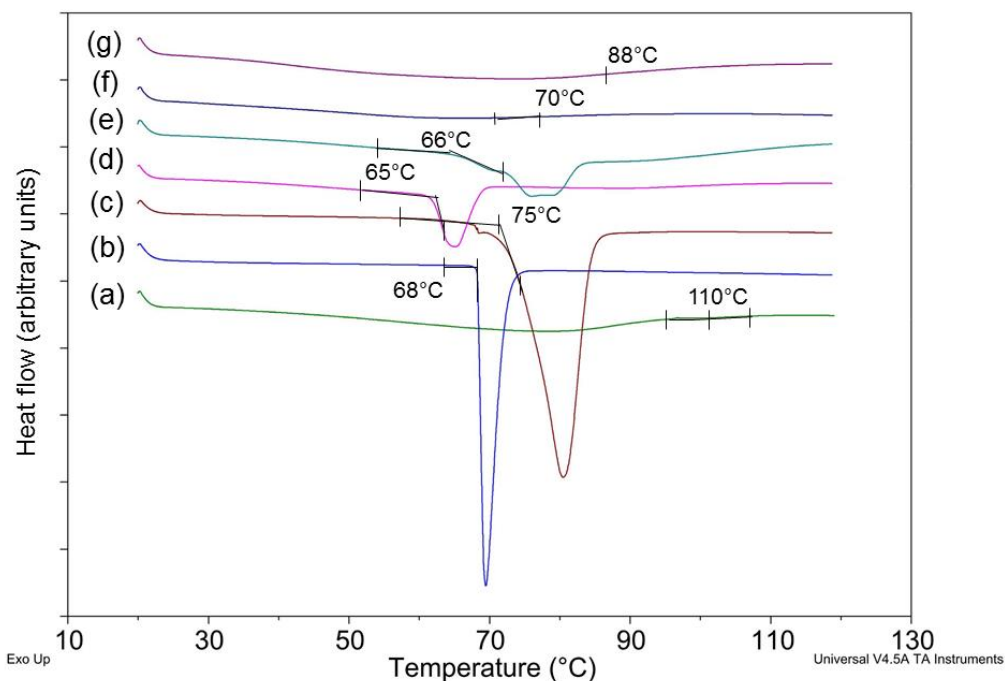
Figure 3.1: DSC thermograms of (a) Eudragit L100-55, (b) lidocaine, (c) lidocaine HCl , (d) physical mixture: 30% lidocaine and 70% Eudragit L100-55, (e) physical mixture: 30% lidocaine HCl and 70% Eudragit L100-55, (f) extrudate: 30% lidocaine and 70% Eudragit L100-55; (g) extrudate: 30% lidocaine HCl and 70% Eudragit L100-55.

The glass transition temperature (T_g) is a crucial factor for amorphous solid dispersions; it reflects the physical state of the drug and polymer carrier, the miscibility of the drug with the carrier, and the potential for specific interactions between the drug and excipients [31]. The difference between the experimental T_g and the theoretical T_g was characterized in order to determine the interaction for the two forms of lidocaine and

135

Eudragit L100-55. The experimental T_g deviated from the theoretical T_g in a pattern that indicates miscibility between the drug and polymer [32]. A negative deviation (experimental $T_g <$ theoretical T_g) suggests strong destabilizing homonuclear (drug–drug and polymer–polymer) interactions, while a positive deviation indicates strong stabilizing heteronuclear (drug–polymer) interactions [33].

Two heating cycles (15–120 °C) were applied in order to measure the T_g of drug–polymer mixtures at various drug weight percentages. Amorphous blends were prepared from the physical blends in the first heating, and the second heating was used to measure the T_g of the resulting blends. Theoretical T_g was calculated using the Gordon–Taylor equation. In order to calculate the theoretical T_g, the density values of lidocaine, lidocaine HCl, and Eudragit L100-55 were determined to be 1.138, 1.223, and 1.142 g/cm^3, respectively, using a helium pycnometer (Micromeritics, Norcross, GA). The T_g of lidocaine, lidocaine HCl, and Eudragit L100-55 was -60 °C [34], 34 °C, and 124 °C, respectively. Figure 3.2 presents T_g as a function of drug loading. A positive deviation was observed for lidocaine–Eudragit L100-55 mixtures, suggesting strong interaction between lidocaine and Eudragit L100-55. The heteronuclear interactions (lidocaine–Eudragit L100-55) in the dispersions were stronger than the sum of the homonuclear interactions (lidocaine–lidocaine and Eudragit L100-55–Eudragit L100-55). In comparison, a negative deviation was observed for lidocaine HCl–Eudragit L100-55 mixtures, indicating a less favorable interaction between lidocaine HCl and Eudragit L100-55. In summary, the interaction of lidocaine freebase with Eudragit L100-55 is much stronger than that of lidocaine HCl. It was hypothesized that the ternary amine group in lidocaine interacts strongly with the carboxylic acid group in Eudragit L100-55 via acid–base interaction. However, for lidocaine HCl, the ternary amine group is protonated with hydrochloric acid. As a weaker acid, methacrylic acid in Eudragit L100-55 cannot replace hydrochloric acid

in lidocaine HCl. IR analysis of melt extrudates presented in the following section confirm this hypothesis regarding drug–Eudragit L100-55 interactions.
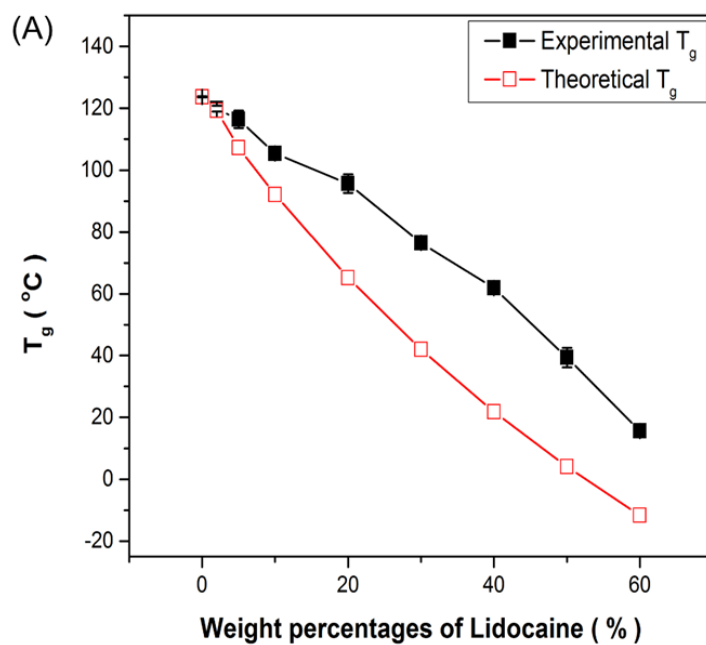
Figure 3.2: continued in next page.
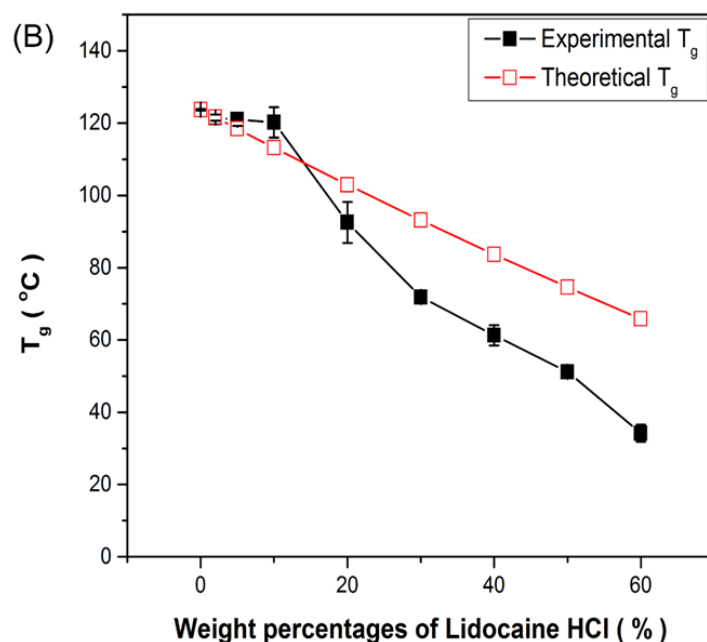
Figure 3.2: Theoretical and experimental glass transition temperature as a function of drug weight fraction. (A) lidocaine, (B) lidocaine HCl. Theoretical values were calculated using the Gordon–Taylor equation. The error bar represents the standard deviation of triplicate analysis.

Baghel et al. [35] report using strong drug–polymer interaction to inhibit the crystallization of ASDs. In their study, the T_g deviations of a cinnarizine ASD were opposite when either polyvinylpyrrolidone (PVP) or polyacrylic acid (PAA) was used as the polymer carrier. Cinnarizine–PVP ASDs exhibited a negative deviation. In contrast, cinnarizine–PAA showed a positive deviation due to ionic interaction.

3.5.2 Melt Extrusion of Eudragit L100-55 and Lidocaine Blends

Table 3.1 lists the formulation, composition, and processing conditions for lidocaine–Eudragit L100-55 and lidocaine HCl–Eudragit L100-55 extrudates. The drug loading in the extrudates was maintained at 30%. In this composition, the molar ratio

between the acrylic acid groups in Eudragit L100-55 and the amine groups in lidocaine was 2.9:1.

A Haake MiniLab corotating extruder was used to process the formulations. The barrel temperature was set above both the Tg and the melting point of the drug. Because of the plasticization effect of lidocaine and lidocaine HCl, plasticizer was not needed to process either formulation. Both extrudates were clear as they exited the die, indicating solubilization of the drugs in polymer melt. The extrudates were then cooled to ambient temperature and reduced to granules in the size range of 16 to 18-mesh using a coffee grinder. The HPLC method was used to verify that the drug content was within 5% of the theoretical drug loading.

For both lidocaine and lidocaine HCl, melt extrudates consisting of 30% drug and 70% Eudragit L100-55 were amorphous. Figure 3.1 presents DSC thermograms of the extrudates. Figure 3.3 presents X-ray diffractograms of the physical blends and the melt extrudates. The T_g of the LC–EL and LH–EL extrudates was 70 °C (Figure 3.1f) and 88 °C (Figure 3.1g), respectively.
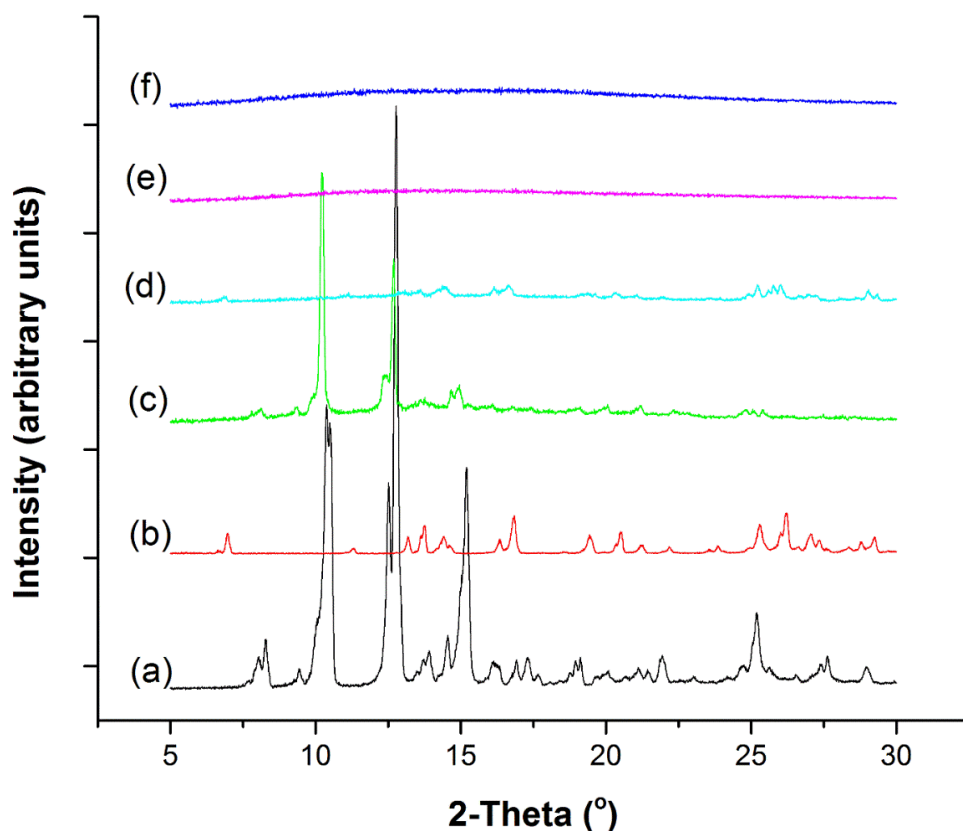
Figure 3.3: X-ray diffractograms of (a) lidocaine, (b) lidocaine HCl, (c) physical mixture of 30% lidocaine and 70% Eudragit L100-55, (d) physical mixture: 30% LH and 70% Eudragit L100-55, (e) extrudate: 30% lidocaine and 70% Eudragit L100-55, and (f) extrudate: 30% lidocaine HCl and 70% Eudragit L100-55.

3.5.3 Characterization of Drug–polymer Interaction Using FTIR and Raman Spectroscopy

FTIR analysis of amorphous lidocaine, amorphous lidocaine HCl, lidocaine–Eudragit L100-55 and LH–Eudragit L100-55 physical mixture, and lidocaine–Eudragit L100-55 extrudate was performed to investigate the molecular interactions between the drugs and the polymer [36, 37]. Figure 3.4 presents the representative spectra. The IR spectra of Eudragit L100-55, amorphous lidocaine and amorphous lidocaine HCl are used as a reference. The intermolecular interactions between the drug and polymer could be

140

depicted by the emergence of new peaks, a shift in the position of the exiting peaks, or a change in the shape of peaks in the spectra [38]. According to previous studies, the indicative bands of the acid–base interaction between the drug and Eudragit L100-55 focus mainly on the region from $1,800$ cm^{-1} to $1,000$ cm^{-1} [39, 40]. In this study, the analysis of spectral changes are focused primarily on highlighted three distinct regions to determine the drug–polymer interactions at a molecular level: Region *I* ($1,800^{-1},630$ cm^{-1}), Region *II* ($1,590^{-1},420$ cm^{-1}), and Region *III* ($1,340^{-1},200$ cm^{-1}).
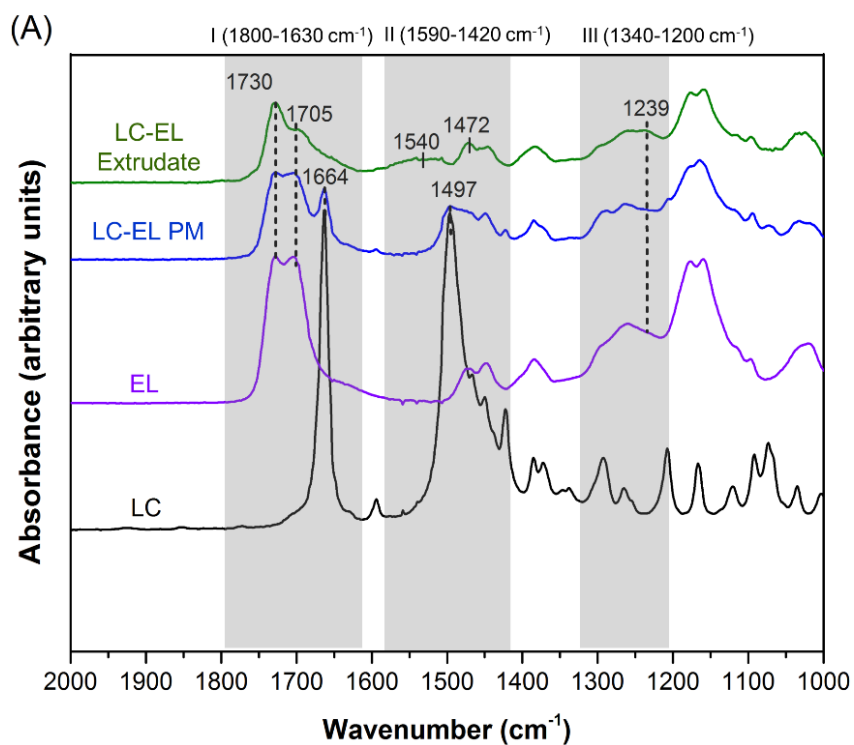
Figure 3.4: continued in next page.
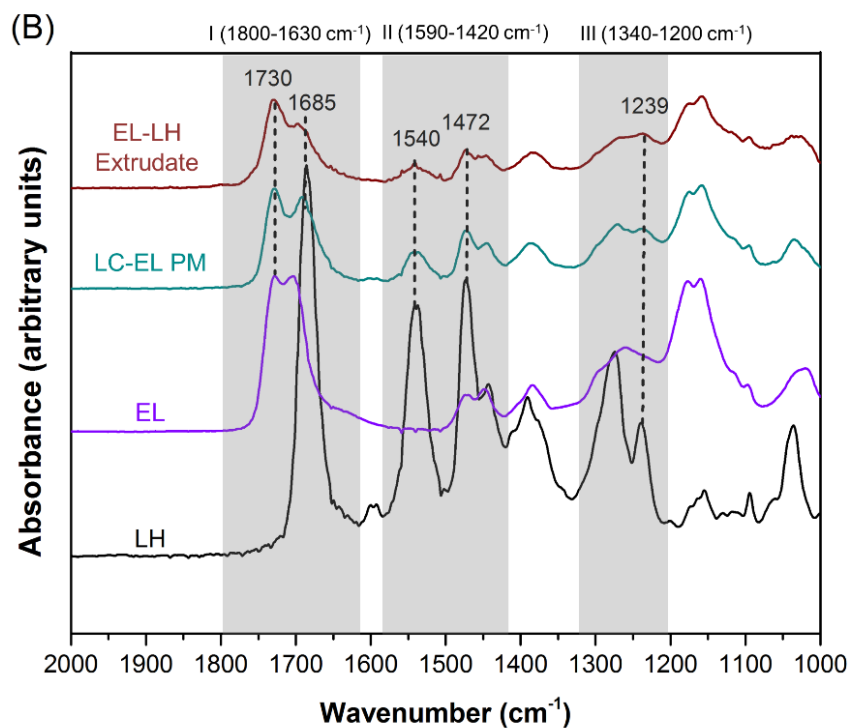
Figure 3.4: IR spectra of (A) Eudragit L100-55 (EL), lidocaine (LC), LC-EL physical mixture, and LC-EL extrudate; (B) Eudragit L100-55, lidocaine hydrochloride (LH), LH-EL physical mixture and LH-EL extrudate.

Spectral changes in Region *I* are suggestive of H-bonding interactions between Eudragit L100-55 and both forms of lidocaine. The sharp peaks in Region *I* can be assigned to the stretching of carbonyl groups of both the polymer and the drugs. Specifically, the IR spectrum of Eudragit L100-55 shows the characteristic bands of the C=O stretching of the carboxylic acid groups ($1,705$ cm^{-1}) and the C=O stretching of the esterified carboxylic groups ($1,730$ cm^{-1}). In the spectra of the amorphous drugs, peaks at $1,664$ cm^{-1} and $1,685$ cm^{-1} represent C=O stretching of the amide group in lidocaine (Figure 3.4A) and lidocaine HCl (Figure 3.4B), respectively. The IR spectrum of the physical mixture is a simple summation of the drug and polymer spectra, which shows no shifting of the carbonyl stretching of the amide. On the other hand, the peak of the amide C=O group in the

142

spectrum of the lidocaine–Eudragit L100-55 extrudate was hypsochromically shifted to $1,730 \text{ cm}^{-1}$. We attributed this blue shift to the H–bonding between the carboxylic groups of Eudragit L100-55 and the amide carbonyl groups of lidocaine.

In addition, the intensity of the C=O stretching of the carboxylic acid groups at $1,705 \text{ cm}^{-1}$ from Eudragit L100-55 decreased significantly, indicating a potential acid–base interaction between Eudragit L100-55 and lidocaine. The carboxylic group functioned as an H-bond donor, and the amide carbonyl group served as an H-bond acceptor. A similar shift of the IR signal due to C=O stretching of the amide group was also observed in the lidocaine HCl–Eudragit L100-55 extrudate.

Sharp peaks in the spectra of Region *II* can be assigned to the N–H bending of drugs. To be specific, two peaks at $1,472 \text{ cm}^{-1}$ and $1,540 \text{ cm}^{-1}$ were observed in the IR spectrum of the lidocaine HCl (Figure 3.4B). One peak represented secondary amide N–H bending next to the aromatic ring, and the other peak represented ternary amine $N–H^+$ bending. In contrast, lidocaine exhibited only one high-intensity peak located at $1,497 \text{ cm}^{-1}$ (Figure 3.4A) due to the lack of an $N–H^+$ group. For the physical mixture of LC–Eudragit L100-55, only a single peak, located at $1,497 \text{ cm}^{-1}$, was observed in the IR spectrum. This indicates that the drug is presented in its free form in the polymeric matrix. Interestingly, two distinct peaks at $1,472 \text{ cm}^{-1}$ and $1,540 \text{ cm}^{-1}$ were observed in lidocaine–Eudragit L100-55 extrudate. Furthermore, the wavenumbers of these two peaks are identical to the peaks of N–H and NH^+ bending in the lidocaine HCl spectrum (Figure 3.4B). It was therefore concluded that acid–base interactions occur between the amine group of lidocaine and the carboxylic acid group of Eudragit L100-55 during the melt extrusion process. At 30% drug loading, the molar ratio between the methacrylic acid in Eudragit L100-55 and lidocaine is 2.9:1. Therefore, there was an excess quantity of methacrylic acid to produce an ionic interaction with lidocaine. This ionic interaction contributed to the improved

physical stability of the lidocaine–Eudragit L100-55 extrudate during the storage. For the lidocaine HCl–Eudragit L100-55 formulation, IR signals in Region *II* remained the same after melt extrusion.

Similar results between two forms of lidocaine and acidic excipients have been reported in a buccal mucoadhesive film prepared with Carbopol, lidocaine, and lidocaine HCl. Salt formation between the acidic carboxylic group of Carbopol and lidocaine was reported, but only H-bonding interaction was observed between Carbopol and lidocaine HCl [27]. Shimada et al. used DSC and NMR to investigate the characteristics of an amorphous complex formed between indomethacin and lidocaine HCl or lidocaine [26, 41]. They find that the interaction mode of indomethacin with lidocaine HCl differs from that of indomethacin with lidocaine. The interaction between indomethacin and lidocaine promotes the formation of a stable amorphous complex via acid–base salt formation; however, a specific interaction between indomethacin and lidocaine HCl was absent.

Spectral Region *III* contains additional evidence of an acid–base interaction between Eudragit L100-55 and lidocaine. A weak peak located at 1,239 cm^{-1} can be attributed to C–C–NH$^+$ bending of the amine group. It is noteworthy that this specific peak was observed with lidocaine HCl (Figure 3.4B) and with the lidocaine–Eudragit L100-55 extrudate (Figure 3.4A), while it was absent with amorphous lidocaine and the lidocaine–Eudragit L100-55 physical mixture.

Our Raman results (Figure 3.5) also show the same conclusion as the FTIR results. The Raman spectrum shows the characteristic region that illustrates significant differences between the physical mixture and the extrudate. In this region (Fig. 3.5A), Eudragit L100-55 shows only a broad peak at 1,724 cm^{-1}, which is attributed to the C=O stretching vibration (Socrates, 2004). lidocaine spectra show two high-intensity peaks at 1,664 cm^{-1}

and 1,594 cm^{-1}, which are attributed the C=O stretching vibration and HNC scissoring vibration, respectively (Badawi et al., 2015).
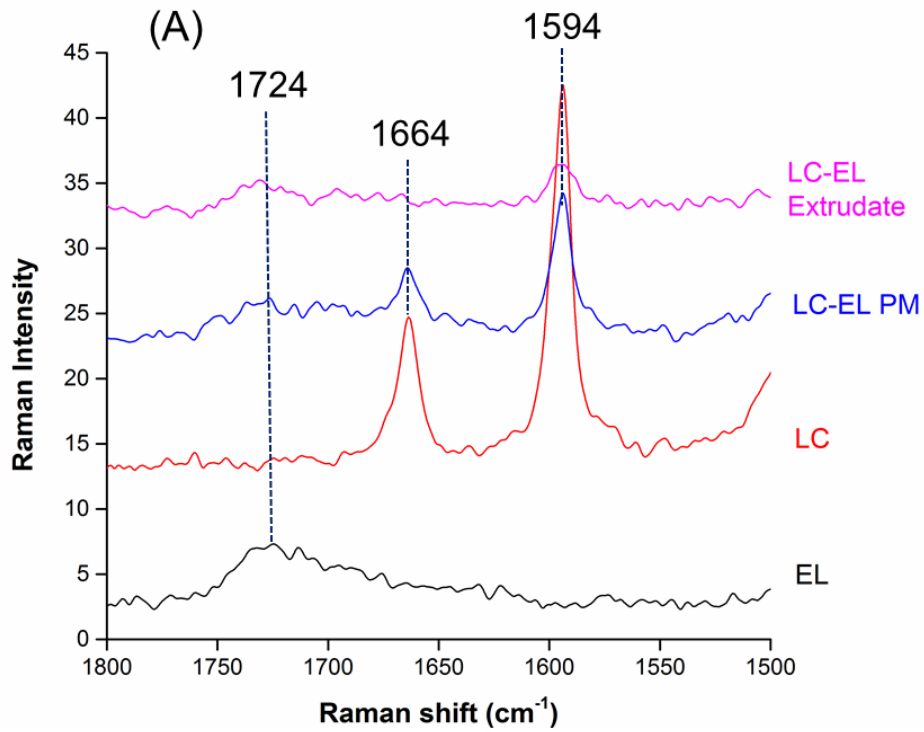
Figure 3.5: continued in next page.
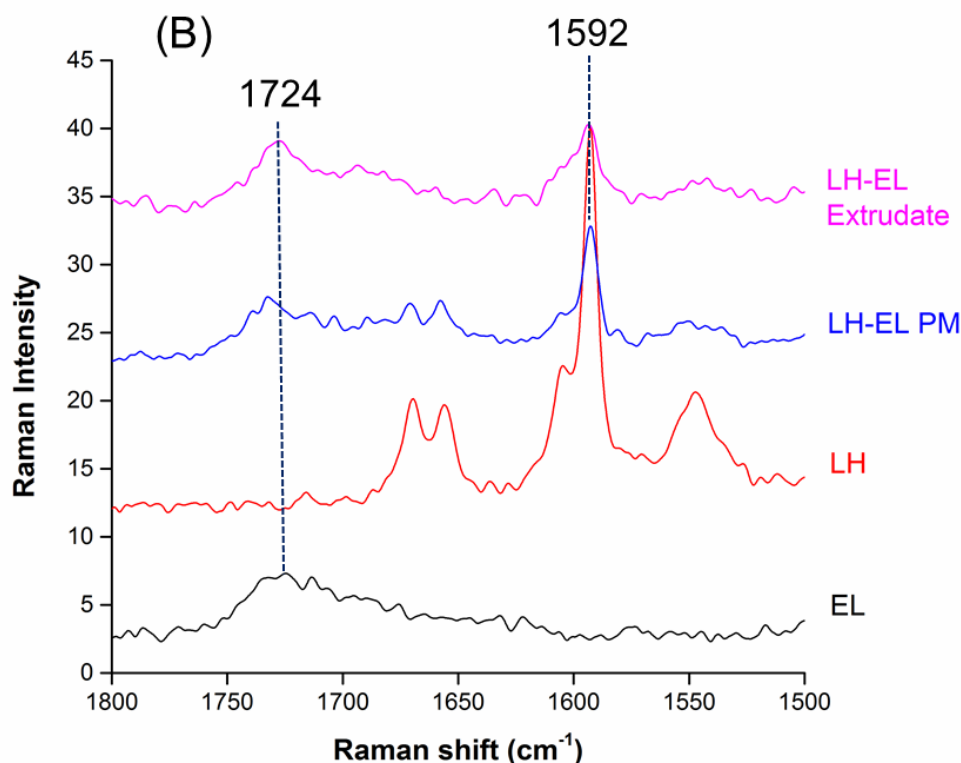
Figure 3.5: Raman spectra of (A) Eudragit L100-55 (EL), lidocaine (LC), LC–EL physical mixture, and LC–EL extrudate; (B) Eudragit L100-55, lidocaine hydrochloride (LH), LH–EL physical mixture and LH–EL extrudate.

These high-intensity peaks also appeared in the lidocaine–Eudragit L100-55 physical mixture. However, the carbonyl group peak disappeared in the lidocaine–Eudragit L100-55 extrudates, and the intensity of the HNC scissoring vibration peak decreased substantially. Due to the different chemical structure of the carbonyl group, lidocaine HCl shows two different peaks at $1{,}670$ cm^{-1} and $1{,}657$ cm^{-1} (Fig. 3.5B). A high-intensity peak at $1{,}592$ cm^{-1}, representing HNC scissoring vibration, could still be observed in lidocaine HCl spectra. The spectra of the lidocaine HCl–Eudragit L100-55 physical mixture is simply the overlap between the lidocaine HCl and Eudragit L100-55. The carbonyl group disappeared in the spectra of the lidocaine HCl–Eudragit L100-55 extrudates, but the

intensity of the tertiary amine group remained the same. This means that the lidocaine HCl and Eudragit L100-55 did not show any ionic interaction with each other.

To conclude the spectroscopic investigation using FTIR and Raman, the polyelectrolyte complex formation of lidocaine (a weak alkaline drug) and Eudragit L100-55 (an acidic polymer) was demonstrated. However, lidocaine HCl could not complex with Eudragit L100-55. Based on the difference between these interactions, one should expect the physical stability and the dissolution behavior of the lidocaine–Eudragit L100-55 and lidocaine HCl–Eudragit L100-55 extrudates to differ as well.

3.5.4 Effect of Drug–Polymer Interaction on the Physical Stabilities of Extrudates

Melt-extruded granules were placed on stability to assess the effect of drug–polymer interactions on their physical stabilities. Of the two pure drug substances, lidocaine crystalizes much faster than lidocaine HCl. lidocaine crystalizes readily from its melt during DSC analysis even at a cooling rate of 20 °C/min. Because of its strong crystallization tendency, lidocaine is categorized as a Class 1 compound in the crystallization classification system proposed by Baird and Taylor [42]. lidocaine HCl has a much lower crystallization tendency and does not crystalize when its melt is cooled at 10 °C/min. Also, the Tg of the lidocaine–Eudragit L100-55 extrudate (70 °C) was lower than that of lidocaine HCl–Eudragit L100-55 extrudate (88 °C). Based on these two factors, one would conclude that the lidocaine–Eudragit L100-55 extrudate is more likely to crystallize during storage.

However, the experimental results of this study contradict this expectation. Figure 3.6 shows the XRPD patterns and PLM images of extrudates after 4 months storage at 40 °C / 75% RH. The lidocaine–Eudragit L100-55 extrudate remained amorphous, and no crystal clusters were detected. In contrast, characteristic diffractions (2 theta of 14.458°,

16.619°, and 25.220°) of crystalline lidocaine HCl were observed in the XRPD pattern of the lidocaine HCl–Eudragit L100-55 extrudate. Crystallization of the lidocaine HCl–Eudragit L100-55 extrudate was also observed under a polarized light microscope. The physical stability study results imply that the ionic interaction between lidocaine and Eudragit L100-55 contributed to the physical stability of the amorphous dispersion system. Similar research has also reported that the ionic interaction between drugs and excipients provide sufficient momentum to inhibit phase separation and recrystallization [36, 43].
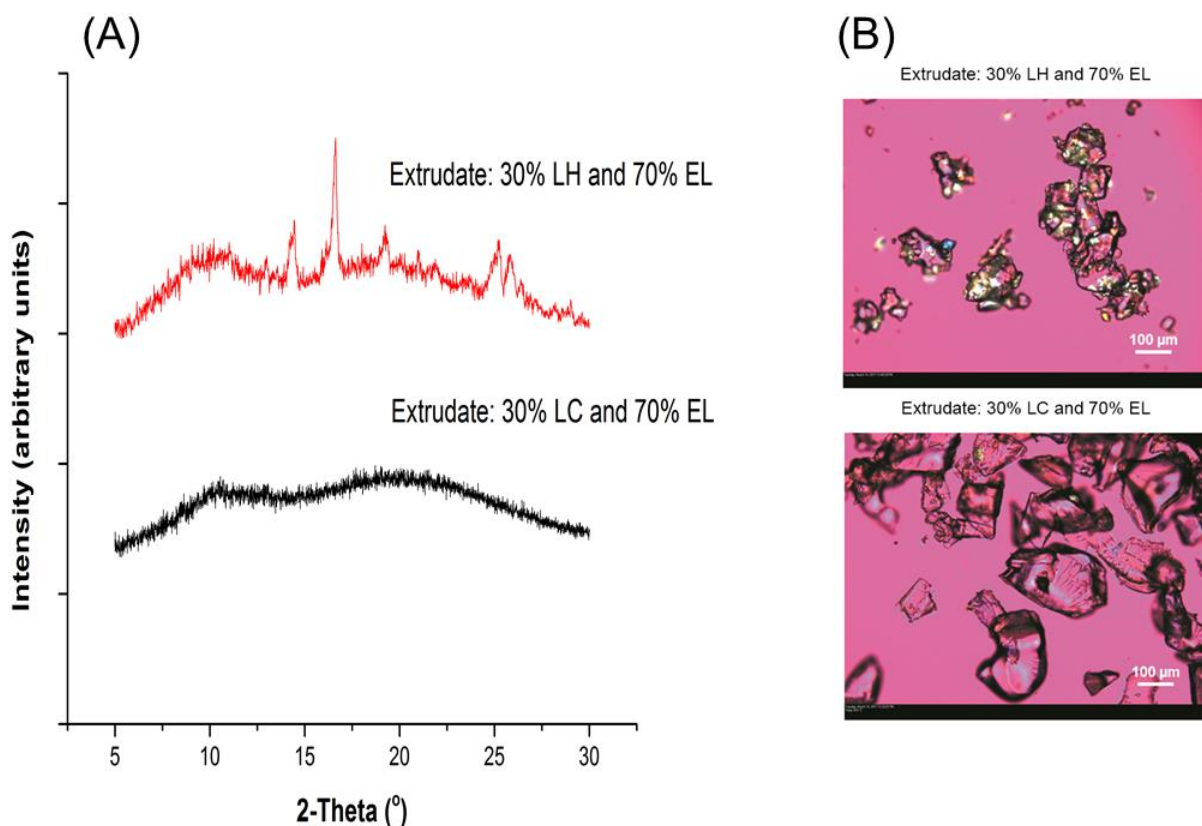
Figure 3.6: XRPD patterns (A) and PLM images (B) of extrudates of lidocaine (LC)–Eudragit L100-55 (EL) and lidocaine HCl (LH)–Eudragit L100-55 (EL) following 4 months of storage at 40 °C with a desiccator.

3.5.5 Comparison of Dissolution Properties

The drug release properties of the extruded granules of 16 to 18-mesh were evaluated in water and buffer solutions at different pH. Since both Eudragit L100-55 and the drug have pH-dependent solubility, one would anticipate that the dissolution of lidocaine and lidocaine HCl from extruded granules would be a function of the pH of the dissolution medium. Additionally, one would anticipate that lidocaine and lidocaine HCl affect drug release by altering the microenvironment pH. The swelling behavior and the microenvironment pH of the extruded granules were investigated to elucidate the difference in the drug release mechanisms of granules containing two different forms of lidocaine.

3.5.5.1 *Dissolution of Extruded Granules in Water*

Figure 3.7 presents the drug release profiles of granules in purified water with or without NaCl as an ionic strength modifier. In purified water, drug release from the lidocaine–Eudragit L100-55 granules was faster than the lidocaine HCl–Eudragit L100-55 granules. Drug release from the lidocaine–Eudragit L100-55 granules plateaued at 80% in 3 h. In contrast, a sustained release of lidocaine HCl from the lidocaine HCl–Eudragit L100-55 granules (over 10 h) was achieved.
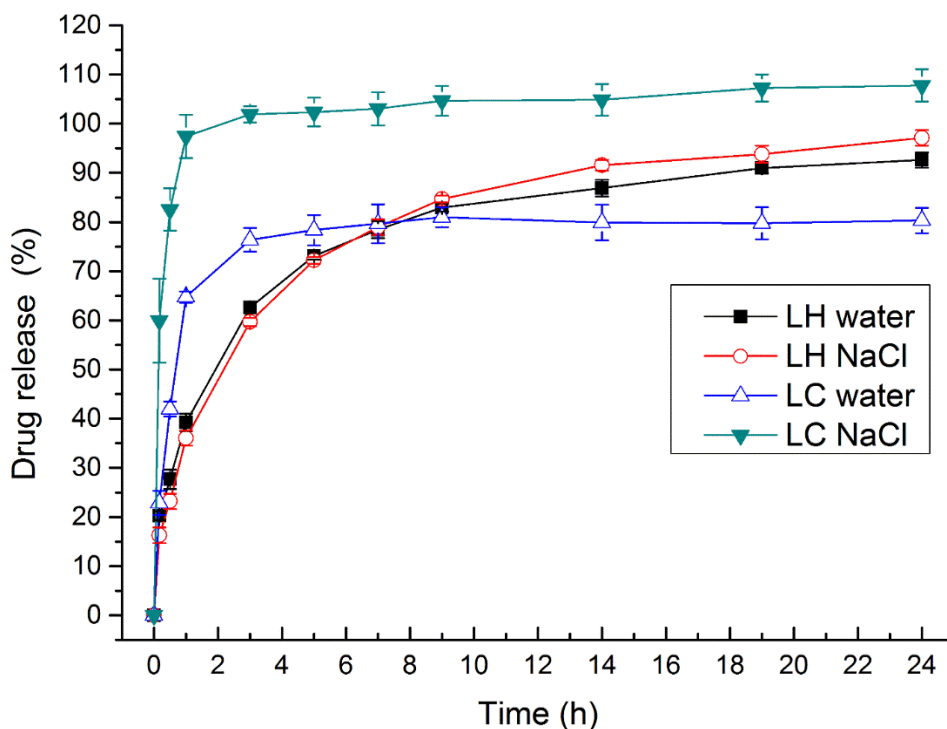
Figure 3.7: Dissolution profiles of 400 mg melt-extruded lidocaine (LC) and lidocaine hydrochloride (LH) 16–18 mesh granules (30% drug loading) in 900 mL water (with or without NaCl) using USP apparatus II at 75 rpm (n = 3). The error bar represents the standard deviation.

Experiments were conducted to study the swelling behavior and microenvironment pH of the granules in water in order to understand this dissolution phenomenon. A blend of extruded granules and bromophenol, a pH indicator, were compressed into tablets. These tablets were clamped between two Plexiglass discs, and they were subjected to dissolution testing in water. At low pH (< 3.0), bromophenol appears yellow, but turns blue at neutral and high pH (> 4.6). As shown in Figure 3.8, lidocaine–Eudragit L100-55 and lidocaine HCl–Eudragit L100-55 tablets displayed different swelling kinetics and microenvironment pH. The different front movement of the gel layer thickness of lidocaine and lidocaine HCl tablets was observed during the dissolution process.

(A)

Bromophenol blue (pH indicator)
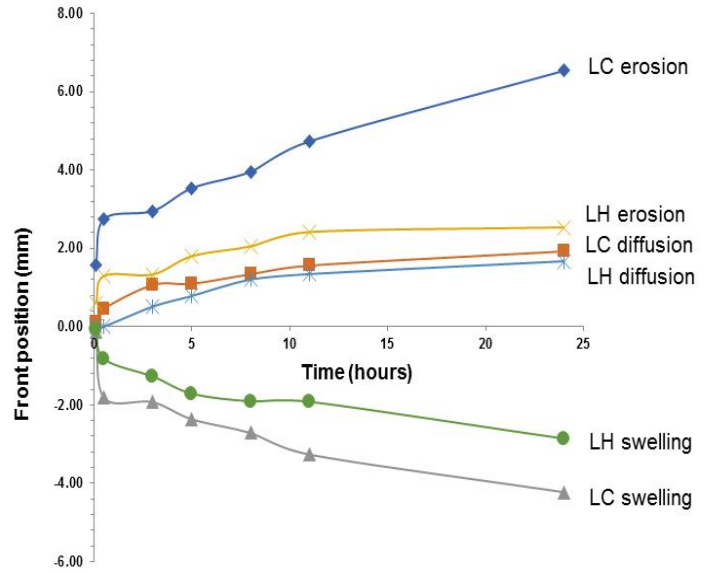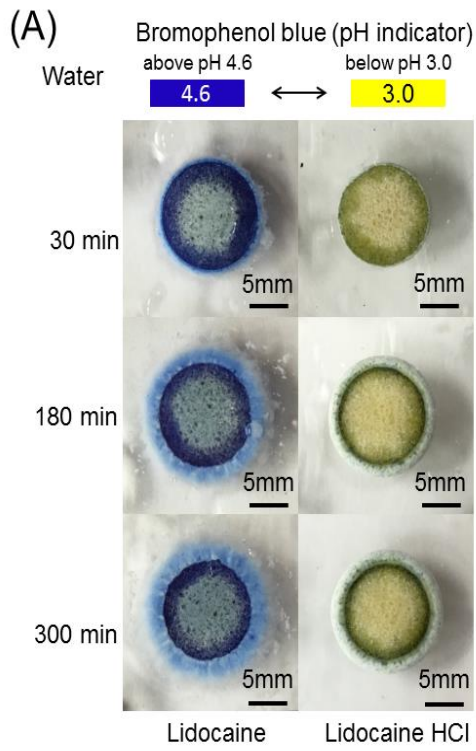
Figure 3.8: continued in next page.
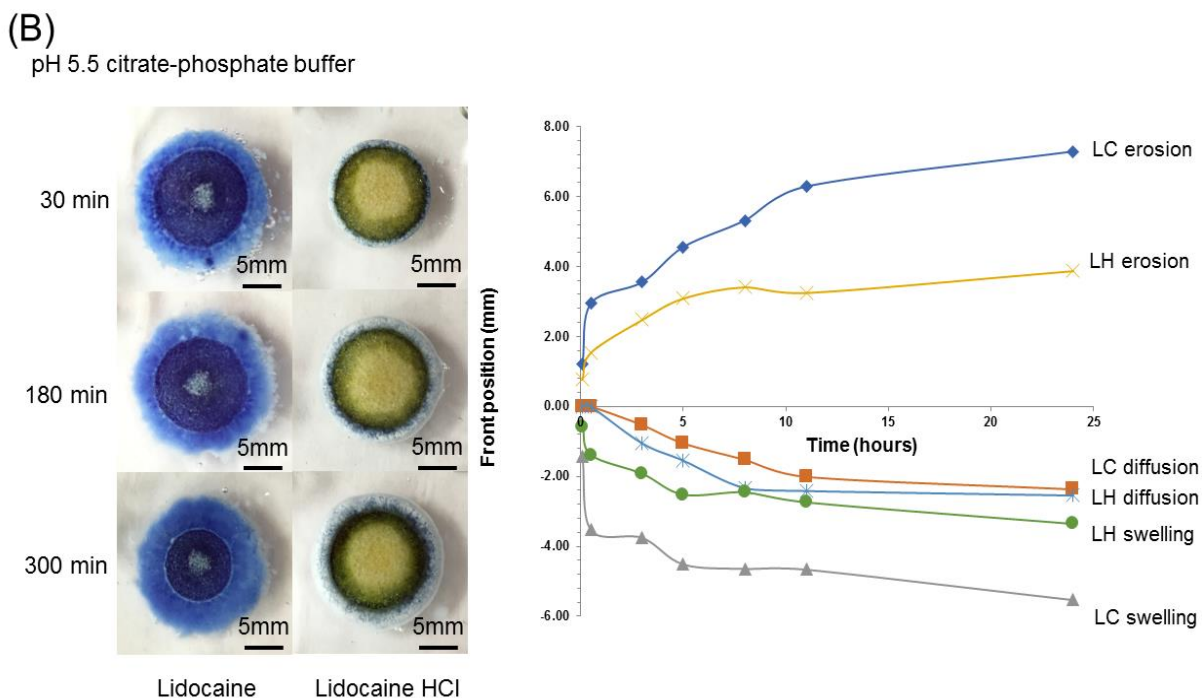
Figure 3.8: Swelling and microenvironmental pH visualization of lidocaine (LC) and lidocaine HCl (LH) melt-extruded granules in water (A) and pH 5.5 buffer (B) (USP apparatus II, 75 rpm, tablets compressed from granules were clamped between two Plexiglass discs).

When the lidocaine tablet was exposed to the dissolution medium, the color of the pH indicator (bromophenol blue) turned dark blue, and the hydrogel layer progressively expanded into three layers simultaneously: The outside layer consisted of the erosion front, the middle layer consisted of the diffusion front, and the inside layer consisted of the swelling front. The erosion front expanded quickly, but the radius of the unwetted portion of the matrix (the swelling front) decreased slowly at a nearly constant rate. The diffusion front slowly followed the swelling front expansion to the outside. As time progressed, the color of the indicator faded from dark blue to light blue, from the swelling front to the erosion front of the layer.

For lidocaine HCl tablets, the pH indicator turned light yellow, and the wetting and swelling also produced a small increase in the diameter of the tablet. Compared to the lidocaine tablet, the erosion front movement was much smaller. A dense white layer formed at the outside of the tablet, preventing water from penetrating to the inside of the tablet. This resulted in a slower rate of swelling front expansion. The similar front movement and microenvironment pH of the lidocaine and lidocaine HCl tablets also have been observed in pH 5.5 citric phosphate buffer.

The microenvironment of the surface of the lidocaine–Eudragit L100-55 tablet was alkaline, while the surface microenvironment of the lidocaine HCl–Eudragit L100-55 tablet was acidic. This microenvironment pH effect was due to the self-buffering of the solubilized drug substances. Using the pH-slurry method, the pH of the microenvironment was measured as 6.50 and 2.46 for the lidocaine–Eudragit L100-55 and lidocaine HCl–Eudragit L100-55 granules, respectively. Although Eudragit L100-55 does not swell in water, the swelling observed in the lidocaine–Eudragit L100-55 formulation was triggered by the alkaline microenvironment induced by the solubilized drug. The loose polymer chain structure in the gel–layer allows lidocaine to transfer quickly to the dissolution medium. As a result, drug release was much faster for lidocaine–Eudragit L100-55 granules. For lidocaine HCl–Eudragit L100-55 granules, the deprotonation and subsequent swelling of the polymer chain would be hindered due to the acidic microenvironment. This resulted in the slower drug release and the release was similar in pH 1.2, 4.5, 5.5 and water.

The drug release of lidocaine–Eudragit L100-55 granules in pure water was dependent on the ionic strength. When the ionic strength of water was adjusted to 0.15 M using sodium chloride, drug release of lidocaine–Eudragit L100-55 granules accelerated, and a complete release was achieved in 2 h. In comparison, the drug release of lidocaine HCl–Eudragit L100-55 granules was not affected by the increase in ionic strength. In the

153

lidocaine–Eudragit L100-55 extrudate, lidocaine interacted with Eudragit L100-55 via ionic complexation to form a polyelectrolyte. At higher ionic strength, the lidocaine cation in the lidocaine–Eudragit L100-55 complex were exchanged by the competing Na^+, resulting in a faster and complete drug release [44, 45].

Similar experimental results have also been observed by other polyelectrolyte drug delivery systems [23, 46]. Jenquin et al. found that the interaction between the drug and polymer significantly influences drug release profiles. The polymer matrices consisting of salicylic acid and Eudragit RL polymer released only 40% of the drug in pure water after 24 h. However, when the sample was switched to a high ionic strength solution (0.15 M NaCl), the matrix released more than 95% of the drug after 12 h. Kindermann also found that the addition of electrolytes can enhance drug release from naproxen–Eudragit E PO polyelectrolyte complex prepared by HME.

3.5.5.2   *Dissolution of Extruded Granules in Aqueous Media at Different pH*

Since the solubility of both lidocaine and Eudragit L100-55 is pH dependent, one might anticipate that drug release from the extruded granules is a function of the pH of the dissolution media. Four different media were evaluated in this study: 0.1 N HCl (pH 1.2) and citrate–phosphate buffers (pH 4.5, 5.5, 6.8). Figure 3.9 presents the dissolution profiles.
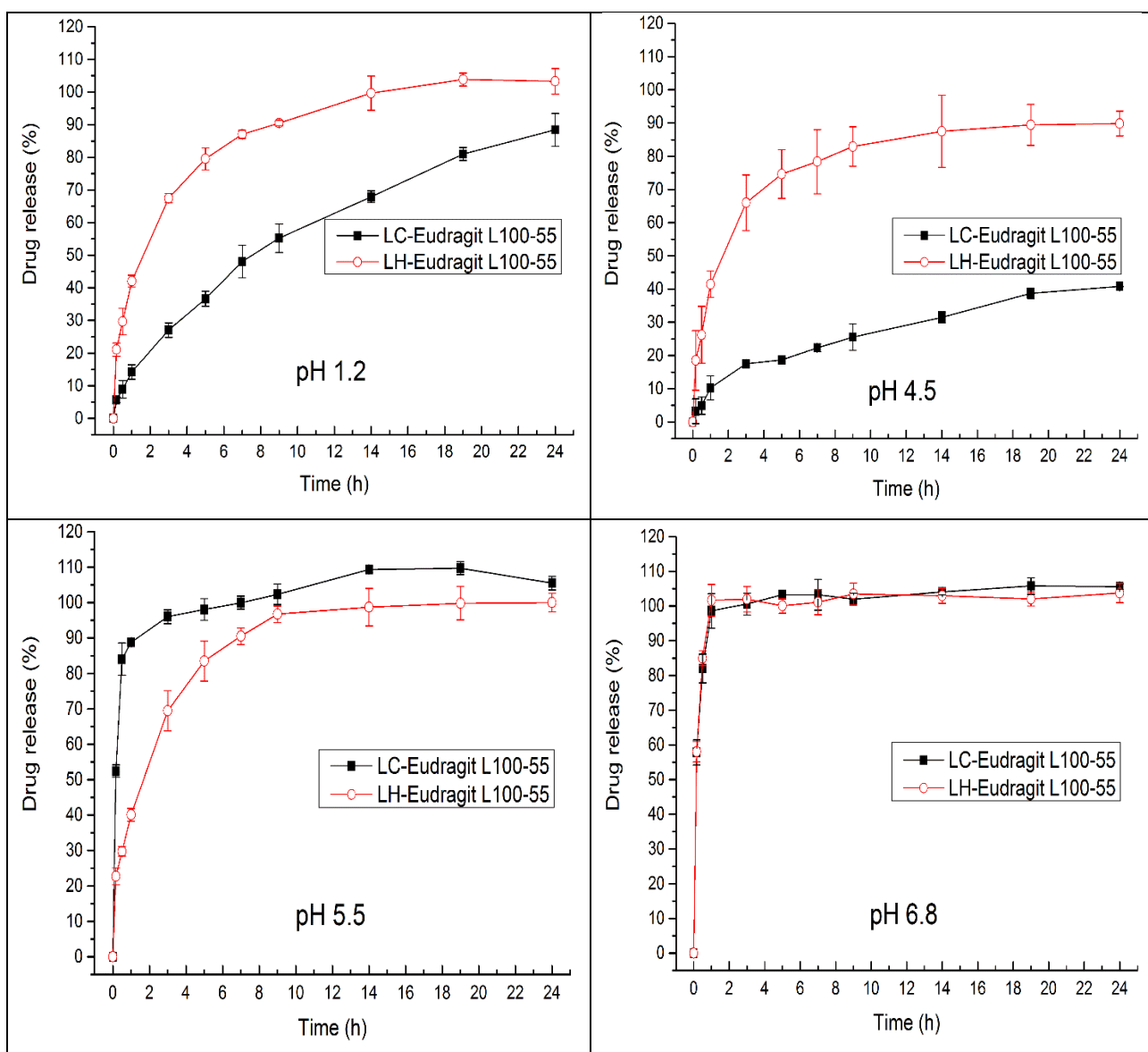
Figure 3.9: Dissolution profiles of 400 mg, 16–18 mesh, melt-extruded lidocaine (LC) and lidocaine HCl (LH) granules (30% drug loading) in 900 mL dissolution media using USP apparatus II at 75 rpm (n = 3). The error bar represents the standard deviation.

Lidocaine HCl–Eudragit L100-55 granules exhibited similar drug release profiles across three different pH: 1.2, 4.5 and 5.5. Drug release was extended over 12 h. The f_2 (similarity factor) value of the dissolution profiles at pH 1.2 and pH 4.5 is 54, and the f_2 of profiles at pH 1.2 and pH 5.5 is 74. Even though Eudragit L100-55 is soluble in aqueous

media at pH 5.5, lidocaine HCl–Eudragit L100-55 matrix remained intact at pH 5.5 for the first 6 h due to the acidic microenvironment pH induced by the solubilized drug.

Drug release from lidocaine–Eudragit L100-55 granules was significantly different from the lidocaine HCl–Eudragit L100-55 granules. The release rate also varied significantly at different pH levels. At pH 1.2, the drug release from the lidocaine–Eudragit L100-55 granules was about half the release from the lidocaine HCl–Eudragit L100-55 granules. At pH 4.5, drug release from the lidocaine–Eudragit L100-55 granules decreased further. At pH 5.5, drug release from the lidocaine–Eudragit L100-55 granules accelerated suddenly and became faster than that of the lidocaine HCl granules.

Compared to lidocaine HCl granules, lidocaine granules are different in several aspects. First, lidocaine as a freebase dissolves more slowly than lidocaine HCl in a given dissolution medium. Second, solubilized lidocaine induces an alkaline microenvironment, as shown in Figure 3.8A. This increase in microenvironmental pH exerts two opposing effects on lidocaine release: On one hand, higher pH can slow down drug release due to the decrease in drug solubility. On the other hand, higher pH can accelerate drug release by inducing greater swelling and solubilization of Eudragit L100-55. When the pH of the dissolution media increased from 1.2 to 4.5, the decrease in lidocaine solubility was predominant. At pH 5.5, the swelling and solubilization of Eudragit L100-55 was predominant. As shown in Figure 3.8B, at pH 5.5, the lidocaine–Eudragit L100-55 matrix swelled to a much greater extent than the lidocaine HCl–Eudragit L100-55 matrix.

The drug release of lidocaine was the slowest at pH 4.5. The reason for this could be that lidocaine and Eudragit L100-55 interact the most strongly at this pH level. Borodkin et al. have studied the effect of pH on the interaction between a polycarboxylic acid ion-exchange resin and eleven basic drugs at equilibrium [1]. They found that, in all cases, the extent of resin–drug interaction reached a maximum at a pH range of 4.5–5.5, although the extent of the interaction varied considerably based on the particular drug being evaluated. The authors conclude that the sharp decrease of the resin–drug interaction below pH 4.5 is caused by the diminishing number of anionic sites on the resin. They also conclude that the

156

decreasing interaction above pH 5.5 could be attributed to a declining affinity of the resin for amine drugs relative to alkali metal cations from the buffer medium. In addition, the increasing portion of drug in unionized form could also contribute to this result. When the pH of the dissolution medium was increased to 6.8, Eudragit L100-55 became soluble and complete drug release was achieved within 1 h for both lidocaine and lidocaine HCl containing extrudates.

Interaction between lidocaine and Eudragit L100-55 in polymer melt during melt extrusion is different from that in solution state during dissolution testing. The ionic interaction between lidocaine and Eudragit L100-55 in solution state is dependent on the ionization state of these two compounds, which is a function of microenvironment pH. Even though there was no ionic interaction between lidocaine HCl and Eudragit L100-55 in melt extruded granules, complexation between lidocaine HCl and Eudragit L100-55 in pH 5.5 buffer media was observed. As shown in Figure 3.10, extruded lidocaine HCl-Eudragit L100-55 granules became a translucent gel at the end of 24 hours. In contrast, lidocaine-Eudragit L100-55 granules completely dissolved at the end of 24 hours. Solution-state interaction between lidocaine and Eudragit L100-55 during dissolution testing needs to be further investigated.
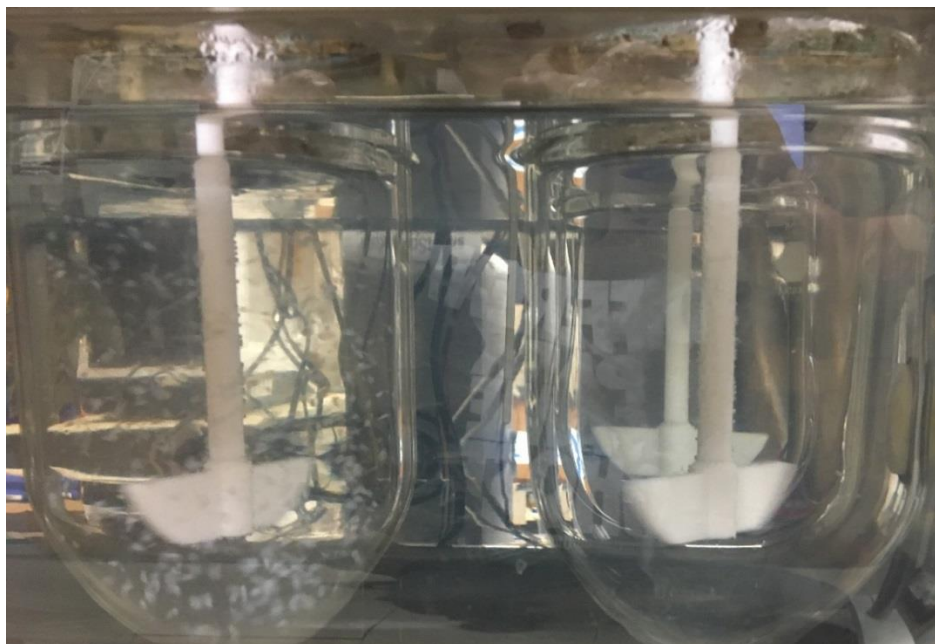
Figure 3.10: Image of dissolution vessel content at 24 hours in pH 5.5 buffer; lidocaine HCl-Eudragit L100-55 extrudate (vessel on the left) and lidocaine-Eudragit L100-55 extrudate (vessel on the right).

In summary, the release of lidocaine from melt-extruded granules in aqueous buffers was a function of the drug form and the pH of the dissolution media. Drug release was also significantly impacted by the microenvironmental pH induced by the solubilized drug. At pH 6.8, no sustained release was achieved for either lidocaine or lidocaine HCl due to the solubilization of Eudragit L100-55. Release of lidocaine HCl over 10 h was consistent across pH 1.2, 4.5, and 5.5; and it was controlled by diffusion mechanisms. For lidocaine, drug release was highly variable across pH 1.2, 4.5, and 5.5. The slowest release was observed at pH 4.5.

3.6 SUMMARY

A polyelectrolyte matrix system for the sustained release of lidocaine was developed through the melt extrusion of either lidocaine freebase or its hydrochloride salt. Our study demonstrates that these two different forms resulted in different drug–polymer

interactions and distinctive release properties. Both lidocaine and lidocaine HCl were uniformly dispersed in molecular state in Eudragit L100-55. However, only lidocaine formed a polyelectrolyte with Eudragit L100-55 via the acid–base ionic interactions between the ternary amine in lidocaine and the methacrylic acid groups in Eudragit L100-55. Because of this ionic interaction, the lidocaine-Eudragit L100-55 extrudate was physically more stable than the LH-Eudragit L100-55 extrudate during storage, despite the lower glass transition temperature of the extrudate and faster crystallization of lidocaine.

The release of the drug from the milled extrudate was a function of the dissolution media pH and the particular form of lidocaine, since both lidocaine and Eudragit L100-55 exhibited pH-dependent solubility. Drug release was also impacted by the microenvironment pH induced by the dissolved drug. Solubilized lidocaine increased the pH, while solubilized lidocaine HCl reduced the pH on the surface of the extrudates. The release of lidocaine HCl in water and in buffers at pH 1.2, 4.5, and 5.5 was consistent (over 10 h) across these four dissolution media. In contrast, the release of lidocaine in water and in buffers at pH 1.2, 4.5, and 5.5 was highly variable, with the slowest release observed at pH 4.5. Since lidocaine formed ionic bonds with Eudragit L100-55 in the extrudate, the release of lidocaine occurred via ion exchange and diffusion. As a result, the release of lidocaine in purified water was accelerated at higher ionic strength. Eudragit L100-55 was soluble at pH 6.8, and both forms were released in 1 h.

Lidocaine HCl–Eudragit L100-55 extrudates maintained a low microenvironment pH and showed pH-independent release profiles in various dissolution media. The drug dissolution rate and release mechanism of lidocaine–Eudragit L100-55 extrudates changed significantly as the dissolution medium or ionic strength varied, which directly correlated with the drug–polymer interaction. Last, the ionic interaction between lidocaine and Eudragit L100-55 also contributed to the improvement of its physical stability. The choice

of drug form should be considered carefully when using melt extrusion to prepare controlled drug delivery systems.

3.7 REFERENCE

1.   Abu-Huwaij, R., Assaf, S., Salem, M., Sallam, A., 2007. Mucoadhesive Dosage form of Lidocaine Hydrochloride: I. Mucoadhesive and Physicochemical Characterization. Drug Development and Industrial Pharmacy 33, 855-864.

2.   Baghel, S., Cathcart, H., O'Reilly, N.J., 2016a. Polymeric Amorphous Solid Dispersions: A Review of Amorphization, Crystallization, Stabilization, Solid-State Characterization, and Aqueous Solubilization of Biopharmaceutical Classification System Class II Drugs. Journal of Pharmaceutical Sciences 105, 2527-2544.

3.   Baghel, S., Cathcart, H., O'Reilly, N.J., 2016b. Theoretical and experimental investigation of drug-polymer interaction and miscibility and its impact on drug supersaturation in aqueous medium. European Journal of Pharmaceutics and Biopharmaceutics 107, 16-31.

4.   Baird, J.A., Van Eerdenbrugh, B., Taylor, L.S., 2010. A classification system to assess the crystallization tendency of organic molecules from undercooled melts. J Pharm Sci 99, 3787-3806.

5.   Borodkin, S., Yunker, M.H., 1970. Interaction of amine drugs with a polycarboxylic acid ion-exchange resin. Journal of Pharmaceutical Sciences 59, 481-486.

6.   Bouvier, J.-M., Campanella, O.H., 2014. The Generic Extrusion Process II, Extrusion Processing Technology. John Wiley & Sons, Ltd, pp. 173-242.

7.   Chen, X., Wen, H., Park, K., 2010. Challenges and New Technologies of Oral Controlled Release, Oral Controlled Release Formulation Design and Drug Delivery. John Wiley & Sons, Inc., pp. 257-277.

8.   Cheow, W.S., Hadinoto, K., 2012. Green Amorphous Nanoplex as a New Supersaturating Drug Delivery System. Langmuir : the ACS journal of surfaces and colloids 28, 6265-6275.

9.   Crawford, D.E., Miskimmin, C.K.G., Albadarin, A.B., Walker, G., James, S.L., 2017. Organic synthesis by Twin Screw Extrusion (TSE): continuous, scalable and solvent-free. Green Chemistry 19, 1507-1518.

10.   Crowley, M.M., Zhang, F., Repka, M.A., Thumma, S., Upadhye, S.B., Battu, S.K., McGinity, J.W., Martin, C., 2007. Pharmaceutical applications of hot-melt extrusion: part I. Drug Dev Ind Pharm 33, 909-926.

11.   Cui, Y., Frank, S.G., 2005. Characterization of supersaturated lidocaine/polyacrylate pressure sensitive adhesive systems: Thermal analysis and FT-IR. Journal of Pharmaceutical Sciences 95, 701-713.

12.   De Robertis, S., Bonferoni, M.C., Elviri, L., Sandri, G., Caramella, C., Bettini, R., 2015. Advances in oral controlled drug delivery: the role of drug–polymer and interpolymer non-covalent interactions. Expert Opinion on Drug Delivery 12, 441-453.

13.   Ferrero, C., Muñoz-Ruiz, A., Jiménez-Castellanos, M.R., 2000. Fronts movement as a useful tool for hydrophilic matrix release mechanism elucidation. International Journal of Pharmaceutics 202, 21-28.

14. Higuchi, T., 1961. Rate of release of medicaments from ointment bases containing drugs in suspension. Journal of pharmaceutical sciences 50, 874-875.

15. Janssens, S., Van den Mooter, G., 2009. Review: physical chemistry of solid dispersions. Journal of Pharmacy and Pharmacology 61, 1571-1586.

16. Jenquin, M.R., McGinity, J.W., 1994. Characterization of acrylic resin matrix films and mechanisms of drug-polymer interactions. International Journal of Pharmaceutics 101, 23-34.

17. Jimenez-Kairuz, A., Allemandi, D., Manzo, R., 2004. The improvement of aqueous chemical stability of a model basic drug by ion pairing with acid groups of polyelectrolytes. International journal of pharmaceutics 269, 149-156.

18. Jimenez-Kairuz, A.F., Llabot, J.M., Allemandi, D.A., Manzo, R.H., 2005. Swellable drug-polyelectrolyte matrices (SDPM). Characterization and delivery properties. Int J Pharm 288, 87-99.

19. Jimenez-Kairuz, A., Allemandi, D., Manzo, R.H., 2002. Mechanism of lidocaine release from carbomer–lidocaine hydrogels. Journal of pharmaceutical sciences 91, 267-272.

20. Kindermann, C., Matthée, K., Sievert, F., Breitkreutz, J., 2012. Electrolyte-Stimulated Biphasic Dissolution Profile and Stability Enhancement for Tablets Containing Drug-Polyelectrolyte Complexes. Pharmaceutical Research 29, 2710-2721.

21. Kindermann, C., Matthée, K., Strohmeyer, J., Sievert, F., Breitkreutz, J., 2011. Tailor-made release triggering from hot-melt extruded complexes of basic polyelectrolyte

and poorly water-soluble drugs. European Journal of Pharmaceutics and Biopharmaceutics 79, 372-381.

22.   Lankalapalli, S., Kolapalli, V.R.M., 2009. Polyelectrolyte Complexes: A Review of their Applicability in Drug Delivery Technology. Indian Journal of Pharmaceutical Sciences 71, 481-487.

23.   Lee, H.L., Vasoya, J.M., Cirqueira, M.d.L., Yeh, K.L., Lee, T., Serajuddin, A.T.M., 2017. Continuous Preparation of 1:1 Haloperidol–Maleic Acid Salt by a Novel Solvent-Free Method Using a Twin Screw Melt Extruder. Molecular Pharmaceutics 14, 1278-1291.

24.   Lin-Vien, D., Colthup, N.B., Fateley, W.G., Grasselli, J.G., 1991. The handbook of infrared and Raman characteristic frequencies of organic molecules. Elsevier.

25.   Liu, X., Lu, M., Guo, Z., Huang, L., Feng, X., Wu, C., 2012. Improving the chemical stability of amorphous solid dispersion with cocrystal technique by hot melt extrusion. Pharm Res 29, 806-817.

26.   Liu, X., Zhou, L., Zhang, F., 2017. Reactive Melt Extrusion to Improve the Dissolution Performance and Physical Stability of Naproxen Amorphous Solid Dispersions. Molecular Pharmaceutics.

27.   Luo, Y., Wang, Q., 2014. Recent development of chitosan-based polyelectrolyte complexes with natural polysaccharides for drug delivery. International Journal of Biological Macromolecules 64, 353-367.

28.   Maniruzzaman, M., Boateng, J.S., Chowdhry, B.Z., Snowden, M.J., Douroumis, D., 2014. A review on the taste masking of bitter APIs: hot-melt extrusion (HME) evaluation. Drug Development and Industrial Pharmacy 40, 145-156.

29.   Maniruzzaman, M., Morgan, D.J., Mendham, A.P., Pang, J., Snowden, M.J., Douroumis, D., 2013. Drug–polymer intermolecular interactions in hot-melt extruded solid dispersions. International Journal of Pharmaceutics 443, 199-208.

30.   Maniruzzaman, M., Snowden, M.J., Bradely, M.S., Douroumis, D., 2015. Studies of intermolecular interactions in solid dispersions using advanced surface chemical analysis. RSC Advances 5, 74212-74219.

31.   Medina, C., Daurio, D., Nagapudi, K., Alvarez-Nunez, F., 2010. Manufacture of pharmaceutical co-crystals using twin screw extrusion: A solvent-less and scalable process. Journal of Pharmaceutical Sciences 99, 1693-1696.

32.   Meka, V.S., Singe, M.K.G., Pichika, M.R., Nali, S.R., Kolapaili, V.R.M., Kesharwani, P., 2017. A comprehensive review on polyelectrolyte complexes. Drug Discovery Today 22, 1697-1706.

33.   Ming, L., Zhefei, G., Yongcheng, L., Huishi, P., Ling, L., Xu, L., Xin, P., Chuanbin, W., 2014. Application of Hot Melt Extrusion for Poorly Water-Soluble Drugs: Limitations, Advances and Future Prospects. Current Pharmaceutical Design 20, 369-387.

34.   Moore, J.W., Flanner, H.H., 1996. Mathematical comparison of dissolution profiles. Pharm. Tech. 20, 64-74.

35.   Müller, M., 2014. Polyelectrolyte Complexes in the Dispersed and Solid State. Springer.

36.   Nie, H., Su, Y., Zhang, M., Song, Y., Leone, A., Taylor, L.S., Marsac, P.J., Li, T., Byrn, S.R., 2016. Solid-State Spectroscopic Investigation of Molecular Interactions

between Clofazimine and Hypromellose Phthalate in Amorphous Solid Dispersions. Molecular Pharmaceutics 13, 3964-3975.

37.   Pavli, M., Baumgartner, S., Kos, P., Kogej, K., 2011. Doxazosin–carrageenan interactions: A novel approach for studying drug–polymer interactions and relation to controlled drug release. International Journal of Pharmaceutics 421, 110-119.

38.   Pudipeddi, M., Zannou, E.A., Vasanthavada, M., Dontabhaktuni, A., Royce, A.E., Joshi, Y.M., Serajuddin, A.T., 2008. Measurement of surface pH of pharmaceutical solids: a critical evaluation of indicator dye-sorption method and its comparison with slurry pH method. J Pharm Sci 97, 1831-1842.

39.   Rumondor, A.C.F., Ivanisevic, I., Bates, S., Alonzo, D.E., Taylor, L.S., 2009. Evaluation of Drug-Polymer Miscibility in Amorphous Solid Dispersion Systems. Pharmaceutical Research 26, 2523-2534.

40.   Shimada, Y., Goto, S., Uchiro, H., Hirabayashi, H., Yamaguchi, K., Hirota, K., Terada, H., 2013a. Features of heat-induced amorphous complex between indomethacin and lidocaine. Colloids and Surfaces B: Biointerfaces 102, 590-596.

41.   Shimada, Y., Goto, S., Uchiro, H., Hirota, K., Terada, H., 2013b. Characteristics of amorphous complex formed between indomethacin and lidocaine hydrochloride. Colloids and Surfaces B: Biointerfaces 105, 98-105.

42.   Siyawamwaya, M., Choonara, Y.E., Bijukumar, D., Kumar, P., Du Toit, L.C., Pillay, V., 2015. A Review: Overview of Novel Polyelectrolyte Complexes as Prospective Drug Bioavailability Enhancers. International Journal of Polymeric Materials and Polymeric Biomaterials 64, 955-968.

43.   Song, Y., Zemlyanov, D., Chen, X., Nie, H., Su, Z., Fang, K., Yang, X., Smith, D., Byrn, S., Lubach, J.W., 2016. Acid-Base Interactions of Polystyrene Sulfonic Acid in Amorphous Solid Dispersions Using a Combined UV/FTIR/XPS/ssNMR Study. Mol Pharm 13, 483-492.

44.   Takka, S., 2003. Propranolol hydrochloride–anionic polymer binding interaction. Il Farmaco 58, 1051-1056.

45.   Telang, C., Mujumdar, S., Mathew, M., 2009. Improved physical stability of amorphous state through acid base interactions. Journal of Pharmaceutical Sciences 98, 2149-2159.

46.   Thompson, C., Ibie, C., 2011. The oral delivery of proteins using interpolymer polyelectrolyte complexes. Ther Deliv 2, 1611-1631.

47.   Wulff, R., Leopold, C.S., 2016. Coatings of Eudragit® RL and L-55 Blends: Investigations on the Drug Release Mechanism. AAPS PharmSciTech 17, 493-503.

48. Xanthos, M., 1992. Reactive extrusion: principles and practice. Hanser Publishers(Germany), 1992, 304.

Chapter 4: A Clay-Polymer Nanocomposites Prepared by Reactive Melt Extrusion for Sustained Drug Release [4]

4.1 ABSTRACT

Clay-polymer nanocomposites have exhibited a great potential as carriers for controlled release drug delivery. This study aims to prepare exfoliated montmorillonite-Eudragit RS nanocomposites using reactive melt extrusion and investigate the influence of claying loading, clay types (sodium montmorillonite (Cloisite Na) vs. organomodified montmorillonite (Cloisite 20)) on clay-polymer interactions and drug release properties. The clays were used as the filler material at various levels in Eudragit RS and theophylline was used as the active pharmaceutical ingredient. The resulting structure of nanocomposites structure was characterized using TEM and XRPD. The hygroscopicity of the nanocomposites was investigated using DVS. The effect of the interfacial interaction between the polymer and clay sheet, the clay loading as well as the clay type on the drug release behavior were further studied by dissolution testing. TEM and XRPD data show that when the clay content is increased from 5% to 15% by weight, the nanocomposites structure switches from a fully exfoliated state to intercalated structures or partial exfoliation with stacked clay layers. FT-IR and ssNMR results suggest that Cloisite Na and Cloisite 20 layers exhibit different interaction strengths with polymer networks, by creating compacted complex structures. The addition of nanoclay in the formulation could robustly adjust drug release profiles and the clay concentration and the type are important factors that affect the crossing-linking density of the nanocomposites, by adjusting in the drug release properties. This study indicates that the clay-Eudragit RS nanocomposites provide

---

an improved oral controlled drug delivery system that minimize the drug dosing frequency, potentially leading to improved patient compliance.

4.2 INTRODUCTION

Oral controlled drug delivery systems are a recognized protocol to prepare materials that can effectively encapsulate drug molecules and release them at the target site for a defined period of time and in a controlled manner. In addition to improving the drug efficacy, specificity, therapeutic index and tolerability of corresponding drugs, oral controlled drug delivery systems can also reduce the patient expenses as well as the risks of toxicity[1, 2]. Because of their multiple and unique advantages, oral controlled drug delivery systems have attracted intense interest from pharmaceutical scientists and formulators for over four decades. Meanwhile, innovative controlled release formulations have remarkably driven the oral drug delivery market to soar in recent years[3, 4]. The incorporation of active pharmaceutical ingredient (API) or biological molecules into the biodegradable polymers for controlled release application has increased dramatically[5].

Hot-melt extrusion (HME) of biodegradable polymers with API, for controlling or modifying the drug release has received increased attention in pharmaceutical literature in recent years[6, 7]. Compared with traditional processing techniques, the advantages of HME include solvent-free of processing, continuous processing with high efficiency, and ease in scaling up[8]. During the HME process, drug, polymer and other excipients are first fed into the barrel at different temperature settings. The rotating screws then mix and melt the materials using heat and intense mechanical shearing force to achieve the molecular level mixing and excellent homogeneity. Because of the high temperature, dispersive and distributive mixing in twin screw extrusion cause suspended drug particles to de-aggregate in the polymer melt, resulting in a more uniform distribution of fine particles. This makes

HME a favorable process for the solid-state chemical reaction. Reactive melt extrusion (RME) has historically referred to combining chemical reactions and polymer melt extrusion into a single process carried out continuously in a screw extruder[9]. RME has been widely applied in the plastic and food industries to improve the properties of material and products, such as polymer chemical modification and food digestibility[10, 11]. Recently, RME have been introduced in pharmaceutical area to prepare cocrystal[12], coamorphous[13], salt[14], and polyelectrolytes complex[15] to improve the oral bioavailability of poorly water soluble drugs. Although there is an increasing number of HME studies in pharmaceutics, the study of RME for sustained release delivery remains limited. In this study, we utilize RME to prepare clay-polymer nanocomposites for sustained drug release.

Nanocomposites based on polymer and clay are attractive materials for development of controlled drug delivery systems due to their advantageous properties such as (1) high drug encapsulation efficiency, (2) enhanced stability of API against pH variation and enzyme action, (3) low burst release of drug, and (4) a controlled and targeted drug release profile[16-18]. In general, nanocomposites are dispersions of two or more components at the nanometric scale with optimized properties compared to the pure materials, which can be obtained by dispersing clay layers or sheets into a polymeric matrix[19, 20]. Clay-polymer nanocomposites can be prepared by various processes, such as melt blending, solution blending, *in-situ* polymerization, and mechano-chemical processing[21, 22]. The intercalation of layered structures with polymers can be performed by noncovalent bonding involving a cation- or anion-exchange reaction[23]. Through the interaction between clay and polymer, nanocomposites provide different characteristics from the parent components, including barrier effects, swelling index, mucoadhesion ability, mechanical and thermal stability. The barrier properties of the polymer-based

169

nanocomposites play a pivotal role in determining dissolution rate, drug uptake, drug release profile, and release mechanism[24]. The presence of clays in the polymer matrix affects the barrier properties by acting as release retardants for drugs and carriers, thereby promoting stable, controlled drug release in the dissolution media, increasing the solubility of the API, and conferring improved mechanical and thermal properties to the nanocomposites[25, 26]. All of these properties are strongly influenced by the surface area and ion exchange capacity of the clay, the type of interactions between clay and polymer and the clay-polymer ratio[27].

There are several different types of clays used in the drug delivery systems, such as kaolin, montmorillonite, saponite, laponite, halloysite and so on[16, 28]. Montmorillonite (MMT) has become prominent among other clays because of its abundance, environment friendliness, and well -studied chemistry. MMT is a natural material with high internal surface area, high cation exchange capacity (CEC), high adsorption and swelling ability, low or null toxicity, good biocompatibility and, furthermore, it is a material "generally recognized as safe" (GRAS) by the FDA[18, 29, 30]. MMT is a layered hydrated aluminum silicate which belongs to the smectite group of phyllosilicates. The layer thickness of each platelet is in the order of 1nm and the lateral dimension is approximately 200 nm. Cloisite Na is a natural MMT without any modification and Cloisite 20 is an organic modified MMT with quaternary ammonium salts. Because of the presence of long alkyl chains, the interlayer spacing of MMT is enhanced, resulting in hydrophobic MMT. MMT has the empirical formula $Al_2O_3 \cdot 4SiO_2 \cdot H_2O$, and due to the substitution of some Al^{3+} with Mg^{2+}, it carries an overall negative charge on its hydrophilic platelet surface. Because of its permanent negative charge, MMT has been used to prepare nanocomposites by electrostatic interactions with cationic polymers such as chitosan and gelatin [29, 31]. In this study, layered silicate nanocomposites have been prepared by melt intercalation.

170

There is many study focus on the application of nanocomposites as a drug delivery system[32, 33]. However, there are few paper focusing on the influence of the clay-polymer interaction on the drug release profiles[34]. No study has compared the effect of Cloisite Na and Cloisite 20 on the resulting Cloisite/Eudragit RS nanocomposites so far. There are also few reports on their structural confinement properties and on the mechanisms that underlie their polymer interactions. Bee et al have investigated the effect of Cloisite Na and Cloisite 20 on the morphology, mechanical and thermal properties of the resulting poly (methyl methacrylate) (PMMA) nanocomposites prepared using a Brabender mixer[35]. They found that Cloisite 20 shows better compatibility with PMMA compared with Cloisite Na. It was found that Cloisite 20 formed nanocomposites with PMMA, while Cloisite Na only formed microcomposites. The results show that the properties of the Cloisite 20 nanocomposites surpassed the neat PMMA and PMMA/Cloisite Na microcomposites, which is attributed to the formation of more favorable polymer-filler interaction. However, the author overlooked the influence of the composites structure on the polymer-filler interaction since insufficient mixing process might limit the polymer-filler interaction. Considering the importance of the water permeation and the different surface properties of Cloisite Na and Cloisite 20, our hypothesis in this study was that the dispersion of Cloisite nanoplatelets into the Eudragit RS matrix might easily control the water uptake and the drug release rate and the difference of the interactions between polymers and pristine clay or organically modified clay and polymers would impact the drug release behaviors.

In this study, Cloisite Na and Cloisite 20 were selected as model clays. The chemical formula of Cloisite Na is $Al_2O_3 \cdot 4SiO_2 \cdot H_2O$, the basal spacing is 1.2 nm and its cation exchange capacity has been reported to be approximately 92 meq/100g [30]. Cloisite 20 is prepared from Cloisite Na with hydrogenated tallow (HT, ~ 65% C18; ~ 30% C16;

and ~ 5% C14) and the modifier concentration is 95 meq/100g and the basal spacing is 2.4 nm. Eudragit RS, a cationic copolymer of ethyl acrylate, methyl methacrylate, and a low content of methacrylic acid ester with quaternary ammonium groups, was selected as the polymer carrier. Figure 4.1 presents the chemical structures and critical attributes of the drug and excipients used in this study. The objective of this study was to compare the difference of the interfacial interactions between polymers and pristine clay and organically modified clay in sustained release hydrophobic matrices prepared by hot melt extrusion, and to investigate the influence of the clay-polymer interactions on the physicochemical properties of the extrudates. The nanocomposite structure and possible interaction between clays and polymer were investigated by DSC, XRPD, TEM, FT-IR, ssNMR and DVS. Dissolution testing was performed in pH 6.8 phosphate buffer dissolution medium to investigate the influence of the clay loading, clay type and polymer-clay interaction on permeability and drug release properties.
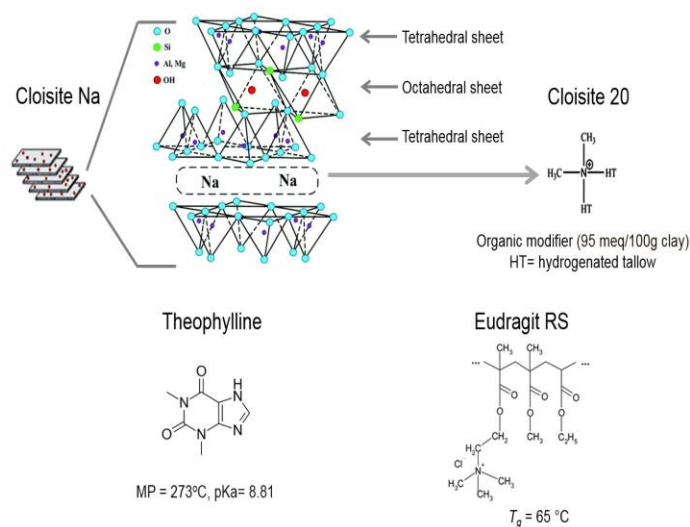
Figure 4.1: Chemical structures and critical properties of Cloisite Na, Cloisite 20, theophylline and Eudragit RS.

4.3 MATERIALS

Cloisite Na and Cloisite 20 were donated by Southern Clay Products, Inc (Gonzales, TX). Eudragit® RS was donated by Evonik Industries (Darmstadt, Germany). Anhydrous theophylline USP was purchased from Acros Organics (Pittsburgh, PA). Sodium phosphate monobasic and sodium phosphate dibasic were purchased from Fisher Scientific (Waltham, MA). All other reagents and solvents were analysis grade or better.
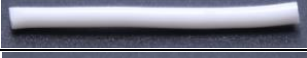
4.4 METHODS

4.4.1 Preparation of Nanocomposites

Clay-polymer nanocomposites were prepared using a Leistritz Nano 16 extruder (Leistritz Corporation, Allendale, NJ). The composition of the various powder blends is summarized in Table 4.1. A Turbula® Shaker-Mixer (Glen Mills, Clifton, NJ) was used to prepare powder blends for extrusion. A twin-screw volumetric feeder (Brabender Technologie, Ontario, Canada) was used to feed the powder blends at a rate of 300 g/hr. The screw profile is shown in Figure 4.2. The screw speed was set at 100 rpm and the barrel temperature was at 160 °C.

Preparation of theophylline granules was performed in two steps. In the first step, clay and polymer nanocomposites were prepared. In the second step, blends of the milled nanocomposites and theophylline (20% loading) were extruded to incorporate the drug. Milling of extrudates was carried out using a Comill (QUADRO, Ontario, Canada). The milled extrudates were stored in a desiccated chamber at room temperature for further analysis.

Table 4.1: Composition, extrusion torque, and images of extrudates.

Extrusion time	Formula #	Clay		Polymer	Drug	Average Torque (G.m)	Extrudates Images
		Cloisite Na	Cloisite 20	Eudragit RS	Theophylline		
1st extrusion to prepare clay-polymer nanocomposites	1	-	-	100%	-	883	
	2	5%	-	95%		841	
	3	-	5%	95%		751	
	4	10%	-	90%		984	
	5	-	10%	90%		761	
	6	15%	-	85%		1156	
	7	-	15%	85%		887	
2nd extrusion to incorporate theophylline	1-1	-	-	80%	20%	477	
	2-1	4%	-	76%		781	
	3-1	-	4%	76%		663	
	4-1	8%	-	72%		1202	
	5-1	-	8%	72%		734	
	6-1	12%	-	68%		1436	
	7-1	-	12%	68%		873	

Screw speed: 100 rpm; feed rate: 300 g/h.

174
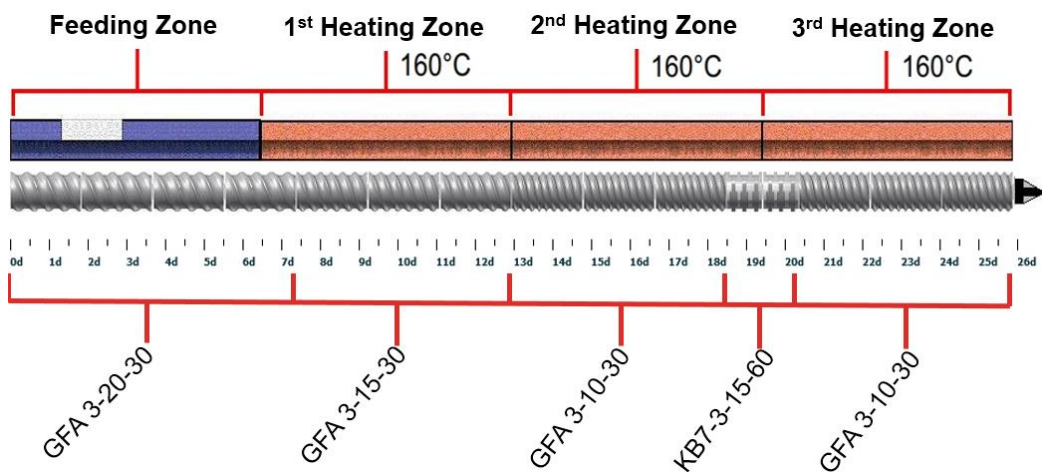
Figure 4.2: Screw configuration and barrel temperature for reactive melt extrusion of theophylline granules.

Data in the screw code (GFA X-XX-XX) represent the trilobal screw, pitch length (mm) and screw length (mm), respectively. Data in the screw code (KB X-X-XX-XX) indicate the number of kneading segments, trilobal screw, screw length (mm) and the angle (°).

4.4.2 Transmission Electron Microscopy (TEM) and Scanning Electronic Microscopy (SEM)

Dispersions of Cloisite Na and Cloisite 20 in Eudragit RS were examined using a high-resolution FEI Tecnai TEM (ThermoFisher Scientific, Hillsboro, OR) with an acceleration voltage of 100 kV. The exposure time varied from 0 to 100 seconds. Ultrathin sections of nanocomposites were prepared with a Leica Ultracut UC7 ultramicrotome (Leica Microsystems Inc., Buffalo Grove, IL) equipped with a diamond knife. All samples were placed on 200 mesh copper grids before loading into the instrument. The surface morphology of the theophylline granules following dissolution testing was examined using Zeiss Supra40 SEM (Carl Zeiss, Thornwood, NY). All samples were tested with 5 kV accelerating voltage and 30 µm aperture coated with 15 nm Pt.

4.4.3 Differential Scanning Calorimetry (DSC)

DSC analysis was performed using a Model Q-2000 DSC (TA Instruments, Newcastle, DE) equipped with the RCS 90 (TA Instrument, Newcastle, DE) refrigerated cooling system accessory under a dry nitrogen purge (50 mL/min). Calibration was performed with an indium

175

standard and an empty TA aluminum pan was used as the reference. Samples were accurately weighed (3-5 mg) in aluminum pans and crimped with aluminum lids. Samples were heated from 20 to 350 °C at a heating rate of 10 °C/min. The DSC data were analyzed using the TA Universal Analysis 2000 software (TA Instrument, Newcastle, DE).

4.4.4 X-Ray Powder Diffraction (XRPD)

XRPD analysis was performed using a Rigaku MiniFlex 600 X-ray diffractometer (Rigaku Corporation, Japan) equipped with a copper X-ray tube (wavelength $\lambda = 0.154$ nm). Milled samples were placed on a silicon sample holder and the measurement was conducted with an acceleration voltage of 40 kV, and a current of 15 mA, 2-theta angles between 5° and 45° with a scan speed of 1°/min, and a step size of 0.02°. The results were analyzed with the MDI Jade 8.5 software (Material Data, Inc., Livermore, CA) and plotted with OriginLab version 9.0 software (OriginLab Corporation, Northampton, MA). The thickness of the silicate layer was calculated using Bragg's equation:

$$n\lambda = 2d \sin \theta$$

Where n is order reflection; λ is the X-ray wavelength (1.54 A); θ is the angle of the basal spacing peak of clay; and d is the thickness of the clay silicate layer.

4.4.5 Fourier Transform Infrared Spectroscopy (FT-IR)

Molecular interactions between clay and polymer were examined with FT-IR. The measurements were performed using a Thermo Nicolet iS50 spectrometer (Waltham, MA). Samples were placed on a germanium crystal surface. A constant torque was applied using the built-in pressure tower to achieve uniform contact between the sample and the crystal. All samples were analyzed at ambient room temperature with a total of 32 scans at a 4 cm^{-1} resolution from 600 cm^{-1} to 4000 cm^{-1}. The peak positions were determined using the OMNIC software peak picking function (ThermoFisher Scientific, Waltham, MA).

4.4.6 Solid-state NMR (ssNMR)

All ssNMR experiments were performed on a triple-channel 400 MHz Bruker AVANCE III spectrometer (Bruker BioSpin, Billerica, MA) in the Biopharmaceutical NMR Lab (BNL) at Pharmaceutical Sciences, MRL (Merck & Co., Inc. West Point, PA). One-dimensional (1D) 13C spectra were obtained at magic angle spinning (MAS) of 12 kHz with a Bruker 4 mm HFX MAS probe in double-resonance mode tuned to 1H and 13C-nucleus frequencies. 13C spectra were referenced to the tetramethylsilane (TMS). All spectra were acquired at 298 K and processed in Bruker Topspin software (Bruker Corporation, Billerica, MA). 1D 13C cross-polarization (CP) transfers were performed with a radio-frequency (RF) strength of 80–100 kHz during a 2 ms contact time. The power level was ramped linearly over a depth of 15-20 kHz on the 1H channel to enhance CP efficiency. 1H heteronuclear decoupling for 13C was performed at a RF strength of 100 kHz using the SPINAL-64 pulse sequence. 1H spin-lattice relaxation times in the laboratory frame (T1) were determined by 13C-detected saturation recovery experiments [36].

4.4.7 Dynamic Vapor Sorption (DVS)

The water sorption-desorption isotherms of the clay dispersion were determined using a TA VTI-SA+DVS analyzer (TA Instruments, Newcastle, DE). Two relative humidity cycles were performed for each sample at 25 °C and water was used as the testing medium. In each cycle, relative humidity was raised in 5 steps, 15% ramp per step, from 0% to 75% and then back to 0%. A rate of change in mass per time unit (dm/dt) of 0.001%/min was set as the equilibration parameter. At each stage, DVS held the set parameters for 30 mins once dm/dt reached 0.001%/min. The DVS water sorption limits were calculated by averaging the mass difference between 75% relative humidity and 0% relative humidity of each cycle.

4.4.8 Dissolution Testing

Dissolution testing of 30-35 mesh theophylline granules was carried out in 900 mL of phosphate buffer with a pH of 6.8 at 37 °C ± 0.5 °C using the USP Type II apparatus (Varian VK7025, Agilent Technology Inc., Santa Clara, CA) at a paddle speed of 75 RPM. 500 mg

theophylline granules were introduced into each dissolution vessel. Three milliliter dissolution samples were withdrawn at specific time points (0.5, 1, 2, 4, 6, 9, 12, and 24 h) using an autosamplers (Varian VK7025, Agilent Technology Inc., Santa Clara, CA) without sample replacement. The samples were filtered through Vankel Full Flow 10 µm filters. The drug concentration was measured with a UV-Vis spectrophotometer at 245 nm (Infinite M200, Tecan Group Ltd., Mannedorf, Switzerland). All samples were tested in triplicate.

4.5 RESULTS AND DISCUSSION

4.5.1 Preparation of Cloisite-Eudragit RS Nanocomposites and Theophylline Granules

Four methods commonly used to prepare clay-polymer nanocomposites are in situ template synthesis, solution intercalation, in situ intercalative polymerization, and melt intercalation. In this study, melt intercalation was applied to prepare clay-Eudragit RS nanocomposites. Melt intercalation was carried out using an intermeshing corotating twin-screw extruder. Twin-screw extrusion is solvent free, efficient, and easy to scale up. Cloisite-Eudragit RS nanocomposites were initially prepared using melt extrusion. Powder blends of the milled nanocomposites and theophylline were then extruded to prepare theophylline granules. The composition, extrusion torque, and extrudate images are listed in Table 4.1. The advantage of nanocomposites is that the relatively small amount of clay loading (1%-20% by weight) would results in the best combination of property improvements to the hybrid materials [37]. Due to the torque limitation of the twin-screw extruder in this study, the maximum clay loading was set at 15%. At a given clay loading, Cloisite Na-containing formulations demonstrated higher extrusion torque than Cloisite 20-containing formulations, indicating stronger Cloisite Na-Eudragit RS interactions.

As shown in Table 4.1, transparent Eudragit RS extrudate became translucent with the incorporation of Cloisite. Theophylline granules were opaque, indicating that the drug was not fully solubilized in the extrudates. Both the dispersion of Cloisite in Eudragit RS and crystallinity of theophylline were thoroughly characterized, and the results are presented in later sections.

178

4.5.2 Characterization of Cloisite-Eudragit RS Nanocomposites

4.5.2.1 The Nanocomposites Structure

Physical properties such as permeability and mechanical strength are defined by the morphology of the clay-polymer nanocomposite. The preparation of nanocomposites requires uniform dispersion of the layered silicate in the polymer matrix at the nanometer scale. Based on the physical state of the clay layers and their morphology, clay-polymer nanocomposites can be categorized into three types: aggregated, intercalated, and exfoliated [38]. In the aggregated structure, the clay tactoids are well distributed in the polymer matrix, but the single clay layers are not delaminated. In the intercalated structure, the clay tactoids are delaminated to some extent and the polymer chains diffuse into the galleries between them. In the exfolicated structure, the clay tactoids are completely broken apart into single layered platelets, which are homogeneously dispersed in the polymer matrix. When aggregation of the clay platelets occurs due to intercalation without complete exfolication, then the tortuous path is correspondingly reduced. As a result, the exfoliated structure is the most desirable state as it can provide excellent barrier and mechanical properties at low clay contents [21, 26]. In general, the goal of compounding clay-polymer nanocomposites is to achieve complete exfoliation of the layered silicate in a polymer matrix. During reactive melt extrusion, delamination and dispersion of the clay particles occur in two steps: (1) the clay particles shear apart and the polymer chains intercalate to clay galleries; and (2) polymer chains enter the galleries of the clay and push platelets apart, which eventually allows the platelets to peel off the intercalated clay stack[38].

The structure of Cloisite Na-Eudragit RS nanocomposites was investigated using XRPD and TEM techniques. As shown in Figure 4.3A, the major diffraction peak of Cloisite Na at 7.73° (Figure 4.3A-a), corresponding to a mean interlayer spacing of 11.8 nm, was present in the diffraction pattern (Figure 4.3A-b) of the Cloisite Na-Eudragit RS physical mixture. At 5% and 10% Cloisite Na loadings, the peak at 7.73° was absent in the XRPD patterns of the nanocomposites (Figure 3A-d, e and f), indicating complete exfoliation of nanoclay platelets in the

polymer matrix. At 15% Cloisite Na loading, a new broad peak at 3.11° implied the formation of an ordered intercalated nanocomposite. The decrease in 2θ angle reflects the enlarged d-spacing of clay platelets and increased gallery gap due to the intercalation of Eudragit RS.

A similar pattern was also observed with Cloisite 20-Eudragit RS nanocomposites. Cloisite 20 exhibited a diffraction peak at 2.80°, corresponding to a d-spacing of 2.42 nm (Figure 4.3B). Positioning of the diffraction peak at such a low 2θ angle is due to the intercalation by the tallow surfactants. At 5% and 10% clay loading, Cloisite 20 was fully exfoliated in the polymer matrix. At 15% clay loading, a broad peak at 2θ of 2.38° corresponding to a gallery gap of 2.42 nm was observed, due to the intercalation of the polymer chain.
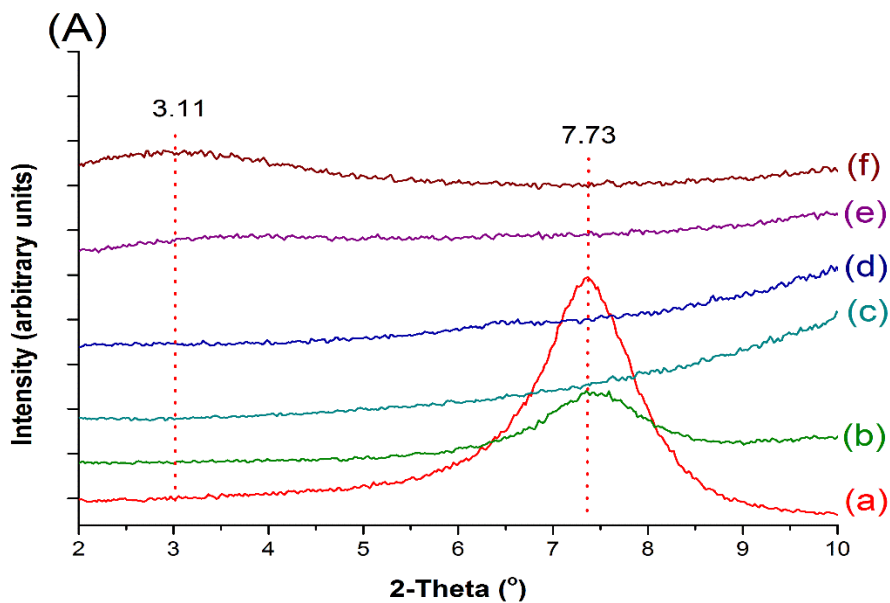
Figure 4.3: continued in next page.
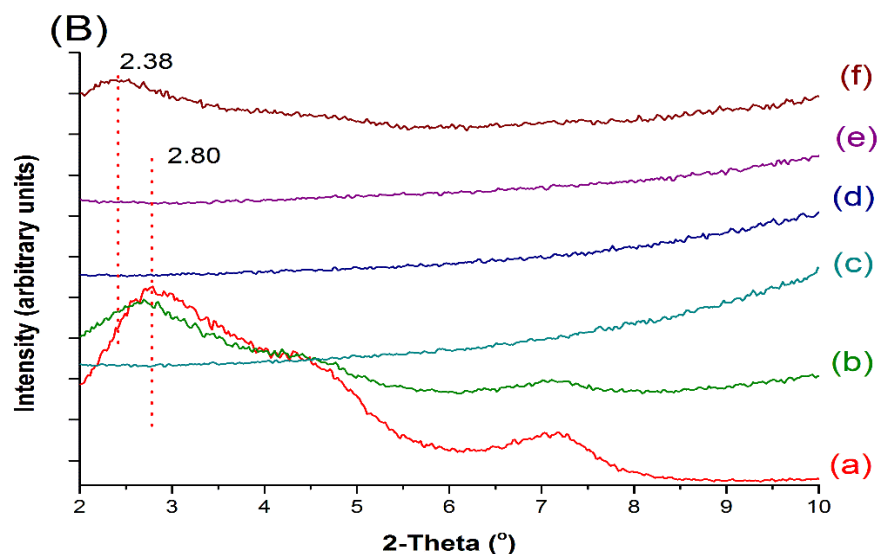
Figure 4.3: XRPD patterns of Cloisite, Eudragit RS, and their extruded nanocomposites. Part A: (a) Cloisite Na; (b) 5% Cloisite Na-95% Eudragit RS physical mixture; (c) Eudragit RS; (d) nanocomposite containing 5% Cloisite Na; (e) nanocomposite containing 10% Cloisite Na; (f) nanocomposite containing 15% Cloisite Na. Part B: (a) Cloisite 20; (b) 5% Cloisite 20-95% Eudragit RS physical mixture; (c) Eudragit RS; (d) nanocomposite containing 5% Cloisite Na; (e) nanocomposite containing 10% Cloisite Na; (f) nanocomposite containing 15% Cloisite Na.

TEM results agreed well with XRPD results. Dark lines or areas in the TEM images represent clay, and the off-white phase was Eudragit RS (Figure 4.4). The TEM images of Cloisite-Eudragit RS showed the exfoliated or intercalated structure, depending on clay loading. Fine and uniform dispersion of Cloisite sheets in Eudragit RS was observed. Most Cloisite sheets aligned perpendicularly to the sample cutting surface. At 5% and 10% loadings, Cloisite Na and Cloisite 20 were uniformly dispersed in the Eudragit RS matrix and an exfoliated nanocomposite structure was observed. At 15% clay loading, the clay sheets became denser and the intercalated nanocomposite structures were observed. It was concluded that the clay type did not impact the dispersion status of the clay in Eudragit RS. The coherent order of the stacked layers strongly depended on the clay loading.
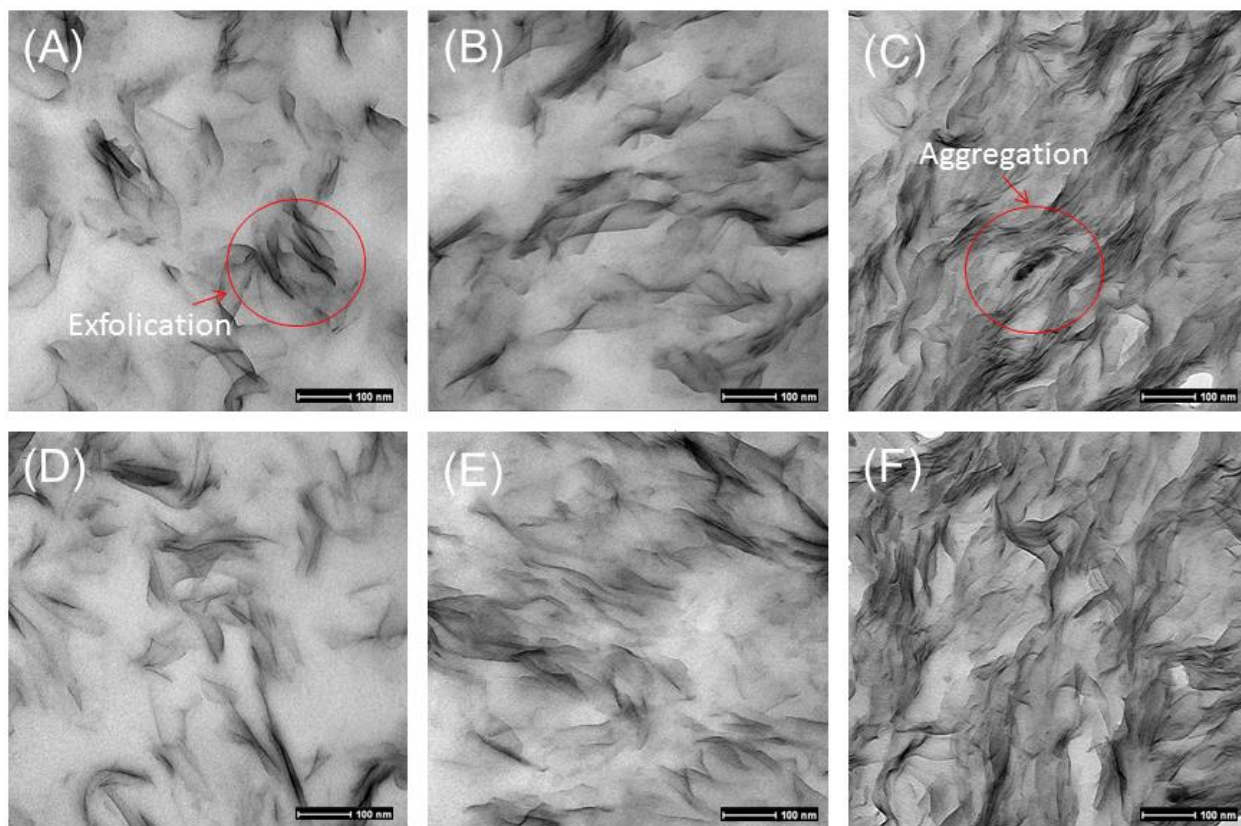
Figure 4.4: TEM images of Cloisite-Eudragit RS nanocomposites prepared using RME. (A) 5% Cloisite Na, (B) 10% Cloisite Na, (C) 15% Cloisite Na, (D) 5% Cloisite 20, (E) 10% Cloisite 20, (F) 15% Cloisite 20.

Exfoliation of Cloisite clays by Eudragit RS was mainly driven by the ionic interactions. As shown in Figure 4.1, quaternary ammonium group in Eudragit RS is positively charged while clay sheet surface is negatively charged. Since the drug molecules could not penetrate through the clay sheets, the increase in tortuosity as a result of ionic interaction would lead to slower diffusion [39]. The interaction could also reduce the hygroscopicity of Eudragit RS because less quaternary ammonium groups are available to interact with water molecules following the clay-polymer complexation.

At 5% and 10% clay loadings, all nanocomposites showed similar exfoliated structures regardless of clay types. For Cloisite 20, 86% of the intercalating sites are blocked by the ternary ammonium surfactant. The decrease in the available intercalating sites of Cloisite 20 could lead to

fewer interactions between the clay and Eudragit RS, potentially impacting drug release behaviors. FT-IR and ssNMR techniques were applied to investigate the molecular mechanisms of Eudragit RS-Cloisite interactions.

4.5.2.2   *Investigation of Cloisite-Eudragit RS Interactions Using FT-IR*

Due to isomorphous substitution, the silicate layers of Cloisite are negatively charged, which is balanced by interlayer Na^+. During the extrusion process, the ion-exchange reaction took place, and the quaternary ammonium groups of Eudragit RS replace the Na^+ and get ionically bound to the silicate layers. This type of interaction has been reported in other nanocomposites prepared with MMT and cationic polymers such as chitosan and gelatin [29, 31, 40].

Interactions between Cloisite and Eudragit RS were studied using FT-IR technique. The functional groups involved in molecular interaction could be reflected in the emergence of a new band, shift in band position, or change in band shape in FT-IR spectra [41]. The band assignment for Cloisite Na, Cloisite 20 and Eudragit RS FT-IR spectra (Figure 4.5A) is summarized in Table 2. The bands indicative of the Cloisite-Eudragit RS interactions are in the range of 500-1800 cm^{-1} [42]. These bands are associated with bending, deformation, and stretching of Si-O-Si, structural OH, and adsorbed water.

In the IR spectrum of Cloisite Na, the band at 1636 cm^{-1} (Figure 4.5A) is attributed to in-plane bending of water in the hydration sphere of the interlayer Na^+ ion [42]. The broad band in the region of 950-1100 cm^{-1} is associated with Si-O stretching vibrations [43]. For Cloisite 20, the ionic interactions between the intercalated surfactant and silicate surfaces significantly impact the arrangement of SiO_4 tetrahedral layers. The loading and alkyl chain length of the surfactant significantly impact the shape and wavenumber of the bands discussed above. In the FT-IR spectrum of Cloisite 20, the frequency of in-plane bending of water in the hydration sphere of the interlayer Na^+ ion shifted from 1636 cm^{-1} to 1645 cm^{-1}, while the intensity of this band decreased significantly. In addition, the peak of Si-O stretching vibrations in plane split into two peaks, one at 1036 cm^{-1} and another at 1027 cm^{-1} (Figure 4.5A).

Two notable changes in the FT-IR spectra of the clay-polymer nanocomposites indicate the interactions between Cloisite Na and Eudragit RS (Figure 4.5B). Firstly, the 1636 cm^{-1} band indicative of water molecules hydrating the interlayer Na$^+$ disappeared because of the displacement of the interlayer Na$^+$ and associated water molecules by Eudragit RS [44, 45]. Secondly, the board band in the region of 950-1100 cm^{-1}, corresponding to the vibration of Si-O, split into two peaks at 1038 and 1028 cm^{-1}. The splitting of the Si-O vibration band is affected by not only the chemical nature of the intercalated components, but also the basal spacing of the clay sheets. Because smaller basal spacing leads to less significant splitting, the splitting was less at higher Cloisite Na loading (by comparing Figure 4.5B), As illustrated in the XRPD and TEM results discussed earlier, the interlayer space decreases significantly with increased the clay loading. In addition to peak splitting, a new band attributed to perpendicular Si-O stretching was observed at 1078 cm^{-1}[46]. The intercalation of the Eudragit RS or surfactants into the Cloisite interlayer space resulted in a marked interlayer swelling during which a perpendicular adsorbate orientation is reached, accounting for the appearance of the new peak at 1078 cm^{-1}. Furthermore, with the decrease in clay loading, SiO_4 tetrahedra oriented toward a more ordered arrangement. Therefore, perpendicular Si-O vibration became more significant [46, 47]. The similar results were observed in Cloisite 20-Eudragit RS nanocomposites (Figure 4.6). It is difficult to differentiate the interaction between Eudragit RS and Cloisite Na or Cloisite 20 at the same clay loading level through FT-IR analysis.

The results not only indicate the clays were entrapped in the polymer matrix, but also that the clay layers interacted with polymer network to create a compacted complex structure for both Cloisite Na and Cloisite 20.

Table 4.2: Band assignment for Cloisite Na, Cloisite 20A, and Eudragit RS.

Components	IR absorption Band (cm^{-1})	Band Assignment
Cloisite Na	1636	δ (O-H) for adsorbed H_2O
	1078	γ (Si-O) (out-of-plane)
	1007	γ (Si-O) (in-of-plane)
	919	δ (Al-Al-OH)
Cloisite 20	1645	δ (O-H) for adsorbed H_2O
	1467	δ (C-H) of Aliphatic
	1080	γ (Si-O) (out-of-plane)
	1035	γ (Si-O) (in-of-plane)
	1027	γ (Si-O) (in-of-plane)
	919	δ (Al-Al-OH)
Eudragit RS	1728	δ(C=O) for ester group
	1448	δ(C-H) of alkyl chains
	1386	δ(C-H) of alkyl chains
	1238	γ (O=C-O) for ester group
	1147	γ (O=C-O) for ester group

δ = Bending vibration; γ = Stretching vibration.
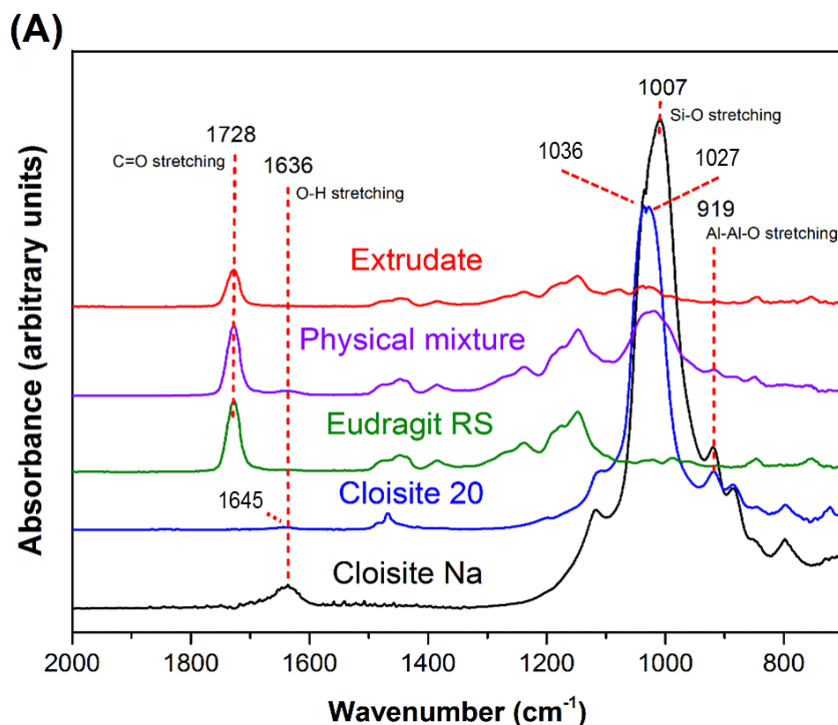
Figure 4.5: continued in next page.
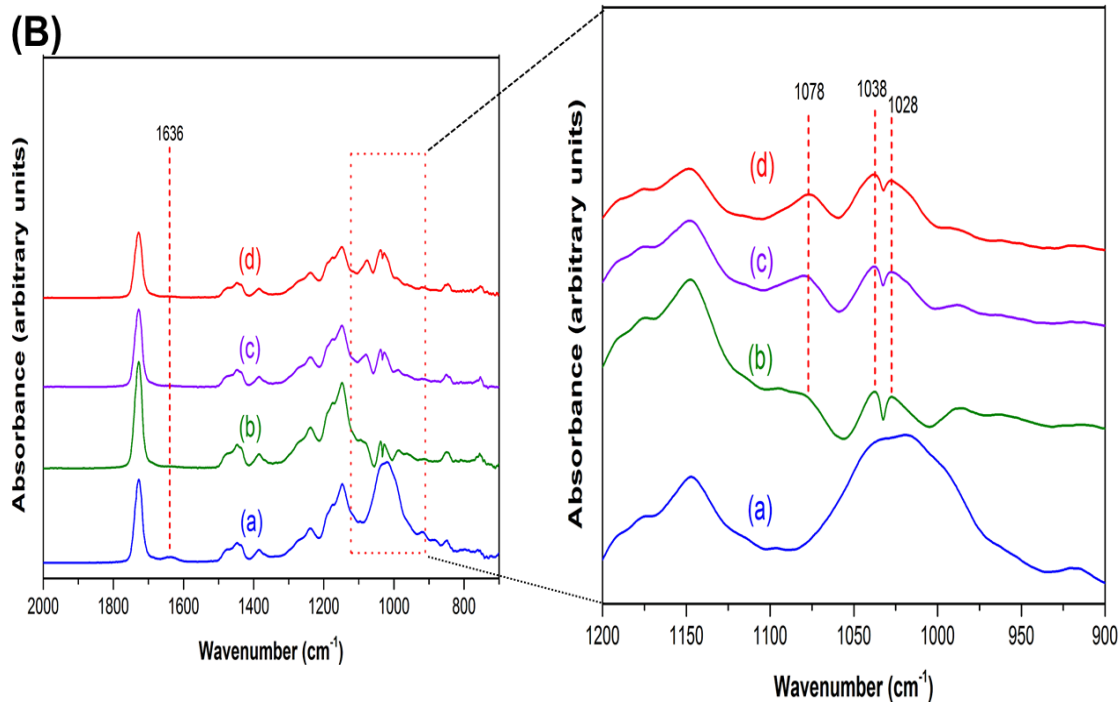
Figure 4.5: FT-IR spectra of extruded Cloisite–Eudragit RS nanocomposites. (A) 10% Cloisite Na–90% Eudragit RS nanocomposite, individual components, and their physical mixture; (B): (a) 5% Cloisite Na–95% Eudragit RS physical mixture; (b) Cloisite Na nanocomposite at 5% clay loading; (c) Cloisite Na nanocomposite at 10% clay loading; (d) Cloisite Na nanocomposite at 15% clay loading.
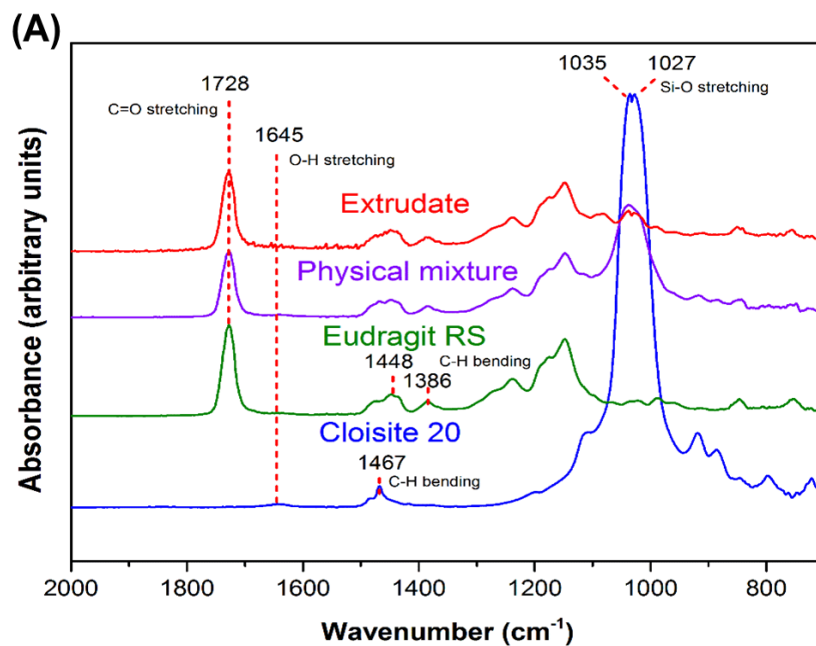
Figure 4.6: continued in next page
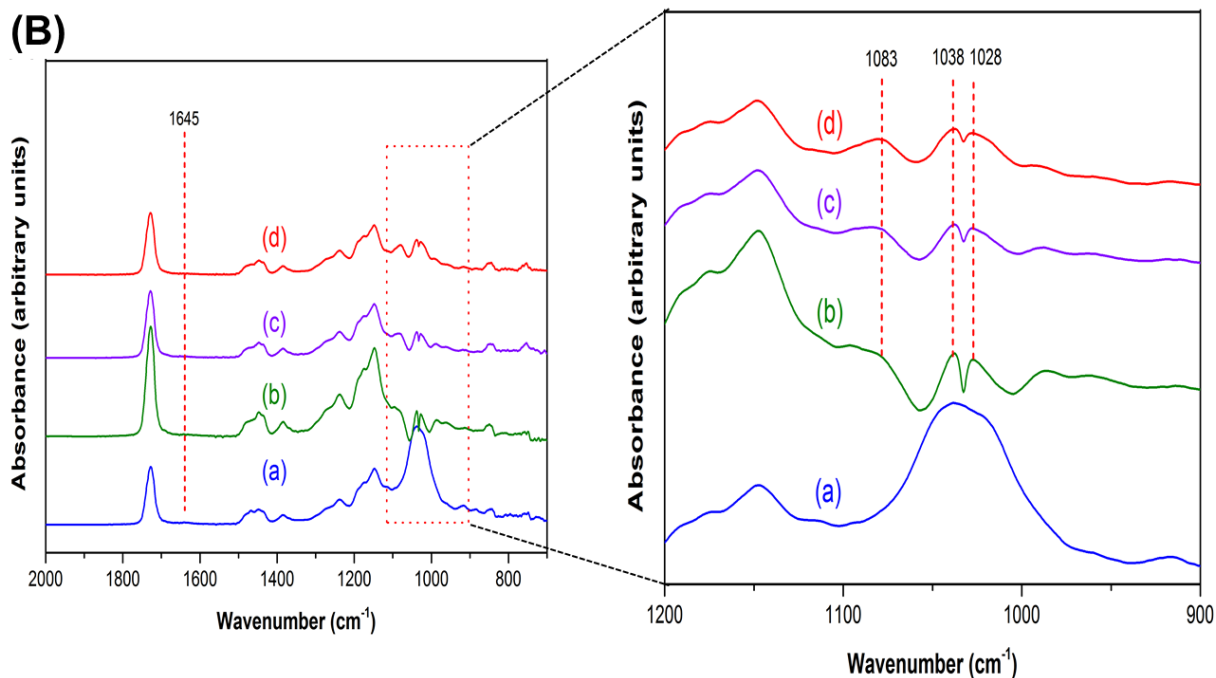
Figure 4.6: FTIR profiles of Cloisite 20 extrudates. (A) From bottom to top, (a) 5% Cloisite 20-95% Eudragit RS physical mixture; (b) Cloisite 20 extrudates at 5% clay loading; (c) Cloisite 20 extrudates at 10% clay loading; (d) Cloisite 20 extrudates at 15% clay loading. (B) From bottom to top, (a) 5% Cloisite 20-95% Eudragit RS physical mixture; (b) Cloisite 20 nanocomposite at 5% clay loading; (c) Cloisite 20 nanocomposite at 10% clay loading; (d) Cloisite 20 nanocomposite at 15% clay loading.

4.5.2.3   *Investigation of Cloisite Na-Eudragit RS Interactions Using ssNMR*

In previous studies, ssNMR was utilized to characterize the molecular interaction between Cloisite-polymer nanocomposites. For example, dynamic behavior of the local domains in between Cloisite and polymer is considered of important to understand the macroscopic properties of a nanocomposite [48]. Molecular motions at frequencies of the order of the Larmor frequency (MHz regime) can strongly influence the nuclear spin-lattice relaxation processes in the laboratory (T_1). We utilized 13C-detected saturation recovery experiments to measure the Eudragit RS 1H spin-lattice relaxation times in the laboratory frame [36]. The ^1H T_1 of Eudragit RS only was measured as 1.1 s and decreased to 0.8 s upon the incorporation of Cloisite Na, presumably exhibiting enhanced molecular dynamics. As a hypothesis, it may indicate that Eudragit RS molecules were well dispersed in between Cloisite Na layers and formed as a flexible dispersion, comparing to its original dense polymer assemblies. Besides molecular motions, ssNMR has been often utilized to probe intermolecular drug-polymer interactions [49]. Therefore, we further analyzed the Cloisite-polymer dispersion using ^{13}C CPMAS. The ^{13}C resonances of Eudragit RS are tentatively assigned. In Figure 4.7, The 1D ^{13}C spectra comparison exhibits an interesting spectral difference at 54.8 ppm between Eudragit RS only and Cloisite Na-Eudragit RS dispersions. This peak can be tentatively assigned as the polymer C23, adjacent to – $N^+(CH_3)_3$ in one of sidechains. While relative intensity of all other carbons remains unchanged, the loss of C23 intensity may suggest the perturbation of its surrounding proton network as well as molecular mobility, both of which attenuate the magnetization transfer during 1H-to-13C CP. For example, C23 can reside in a more diluted proton environment and exhibit faster molecular dynamics if the $–N^+(CH_3)_3$ sidechain is involved in between Cloisite Na layers. These molecular details will be further investigated by utilizing more

quantitative multiCP and two-dimensional site-specific ssNMR experiments in future studies [49, 50].
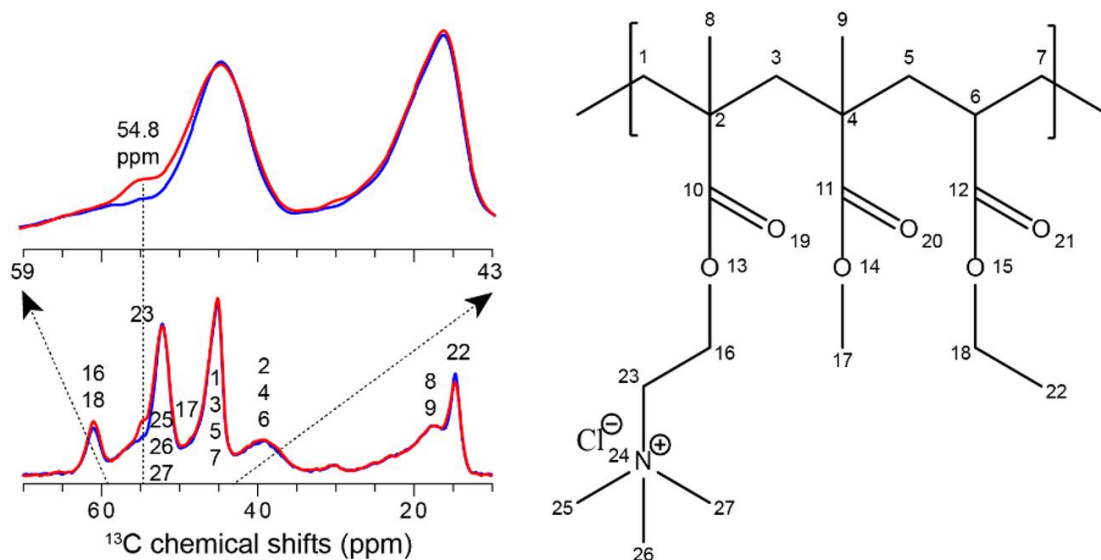
Figure 4.7: 1D 13C spectral comparison between Eudragit RS (red) and Cloisite Na–Eudragit RS dispersions (blue). Enlarged spectra were displayed in an overlaid manner. Tentative 13C chemical shift assignments are labeled using 13C numbers correspondingly shown in the Eudragit RS molecule structure.

4.5.2.4 *Hygroscopicity of Nanocomposites*

Eudragit RS is a copolymer of ethyl acrylate, methyl acrylate, and 3.3% (molar) of methacrylic acid ester with quaternary ammonium groups (trimethylammonioethyl methacrylate chloride). The ammonium groups are present as salt and make the polymer hygroscopic and permeable. Ion-exchange interaction between clay and polymer lowers the hygroscopicity of Eudragit RS. With the dispersion of silicate layers throughout the polymer matrix, the water barrier properties of the Eudragit RS are expected to be enhanced since water molecules must bypass impenetrable silicate platelets and permeate through a more tortuous diffusion path [37, 51].

189

The moisture sorption isotherms were determined for Eudragit RS and its Cloisite nanocomposites. As shown in Figure 4.8A, hygroscopicity of nanocomposites ranked in the following order: 10% Cloisite Na < 15% Cloisite Na < 5% Cloisite Na < Eudragit RS only. The Cloisite Na nanocomposite at 10% clay loading was the least hygroscopic. An initial decrease followed with increase in hygroscopicity beyond a threshold value was also reported with other clay-polymer nanocomposites [51-53]. Duan et. al. reported the lowest water vapor transmission rate at 5% clay loading for MMT-PLA nanocomposites containing 1% to 6% clay. The experimental data agreed well with the predictions from the Nielsen "tortuous path" model [54]. Increase in hygroscopicity above a clay-loading threshold was attributed to nanoclay agglomeration effect [37]. The increase in water permeability can also be explained by the increasing level of nonexfoliated silicate layers that formed tactoids and intercalated structures [55]. Aggregates in the intercalated structure facilitated the diffusion of water molecules via the connecting pathways along the polymer-clay interfacial zones [56]. In Cloisite-Eudragit RS nanocomposites, Cloisite Na platelets started to aggregate at 15% clay loading due to the intercalation without complete exfoliation.
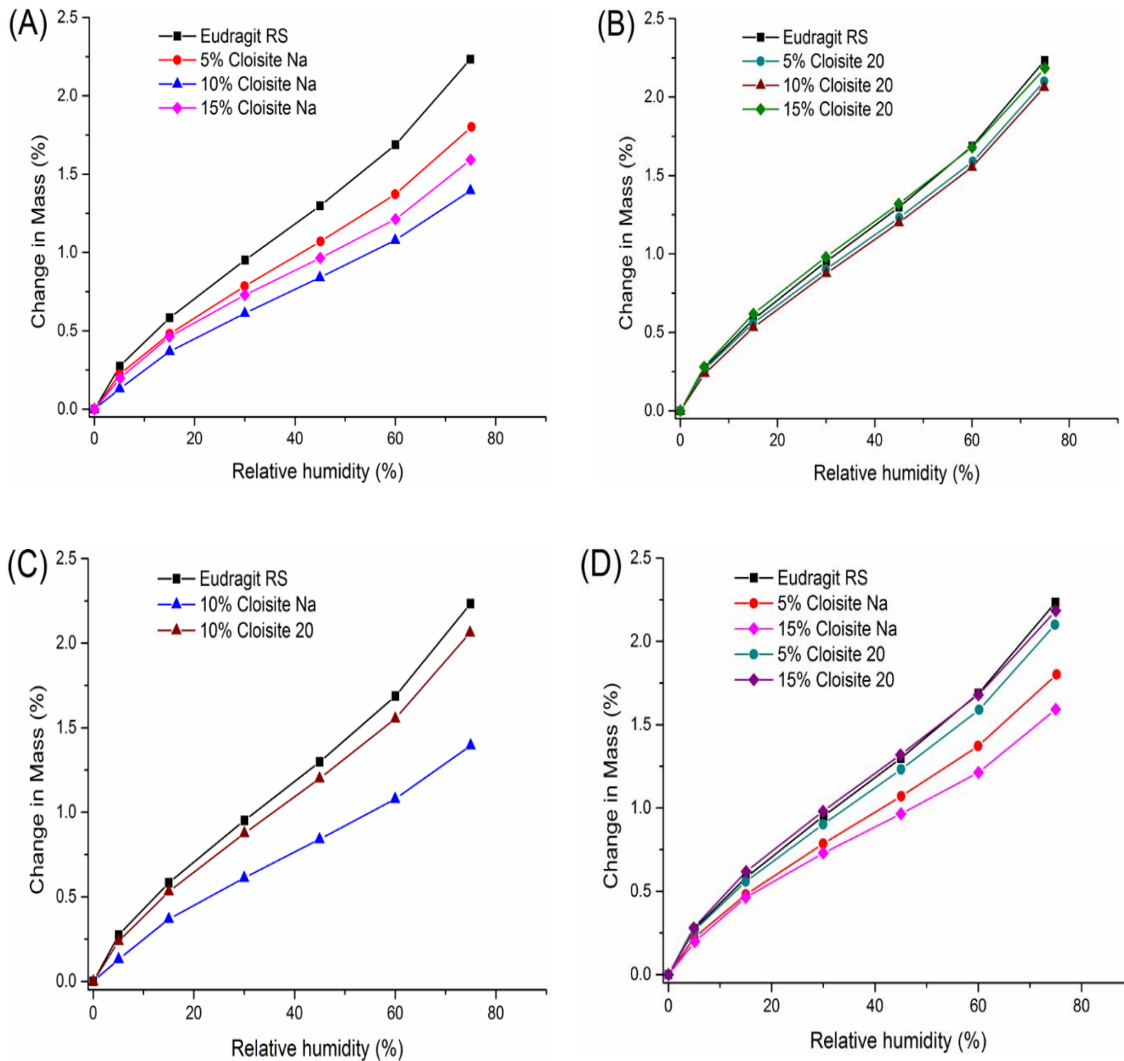
Figure 4.8: DVS profiles comparison of extruded Cloisite–Eudragit RS nanocomposites (35–50 mesh). (A) nanocomposites with different Cloisite Na loadings (B) nanocomposites with different Cloisite 20 loadings (C) nanocomposites with different clays at 10% loading (D) nanocomposites with different clays at 5% and 15% loadings.

In our study, we found that the exfoliated nanocomposites could be achieved at 10% Cloisite Na loading, which shows the maximum water-barrier effect. The exfoliated nanocomposites with higher clay loading could be made probably related with the higher

shear stresses generated during the twin screw extrusion process and the good miscibility of Cloisite Na and Eudragit RS.

Yet, the moisture sorption of Cloisite 20-Eudragit RS nanocomposites were similar across different Cloisite 20 loadings (Figure 4.8B). Equilibrium moisture content of nanocomposites containing 5% and 10% Cloisite 20 was 5.8% and 7.6% equilibrium moisture content was achieved at 25 °C/75% RH. The 15% Cloisite 20 nanocomposites even show slightly higher water hygroscopicity than Eudragit RS.

At a given clay loading, Cloisite Na is more effective than Cloisite 20 in reducing hygroscopicity of Eudragit RS, even though Cloisite 20 itself is less hygroscopic than Cloisite Na [57, 58]. Our DVS data shown the hygroscopicity of Cloisite Na was about 15 times than Cloisite 20 at 25 °C and 75 % RH condition (Figure 4.9). However, Cloisite Na nanocomposite show 32% less hygroscopicity than Cloisite 20 nanocomposites at 25 °C and 75 % RH at 10% clay loading (Figure 8C). This is attributed to difference in stronger clay-Eudragit RS interaction for Cloisite Na. For Cloisite 20-Eudragit RS nanocomposites, the intercalation of the polymer chain to the silicate layers enhances the exfoliation because the surfactant molecules cannot be squeezed out upon collapse of the layer.
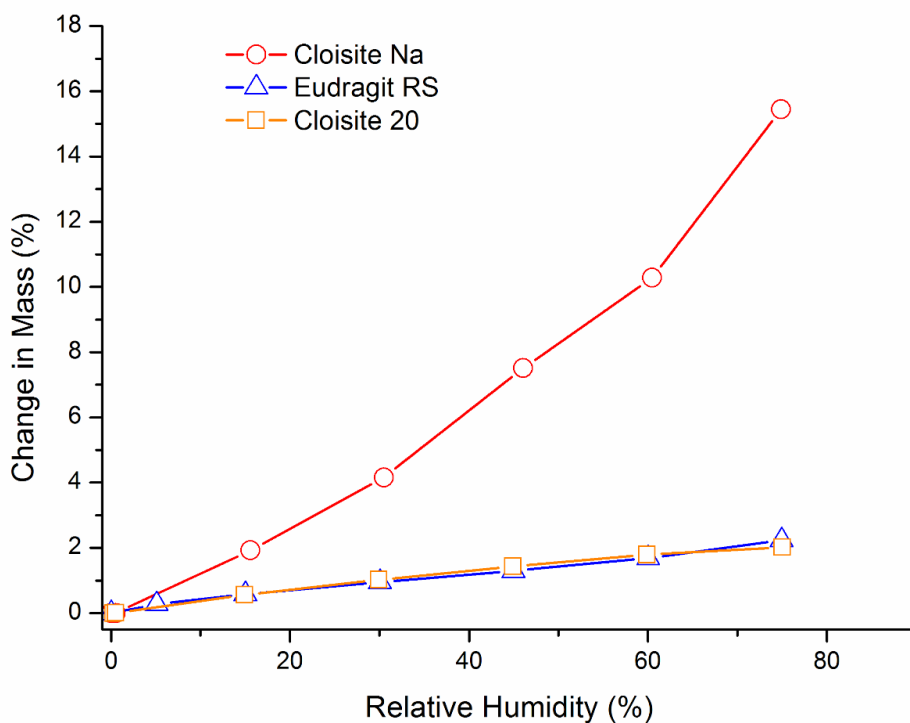
Figure 4.9: DVS profiles comparison of Cloisite Na, Eudragit RS and Cloisite20.

Moisture absorption of Eudragit RS is mainly controlled by its tertiary amine group. Due to the surfactant coating, Cloisite 20 has less cation exchange capacity compared with Cloisite Na. As a result, the quaternary ammonium groups of Eudragit RS have stronger interaction with the Cloisite Na.

At the same clay loading, the transmission rate of water through the composites is more influenced by polymer-silicate layer interactions. The nanofiller did not influence the water sorption capacity in the amorphous domains, however, the polymer interacted with the clay in the interlayer space, leading to the lowered hygroscopicity of this phase. Different kinds of interactions between the polymer and inorganic platelets may affect the free volume in the matrix, the interfacial regions between the two different phases and the degree of delamination of the silicate layers. A number of studies compare the efficacy of

different filler types in specific polymer systems. Alexandre et al also compared the water barrier properties of polyamide 12/organically modified MMT nanocomposites [56]. They found that the water permeability and diffusivity decrease with increasing clay volume fraction up to 2.5%. However, the water barrier effect was not improved by further addition of clay. The loss of barrier properties was attributed to several concomitant effects, such as the change of the polymer crystallinity, the water-induced plasticization and the structure heterogeneity.

In summary, Cloisite Na nanocomposites are more effective in inhibiting water absorption than Cloisite 20 nanocomposites and this is attributed to the difference in the interactions between Eudragit RS and silicate layers.

4.5.3 Characterization of Cloisite-Eudragit RS Nanocomposites Loaded with Theophylline

4.5.3.1 Characterization of Physical State of Theophylline in Extrudate

The theophylline extrudates were prepared at 160 °C, significantly below the melting point (273 °C) of theophylline. As shown in Figure 4.10, all major characteristic peaks (7.30°, 12.77°, 14.51°, and 25.76°) of theophylline were present in XRPD patterns of Cloisite Na or Cloisite 20-based theophylline granules. The intensity of theophylline diffraction increased with the increase in clay loading. These results indicated that the theophylline was not fully dissolved in the extrudates. The DSC data (Figure 4.11) confirmed XPRD results. Theophylline melts at 271 °C with a melting enthalpy of 197 J/g (Figure 4.11A). The higher the clay loading is, the lower the theophylline melting enthalpy of the extrudates. Via DSC analysis, the percentage of theophylline remaining crystalline in Cloisite Na-based formulations was determined to be 45.4%, 54.83%, and 72.43% at 4, 8, and 12% clay loading, respectively. Similar results have been observed in Cloisite 20-

based formulations (Figure 4.11B). It is noteworthy that under the same clay loading, the drug crystallinity in Cloisite Na and Cloisite 20-based formulations are similar.
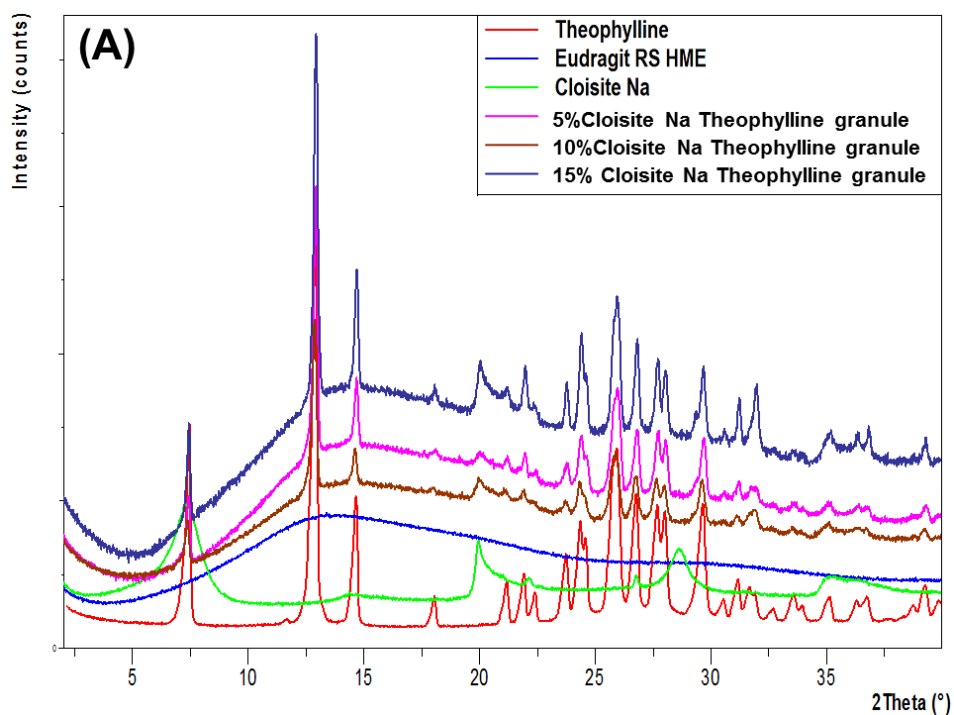
Figure 4.10: continued in next page.
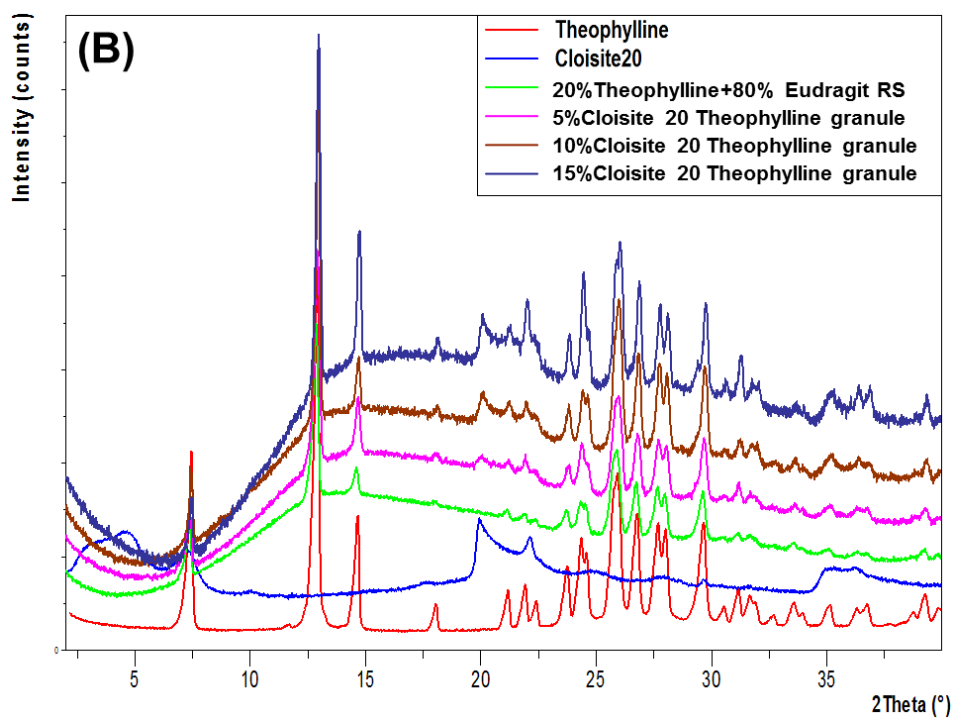
Figure 4.10: XRPD patterns of theophylline granules (20%) based on Cloisite–Eudragit RS nanocomposites and individual components. (A) Cloisite Na–Eudragit RS nanocomposites at different clay to polymer ratios, (B) Cloisite 20-Eudragit RS nanocomposites at different clay to polymer ratios.
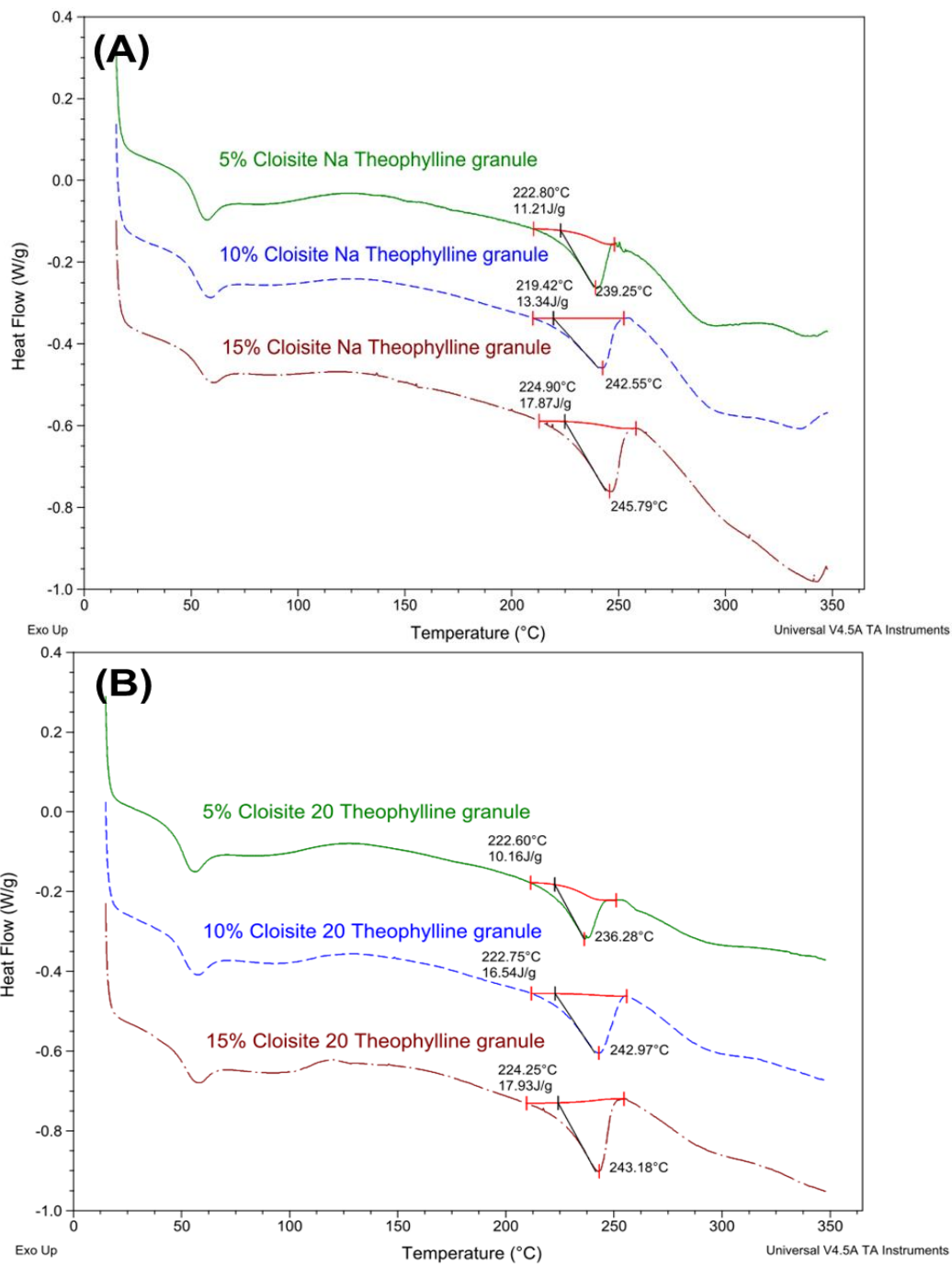
Figure 4.11: DSC profiles of theophylline granules (20%) based on Cloisite–Eudragit RS nanocomposites. (A) Cloisite Na–Eudragit RS nanocomposites at different clay to polymer ratios (B) Cloisite 20-Eudragit RS nanocomposites at different clay to polymer ratios.

Higher crystalline theophylline content at higher clay loading is due to two factors. Firstly, there is less Eudragit RS to solubilize theophylline in clay-polymer nanocomposites containing with a higher level of clay loading. Secondly, higher clay loading results in less distributive mixing. As discussed earlier, higher clay loading resulted in higher extrusion torque, which was indicative of a higher melt viscosity for the formulation. The distributive mixing during the extrusion process is limited due to the higher viscosity of the extrudates, which result in higher residual crystallinity in the formulation.

In summary, theophylline exists in a partially crystalline state in both Cloisite Na and Cloisite 20 nanocomposite matrices and the clay type does not impact the physical state of drug during the extrusion process.

4.5.3.2 Dissolution Study

Our Eudragit RS is a copolymer of ethyl acrylate, methyl methacrylate and a low content of methacrylic acid ester with quaternary ammonium groups. Not soluble in aqueous media across the entire physiological pH range, Eudragit RS exhibits low permeability with pH-independent swelling. It is reported in the literature that Eudragit RS is used extensively in the preparation of matrix tablets for oral sustained release, in tablet coating and in the microencapsulation of drugs[59].

Since both Cloisite and Eudragit RS are insoluble in water, theophylline is released from the granules via a diffusion process. Release of theophylline follows these steps: (1) penetration of the dissolution medium into the theophylline granules, (2) dissolution of theophylline, and (3) diffusion of dissolved theophylline out of the matrix[60].

Since theophylline, a weakly-acidic drug, is unable to complex with Cloisite clays, theophylline release from the nanocomposite matrix is controlled by the ionic interactions

between the Cloisite and Eudragit RS. As discussed earlier, the ionic interactions reduce the water permeability and equilibrium moisture content of Eudragit RS. Change in drug release rate is also related to the changes in the local permeability due to the molecular level transformation of Eudragit RS in the presence of the silicate sheets[61]. Eudragit RS chains are ionically bound to the dispersed Cloisite layers through the positively charged quaternary amine group. This ionic interaction restricts polymer chain mobility.

Drug release as a function of the clay content in the nanocomposites is plotted in Figure 4.12. Burst release in the initial 30 minutes observed for all theophylline granules was due to the release of theophylline located on the surface of the granules. After the initial burst, theophylline release followed a zero-order profile. As shown in Figure 4.12A, the addition of 5-10% Cloisite Na in nanocomposites resulted in slower drug release. The percentage theophylline released at 12 hours was reduced from 29% (clay-free granules) to 24% (5% Cloisite Na) and 16% (10% Cloisite Na). However, drug release accelerated with further increase of clay content to 15%. The trend in drug release rate as a function of Cloisite Na loading matched well with the DVS results discussed earlier. Equilibrium moisture content decreased with initial increase in Cloisite Na content. Beyond 10%, further increase in clay loading resulted in higher equilibrium moisture content. This increase in equilibrium content at 15% clay loading can be explained by the increasing quantity of nonexfoliated silicate layers that formed tactoids and intercalated structures, as revealed by the TEM and XRPD analyses.

As shown in Figure 4.12B, the inclusion of Cloisite 20 in the Eudragit RS matrix showed a reduced impact on theophylline release compared to Cloisite Na. After 12 hours, the percentage of theophylline released was 29%, 26%, 22% and 30%, for formulations based on clay-polymer nanocomposites containing 0%, 5%, 10%, and 15% Cloisite 20, respectively.

199

It is concluded that the clay type has a critical influence on drug release profiles. As shown in Figure 4.12, compared with Cloisite 20, the Cloisite Na is more effective in hindering the release of theophylline. For Cloisite 20, the organic modification hindered its interaction with Eudragit RS.

In summary, the presence of Cloisite nanoclay in the Eudragit RS matrix significantly impacted theophylline release profiles. Clay loading and clay type are the most important factors that would impacts the drug release behaviors.
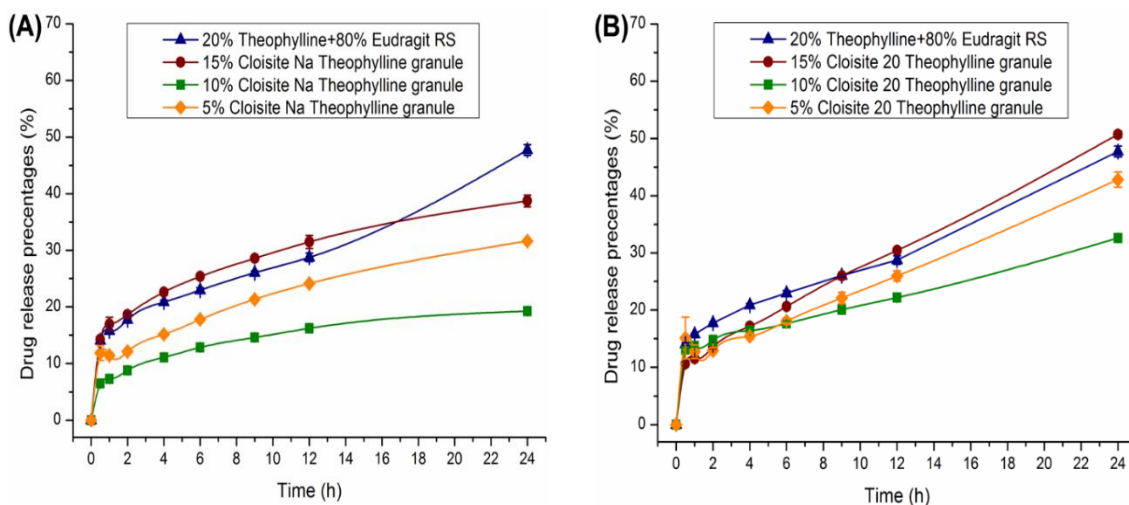
Figure 4.12: Dissolution profiles of 500 mg theophylline granules 30–35 mesh, 20% theophylline) in 900 mL phosphate buffer pH 6.8 using USP apparatus II at 75 RPM (n = 3), (A) Cloisite Na nanocomposites of different clay loadings; (B) Cloisite 20 nanocomposites of different clay loadings.

As shown in Figure 4.13, dissolution samples showed different surface morphology after 24 hours of dissolution testing. After 24 hours of dissolution testing, the surface pore size of the Cloisite 20 samples and Eudragit RS sample is larger than that of the Cloisite Na samples. Difference in porosity are attributed to the different release rates. DSC and XRPD data indicated the Cloisite Na and Cloisite 20 samples had similar crystallinity. We

hypothesize that the difference in the porosity was attributed to the difference in the size of the drug crystals dispersed in the extruded granules, since Cloisite Na and Cloisite 20 nanocomposites are water insoluble and the drug particles on the matrix surface are dissolved and released first. Upon exhaustion of the drug on the surface, the depletion zone will then increase progressively as the solid drug front recedes into the matrix while the larger pore size will facilitate the drug release from the matrix. Another important factors that will impact the drug release behaviors is the tortuosity, the molecular level interaction of polymer matrix with silicate layers and the interaction between the API molecule and the nanoclay. There are numerous mechanisms that may be involved in the interaction between clay and organic molecules. The predominant mechanism depends on largely on the type of clay, the functional groups of the polymer and the physical chemical properties of the API [62, 63].
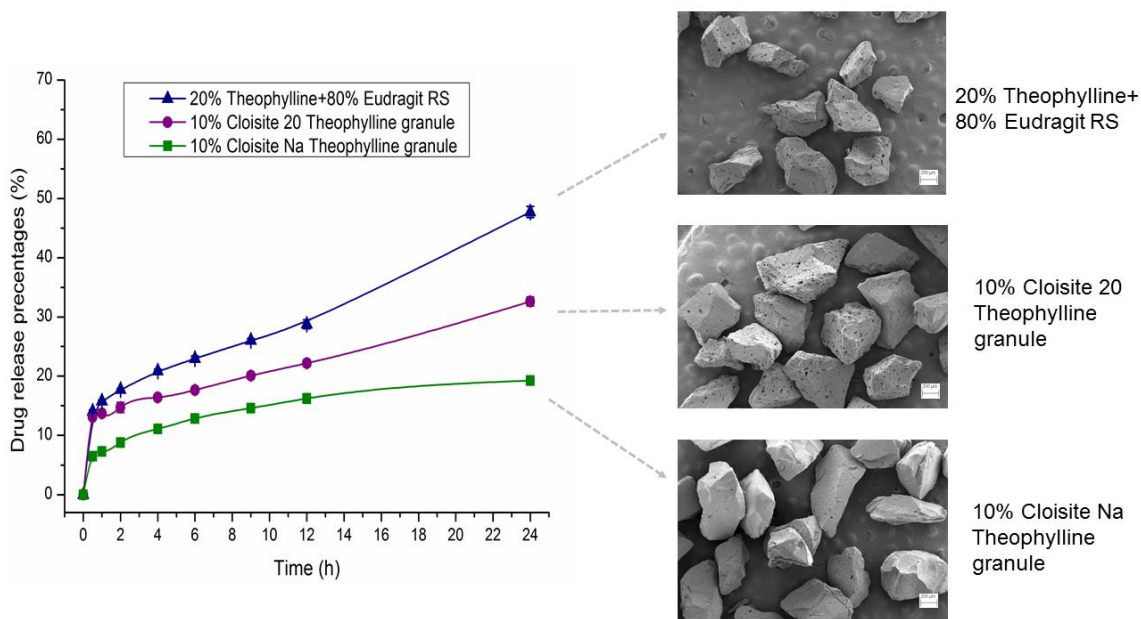
Figure 4.13: Dissolution profiles of 500 mg theophylline granules (30–35 mesh, 20% theophylline) in 900 mL phosphate buffer pH 6.8 using USP apparatus II at 75 RPM (n = 3) and the SEM images of remaining nanocomposites collected at the end of dissolution testing.

4.6 SUMMARY

The study has demonstrated that both Cloisite Na and Cloisite 20 could be exfoliated in Eudragit RS through hot melt extrusion. The XRPD and TEM analyses of the nanocomposites have shown that under the same processing conditions, the nanocomposites' structures depend on the clay loading and clay structure. When the clay content increases from 5% to 15% by weight, the nanocomposites structures switch from a fully exfoliated state to intercalated structures or partial exfoliation with stacked clay layers. FT-IR results indicated that Cloisite Na and Cloisite 20 layers show different interaction strength with the polymer network, which create a compacted complex structure. DVS data showed that the Cloisite Na nanocomposite is more effective in inhibiting the water absorption than the Cloisite 20 nanocomposite. ssNMR data shown the

202

quaternary ammonium groups of Eudragit RS engaged in the interfacial ionic interaction with the surface negative charged Cloisite clay sheet. Due to the less cation exchange capacity of Cloisite 20, Eudragit RS have stronger interaction with Cloisite Na. The hygroscopicity difference between Cloisite Na and Cloisite 20 nanocomposites could be attributed to the variation of the interaction between the clay sheet and polymer. The nanocomposites show high drug encapsulation efficiency, and theophylline exists in a crystal state in the matrix. The addition of nanoclay in the formulation could robustly adjust drug release profiles and the clay concentration and the clay type are the most important factors that impact the drug release behaviors, as they affect the crossing-linking density of the nanocomposites.

4.7 REFERENCE

1.   Wen, H.; Park, K., Oral controlled release formulation design and drug delivery: theory to practice. John Wiley & Sons: 2011.

2.   Tibbitt, M. W.; Dahlman, J. E.; Langer, R., Emerging Frontiers in Drug Delivery. Journal of the American Chemical Society 2016, 138 (3), 704-717.

3.   Nokhodchi, A.; Raja, S.; Patel, P.; Asare-Addo, K., The Role of Oral Controlled Release Matrix Tablets in Drug Delivery Systems. BioImpacts : BI 2012, 2 (4), 175-187.

4.   Siepmann, J.; Siegel, R.; Rathbone, M. J., Fundamentals and applications of controlled release drug delivery. 2012; p 1-594.

5.   Maincent, J.; Williams, R. O., Sustained-release amorphous solid dispersions. Drug Delivery and Translational Research 2018, 8 (6), 1714-1725.

6.   Ming, L.; Zhefei, G.; Yongcheng, L.; Huishi, P.; Ling, L.; Xu, L.; Xin, P.; Chuanbin, W., Application of Hot Melt Extrusion for Poorly Water-Soluble Drugs:

Limitations, Advances and Future Prospects. Current Pharmaceutical Design 2014, 20 (3), 369-387.

7.   Repka, M. A.; Bandari, S.; Kallakunta, V. R.; Vo, A. Q.; McFall, H.; Pimparade, M. B.; Bhagurkar, A. M., Melt extrusion with poorly soluble drugs – An integrated review. International Journal of Pharmaceutics 2018, 535 (1), 68-85.

8.   Tiwari, R. V.; Patil, H.; Repka, M. A., Contribution of hot-melt extrusion technology to advance drug delivery in the 21st century. Expert Opinion on Drug Delivery 2016, 13 (3), 451-464.

9.   Bouvier, J.-M.; Campanella, O. H., Extrusion Processing Technology: Food and Non-Food Biomaterials. John Wiley & Sons: 2014.

10.   Raquez, J. M.; Narayan, R.; Dubois, P., Recent Advances in Reactive Extrusion Processing of Biodegradable Polymer-Based Compositions. Macromolecular Materials and Engineering 2008, 293 (6), 447-470.

11.   Singh, S.; Gamlath, S.; Wakeling, L., Nutritional aspects of food extrusion: a review. International Journal of Food Science & Technology 2007, 42 (8), 916-929.

12.   Lu, M., Continuous Co-crystallisation of Poorly Soluble Active Pharmaceutical Ingredients to Enhance Dissolution. In Practical Guide to Hot-Melt Extrusion: Continuous Manufacturing and Scale-up, Maniruzzaman, M., Ed. Smithers Rapra: 2016; pp 75-93.

13.   Arnfast, L.; Kamruzzaman, M.; Löbmann, K.; Aho, J.; Baldursdottir, S.; Rades, T.; Rantanen, J., Melt Extrusion of High-Dose Co-Amorphous Drug-Drug Combinations. Pharmaceutical Research 2017, 34 (12), 2689-2697.

14.   Liu, X.; Zhou, L.; Zhang, F., Reactive Melt Extrusion To Improve the Dissolution Performance and Physical Stability of Naproxen Amorphous Solid Dispersions. Molecular Pharmaceutics 2017, 14 (3), 658-673.

15.   Kindermann, C.; Matthée, K.; Strohmeyer, J.; Sievert, F.; Breitkreutz, J., Tailor-made release triggering from hot-melt extruded complexes of basic polyelectrolyte and poorly water-soluble drugs. European Journal of Pharmaceutics and Biopharmaceutics 2011, 79 (2), 372-381.

16.   Gârea, S. A.; Voicu, A. I.; Iovu, H., Clay–Polymer Nanocomposites for Controlled Drug Release. In Clay-Polymer Nanocomposites, Elsevier: 2017; pp 475-509.

17.   Rodrigues, L. A. D.; Figueiras, A.; Veiga, F.; de Freitas, R. M.; Nunes, L. C. C.; da Silva, E. C.; Leite, C. M. D., The systems containing clays and clay minerals from modified drug release: A review. Colloids and Surfaces B-Biointerfaces 2013, 103, 642-651.

18.   Jayrajsinh, S.; Shankar, G.; Agrawal, Y. K.; Bakre, L., Montmorillonite nanoclay as a multifaceted drug-delivery carrier: A review. Journal of Drug Delivery Science and Technology 2017, 39, 200-209.

19.   Meirelles, L. M. A.; Raffin, F. N., Clay and Polymer-Based Composites Applied to Drug Release: A Scientific and Technological Prospection. Journal of Pharmacy & Pharmaceutical Sciences 2017, 20, 115-134.

20.   Kotal, M.; Bhowmick, A. K., Polymer nanocomposites from modified clays: Recent advances and challenges. Progress in Polymer Science 2015, 51, 127-187.

21.   Sinha Ray, S.; Okamoto, M., Polymer/layered silicate nanocomposites: a review from preparation to processing. Progress in Polymer Science 2003, 28 (11), 1539-1641.

22.   Zang, Y.; Xu, W.; Qiu, D.; Chen, D.; Chen, R.; Su, S., Synthesis, characterization and thermal stability of different polystyryl quaternary ammonium surfactants and their montmorillonite complexes. Thermochimica Acta 2008, 474 (1), 1-7.

23.   Chiu, C.-W.; Huang, T.-K.; Wang, Y.-C.; Alamani, B. G.; Lin, J.-J., Intercalation strategies in clay/polymer hybrids. Progress in Polymer Science 2014, 39 (3), 443-485.

24.   Choudalakis, G.; Gotsis, A. D., Permeability of polymer/clay nanocomposites: A review. European Polymer Journal 2009, 45 (4), 967-984.

25.   Salahuddin, N.; Kenawy, E.-R.; Abdeen, R., Polyoxypropylene–montmorillonite nanocomposites for drug-delivery vehicles: Preparation and characterization. J. Appl. Polym. Sci. 2012, 125 (S1), E157-E166.

26.   Pavlidou, S.; Papaspyrides, C. D., A review on polymer–layered silicate nanocomposites. Progress in Polymer Science 2008, 33 (12), 1119-1198.

27.   Bharadwaj, R. K., Modeling the barrier properties of polymer-layered silicate nanocomposites. Macromolecules 2001, 34 (26), 9189-9192.

28.   Riela, S.; Fakhrullin, R. F., Clay-based drug-delivery systems: what does the future hold? Therapeutic delivery 2017, 8 (8), 633-646.

29.   García Guzmán, P.; Medina-Torres, L.; Calderas, F.; Josefa Bernad-Bernad, M.; Gracia-Mora, J.; Mena, B.; Manero, O., Characterization of hybrid microparticles/Montmorillonite composite with raspberry-like morphology for Atorvastatin controlled release. 2018; Vol. 167.

30.   Sharma, A. K.; Mortensen, A.; Schmidt, B.; Frandsen, H.; Hadrup, N.; Larsen, E. H.; Binderup, M. L., In-vivo study of genotoxic and inflammatory effects of the organo-

modified Montmorillonite Cloisite® 30B. Mutation Research/Genetic Toxicology and Environmental Mutagenesis 2014, 770, 66-71.

31.   Khlibsuwan, R.; Siepmann, F.; Siepmann, J.; Pongjanyakul, T., Chitosan-clay nanocomposite microparticles for controlled drug delivery: Effects of the MAS content and TPP crosslinking. Journal of Drug Delivery Science and Technology 2017, 40 (Supplement C), 1-10.

32.   Campbell, K. T.; Craig, D. Q. M.; McNally, T., Modification of ibuprofen drug release from poly(ethylene glycol) layered silicate nanocomposites prepared by hot-melt extrusion. Journal of Applied Polymer Science 2014, 131 (10), n/a-n/a.

33.   Rives, V.; del Arco, M.; Martín, C., Intercalation of drugs in layered double hydroxides and their controlled release: A review. Applied Clay Science 2014, 88, 239-269.

34.   Rives, V.; del Arco, M.; Martín, C., Layered double hydroxides as drug carriers and for controlled release of non-steroidal antiinflammatory drugs (NSAIDs): A review. Journal of Controlled Release 2013, 169 (1), 28-39.

35.   Bee, S.-L.; Abdullah, M. A. A.; Mamat, M.; Bee, S.-T.; Sin, L. T.; Hui, D.; Rahmat, A. R., Characterization of silylated modified clay nanoparticles and its functionality in PMMA. Composites Part B: Engineering 2017, 110, 83-95.

36.   Hanada, M.; Jermain, S. V.; Lu, X.; Su, Y.; Williams, R. O., Predicting physical stability of ternary amorphous solid dispersions using specific mechanical energy in a hot melt extrusion process. International Journal of Pharmaceutics 2018, 548 (1), 571-585.

37.   Tan, B.; Thomas, N. L., A review of the water barrier properties of polymer/clay and polymer/graphene nanocomposites. Journal of Membrane Science 2016, 514, 595-612.

38.   Paul, D. R.; Robeson, L. M., Polymer nanotechnology: Nanocomposites. Polymer 2008, 49 (15), 3187-3204.

39.   Carretero, M. I.; Pozo, M., Clay and non-clay minerals in the pharmaceutical industry: Part I. Excipients and medical applications. Applied Clay Science 2009, 46 (1), 73-80.

40.   Liu, K.-H.; Liu, T.-Y.; Chen, S.-Y.; Liu, D.-M., Drug release behavior of chitosan–montmorillonite nanocomposite hydrogels following electrostimulation. Acta Biomaterialia 2008, 4 (4), 1038-1045.

41.   Lin-Vien, D.; Colthup, N. B.; Fateley, W. G.; Grasselli, J. G., The handbook of infrared and Raman characteristic frequencies of organic molecules. Elsevier: 1991.

42.   He, H. P.; Zhu, J., Chapter 10 - Analysis of Organoclays and Organic Adsorption by Clay Minerals. In Developments in Clay Science, Gates, W. P.; Kloprogge, J. T.; Madejová, J.; Bergaya, F., Eds. Elsevier: 2017; Vol. 8, pp 310-342.

43.   Madejová, J.; Gates, W. P.; Petit, S., Chapter 5 - IR Spectra of Clay Minerals. In Developments in Clay Science, Gates, W. P.; Kloprogge, J. T.; Madejová, J.; Bergaya, F., Eds. Elsevier: 2017; Vol. 8, pp 107-149.

44.   Johnston, C. T., Chapter 9 - Infrared Studies of Clay Mineral-Water Interactions. In Developments in Clay Science, Gates, W. P.; Kloprogge, J. T.; Madejová, J.; Bergaya, F., Eds. Elsevier: 2017; Vol. 8, pp 288-309.

45.   Xu, W.; Johnston, C. T.; Parker, P.; Agnew, S. F., Infrared study of water sorption on Na-, Li-, Ca-, and Mg-exchanged (SWy-1 and SAz-1) montmorillonite. Clays and Clay Minerals 2000, 48 (1), 120-131.

46.   Slosiariková, H.; Bujdák, J.; Hlavatý, V., IR spectra of octadecylammonium-montmorillonite in the range of the Si-O vibrations. Journal of inclusion phenomena and molecular recognition in chemistry 1992, 13 (3), 267-272.

47.   Ma, Y.; Zhu, J.; He, H.; Yuan, P.; Shen, W.; Liu, D., Infrared investigation of organo-montmorillonites prepared from different surfactants. Spectrochimica Acta Part A: Molecular and Biomolecular Spectroscopy 2010, 76 (2), 122-129.

48.   Martini, F.; Geppi, M.; Borsacchi, S., Chapter 9 - NMR Spectroscopy of Clay–Polymer Nanocomposites A2 - Jlassi, Khouloud. In Clay-Polymer Nanocomposites, Chehimi, M. M.; Thomas, S., Eds. Elsevier: 2017; pp 307-325.

49.   Lu, X.; Huang, C.; Lowinger, M. B.; Yang, F.; Xu, W.; Brown, C. D.; Hesk, D.; Koynov, A.; Schenck, L.; Su, Y., Molecular Interactions in Posaconazole Amorphous Solid Dispersions from Two-Dimensional Solid-State NMR Spectroscopy. Molecular Pharmaceutics 2019, 16 (6), 2579-2589.

50.   Duan, P.; Schmidt-Rohr, K., Composite-pulse and partially dipolar dephased multiCP for improved quantitative solid-state 13C NMR. Journal of Magnetic Resonance 2017, 285, 68-78.

51.   Becker, O.; Varley, R. J.; Simon, G. P., Thermal stability and water uptake of high performance epoxy layered silicate nanocomposites. European Polymer Journal 2004, 40 (1), 187-195.

52.   Liu, X.; Wu, Q., Polyamide 66/Clay Nanocomposites via Melt Intercalation. 2002, 287 (3), 180-186.

53.   Rhim, J.-W.; Hong, S.-I.; Ha, C.-S., Tensile, water vapor barrier and antimicrobial properties of PLA/nanoclay composite films. LWT - Food Science and Technology 2009, 42 (2), 612-617.

54.   Duan, Z.; Thomas, N. L.; Huang, W., Water vapour permeability of poly(lactic acid) nanocomposites. Journal of Membrane Science 2013, 445, 112-118.

55.   Jesus, C. R. N.; Molina, E. F.; Pulcinelli, S. H.; Santilli, C. V., Highly Controlled Diffusion Drug Release from Ureasil–Poly(ethylene oxide)–Na+–Montmorillonite Hybrid Hydrogel Nanocomposites. ACS Applied Materials & Interfaces 2018, 10 (22), 19059-19068.

56.   Alexandre, B.; Langevin, D.; Médéric, P.; Aubry, T.; Couderc, H.; Nguyen, Q. T.; Saiter, A.; Marais, S., Water barrier properties of polyamide 12/montmorillonite nanocomposite membranes: Structure and volume fraction effects. Journal of Membrane Science 2009, 328 (1), 186-204.

57.   Huskić, M.; Žigon, M.; Ivanković, M., Comparison of the properties of clay polymer nanocomposites prepared by montmorillonite modified by silane and by quaternary ammonium salts. Applied Clay Science 2013, 85, 109-115.

58.   Ianchis, R.; Cinteza, L. O.; Donescu, D.; Petcu, C.; Corobea, M. C.; Somoghi, R.; Ghiurea, M.; Spataru, C., Implications of silylated montmorillonite on montmorillonite–polyacrylate nanocomposites. Applied Clay Science 2011, 52 (1), 96-103.

59.   Patra, C. N.; Priya, R.; Swain, S.; Kumar Jena, G.; Panigrahi, K. C.; Ghose, D., Pharmaceutical significance of Eudragit: A review. Future Journal of Pharmaceutical Sciences 2017, 3 (1), 33-45.

60.   Azarmi, S.; Farid, J.; Nokhodchi, A.; Bahari-Saravi, S. M.; Valizadeh, H., Thermal treating as a tool for sustained release of indomethacin from Eudragit RS and RL matrices. International Journal of Pharmaceutics 2002, 246 (1), 171-177.

61.   Lyons, J. G.; Holehonnur, H.; Devine, D. M.; Kennedy, J. E.; Geever, L. M.; Blackie, P.; Higginbotham, C. L., The incorporation of an organically modified layered silicate in monolithic polymeric matrices produced using hot melt extrusion. Mater Chem Phys 2007, 103 (2–3), 419-426.

62.   Ha, J. U.; Xanthos, M., Drug release characteristics from nanoclay hybrids and their dispersions in organic polymers. International Journal of Pharmaceutics 2011, 414 (1–2), 321-331.

63.   Dening, T. J.; Rao, S.; Thomas, N.; Prestidge, C. A., Montmorillonite-lipid hybrid carriers for ionizable and neutral poorly water-soluble drugs: Formulation, characterization and in vitro lipolysis studies. International Journal of Pharmaceutics 2017, 526 (1–2), 95-105.

Bibliography

R.O. Williams III, A.B. Watts, D.A. Miller, Formulating poorly water-soluble drugs, Springer Science & Business Media2011.

S. Jain, N. Patel, S. Lin, Solubility and dissolution enhancement strategies: current understanding and recent trends, Drug Development and Industrial Pharmacy 41(6) (2015) 875-887.

Y. He, C. Ho, Amorphous Solid Dispersions: Utilization and Challenges in Drug Discovery and Development, Journal of Pharmaceutical Sciences (2015) n/a-n/a.

W.L. Chiou, S. Riegelman, Pharmaceutical applications of solid dispersion systems, Journal of pharmaceutical sciences 60(9) (1971) 1281-1302.

H. Grohganz, P.A. Priemel, K. Lobmann, L.H. Nielsen, R. Laitinen, A. Mullertz, G. Van den Mooter, T. Rades, Refining stability and dissolution rate of amorphous drug formulations, Expert Opinion on Drug Delivery 11(6) (2014) 977-989.

L.S. Taylor, G.G.Z. Zhang, Physical chemistry of supersaturated solutions and implications for oral absorption, Advanced Drug Delivery Reviews (2016).

F.G. Vogt, solid state characterization of amorphous solid dispersions, Pharmaceutical Amorphous Solid Dispersions (2015).

J.A. Baird, L.S. Taylor, Evaluation of amorphous solid dispersion properties using thermal analysis techniques, Adv Drug Deliv Rev 64(5) (2012) 396-421.

S. Thakral, M.W. Terban, N.K. Thakral, R. Suryanarayanan, Recent advances in the characterization of amorphous pharmaceuticals by X-ray diffractometry, Advanced Drug Delivery Reviews 100 (2016) 183-193.

M.M. Knopp, K. Löbmann, D.P. Elder, T. Rades, R. Holm, Recent advances and potential applications of modulated differential scanning calorimetry (mDSC) in drug development, European Journal of Pharmaceutical Sciences 87 (2016) 164-173.

A. Hedoux, Recent developments in the Raman and infrared investigations of amorphous pharmaceuticals and protein formulations: A review, Advanced Drug Delivery Reviews 100 (2016) 133-146.

Y.-C. Shen, Terahertz pulsed spectroscopy and imaging for pharmaceutical applications: A review, International Journal of Pharmaceutics 417(1–2) (2011) 48-60.

N. Chieng, T. Rades, J. Aaltonen, An overview of recent studies on the analysis of pharmaceutical polymorphs, Journal of Pharmaceutical and Biomedical Analysis 55(4) (2011) 618-644.

G. Nichols, Light Microscopy, Polymorphism, Wiley-VCH Verlag GmbH & Co. KGaA2006, pp. 167-209.

C. Telang, S. Mujumdar, M. Mathew, Improved physical stability of amorphous state through acid base interactions, Journal of Pharmaceutical Sciences 98(6) (2009) 2149-2159.

S.A. Raina, D.E. Alonzo, G.G. Zhang, Y. Gao, L.S. Taylor, Impact of Polymers on the Crystallization and Phase Transition Kinetics of Amorphous Nifedipine during Dissolution in Aqueous Media, Mol Pharm 11(10) (2014) 3565-76.

T. Cai, L. Zhu, L. Yu, Crystallization of Organic Glasses: Effects of Polymer Additives on Bulk and Surface Crystal Growth in Amorphous Nifedipine, Pharmaceutical Research 28(10) (2011) 2458-2466.

Y. Li, H. Pang, Z. Guo, L. Lin, Y. Dong, G. Li, M. Lu, C. Wu, Interactions between drugs and polymers influencing hot melt extrusion, Journal of Pharmacy and Pharmacology 66(2) (2014) 148-166.

X. Liu, M. Lu, Z. Guo, L. Huang, X. Feng, C. Wu, Improving the chemical stability of amorphous solid dispersion with cocrystal technique by hot melt extrusion, Pharm Res 29(3) (2012) 806-17.

X. Liu, L. Zhou, F. Zhang, Reactive Melt Extrusion to Improve the Dissolution Performance and Physical Stability of Naproxen Amorphous Solid Dispersions, Molecular Pharmaceutics (2017).

J. Moffat, S. Qi, D.M. Craig, Spatial Characterization of Hot Melt Extruded Dispersion Systems Using Thermal Atomic Force Microscopy Methods: The Effects of Processing Parameters on Phase Separation, Pharmaceutical Research 31(7) (2014) 1744-1752.

A. Bohr, M.S. Yang, S. Baldursdottir, J. Kristensen, M. Dyas, E. Stride, M. Edirisinghe, Particle formation and characteristics of Celecoxib-loaded poly(lactic-co-glycolic acid) microparticles prepared in different solvents using electrospraying, Polymer 53(15) (2012) 3220-3229.

X. Ye, H. Patil, X. Feng, R.V. Tiwari, J. Lu, A. Gryczke, K. Kolter, N. Langley, S. Majumdar, D. Neupane, S.R. Mishra, M.A. Repka, Conjugation of Hot-Melt Extrusion with High-Pressure Homogenization: a Novel Method of Continuously Preparing Nanocrystal Solid Dispersions, AAPS PharmSciTech 17(1) (2016) 78-88.

C. Bruce, K.A. Fegely, A.R. Rajabi-Siahboomi, J.W. McGinity, Crystal growth formation in melt extrudates, Int J Pharm 341(1-2) (2007) 162-72.

P.A. Priemel, R. Laitinen, H. Grohganz, T. Rades, C.J. Strachan, In situ amorphisation of indomethacin with Eudragit (R) E during dissolution, European Journal of Pharmaceutics and Biopharmaceutics 85(3) (2013) 1259-1265.

P.J. Marsac, A.C. Rumondor, D.E. Nivens, U.S. Kestur, L. Stanciu, L.S. Taylor, Effect of temperature and moisture on the miscibility of amorphous dispersions of felodipine and poly(vinyl pyrrolidone), J Pharm Sci 99(1) (2010) 169-85.R.G. Ricarte, T.P. Lodge, M.A.

215

Hillmyer, Detection of pharmaceutical drug crystallites in solid dispersions by transmission electron microscopy, Mol Pharm 12(3) (2015) 983-90.

H. Ma, D.S. Choi, Y.-E. Zhang, H. Tian, N. Shah, H.P. Chokshi, Evaluation on the Drug–Polymer Mixing Status in Amorphous Solid Dispersions at the Early Stage Formulation and Process Development, Journal of Pharmaceutical Innovation 8(3) (2013) 163-174.

Y.T.A. Turner, C.J. Roberts, M.C. Davies, Scanning probe microscopy in the field of drug delivery, Advanced Drug Delivery Reviews 59(14) (2007) 1453-1473.

J. Sitterberg, A. Özcetin, C. Ehrhardt, U. Bakowsky, Utilising atomic force microscopy for the characterisation of nanoscale drug delivery systems, European Journal of Pharmaceutics and Biopharmaceutics 74(1) (2010) 2-13.

M.E. Lauer, O. Grassmann, M. Siam, J. Tardio, L. Jacob, S. Page, J.H. Kindt, A. Engel, J. Alsenz, Atomic Force Microscopy-Based Screening of Drug-Excipient Miscibility and Stability of Solid Dispersions, Pharmaceutical Research 28(3) (2011) 572-584.

M.S. Lamm, J. DiNunzio, N.N. Khawaja, L.S. Crocker, A. Pecora, Assessing Mixing Quality of a Copovidone-TPGS Hot Melt Extrusion Process with Atomic Force Microscopy and Differential Scanning Calorimetry, AAPS PharmSciTech 17(1) (2016) 89-98.

J. Meeus, D.J. Scurr, X. Chen, K. Amssoms, M.C. Davies, C.J. Roberts, G. Van den Mooter, Combination of (M) DSC and Surface Analysis to Study the Phase Behaviour and Drug Distribution of Ternary Solid Dispersions, Pharmaceutical research (2014) 1-10.

M. Lauer, M. Siam, J. Tardio, S. Page, J. Kindt, O. Grassmann, Rapid Assessment of Homogeneity and Stability of Amorphous Solid Dispersions by Atomic Force Microscopy—From Bench to Batch, Pharmaceutical Research 30(8) (2013) 2010-2022.

J.S. Stevens, S.J. Byard, C.C. Seaton, G. Sadiq, R.J. Davey, S.L.M. Schroeder, Proton transfer and hydrogen bonding in the organic solid state: a combined XRD/XPS/ssNMR study of 17 organic acid-base complexes, Physical Chemistry Chemical Physics 16(3) (2014) 1150-1160.

H.-L. Lee, N.T. Flynn, X-RAY Photoelectron Spectroscopy, in: D.R. Vij (Ed.), Handbook of Applied Solid State Spectroscopy, Springer US, Boston, MA, 2006, pp. 485-507.

C. Dahlberg, A. Millqvist-Fureby, M. Schuleit, Surface composition and contact angle relationships for differently prepared solid dispersions, European Journal of Pharmaceutics and Biopharmaceutics 70(2) (2008) 478-485.

Y. Song, D. Zemlyanov, X. Chen, H. Nie, Z. Su, K. Fang, X. Yang, D. Smith, S. Byrn, J.W. Lubach, Acid-Base Interactions of Polystyrene Sulfonic Acid in Amorphous Solid Dispersions Using a Combined UV/FTIR/XPS/ssNMR Study, Mol Pharm 13(2) (2016) 483-92.

Y. Song, D. Zemlyanov, X. Chen, Z.Y. Su, H.C. Nie, J.W. Lubach, D. Smith, S. Byrn, R. Pinal, Acid-base interactions in amorphous solid dispersions of lumefantrine prepared by spray-drying and hot-melt extrusion using X-ray photoelectron spectroscopy, International Journal of Pharmaceutics 514(2) (2016) 456-464.

G.L.B. de Araujo, C.J. Benmore, S.R. Byrn, Local Structure of Ion Pair Interaction in Lapatinib Amorphous Dispersions characterized by Synchrotron X-Ray diffraction and Pair Distribution Function Analysis, Scientific Reports 7 (2017) 46367.

C.J. Gilmore, X-Ray Diffraction, Solid State Characterization of Pharmaceuticals, John Wiley & Sons, Ltd2011, pp. 35-70.

R.E. Dinnebier, Powder diffraction: theory and practice, Royal Society of Chemistry2008.

A.C. Rumondor, L.A. Stanford, L.S. Taylor, Effects of polymer type and storage relative humidity on the kinetics of felodipine crystallization from amorphous solid dispersions, Pharm Res 26(12) (2009) 2599-606.

I. Takeuchi, K. Shimakura, H. Kuroda, T. Nakajima, S. Goto, K. Makino, Estimation of Crystallinity of Nifedipine–Polyvinylpyrrolidone Solid Dispersion by Usage of Terahertz Time-Domain Spectroscopy and of X-Ray Powder Diffractometer, Journal of Pharmaceutical Sciences 104(12) (2015) 4307-4313.

T. Egami, S.J. Billinge, Underneath the Bragg peaks: structural analysis of complex materials, Newnes2012.

C.A. Young, A.L. Goodwin, Applications of pair distribution function methods to contemporary problems in materials chemistry, Journal of Materials Chemistry 21(18) (2011) 6464-6476.

K. Nollenberger, A. Gryczke, C. Meier, J. Dressman, M.U. Schmidt, S. Brühne, Pair distribution function X-ray analysis explains dissolution characteristics of felodipine melt extrusion products, Journal of Pharmaceutical Sciences 98(4) (2008) 1476-1486.

A. Newman, D. Engers, S. Bates, I. Ivanisevic, R.C. Kelly, G. Zografi, Characterization of Amorphous API:Polymer Mixtures Using X-Ray Powder Diffraction, Journal of Pharmaceutical Sciences 97(11) (2008) 4840-4856.

T. Dykhne, R. Taylor, A. Florence, S.J. Billinge, Data requirements for the reliable use of atomic pair distribution functions in amorphous pharmaceutical fingerprinting, Pharm Res 28(5) (2011) 1041-8.

C. Nunes, A. Mahendrasingam, R. Suryanarayanan, Quantification of crystallinity in substantially amorphous materials by synchrotron X-ray powder diffractometry, Pharm Res 22(11) (2005) 1942-53.

Q. Zhu, S.J. Toth, G.J. Simpson, H.Y. Hsu, L.S. Taylor, M.T. Harris, Crystallization and dissolution behavior of naproxen/polyethylene glycol solid dispersions, The journal of physical chemistry. B 117(5) (2013) 1494-500.

J.A. Newman, P.D. Schmitt, S.J. Toth, F. Deng, S. Zhang, G.J. Simpson, Parts per Million Powder X-ray Diffraction, Analytical Chemistry 87(21) (2015) 10950-10955.

A. Bohr, F. Wan, J. Kristensen, M. Dyas, E. Stride, S. Baldursdottír, M. Edirisinghe, M. Yang, Pharmaceutical microparticle engineering with electrospraying: the role of mixed solvent systems in particle formation and characteristics, Journal of Materials Science: Materials in Medicine 26(2) (2015) 1-13.

F. Wan, A. Bohr, M. Maltesen, S. Bjerregaard, C. Foged, J. Rantanen, M. Yang, Critical Solvent Properties Affecting the Particle Formation Process and Characteristics of Celecoxib-Loaded PLGA Microparticles via Spray-Drying, Pharmaceutical Research 30(4) (2013) 1065-1076.

G.W.H. Höhne, W. Hemminger, H.-J. Flammersheim, Theoretical Fundamentals of Differential Scanning Calorimeters, Differential Scanning Calorimetry, Springer1996, pp. 21-40.

K. Kawakami, T. Usui, M. Hattori, Understanding the glass-forming ability of active pharmaceutical ingredients for designing supersaturating dosage forms, Journal of Pharmaceutical Sciences 101(9) (2012) 3239-3248.

I. Weuts, D. Kempen, A. Decorte, G. Verreck, J. Peeters, M. Brewster, G. Van den Mooter, Phase behaviour analysis of solid dispersions of loperamide and two structurally related compounds with the polymers PVP-K30 and PVP-VA64, Eur J Pharm Sci 22(5) (2004) 375-85.

B. Van Eerdenbrugh, L.S. Taylor, Small scale screening to determine the ability of different polymers to inhibit drug crystallization upon rapid solvent evaporation, Mol Pharm 7(4) (2010) 1328-37.

J.A. Baird, B. Van Eerdenbrugh, L.S. Taylor, A classification system to assess the crystallization tendency of organic molecules from undercooled melts, J Pharm Sci 99(9) (2010) 3787-806.

D.T. Friesen, R. Shanker, M. Crew, D.T. Smithey, W.J. Curatolo, J.A.S. Nightingale, Hydroxypropyl Methylcellulose Acetate Succinate-Based Spray-Dried Dispersions: An Overview, Molecular Pharmaceutics 5(6) (2008) 1003-1019.

A.M. Kaushal, A.K. Bansal, Thermodynamic behavior of glassy state of structurally related compounds, European Journal of Pharmaceutics and Biopharmaceutics 69(3) (2008) 1067-1076.

X. Feng, X. Ye, J.-B. Park, W. Lu, J. Morott, B. Beissner, Z.J. Lian, E. Pinto, V. Bi, S. Porter, T. Durig, S. Majumdar, M.A. Repka, Evaluation of the recrystallization kinetics of hot-melt extruded polymeric solid dispersions using an improved Avrami equation, Drug Development and Industrial Pharmacy 0(0) (2014) 1-9.

M. Tobyn, J. Brown, A.B. Dennis, M. Fakes, Q. Gao, J. Gamble, Y.Z. Khimyak, G. McGeorge, C. Patel, W. Sinclair, P. Timmins, S. Yin, Amorphous drug–PVP dispersions: Application of theoretical, thermal and spectroscopic analytical techniques to the study of

a molecule with intermolecular bonds in both the crystalline and pure amorphous state, Journal of Pharmaceutical Sciences 98(9) (2009) 3456-3468.

A.C.F. Rumondor, P.J. Marsac, L.A. Stanford, L.S. Taylor, Phase Behavior of Poly(vinylpyrrolidone) Containing Amorphous Solid Dispersions in the Presence of Moisture, Molecular Pharmaceutics 6(5) (2009) 1492-1505.

G.P. Andrews, O.A. AbuDiak, D.S. Jones, Physicochemical characterization of hot melt extruded bicalutamide–polyvinylpyrrolidone solid dispersions, Journal of Pharmaceutical Sciences 99(3) (2010) 1322-1335.

F. Qian, J. Huang, Q. Zhu, R. Haddadin, J. Gawel, R. Garmise, M. Hussain, Is a distinctive single Tg a reliable indicator for the homogeneity of amorphous solid dispersion?, International Journal of Pharmaceutics 395(1-2) (2010) 232-235.

P.J. Marsac, T. Li, L.S. Taylor, Estimation of drug-polymer miscibility and solubility in amorphous solid dispersions using experimentally determined interaction parameters, Pharm Res 26(1) (2009) 139-51.

J. Tao, Y. Sun, G.G.Z. Zhang, L. Yu, Solubility of Small-Molecule Crystals in Polymers: d-Mannitol in PVP, Indomethacin in PVP/VA, and Nifedipine in PVP/VA, Pharmaceutical Research 26(4) (2009) 855-864.

A.N. Ghebremeskel, C. Vernavarapu, M. Lodaya, Use of surfactants as plasticizers in preparing solid dispersions of poorly soluble API: Selection of polymer-surfactant

combinations using solubility parameters and testing the processability, International Journal of Pharmaceutics 328(2) (2007) 119-129.

M.C. Righetti, C. Cardelli, M. Scalari, E. Tombari, G. Conti, Thermodynamics of mixing of poly(vinyl chloride) and poly(ethylene-co-vinyl acetate), Polymer 43(18) (2002) 5035-5042.

P. Gupta, V.K. Kakumanu, A.K. Bansal, Stability and solubility of celecoxib-PVP amorphous dispersions: a molecular perspective, Pharm Res 21(10) (2004) 1762-9.

M. Vasanthavada, W.Q. Tong, Y. Joshi, M.S. Kislalioglu, Phase Behavior of amorphous molecular dispersions I: Determination of the degree and mechanism of solid solubility, Pharmaceutical Research 21(9) (2004) 1598-1606.

M. Vasanthavada, W.Q. Tong, Y. Joshi, M.S. Kislalioglu, Phase behavior of amorphous molecular dispersions - II: Role of hydrogen bonding in solid solubility and phase separation kinetics, Pharmaceutical Research 22(3) (2005) 440-448.

P. Tong, L.S. Taylor, G. Zografi, Influence of Alkali Metal Counterions on the Glass Transition Temperature of Amorphous Indomethacin Salts, Pharmaceutical Research 19(5) (2002) 649-654.

I. Weuts, D. Kempen, G. Verreck, J. Peeters, M. Brewster, N. Blaton, G. Van den Mooter, Salt formation in solid dispersions consisting of polyacrylic acid as a carrier and three basic model compounds resulting in very high glass transition temperatures and constant

dissolution properties upon storage, European Journal of Pharmaceutical Sciences 25(4–5) (2005) 387-393.

L. Yu, Amorphous pharmaceutical solids: preparation, characterization and stabilization, Advanced Drug Delivery Reviews 48(1) (2001) 27-42.

A.C.F. Rumondor, I. Ivanisevic, S. Bates, D.E. Alonzo, L.S. Taylor, Evaluation of Drug-Polymer Miscibility in Amorphous Solid Dispersion Systems, Pharmaceutical Research 26(11) (2009) 2523-2534.

L.C. Grisedale, M.J. Jamieson, P. Belton, S.A. Barker, D.Q.M. Craig, Characterization and Quantification of Amorphous Material in Milled and Spray-Dried Salbutamol Sulfate: A Comparison of Thermal, Spectroscopic, and Water Vapor Sorption Approaches, Journal of Pharmaceutical Sciences 100(8) (2011) 3114-3129.

B. Shah, V.K. Kakumanu, A.K. Bansal, Analytical techniques for quantification of amorphous/crystalline phases in pharmaceutical solids, Journal of Pharmaceutical Sciences 95(8) (2006) 1641-1665.

P. Mistry, S. Mohapatra, T. Gopinath, F.G. Vogt, R. Suryanarayanan, Role of the Strength of Drug–Polymer Interactions on the Molecular Mobility and Crystallization Inhibition in Ketoconazole Solid Dispersions, Molecular Pharmaceutics (2015).

O. Korhonen, C. Bhura, M.J. Pikal, Correlation between molecular mobility and crystal growth of amorphous phenobarbital and phenobarbital with polyvinylpyrrolidone and L-proline, Journal of Pharmaceutical Sciences 97(9) (2008) 3830-3841.

Y. Aso, S. Yoshioka, S. Kojima, Molecular mobility-based estimation of the crystallization rates of amorphous nifedipine and phenobarbital in poly(vinylpyrrolidone) solid dispersions, J Pharm Sci 93(2) (2004) 384-91.

L. Yu, Surface mobility of molecular glasses and its importance in physical stability, Advanced Drug Delivery Reviews 100 (2016) 3-9.

D.Q.M. Craig, V.L. Kett, C.S. Andrews, P.G. Royall, Pharmaceutical Applications of Micro-Thermal Analysis, Journal of Pharmaceutical Sciences 91(5) (2002) 1201-1213.

X. Dai, J.G. Moffat, J. Wood, M. Reading, Thermal scanning probe microscopy in the development of pharmaceuticals, Advanced Drug Delivery Reviews 64(5) (2012) 449-460.

K. Six, J. Murphy, I. Weuts, D.M. Craig, G. Verreck, J. Peeters, M. Brewster, G. Van den Mooter, Identification of Phase Separation in Solid Dispersions of Itraconazole and Eudragit® E100 Using Microthermal Analysis, Pharmaceutical Research 20(1) (2003) 135-138.

L. Harding, W.P. King, X. Dai, D.Q. Craig, M. Reading, Nanoscale characterisation and imaging of partially amorphous materials using local thermomechanical analysis and heated tip AFM, Pharm Res 24(11) (2007) 2048-54.

J. Zhang, M. Bunker, X. Chen, A.P. Parker, N. Patel, C.J. Roberts, Nanoscale thermal analysis of pharmaceutical solid dispersions, International Journal of Pharmaceutics 380(1–2) (2009) 170-173.

S. Qi, J.G. Moffat, Z. Yang, Early Stage Phase Separation in Pharmaceutical Solid Dispersion Thin Films under High Humidity: Improved Spatial Understanding Using Probe-Based Thermal and Spectroscopic Nanocharacterization Methods, Molecular Pharmaceutics 10(3) (2013) 918-930.

M. Alhijjaj, M. Reading, P. Belton, S. Qi, Thermal Analysis by Structural Characterization as a Method for Assessing Heterogeneity in Complex Solid Pharmaceutical Dosage Forms, Anal Chem 87(21) (2015) 10848-55.

M. Alhijjaj, S. Yassin, M. Reading, J.A. Zeitler, P. Belton, S. Qi, Characterization of Heterogeneity and Spatial Distribution of Phases in Complex Solid Dispersions by Thermal Analysis by Structural Characterization and X-ray Micro Computed Tomography, Pharmaceutical Research 34(5) (2017) 971-989.

A. Heinz, C.J. Strachan, K.C. Gordon, T. Rades, Analysis of solid-state transformations of pharmaceutical compounds using vibrational spectroscopy, Journal of Pharmacy and Pharmacology 61(8) (2009) 971-988.

B. Tian, X. Tang, L.S. Taylor, Investigating the Correlation between Miscibility and Physical Stability of Amorphous Solid Dispersions Using Fluorescence-Based Techniques, Mol. Pharmaceutics (2016) Ahead of Print.
226

H.G. Brittain, Spectroscopy of pharmaceutical solids, Taylor & Francis New York2006.

G.A. Ilevbare, L.S. Taylor, Liquid–Liquid Phase Separation in Highly Supersaturated Aqueous Solutions of Poorly Water-Soluble Drugs: Implications for Solubility Enhancing Formulations, Crystal Growth & Design 13(4) (2013) 1497-1509.

S. Raina, D. Alonzo, G.Z. Zhang, Y. Gao, L. Taylor, Using Environment-Sensitive Fluorescent Probes to Characterize Liquid-Liquid Phase Separation in Supersaturated Solutions of Poorly Water Soluble Compounds, Pharmaceutical Research (2015) 1-14.

A.C. Rumondor, L.S. Taylor, Effect of polymer hygroscopicity on the phase behavior of amorphous solid dispersions in the presence of moisture, Mol Pharm 7(2) (2010) 477-90.

X. Feng, A. Vo, H. Patil, R.V. Tiwari, A.S. Alshetaili, M.B. Pimparade, M.A. Repka, The effects of polymer carrier, hot melt extrusion process and downstream processing parameters on the moisture sorption properties of amorphous solid dispersions, J Pharm Pharmacol 68(5) (2016) 692-704.

B. Van Eerdenbrugh, M. Lo, K. Kjoller, C. Marcott, L.S. Taylor, Nanoscale mid-infrared imaging of phase separation in a drug-polymer blend, J Pharm Sci 101(6) (2012) 2066-73.

L. Saerens, C. Vervaet, J.P. Remon, T. De Beer, Process monitoring and visualization solutions for hot-melt extrusion: a review, Journal of Pharmacy and Pharmacology 66(2) (2014) 180-203.

227

A. Almeida, L. Saerens, T. De Beer, J.P. Remon, C. Vervaet, Upscaling and in-line process monitoring via spectroscopic techniques of ethylene vinyl acetate hot-melt extruded formulations, International journal of pharmaceutics 439(1) (2012) 223-229.

S.G. Kazarian, A.V. Ewing, Applications of Fourier transform infrared spectroscopic imaging to tablet dissolution and drug release, Expert Opinion on Drug Delivery 10(9) (2013) 1207-1221.

M. Pudlas, S.O. Kyeremateng, L.A.M. Williams, J.A. Kimber, H. van Lishaut, S.G. Kazarian, G.H. Woehrle, Analyzing the impact of different excipients on drug release behavior in hot-melt extrusion formulations using FTIR spectroscopic imaging, European Journal of Pharmaceutical Sciences 67(0) (2015) 21-31.

K. Punčochová, A.V. Ewing, M. Gajdošová, T. Pekárek, J. Beránek, S.G. Kazarian, F. Štěpánek, The Combined Use of Imaging Approaches to Assess Drug Release from Multicomponent Solid Dispersions, Pharmaceutical Research (2016) 1-12.

A. Paudel, D. Raijada, J. Rantanen, Raman spectroscopy in pharmaceutical product design, Advanced Drug Delivery Reviews 89 (2015) 3-20.

A. Lust, C.J. Strachan, P. Veski, J. Aaltonen, J. Heinämäki, J. Yliruusi, K. Kogermann, Amorphous solid dispersions of piroxicam and Soluplus®: Qualitative and quantitative analysis of piroxicam recrystallization during storage, International Journal of Pharmaceutics 486(1–2) (2015) 306-314.

G.P. Andrews, H. Zhai, S. Tipping, D.S. Jones, Characterisation of the Thermal, Spectroscopic and Drug Dissolution Properties of Mefenamic Acid and Polyoxyethylene-Polyoxypropylene Solid Dispersions, Journal of Pharmaceutical Sciences 98(12) (2009) 4545-4556.

F. Tres, K. Treacher, J. Booth, L.P. Hughes, S.A.C. Wren, J.W. Aylott, J.C. Burley, Real time Raman imaging to understand dissolution performance of amorphous solid dispersions, Journal of Controlled Release 188(0) (2014) 53-60.

A. Paudel, M. Geppi, G. Van den Mooter, Structural and Dynamic Properties of Amorphous Solid Dispersions: The Role of Solid-State Nuclear Magnetic Resonance Spectroscopy and Relaxometry, Journal of Pharmaceutical Sciences 103(9) (2014) 2635-2662.

Y. Aso, S. Yoshioka, S. Kojima, Relationship Between the Crystallization Rates of Amorphous Nifedipine, Phenobarbital, and Flopropione, and Their Molecular Mobility as Measured by Their Enthalpy Relaxation and 1H NMR Relaxation Times, Journal of Pharmaceutical Sciences 89(3) (2000) 408-416.

Y. Aso, S. Yoshioka, T. Miyazaki, T. Kawanishi, Feasibility of ^{19}F-NMR for Assessing the Molecular Mobility of Flufenamic Acid in Solid Dispersions, Chemical and Pharmaceutical Bulletin 57(1) (2009) 61-64.

T.N. Pham, S.A. Watson, A.J. Edwards, M. Chavda, J.S. Clawson, M. Strohmeier, F.G. Vogt, Analysis of Amorphous Solid Dispersions Using 2D Solid-State NMR and 1H T1 Relaxation Measurements, Molecular Pharmaceutics 7(5) (2010) 1667-1691.

A. Ito, T. Watanabe, S. Yada, T. Hamaura, H. Nakagami, K. Higashi, K. Moribe, K. Yamamoto, Prediction of recrystallization behavior of troglitazone/polyvinylpyrrolidone solid dispersion by solid-state NMR, International Journal of Pharmaceutics 383(1–2) (2010) 18-23.

Y. Song, X. Yang, X. Chen, H. Nie, S. Byrn, J.W. Lubach, Investigation of Drug–Excipient Interactions in Lapatinib Amorphous Solid Dispersions Using Solid-State NMR Spectroscopy, Molecular Pharmaceutics 12(3) (2015) 857-866.

C. Dahlberg, S.V. Dvinskikh, M. Schuleit, I. Furó, Polymer Swelling, Drug Mobilization and Drug Recrystallization in Hydrating Solid Dispersion Tablets Studied by Multinuclear NMR Microimaging and Spectroscopy, Molecular Pharmaceutics 8(4) (2011) 1247-1256.

N. Fotaki, C.M. Long, K. Tang, H. Chokshi, Dissolution of Amorphous Solid Dispersions: Theory and Practice, in: N. Shah, H. Sandhu, D.S. Choi, H. Chokshi, A.W. Malick (Eds.), Amorphous Solid Dispersions: Theory and Practice, Springer New York, New York, NY, 2014, pp. 487-514.

J. Østergaard, J. Lenke, S.S. Jensen, Y. Sun, F. Ye, UV imaging for in vitro dissolution and release studies: initial experiences, Dissolut Technol 21(4) (2014) 27-38.

Y. Sun, J. Østergaard, Application of UV Imaging in Formulation Development, Pharmaceutical Research (2016) 1-12.

S. Wartewig, R.H.H. Neubert, Pharmaceutical applications of Mid-IR and Raman spectroscopy, Advanced Drug Delivery Reviews 57(8) (2005) 1144-1170.

D.E. Alonzo, G.G. Zhang, D. Zhou, Y. Gao, L.S. Taylor, Understanding the behavior of amorphous pharmaceutical systems during dissolution, Pharm Res 27(4) (2010) 608-18.

Z.A. Langham, J. Booth, L.P. Hughes, G.K. Reynolds, S.A.C. Wren, Mechanistic insights into the dissolution of spray-dried amorphous solid dispersions, Journal of Pharmaceutical Sciences 101(8) (2012) 2798-2810.

F. Tres, S.R. Coombes, A.R. Phillips, L.P. Hughes, S.A. Wren, J.W. Aylott, J.C. Burley, Investigating the Dissolution Performance of Amorphous Solid Dispersions Using Magnetic Resonance Imaging and Proton NMR, Molecules 20(9) (2015) 16404-18.

S.R. Coombes, L.P. Hughes, A.R. Phillips, S.A.C. Wren, Proton NMR: A New Tool for Understanding Dissolution, Analytical Chemistry 86(5) (2014) 2474-2480.

J. Kanzer, S. Hupfeld, T. Vasskog, I. Tho, P. Hölig, M. Mägerlein, G. Fricker, M. Brandl, In situ formation of nanoparticles upon dispersion of melt extrudate formulations in aqueous medium assessed by asymmetrical flow field-flow fractionation, Journal of Pharmaceutical and Biomedical Analysis 53(3) (2010) 359-365.

P. Harmon, K. Galipeau, W. Xu, C. Brown, W.P. Wuelfing, Mechanism of Dissolution-Induced Nanoparticle Formation from a Copovidone-Based Amorphous Solid Dispersion, Mol Pharm (2016).

S. Colombo, M. Brisander, J. Haglöf, P. Sjövall, P. Andersson, J. Østergaard, M. Malmsten, Matrix effects in nilotinib formulations with pH-responsive polymer produced by carbon dioxide-mediated precipitation, International Journal of Pharmaceutics 494(1) (2015) 205-217.

A. Paudel, J. Meeus, G.V.d. Mooter, Structural Characterization of Amorphous Solid Dispersions, in: N. Shah, H. Sandhu, D.S. Choi, H. Chokshi, A.W. Malick (Eds.), Amorphous Solid Dispersions: Theory and Practice, Springer New York, New York, NY, 2014, pp. 421-485.

S.-Y. Lin, S.-L. Wang, Advances in simultaneous DSC–FTIR microspectroscopy for rapid solid-state chemical stability studies: Some dipeptide drugs as examples, Advanced Drug Delivery Reviews 64(5) (2012) 461-478.

T. Wu, S.Y. Lin, H.L. Lin, Y.T. Huang, Simultaneous DSC-FTIR Microspectroscopy Used to Screen and Detect the Co-crystal Formation in Real Time, Bioorganic & Medicinal Chemistry Letters (2011).

J. Huang, M. Dali, Evaluation of integrated Raman-DSC technology in early pharmaceutical development: Characterization of polymorphic systems, Journal of Pharmaceutical and Biomedical Analysis 86 (2013) 92-99.

B. Pili, C. Bourgaux, H. Amenitsch, G. Keller, S. Lepêtre-Mouelhi, D. Desmaële, P. Couvreur, M. Ollivon, Interaction of a new anticancer prodrug, gemcitabine–squalene, with a model membrane: Coupled DSC and XRD study, Biochimica et Biophysica Acta (BBA) - Biomembranes 1798(8) (2010) 1522-1532.

A. Dazzi, C.B. Prater, Q. Hu, D.B. Chase, J.F. Rabolt, C. Marcott, AFM–IR: Combining Atomic Force Microscopy and Infrared Spectroscopy for Nanoscale Chemical Characterization, Applied Spectroscopy 66(12) (2012) 1365-1384.

S.-Y. Lin, C.-J. Lee, Y.-Y. Lin, Drug-polymer interaction affecting the mechanical properties, adhesion strength and release kinetics of piroxicam-loaded Eudragit E films plasticized with different plasticizers, Journal of Controlled Release 33(3) (1995) 375-381.

N. Li, L.S. Taylor, Nanoscale Infrared, Thermal, and Mechanical Characterization of Teleprevir–Polymer Miscibility in Amorphous Solid Dispersions Prepared by Solvent Evaporation, Molecular Pharmaceutics 13(3) (2016) 1123-1136.

J. Sibik, K. Löbmann, T. Rades, J.A. Zeitler, Predicting Crystallization of Amorphous Drugs with Terahertz Spectroscopy, Molecular Pharmaceutics 12(8) (2015) 3062-3068.

J.A. Zeitler, P.F. Taday, M. Pepper, T. Rades, Relaxation and crystallization of amorphous carbamazepine studied by terahertz pulsed spectroscopy, Journal of Pharmaceutical Sciences 96(10) (2007) 2703-2709.

J. Sibik, J.A. Zeitler, Direct measurement of molecular mobility and crystallisation of amorphous pharmaceuticals using terahertz spectroscopy, Advanced Drug Delivery Reviews 100 (2016) 147-157.

S.P. Bhardwaj, R. Suryanarayanan, Molecular Mobility as an Effective Predictor of the Physical Stability of Amorphous Trehalose, Molecular Pharmaceutics 9(11) (2012) 3209-3217.

K. Grzybowska, S. Capaccioli, M. Paluch, Recent developments in the experimental investigations of relaxations in pharmaceuticals by dielectric techniques at ambient and elevated pressure, Advanced Drug Delivery Reviews 100 (2016) 158-182.

K. Kothari, V. Ragoonanan, R. Suryanarayanan, The Role of Polymer Concentration on the Molecular Mobility and Physical Stability of Nifedipine Solid Dispersions, Molecular Pharmaceutics 12(5) (2015) 1477-1484.

J.F. Gamble, M. Terada, C. Holzner, L. Lavery, S.J. Nicholson, P. Timmins, M. Tobyn, Application of X-ray microtomography for the characterisation of hollow polymer-stabilised spray dried amorphous dispersion particles, International Journal of Pharmaceutics 510(1) (2016) 1-8.

J. Wong, D. D'Sa, M. Foley, J.G.Y. Chan, H.-K. Chan, NanoXCT: A Novel Technique to Probe the Internal Architecture of Pharmaceutical Particles, Pharmaceutical Research 31(11) (2014) 3085-3094.

234

M. Álvarez-Murga, P. Bleuet, J.L. Hodeau, Diffraction/scattering computed tomography for three-dimensional characterization of multi-phase crystalline and amorphous materials, Journal of Applied Crystallography 45(6) (2012) 1109-1124.

K. Kawakami, Supersaturation and crystallization: non-equilibrium dynamics of amorphous solid dispersions for oral drug delivery, Expert Opinion on Drug Delivery (2016) 1-9.

S. Janssens, G. Van den Mooter, Review: physical chemistry of solid dispersions, Journal of Pharmacy and Pharmacology 61(12) (2009) 1571-1586.

T. Vasconcelos, S. Marques, J. das Neves, B. Sarmento, Amorphous solid dispersions: Rational selection of a manufacturing process, Advanced drug delivery reviews 100 (2016) 85-101.

Recall, <http://www.fda.gov/Safety/Recalls/ArchiveRecalls/default.htm>. (2011-2013).

Rumondor, A. C. F.; Dhareshwar, S. S.; Kesisoglou, F. Amorphous solid dispersions or prodrugs: complementary strategies to increase drug absorption. J. Pharm. Sci. 2016, 105(9), 2498-2508.

Williams III, R. O.; Watts, A. B.; Miller, D. A., Eds. Formulating poorly water-soluble drugs. Springer: New York, 2012.

Jain, S.; Patel, N.; Lin, S. Solubility and dissolution enhancement strategies: current understanding and recent trends. Drug Dev. Ind. Pharm. 2015, 41(6), 875-887.

Serajuddin, A. T. M. Salt formation to improve drug solubility. Adv. Drug Delivery Rev. 2007, 59(7), 603-616.

Kumar, L.; Baheti, A.; Bansal, A. K. Effect of a counterion on the glass transition temperature (Tg) during lyophilization of ganciclovir salt forms. Mol. Pharmaceutics 2010, 8(1), 309-314.

Towler, C. S.; Li, T.; Wikström, H.; Remick, D. M.; Sanchez-Felix, M. V.; Taylor, L. S. An investigation into the influence of counterion on the properties of some amorphous organic salts. Mol. Pharmaceutics 2008, 5(6), 946-955.

Stephenson, G. A.; Aburub, A.; Woods, T. A. Physical stability of salts of weak bases in the solid-state. J. Pharm. Sci. 2011, 100(5), 1607-1617.

Shah, N.; Sandhu, H.; Choi, D. S.; Chokshi, H.; Malick, A. W., Eds. Amorphous solid dispersions-theory and practice, Springer: New York, 2014.

Chiou, W. L.; Riegelman, S. Pharmaceutical applications of solid dispersion systems. J. Pharm. Sci. 1971, 60(9), 1281-1302.

Lee, T. W.; Boersen, N. A.; Hui, H. W.; Chow, S. F.; Wan, K. Y.; Chow, A. H. Delivery of poorly soluble compounds by amorphous solid dispersions. Curr. Pharm. Des. 2014, 20(3), 303-324.

Krupa, A.; Majda, D.; Jachowicz, R.; Mozgawa, W. Solid-state interaction of ibuprofen and Neusilin US2. Thermochim. Acta 2010, 509(1–2), 12-17.

Telang, C.; Mujumdar, S.; Mathew, M. Improved physical stability of amorphous state through acid base interactions. J. Pharm. Sci. 2009, 98(6), 2149-2159.

Jensen, K. T.; Larsen, F. H.; Cornett, C.; Löbmann, K.; Grohganz, H.; Rades, T. Formation mechanism of coamorphous drug–amino acid mixtures. Mol. Pharmaceutics 2015, 12(7), 2484-2492.

Weuts, I.; Kempen, D.; Verreck, G.; Peeters, J.; Brewster, M.; Blaton, N.; Van den Mooter, G. Salt formation in solid dispersions consisting of polyacrylic acid as a carrier and three basic model compounds resulting in very high glass transition temperatures and constant dissolution properties upon storage. Eur. J. Pharm. Sci. 2005, 25(4–5), 387-393.

Laitinen, R.; Löbmann, K.; Strachan, C. J.; Grohganz, H.; Rades, T. Emerging trends in the stabilization of amorphous drugs. Int. J. Pharm. 2013, 453(1), 65-79.

Mallick, S.; Pattnaik, S.; Swain, K.; De, P. K.; Saha, A.; Ghoshal, G.; Mondal, A. Formation of physically stable amorphous phase of ibuprofen by solid state milling with kaolin. Eur. J. Pharm. Biopharm. 2008, 68(2), 346-351.

Dengale, S. J.; Grohganz, H.; Rades, T.; Löbmann, K. Recent advances in co-amorphous drug formulations. Adv. Drug Delivery Rev. 2016, 100, 116-125.

Song, Y.; Yang, X.; Chen, X.; Nie, H.; Byrn, S.; Lubach, J. W. Investigation of drug–excipient interactions in lapatinib amorphous solid dispersions using solid-state NMR spectroscopy. Mol. Pharmaceutics 2015, 12(3), 857-866.

Song, Y.; Zemlyanov, D.; Chen, X.; Nie, H.; Su, Z.; Fang, K.; Yang, X.; Smith, D.; Byrn, S.; Lubach, J. W. Acid-base interactions of polystyrene sulfonic acid in amorphous solid dispersions using a combined UV/FTIR/XPS/ssNMR study. Mol. Pharmaceutics 2016, 13(2), 483-492.

Hasa, D.; Perissutti, B.; Cepek, C.; Bhardwaj, S.; Carlino, E.; Grassi, M.; Invernizzi, S.; Voinovich, D. Drug salt formation via mechanochemistry: the case study of vincamine. Mol. Pharmaceutics 2013, 10(1), 211-224.

Tiwari, R. V.; Patil, H.; Repka, M. A. Contribution of hot-melt extrusion technology to advance drug delivery in the 21st century. Expert Opin. Drug Delivery 2016, 13(3), 451-464.

Bouvier, J.M.; Campanella, O. H., Extrusion Processing Technology: Food and Non-Food Biomaterials. John Wiley & Sons: Hoboken,NJ, 2014.

Moad, G. Chemical modification of starch by reactive extrusion. Prog. Polym. Sci. 2011, 36(2), 218-237.

Raquez, J.-M.; Narayan, R.; Dubois, P. Recent advances in reactive extrusion processing of biodegradable polymer-based compositions. Macromol. Mater. Eng. 2008, 293(6), 447-470.

Daurio, D.; Nagapudi, K.; Alvarez-Núñez, F., Manufacture of pharmaceutically relevant materials by mechanochemistry using twin screw extrusion. In melt extrusion: materials, technology and drug product design, Repka, M. A.; Langley, N.; DiNunzio, J., Eds. Springer New York: New York, NY, 2013; pp 223-242.

Liu, X.; Lu, M.; Guo, Z.; Huang, L.; Feng, X.; Wu, C. Improving the chemical stability of amorphous solid dispersion with cocrystal technique by hot melt extrusion. Pharm. Res. 2012, 29(3), 806-17.

Kindermann, C.; Matthée, K.; Sievert, F.; Breitkreutz, J. Electrolyte-stimulated biphasic dissolution profile and stability enhancement for tablets containing drug-polyelectrolyte complexes. Pharm. Res. 2012, 29(10), 2710-2721.

Moustafine, R. I.; Bukhovets, A. V.; Sitenkov, A. Y.; Kemenova, V. A.; Rombaut, P.; Van den Mooter, G. Eudragit EPO as a complementary material for designing oral drug delivery systems with controlled release properties: comparative evaluation of new interpolyelectrolyte complexes with countercharged Eudragit L100 copolymers. Mol. Pharmaceutics 2013, 10(7), 2630-2641.

Herzfeldt, C. D.; Kümmel, R. Dissociation constants, solubilities and dissolution rates of some selected nonsteroidal antiinflammatories. Drug Dev. Ind. Pharm. 1983, 9(5), 767-793.

Allesø, M.; Chieng, N.; Rehder, S.; Rantanen, J.; Rades, T.; Aaltonen, J. Enhanced dissolution rate and synchronized release of drugs in binary systems through formulation: Amorphous naproxen–cimetidine mixtures prepared by mechanical activation. J. Controlled Release 2009, 136(1), 45-53.

Svärd, M.; Hjorth, T.; Bohlin, M.; Rasmuson, Å. C. Calorimetric properties and solubility in five pure organic solvents of N-methyl-d-glucamine (meglumine). J. Chem. Eng. Data 2016, 61(3), 1199-1204.

Childs, S. L.; Stahly, G. P.; Park, A. The salt−cocrystal continuum: The influence of crystal structure on ionization State. Mol. Pharmaceutics 2007, 4(3), 323-338.

Cruz-Cabeza, A. J. Acid-base crystalline complexes and the pKa rule. CrystEngComm 2012, 14(20), 6362-6365.

Veronesi, P. A., Water soluble salts of an NSAID with meglumine/glucamine. U.S. Patent 4,748,174 A, May 31, 1988.

Kraudelt, H.; Schilde, U.; Uhlemann, E., Crystal structures of 1-methylamino-D-1-deoxy-glucitol, C7H17NO5 and 1-methylamino-D-1-deoxy-glucitol hydrochloride, C7H18CINO5. Z. Kristallogr. − New Cryst. Struct.1998, 213, 177-179.

James, S. L.; Adams, C. J.; Bolm, C.; Braga, D.; Collier, P.; Friscic, T.; Grepioni, F.; Harris, K. D. M.; Hyett, G.; Jones, W.; Krebs, A.; Mack, J.; Maini, L.; Orpen, A. G.; Parkin, I. P.; Shearouse, W. C.; Steed, J. W.; Waddell, D. C. Mechanochemistry: opportunities for new and cleaner synthesis. Chem. Soc. Rev. 2012, 41(1), 413-447.

Baird, J. A.; Taylor, L. S. Evaluation of amorphous solid dispersion properties using thermal analysis techniques. Adv. Drug Delivery Rev. 2012, 64(5), 396-421.

Tong, P.; Taylor, L. S.; Zografi, G. Influence of alkali metal counterions on the glass transition temperature of amorphous indomethacin salts. Pharm. Res. 2002, 19(5), 649-654.

Cassimiro, D. L.; Kobelnik, M.; Ribeiro, C. A.; Crespi, M. S.; Boralle, N. Structural aspects, thermal behavior, and stability of a self-assembled supramolecular polymer derived from flunixin–meglumine supramolecular adducts. Thermochim. Acta 2012, 529, 59-67.

Stepanovs, D.; Jure, M.; Yanichev, A.; Belyakov, S.; Mishnev, A. Molecular salts of propranolol with dicarboxylic acids: diversity of stoichiometry, supramolecular structures and physicochemical properties. CrystEngComm 2015, 17(47), 9023-9028.

Friščić, T.; Halasz, I.; Beldon, P. J.; Belenguer, A. M.; Adams, F.; Kimber, S. A. J.; Honkimäki, V.; Dinnebier, R. E. Real-time and in situ monitoring of mechanochemical milling reactions. Nat. Chem. 2013, 5(1), 66-73.

Seefeldt, K.; Miller, J.; Alvarez-Nunez, F.; Rodriguez-Hornedo, N. Crystallization pathways and kinetics of carbamazepine-nicotinamide cocrystals from the amorphous state by in situ thermomicroscopy, spectroscopy, and calorimetry studies. J. Pharm. Sci. 2007, 96(5), 1147-1158.

Sun, C. C. Cocrystallization for successful drug delivery. Expert Opin. Drug Delivery 2013, 10(2), 201-213.

Neurohr, C.; Revelli, A. L.; Billot, P.; Marchivie, M.; Lecomte, S.; Laugier, S.; Massip, S.; Subra-Paternault, P. Naproxen–nicotinamide cocrystals produced by CO2 antisolvent. J. Supercrit. Fluids 2013, 83, 78-85.

Bogdanova, S.; Pajeva, I.; Nikolova, P.; Tsakovska, I.; Müller, B. Interactions of poly(vinylpyrrolidone) with ibuprofen and naproxen: Experimental and modeling studies. Pharm. Res. 2005, 22(5), 806-815.

Mura, P.; Bettinetti, G. P.; Cirri, M.; Maestrelli, F.; Sorrenti, M.; Catenacci, L. Solid-state characterization and dissolution properties of Naproxen–Arginine–Hydroxypropyl-β-cyclodextrin ternary system. Eur. J. Pharm. Biopharm. 2005, 59(1), 99-106.

Lin-Vien, D.; Colthup, N. B.; Fateley, W. G.; Grasselli, J. G.; Eds. The handbook of infrared and Raman characteristic frequencies of organic molecules. Academic Press: New York 1991.

242

Stevens, J. S.; Byard, S. J.; Seaton, C. C.; Sadiq, G.; Davey, R. J.; Schroeder, S. L. M. Proton transfer and hydrogen bonding in the organic solid state: a combined XRD/XPS/ssNMR study of 17 organic acid-base complexes. Phys. Chem. Chem. Phys. 2014, 16(3), 1150-1160.

Stevens, J. S.; Newton, L. K.; Jaye, C.; Muryn, C. A.; Fischer, D. A.; Schroeder, S. L. M. Proton transfer, hydrogen bonding, and disorder: Nitrogen near-edge X-ray absorption fine structure and X-ray photoelectron spectroscopy of bipyridine–acid salts and co-crystals. Cryst. Growth Des. 2015, 15(4), 1776-1783.

Baird, J. A.; Van Eerdenbrugh, B.; Taylor, L. S. A classification system to assess the crystallization tendency of organic molecules from undercooled melts. J. Pharm. Sci. 2010, 99(9), 3787-806.

He, Y.; Ho, C. Amorphous solid dispersions: Utilization and challenges in drug discovery and development. J. Pharm. Sci. 2015, 104(10), 3237-3258.

Löbmann, K.; Laitinen, R.; Grohganz, H.; Strachan, C.; Rades, T.; Gordon, K. C. A theoretical and spectroscopic study of co-amorphous naproxen and indomethacin. Int. J. Pharm. 2013, 453(1), 80-87.

Löbmann, K.; Laitinen, R.; Grohganz, H.; Gordon, K. C.; Strachan, C.; Rades, T. Coamorphous drug systems: Enhanced physical stability and dissolution rate of indomethacin and naproxen. Mol. Pharmaceutics 2011, 8(5), 1919-1928.

Ueda, H.; Muranushi, N.; Sakuma, S.; Ida, Y.; Endoh, T.; Kadota, K.; Tozuka, Y. A Strategy for co-former selection to design stable co-amorphous formations based on physicochemical properties of non-steroidal inflammatory drugs. Pharm. Res. 2016, 33(4), 1018-1029.

Perlovich, G. L.; Kurkov, S. V.; Kinchin, A. N.; Bauer-Brandl, A. Thermodynamics of solutions III: Comparison of the solvation of (+)-naproxen with other NSAIDs. Eur. J. Pharm. Biopharm. 2004, 57(2), 411-420.

Cao, X.J.; Sun, C.R.; Pan, Y.J. The complex of flunixin and meglumine. Acta Cryst. 2003, 59(10), 1471-1473.

Paudel, A.; Loyson, Y.; Van den Mooter, G. An investigation into the effect of spray drying temperature and atomizing conditions on miscibility, physical stability, and performance of naproxen–PVP K 25 solid dispersions. J. Pharm. Sci. 2013, 102(4), 1249-1267.

Nair, R.; Nyamweya, N.; Gonen, S.; Martinez-Miranda, L. J.; Hoag, S. W. Influence of various drugs on the glass transition temperature of poly(vinylpyrrolidone): a thermodynamic and spectroscopic investigation. Int. J. Pharm.2001, 225(1-2), 83-96.

Tran, T. T.D.; Tran, P. H.L.; Choi, H.G.; Han, H.K.; Lee, B.J. The roles of acidifiers in solid dispersions and physical mixtures. Int. J. Pharm.2010, 384(1–2), 60-66.

Tran, P. H. L.; Tran, H. T. T.; Lee, B.-J. Modulation of microenvironmental pH and crystallinity of ionizable telmisartan using alkalizers in solid dispersions for controlled release. J. Controlled Release 2008, 129(1), 59-65.

Nielsen, L. H.; Gordon, S.; Holm, R.; Selen, A.; Rades, T.; Müllertz, A. Preparation of an amorphous sodium furosemide salt improves solubility and dissolution rate and leads to a faster Tmax after oral dosing to rats. Eur. J. Pharm. Biopharm. 2013, 85(3, Part B), 942-951.

Kadoya, S.; Izutsu, K.I.; Yonemochi, E.; Terada, K.; Yomota, C.; Kawanishi, T. Glass-state amorphous salt solids formed by freeze-drying of amines and hydroxy carboxylic acids: effect of hydrogen-bonding and electrostatic interactions. Chem. Pharm. Bull. 2008, 56(6), 821-826.

Zhu, Z.; Yang, T.; Zhao, Y.; Gao, N.; Leng, D.; Ding, P. A simple method to improve the dissolution of repaglinide and exploration of its mechanism. Asian J. Pharm. Sci. 2014, 9(4), 218-225.

Tomasko, D. L.; Timko, M. T. Tailoring of specific interactions to modify the morphology of naproxen. J. Cryst. Growth 1999, 205(1–2), 233-243.

Paudel, A.; Nies, E.; Van den Mooter, G. Relating hydrogen-bonding interactions with the phase behavior of naproxen/PVP K 25 solid dispersions: Evaluation of solution-cast and quench-cooled films. Mol. Pharmaceutics 2012, 9(11), 3301-3317.

Abu-Huwaij, R., Assaf, S., Salem, M., Sallam, A., 2007. Mucoadhesive Dosage form of Lidocaine Hydrochloride: I. Mucoadhesive and Physicochemical Characterization. Drug Development and Industrial Pharmacy 33, 855-864.

Baghel, S., Cathcart, H., O'Reilly, N.J., 2016a. Polymeric Amorphous Solid Dispersions: A Review of Amorphization, Crystallization, Stabilization, Solid-State Characterization, and Aqueous Solubilization of Biopharmaceutical Classification System Class II Drugs. Journal of Pharmaceutical Sciences 105, 2527-2544.

Baghel, S., Cathcart, H., O'Reilly, N.J., 2016b. Theoretical and experimental investigation of drug-polymer interaction and miscibility and its impact on drug supersaturation in aqueous medium. European Journal of Pharmaceutics and Biopharmaceutics 107, 16-31.

Baird, J.A., Van Eerdenbrugh, B., Taylor, L.S., 2010. A classification system to assess the crystallization tendency of organic molecules from undercooled melts. J Pharm Sci 99, 3787-3806.

Borodkin, S., Yunker, M.H., 1970. Interaction of amine drugs with a polycarboxylic acid ion-exchange resin. Journal of Pharmaceutical Sciences 59, 481-486.

Bouvier, J.-M., Campanella, O.H., 2014. The Generic Extrusion Process II, Extrusion Processing Technology. John Wiley & Sons, Ltd, pp. 173-242.

Chen, X., Wen, H., Park, K., 2010. Challenges and New Technologies of Oral Controlled Release, Oral Controlled Release Formulation Design and Drug Delivery. John Wiley & Sons, Inc., pp. 257-277.

Cheow, W.S., Hadinoto, K., 2012. Green Amorphous Nanoplex as a New Supersaturating Drug Delivery System. Langmuir : the ACS journal of surfaces and colloids 28, 6265-6275.

Crawford, D.E., Miskimmin, C.K.G., Albadarin, A.B., Walker, G., James, S.L., 2017. Organic synthesis by Twin Screw Extrusion (TSE): continuous, scalable and solvent-free. Green Chemistry 19, 1507-1518.

Crowley, M.M., Zhang, F., Repka, M.A., Thumma, S., Upadhye, S.B., Battu, S.K., McGinity, J.W., Martin, C., 2007. Pharmaceutical applications of hot-melt extrusion: part I. Drug Dev Ind Pharm 33, 909-926.

Cui, Y., Frank, S.G., 2005. Characterization of supersaturated lidocaine/polyacrylate pressure sensitive adhesive systems: Thermal analysis and FT-IR. Journal of Pharmaceutical Sciences 95, 701-713.

De Robertis, S., Bonferoni, M.C., Elviri, L., Sandri, G., Caramella, C., Bettini, R., 2015. Advances in oral controlled drug delivery: the role of drug–polymer and interpolymer non-covalent interactions. Expert Opinion on Drug Delivery 12, 441-453.

Ferrero, C., Muñoz-Ruiz, A., Jiménez-Castellanos, M.R., 2000. Fronts movement as a useful tool for hydrophilic matrix release mechanism elucidation. International Journal of Pharmaceutics 202, 21-28.

Higuchi, T., 1961. Rate of release of medicaments from ointment bases containing drugs in suspension. Journal of pharmaceutical sciences 50, 874-875.

Janssens, S., Van den Mooter, G., 2009. Review: physical chemistry of solid dispersions. Journal of Pharmacy and Pharmacology 61, 1571-1586.

Jenquin, M.R., McGinity, J.W., 1994. Characterization of acrylic resin matrix films and mechanisms of drug-polymer interactions. International Journal of Pharmaceutics 101, 23-34.

Jimenez-Kairuz, A., Allemandi, D., Manzo, R., 2004. The improvement of aqueous chemical stability of a model basic drug by ion pairing with acid groups of polyelectrolytes. International journal of pharmaceutics 269, 149-156.

Jimenez-Kairuz, A.F., Llabot, J.M., Allemandi, D.A., Manzo, R.H., 2005. Swellable drug-polyelectrolyte matrices (SDPM). Characterization and delivery properties. Int J Pharm 288, 87-99.

Jimenez-Kairuz, A., Allemandi, D., Manzo, R.H., 2002. Mechanism of lidocaine release from carbomer–lidocaine hydrogels. Journal of pharmaceutical sciences 91, 267-272.

Kindermann, C., Matthée, K., Sievert, F., Breitkreutz, J., 2012. Electrolyte-Stimulated Biphasic Dissolution Profile and Stability Enhancement for Tablets Containing Drug-Polyelectrolyte Complexes. Pharmaceutical Research 29, 2710-2721.

Kindermann, C., Matthée, K., Strohmeyer, J., Sievert, F., Breitkreutz, J., 2011. Tailor-made release triggering from hot-melt extruded complexes of basic polyelectrolyte and poorly water-soluble drugs. European Journal of Pharmaceutics and Biopharmaceutics 79, 372-381.

Lankalapalli, S., Kolapalli, V.R.M., 2009. Polyelectrolyte Complexes: A Review of their Applicability in Drug Delivery Technology. Indian Journal of Pharmaceutical Sciences 71, 481-487.

Lee, H.L., Vasoya, J.M., Cirqueira, M.d.L., Yeh, K.L., Lee, T., Serajuddin, A.T.M., 2017. Continuous Preparation of 1:1 Haloperidol–Maleic Acid Salt by a Novel Solvent-Free Method Using a Twin Screw Melt Extruder. Molecular Pharmaceutics 14, 1278-1291.

Lin-Vien, D., Colthup, N.B., Fateley, W.G., Grasselli, J.G., 1991. The handbook of infrared and Raman characteristic frequencies of organic molecules. Elsevier.

Liu, X., Lu, M., Guo, Z., Huang, L., Feng, X., Wu, C., 2012. Improving the chemical stability of amorphous solid dispersion with cocrystal technique by hot melt extrusion. Pharm Res 29, 806-817.

Liu, X., Zhou, L., Zhang, F., 2017. Reactive Melt Extrusion to Improve the Dissolution Performance and Physical Stability of Naproxen Amorphous Solid Dispersions. Molecular Pharmaceutics.

Luo, Y., Wang, Q., 2014. Recent development of chitosan-based polyelectrolyte complexes with natural polysaccharides for drug delivery. International Journal of Biological Macromolecules 64, 353-367.

Maniruzzaman, M., Boateng, J.S., Chowdhry, B.Z., Snowden, M.J., Douroumis, D., 2014. A review on the taste masking of bitter APIs: hot-melt extrusion (HME) evaluation. Drug Development and Industrial Pharmacy 40, 145-156.

Maniruzzaman, M., Morgan, D.J., Mendham, A.P., Pang, J., Snowden, M.J., Douroumis, D., 2013. Drug–polymer intermolecular interactions in hot-melt extruded solid dispersions. International Journal of Pharmaceutics 443, 199-208.

Maniruzzaman, M., Snowden, M.J., Bradely, M.S., Douroumis, D., 2015. Studies of intermolecular interactions in solid dispersions using advanced surface chemical analysis. RSC Advances 5, 74212-74219.

Medina, C., Daurio, D., Nagapudi, K., Alvarez-Nunez, F., 2010. Manufacture of pharmaceutical co-crystals using twin screw extrusion: A solvent-less and scalable process. Journal of Pharmaceutical Sciences 99, 1693-1696.

Meka, V.S., Singe, M.K.G., Pichika, M.R., Nali, S.R., Kolapaili, V.R.M., Kesharwani, P., 2017. A comprehensive review on polyelectrolyte complexes. Drug Discovery Today 22, 1697-1706.

Ming, L., Zhefei, G., Yongcheng, L., Huishi, P., Ling, L., Xu, L., Xin, P., Chuanbin, W., 2014. Application of Hot Melt Extrusion for Poorly Water-Soluble Drugs: Limitations, Advances and Future Prospects. Current Pharmaceutical Design 20, 369-387.

Moore, J.W., Flanner, H.H., 1996. Mathematical comparison of dissolution profiles. Pharm. Tech. 20, 64-74.

Müller, M., 2014. Polyelectrolyte Complexes in the Dispersed and Solid State. Springer.

Nie, H., Su, Y., Zhang, M., Song, Y., Leone, A., Taylor, L.S., Marsac, P.J., Li, T., Byrn, S.R., 2016. Solid-State Spectroscopic Investigation of Molecular Interactions between Clofazimine and Hypromellose Phthalate in Amorphous Solid Dispersions. Molecular Pharmaceutics 13, 3964-3975.

Pavli, M., Baumgartner, S., Kos, P., Kogej, K., 2011. Doxazosin–carrageenan interactions: A novel approach for studying drug–polymer interactions and relation to controlled drug release. International Journal of Pharmaceutics 421, 110-119.

Pudipeddi, M., Zannou, E.A., Vasanthavada, M., Dontabhaktuni, A., Royce, A.E., Joshi, Y.M., Serajuddin, A.T., 2008. Measurement of surface pH of pharmaceutical solids: a

critical evaluation of indicator dye-sorption method and its comparison with slurry pH method. J Pharm Sci 97, 1831-1842.

Rumondor, A.C.F., Ivanisevic, I., Bates, S., Alonzo, D.E., Taylor, L.S., 2009. Evaluation of Drug-Polymer Miscibility in Amorphous Solid Dispersion Systems. Pharmaceutical Research 26, 2523-2534.

Shimada, Y., Goto, S., Uchiro, H., Hirabayashi, H., Yamaguchi, K., Hirota, K., Terada, H., 2013a. Features of heat-induced amorphous complex between indomethacin and lidocaine. Colloids and Surfaces B: Biointerfaces 102, 590-596.

Shimada, Y., Goto, S., Uchiro, H., Hirota, K., Terada, H., 2013b. Characteristics of amorphous complex formed between indomethacin and lidocaine hydrochloride. Colloids and Surfaces B: Biointerfaces 105, 98-105.

Siyawamwaya, M., Choonara, Y.E., Bijukumar, D., Kumar, P., Du Toit, L.C., Pillay, V., 2015. A Review: Overview of Novel Polyelectrolyte Complexes as Prospective Drug Bioavailability Enhancers. International Journal of Polymeric Materials and Polymeric Biomaterials 64, 955-968.

Song, Y., Zemlyanov, D., Chen, X., Nie, H., Su, Z., Fang, K., Yang, X., Smith, D., Byrn, S., Lubach, J.W., 2016. Acid-Base Interactions of Polystyrene Sulfonic Acid in Amorphous Solid Dispersions Using a Combined UV/FTIR/XPS/ssNMR Study. Mol Pharm 13, 483-492.

Takka, S., 2003. Propranolol hydrochloride–anionic polymer binding interaction. Il Farmaco 58, 1051-1056.

Telang, C., Mujumdar, S., Mathew, M., 2009. Improved physical stability of amorphous state through acid base interactions. Journal of Pharmaceutical Sciences 98, 2149-2159.

Thompson, C., Ibie, C., 2011. The oral delivery of proteins using interpolymer polyelectrolyte complexes. Ther Deliv 2, 1611-1631.

Wulff, R., Leopold, C.S., 2016. Coatings of Eudragit® RL and L-55 Blends: Investigations on the Drug Release Mechanism. AAPS PharmSciTech 17, 493-503.

Xanthos, M., 1992. Reactive extrusion: principles and practice. Hanser Publishers(Germany), 1992, 304.

Wen, H.; Park, K., Oral controlled release formulation design and drug delivery: theory to practice. John Wiley & Sons: 2011.

Tibbitt, M. W.; Dahlman, J. E.; Langer, R., Emerging Frontiers in Drug Delivery. Journal of the American Chemical Society 2016, 138 (3), 704-717.

Nokhodchi, A.; Raja, S.; Patel, P.; Asare-Addo, K., The Role of Oral Controlled Release Matrix Tablets in Drug Delivery Systems. BioImpacts : BI 2012, 2 (4), 175-187.

Siepmann, J.; Siegel, R.; Rathbone, M. J., Fundamentals and applications of controlled release drug delivery. 2012; p 1-594.

Maincent, J.; Williams, R. O., Sustained-release amorphous solid dispersions. Drug Delivery and Translational Research 2018, 8 (6), 1714-1725.

Ming, L.; Zhefei, G.; Yongcheng, L.; Huishi, P.; Ling, L.; Xu, L.; Xin, P.; Chuanbin, W., Application of Hot Melt Extrusion for Poorly Water-Soluble Drugs: Limitations, Advances and Future Prospects. Current Pharmaceutical Design 2014, 20 (3), 369-387.

Repka, M. A.; Bandari, S.; Kallakunta, V. R.; Vo, A. Q.; McFall, H.; Pimparade, M. B.; Bhagurkar, A. M., Melt extrusion with poorly soluble drugs – An integrated review. International Journal of Pharmaceutics 2018, 535 (1), 68-85.

Tiwari, R. V.; Patil, H.; Repka, M. A., Contribution of hot-melt extrusion technology to advance drug delivery in the 21st century. Expert Opinion on Drug Delivery 2016, 13 (3), 451-464.

Bouvier, J.-M.; Campanella, O. H., Extrusion Processing Technology: Food and Non-Food Biomaterials. John Wiley & Sons: 2014.

Raquez, J. M.; Narayan, R.; Dubois, P., Recent Advances in Reactive Extrusion Processing of Biodegradable Polymer-Based Compositions. Macromolecular Materials and Engineering 2008, 293 (6), 447-470.

Singh, S.; Gamlath, S.; Wakeling, L., Nutritional aspects of food extrusion: a review. International Journal of Food Science & Technology 2007, 42 (8), 916-929.

Lu, M., Continuous Co-crystallisation of Poorly Soluble Active Pharmaceutical Ingredients to Enhance Dissolution. In Practical Guide to Hot-Melt Extrusion: Continuous Manufacturing and Scale-up, Maniruzzaman, M., Ed. Smithers Rapra: 2016; pp 75-93.

Arnfast, L.; Kamruzzaman, M.; Löbmann, K.; Aho, J.; Baldursdottir, S.; Rades, T.; Rantanen, J., Melt Extrusion of High-Dose Co-Amorphous Drug-Drug Combinations. Pharmaceutical Research 2017, 34 (12), 2689-2697.

Liu, X.; Zhou, L.; Zhang, F., Reactive Melt Extrusion To Improve the Dissolution Performance and Physical Stability of Naproxen Amorphous Solid Dispersions. Molecular Pharmaceutics 2017, 14 (3), 658-673.

Kindermann, C.; Matthée, K.; Strohmeyer, J.; Sievert, F.; Breitkreutz, J., Tailor-made release triggering from hot-melt extruded complexes of basic polyelectrolyte and poorly water-soluble drugs. European Journal of Pharmaceutics and Biopharmaceutics 2011, 79 (2), 372-381.

Gârea, S. A.; Voicu, A. I.; Iovu, H., Clay–Polymer Nanocomposites for Controlled Drug Release. In Clay-Polymer Nanocomposites, Elsevier: 2017; pp 475-509.

Rodrigues, L. A. D.; Figueiras, A.; Veiga, F.; de Freitas, R. M.; Nunes, L. C. C.; da Silva, E. C.; Leite, C. M. D., The systems containing clays and clay minerals from modified drug release: A review. Colloids and Surfaces B-Biointerfaces 2013, 103, 642-651.

Jayrajsinh, S.; Shankar, G.; Agrawal, Y. K.; Bakre, L., Montmorillonite nanoclay as a multifaceted drug-delivery carrier: A review. Journal of Drug Delivery Science and Technology 2017, 39, 200-209.

Meirelles, L. M. A.; Raffin, F. N., Clay and Polymer-Based Composites Applied to Drug Release: A Scientific and Technological Prospection. Journal of Pharmacy & Pharmaceutical Sciences 2017, 20, 115-134.

Kotal, M.; Bhowmick, A. K., Polymer nanocomposites from modified clays: Recent advances and challenges. Progress in Polymer Science 2015, 51, 127-187.

Sinha Ray, S.; Okamoto, M., Polymer/layered silicate nanocomposites: a review from preparation to processing. Progress in Polymer Science 2003, 28 (11), 1539-1641.

Zang, Y.; Xu, W.; Qiu, D.; Chen, D.; Chen, R.; Su, S., Synthesis, characterization and thermal stability of different polystyryl quaternary ammonium surfactants and their montmorillonite complexes. Thermochimica Acta 2008, 474 (1), 1-7.

Chiu, C.-W.; Huang, T.-K.; Wang, Y.-C.; Alamani, B. G.; Lin, J.-J., Intercalation strategies in clay/polymer hybrids. Progress in Polymer Science 2014, 39 (3), 443-485.

256

Choudalakis, G.; Gotsis, A. D., Permeability of polymer/clay nanocomposites: A review. European Polymer Journal 2009, 45 (4), 967-984.

Salahuddin, N.; Kenawy, E.-R.; Abdeen, R., Polyoxypropylene–montmorillonite nanocomposites for drug-delivery vehicles: Preparation and characterization. J. Appl. Polym. Sci. 2012, 125 (S1), E157-E166.

Pavlidou, S.; Papaspyrides, C. D., A review on polymer–layered silicate nanocomposites. Progress in Polymer Science 2008, 33 (12), 1119-1198.

Bharadwaj, R. K., Modeling the barrier properties of polymer-layered silicate nanocomposites. Macromolecules 2001, 34 (26), 9189-9192.

Riela, S.; Fakhrullin, R. F., Clay-based drug-delivery systems: what does the future hold? Therapeutic delivery 2017, 8 (8), 633-646.

García Guzmán, P.; Medina-Torres, L.; Calderas, F.; Josefa Bernad-Bernad, M.; Gracia-Mora, J.; Mena, B.; Manero, O., Characterization of hybrid microparticles/Montmorillonite composite with raspberry-like morphology for Atorvastatin controlled release. 2018; Vol. 167.

Sharma, A. K.; Mortensen, A.; Schmidt, B.; Frandsen, H.; Hadrup, N.; Larsen, E. H.; Binderup, M. L., In-vivo study of genotoxic and inflammatory effects of the organo-modified Montmorillonite Cloisite® 30B. Mutation Research/Genetic Toxicology and Environmental Mutagenesis 2014, 770, 66-71.

Khlibsuwan, R.; Siepmann, F.; Siepmann, J.; Pongjanyakul, T., Chitosan-clay nanocomposite microparticles for controlled drug delivery: Effects of the MAS content and TPP crosslinking. Journal of Drug Delivery Science and Technology 2017, 40 (Supplement C), 1-10.

Campbell, K. T.; Craig, D. Q. M.; McNally, T., Modification of ibuprofen drug release from poly(ethylene glycol) layered silicate nanocomposites prepared by hot-melt extrusion. Journal of Applied Polymer Science 2014, 131 (10), n/a-n/a.

Rives, V.; del Arco, M.; Martín, C., Intercalation of drugs in layered double hydroxides and their controlled release: A review. Applied Clay Science 2014, 88, 239-269.

Rives, V.; del Arco, M.; Martín, C., Layered double hydroxides as drug carriers and for controlled release of non-steroidal antiinflammatory drugs (NSAIDs): A review. Journal of Controlled Release 2013, 169 (1), 28-39.

Bee, S.-L.; Abdullah, M. A. A.; Mamat, M.; Bee, S.-T.; Sin, L. T.; Hui, D.; Rahmat, A. R., Characterization of silylated modified clay nanoparticles and its functionality in PMMA. Composites Part B: Engineering 2017, 110, 83-95.

Hanada, M.; Jermain, S. V.; Lu, X.; Su, Y.; Williams, R. O., Predicting physical stability of ternary amorphous solid dispersions using specific mechanical energy in a hot melt extrusion process. International Journal of Pharmaceutics 2018, 548 (1), 571-585.

Tan, B.; Thomas, N. L., A review of the water barrier properties of polymer/clay and polymer/graphene nanocomposites. Journal of Membrane Science 2016, 514, 595-612.

Paul, D. R.; Robeson, L. M., Polymer nanotechnology: Nanocomposites. Polymer 2008, 49 (15), 3187-3204.

Carretero, M. I.; Pozo, M., Clay and non-clay minerals in the pharmaceutical industry: Part I. Excipients and medical applications. Applied Clay Science 2009, 46 (1), 73-80.

Liu, K.-H.; Liu, T.-Y.; Chen, S.-Y.; Liu, D.-M., Drug release behavior of chitosan–montmorillonite nanocomposite hydrogels following electrostimulation. Acta Biomaterialia 2008, 4 (4), 1038-1045.

Lin-Vien, D.; Colthup, N. B.; Fateley, W. G.; Grasselli, J. G., The handbook of infrared and Raman characteristic frequencies of organic molecules. Elsevier: 1991.

He, H. P.; Zhu, J., Chapter 10 - Analysis of Organoclays and Organic Adsorption by Clay Minerals. In Developments in Clay Science, Gates, W. P.; Kloprogge, J. T.; Madejová, J.; Bergaya, F., Eds. Elsevier: 2017; Vol. 8, pp 310-342.

Madejová, J.; Gates, W. P.; Petit, S., Chapter 5 - IR Spectra of Clay Minerals. In Developments in Clay Science, Gates, W. P.; Kloprogge, J. T.; Madejová, J.; Bergaya, F., Eds. Elsevier: 2017; Vol. 8, pp 107-149.

Johnston, C. T., Chapter 9 - Infrared Studies of Clay Mineral-Water Interactions. In Developments in Clay Science, Gates, W. P.; Kloprogge, J. T.; Madejová, J.; Bergaya, F., Eds. Elsevier: 2017; Vol. 8, pp 288-309.

Xu, W.; Johnston, C. T.; Parker, P.; Agnew, S. F., Infrared study of water sorption on Na-, Li-, Ca-, and Mg-exchanged (SWy-1 and SAz-1) montmorillonite. Clays and Clay Minerals 2000, 48 (1), 120-131.

Slosiariková, H.; Bujdák, J.; Hlavatý, V., IR spectra of octadecylammonium-montmorillonite in the range of the Si-O vibrations. Journal of inclusion phenomena and molecular recognition in chemistry 1992, 13 (3), 267-272.

Ma, Y.; Zhu, J.; He, H.; Yuan, P.; Shen, W.; Liu, D., Infrared investigation of organo-montmorillonites prepared from different surfactants. Spectrochimica Acta Part A: Molecular and Biomolecular Spectroscopy 2010, 76 (2), 122-129.

Martini, F.; Geppi, M.; Borsacchi, S., Chapter 9 - NMR Spectroscopy of Clay–Polymer Nanocomposites A2 - Jlassi, Khouloud. In Clay-Polymer Nanocomposites, Chehimi, M. M.; Thomas, S., Eds. Elsevier: 2017; pp 307-325.

Lu, X.; Huang, C.; Lowinger, M. B.; Yang, F.; Xu, W.; Brown, C. D.; Hesk, D.; Koynov, A.; Schenck, L.; Su, Y., Molecular Interactions in Posaconazole Amorphous Solid Dispersions from Two-Dimensional Solid-State NMR Spectroscopy. Molecular Pharmaceutics 2019, 16 (6), 2579-2589.

Duan, P.; Schmidt-Rohr, K., Composite-pulse and partially dipolar dephased multiCP for improved quantitative solid-state 13C NMR. Journal of Magnetic Resonance 2017, 285, 68-78.

Becker, O.; Varley, R. J.; Simon, G. P., Thermal stability and water uptake of high performance epoxy layered silicate nanocomposites. European Polymer Journal 2004, 40 (1), 187-195.

Liu, X.; Wu, Q., Polyamide 66/Clay Nanocomposites via Melt Intercalation. 2002, 287 (3), 180-186.

Rhim, J.-W.; Hong, S.-I.; Ha, C.-S., Tensile, water vapor barrier and antimicrobial properties of PLA/nanoclay composite films. LWT - Food Science and Technology 2009, 42 (2), 612-617.

Duan, Z.; Thomas, N. L.; Huang, W., Water vapour permeability of poly(lactic acid) nanocomposites. Journal of Membrane Science 2013, 445, 112-118.

Jesus, C. R. N.; Molina, E. F.; Pulcinelli, S. H.; Santilli, C. V., Highly Controlled Diffusion Drug Release from Ureasil–Poly(ethylene oxide)–Na+–Montmorillonite Hybrid Hydrogel Nanocomposites. ACS Applied Materials & Interfaces 2018, 10 (22), 19059-19068.

Alexandre, B.; Langevin, D.; Médéric, P.; Aubry, T.; Couderc, H.; Nguyen, Q. T.; Saiter, A.; Marais, S., Water barrier properties of polyamide 12/montmorillonite nanocomposite

membranes: Structure and volume fraction effects. Journal of Membrane Science 2009, 328 (1), 186-204.

Huskić, M.; Žigon, M.; Ivanković, M., Comparison of the properties of clay polymer nanocomposites prepared by montmorillonite modified by silane and by quaternary ammonium salts. Applied Clay Science 2013, 85, 109-115.

Ianchis, R.; Cinteza, L. O.; Donescu, D.; Petcu, C.; Corobea, M. C.; Somoghi, R.; Ghiurea, M.; Spataru, C., Implications of silylated montmorillonite on montmorillonite–polyacrylate nanocomposites. Applied Clay Science 2011, 52 (1), 96-103.

Patra, C. N.; Priya, R.; Swain, S.; Kumar Jena, G.; Panigrahi, K. C.; Ghose, D., Pharmaceutical significance of Eudragit: A review. Future Journal of Pharmaceutical Sciences 2017, 3 (1), 33-45.

Azarmi, S.; Farid, J.; Nokhodchi, A.; Bahari-Saravi, S. M.; Valizadeh, H., Thermal treating as a tool for sustained release of indomethacin from Eudragit RS and RL matrices. International Journal of Pharmaceutics 2002, 246 (1), 171-177.

Lyons, J. G.; Holehonnur, H.; Devine, D. M.; Kennedy, J. E.; Geever, L. M.; Blackie, P.; Higginbotham, C. L., The incorporation of an organically modified layered silicate in monolithic polymeric matrices produced using hot melt extrusion. Mater Chem Phys 2007, 103 (2–3), 419-426.

Ha, J. U.; Xanthos, M., Drug release characteristics from nanoclay hybrids and their dispersions in organic polymers. International Journal of Pharmaceutics 2011, 414 (1–2), 321-331.

Dening, T. J.; Rao, S.; Thomas, N.; Prestidge, C. A., Montmorillonite-lipid hybrid carriers for ionizable and neutral poorly water-soluble drugs: Formulation, characterization and in vitro lipolysis studies. International Journal of Pharmaceutics 2017, 526 (1–2), 95-105.

Vita

Xu Liu was born in Hengyang, China. He graduated from Qidong Yuxian School in 2004. He got his B.S. degree in pharmacy from Southern Medical University (First Military Medical University) in 2008. He served as an undergraduate research assistant in Prof. Jianxin Pang's lab from 2007 to 2008 to study the human telomerase catalytic submit prey fusion protein for drug screening. After graduation from Southern Medical University, he joined the Pharmaceutical Sciences master program at Sun Yat-Sen University in 2008, working in Prof. Chuanbin Wu's group. His master research focused on investigating the application of cocrystal technique to improve the chemical stability of amorphous solid dispersion prepared by hot melt extrusion. He published eight articles and filed one patent during his master study. He was awarded "First-Prize Professional Scholarship" by The Sun Yat-Sen University. After graduation in 2011, he worked a formulation scientist in Guangzhou Baiyunshan Pharmaceutical company. In 2014, he joined The University of Texas at Austin to pursue his Ph.D. degree in Pharmaceutic Sciences under the supervision of Dr. Feng Zhang. His research focused on the application of hot melt extrusion in drug delivery area. During his Ph.D. study, he was awarded several prestigious fellowships, include: the Duane A. Boyle Fellowship (2017-2018); the ACPA Research Award (2018); the AAPS Best Abstract Award (2019); The Dr. James W. McGinity Graduate Fellowship (2019-2020); and the University of Texas at Austin Graduate School Dissertation Writing Fellowship (2020 Spring).

Permanent e-mail address: xliu@utexas.edu

This dissertation was typed by the author.